

2016

Expanding the Applications of Ion Mobility Spectrometry and Mass Spectrometry in Integrative 'Omics Analyses

Gregory C. Donohoe

Follow this and additional works at: <https://researchrepository.wvu.edu/etd>

Recommended Citation

Donohoe, Gregory C., "Expanding the Applications of Ion Mobility Spectrometry and Mass Spectrometry in Integrative 'Omics Analyses" (2016). *Graduate Theses, Dissertations, and Problem Reports*. 5505.
<https://researchrepository.wvu.edu/etd/5505>

This Dissertation is protected by copyright and/or related rights. It has been brought to you by the The Research Repository @ WVU with permission from the rights-holder(s). You are free to use this Dissertation in any way that is permitted by the copyright and related rights legislation that applies to your use. For other uses you must obtain permission from the rights-holder(s) directly, unless additional rights are indicated by a Creative Commons license in the record and/ or on the work itself. This Dissertation has been accepted for inclusion in WVU Graduate Theses, Dissertations, and Problem Reports collection by an authorized administrator of The Research Repository @ WVU. For more information, please contact researchrepository@mail.wvu.edu.

Expanding the Applications of Ion Mobility Spectrometry and Mass Spectrometry in Integrative 'Omics Analyses

Gregory C. Donohoe

Dissertation submitted to the
Eberly College of Arts and Sciences
at West Virginia University
in partial fulfillment of the requirements
for the degree of

Doctor of Philosophy
In
Analytical Chemistry

Approved by
Stephen J. Valentine, Ph.D., Committee Chairperson
Lisa A. Holland, Ph.D.
Fred L. King, Ph.D.
Brian V. Popp, Ph.D.
Andrew K. Shiemke, Ph.D.

C. Eugene Bennett Dept. of Chemistry

Morgantown, West Virginia
2016

Key Terms: ion mobility, mass spectrometry, hydrogen deuterium exchange (HDX),
'omics, electron transfer dissociation, parallel dissociation, collision induced
dissociation, charge transfer dissociation, metabolomics, phosphoproteomics,
proteomics, ubiquitin,

Copyright 2016 Gregory C. Donohoe

ABSTRACT

Expanding the Applications of Ion Mobility Spectrometry and Mass Spectrometry in Integrative 'Omics Analyses

Gregory C. Donohoe

Over the past few decades, biomolecular analyses ranging from the study of complex mixtures to protein structural interrogation have increased significantly. These studies range from small molecule separations[1, 2] to observing structural trends in large proteins and protein sub-complexes.[3, 4] Traditionally, the use of liquid chromatography mass spectrometry (LC-MS), electrophoresis and nuclear magnetic resonance (NMR) spectroscopy have been at the forefront of these respective studies. Because complex mixtures can contain a variety of components over a wide dynamic range and proteins and their complexes can contain a diverse array of structures, few analytical techniques are capable of providing information across all experimental areas (e.g. small molecule mixtures to large individual proteins). In contrast, the use of Ion Mobility Spectrometry-Mass Spectrometry (IMS-MS) has emerged as a powerful tool for measuring ion(s) structural heterogeneity. While IMS-MS is a relatively newer method, workflows are becoming more common as the commercialization of IMS instruments has created a larger user base. Such workflows now include metabolomic,[1, 5, 6] lipidomic,[7] proteomics and protein structural analyses[8, 9]. Taken collectively, these areas encompass the field of 'omics' analysis. While each field has its respective difficulties, IMS-MS is well poised to enhance and even expand the repertoire of analytical platforms for omics analyses.

Much of the current bottlenecks in traditional techniques suffer from an inability to sample measureable species rapidly in a reproducible manner over a wide dynamic range. For example, Anderson and coworkers have proposed that the plasma proteome includes 10^6 - 10^7 species that span a concentration range of 10^{11} . [10] In many cases, IMS has shown improved resolution of isomeric species compared to either LC or Gas Chromatography (GC) analyses.[11, 12] The utility of IMS-MS in profiling is largely attributed to its rapid ability to resolve low-abundance species from spectral regions containing high-abundance species, thereby increasing measurement sensitivity, dynamic range and peak capacity.[13-17] Additionally, IMS is capable of separating isobaric species that cannot be resolved by MS alone. In 'omic profiling directed toward biomarker discovery, it is imperative to identify compounds of interest. The identification is complicated by compound diversity (class and structural variation).

Traditionally, as well as all commercially available, IMS-MS instruments use Time-of-Flight (ToF) mass analyzers for determining an ion's mass-to-charge ratio (m/z). The obvious advantage is the ability to nest the m/z measurement (μ s) within the drift measurement (ms). This creates an orthogonal separation where many m/z measurements are made during the drift separation. Although this combination creates a rapid, multidimensional analysis, ToF mass analyzers are not capable of multistage

tandem mass spectrometry (MS^n) or nonergodic dissociation methods such as electron transfer dissociation (ETD). These MS fragmentation methods are often used as standalone techniques in applications ranging from small molecule identification within complex mixtures to identifying high order structure in proteins using Hydrogen Deuterium exchange (HDX) MS. To this end, new applications of IMS-MS that leverage the use of ion trapping MS are useful for supplementing these limitations of ToF analyzers. Trapping mass analyzers add the capability to perform ion-neutral or ion-ion reactions on drift-selected ions. In such experiments, fragment ions are generated and are structurally useful in identifying and quantifying individual components or those that compose protein structures or post translational modifications (PTMs). *To date, very few, if any, experiments have attempted to combine the unique capabilities of IMS-MS with MS^n or ETD-MS for uncovering ion structural information or heterogeneity.* As will be shown in the coming chapters, coupling IMS to trapping mass analyzers expands the capabilities into new areas of 'omics analysis and enhances the information that can be obtained from either technique alone.

1. Dwivedi, P., et al., *Metabolic profiling by ion mobility mass spectrometry (IMMS)*. *Metabolomics*, 2008. **4**(1): p. 63-80.
2. Valentine, S.J., et al., *Gas-phase separations of protease digests*. *Journal of the American Society for Mass Spectrometry*, 1998. **9**(11): p. 1213-1216.
3. Ruotolo, B.T., et al., *Evidence for macromolecular protein rings in the absence of bulk water*. *Science*, 2005. **310**(5754): p. 1658-1661.
4. van Duijn, E., et al., *Native tandem and ion mobility mass spectrometry highlight structural and modular similarities in clustered-regularly-interspaced shot-palindromic-repeats (CRISPR)-associated protein complexes from Escherichia coli and Pseudomonas aeruginosa*. *Mol Cell Proteomics*, 2012. **11**(11): p. 1430-41.
5. Zhang, X., et al., *Metabolic Analysis of Striatal Tissues from Parkinson's Disease-like Rats by Electrospray Ionization Ion Mobility Mass Spectrometry*. *Analytical Chemistry*, 2014.
6. Paglia, G., et al., *Ion Mobility Derived Collision Cross Sections to Support Metabolomics Applications*. *Analytical Chemistry*, 2014. **86**(8): p. 3985-3993.
7. Kliman, M., J.C. May, and J.A. McLean, *Lipid analysis and lipidomics by structurally selective ion mobility-mass spectrometry*. *Biochimica et Biophysica Acta (BBA) - Molecular and Cell Biology of Lipids*, 2011. **1811**(11): p. 935-945.
8. Zhuang, X., et al., *Identification of Unfolding and Dissociation Pathways of Superoxide Dismutase in the Gas Phase by Ion-Mobility Separation and Tandem Mass Spectrometry*. *Analytical Chemistry*, 2014. **86**(23): p. 11599-11605.
9. Allen, S.J., A.M. Schwartz, and M.F. Bush, *Effects of polarity on the structures and charge states of native-like proteins and protein complexes in the gas phase*. *Anal Chem*, 2013. **85**(24): p. 12055-61.
10. Anderson, N.L., et al., *The human plasma proteome: a nonredundant list developed by combination of four separate sources*. *Mol Cell Proteomics*, 2004. **3**(4): p. 311-26.
11. Wu, C., et al., *Separation of isomeric peptides using electrospray ionization/high-resolution ion mobility spectrometry*. *Anal Chem*, 2000. **72**(2): p. 391-5.
12. Dwivedi, P., et al., *Rapid Resolution of Carbohydrate Isomers by Electrospray Ionization Ambient Pressure Ion Mobility Spectrometry-Time-of-Flight Mass Spectrometry (ESI-APIMS-TOFMS)*. *Journal of the American Society for Mass Spectrometry*, 2007. **18**(7): p. 1163-1175.
13. Valentine, S.J., et al., *Toward Plasma Proteome Profiling with Ion Mobility-Mass Spectrometry*. *Journal of Proteome Research*, 2006. **5**(11): p. 2977-2984.
14. Zinnel, N.F., P.J. Pai, and D.H. Russell, *Ion Mobility-Mass Spectrometry (IM-MS) for Top-Down Proteomics: Increased Dynamic Range Affords Increased Sequence Coverage*. *Analytical Chemistry*, 2012. **84**(7): p. 3390-3397.

15. Dwivedi, P., A.J. Schultz, and H.H. Hill, *Metabolic profiling of human blood by high-resolution ion mobility mass spectrometry (IM-MS)*. International Journal of Mass Spectrometry, 2010. **298**(1-3): p. 78-90.
16. Ruotolo, B.T., et al., *Peak capacity of ion mobility mass spectrometry: Separation of peptides in helium buffer gas*. Journal of Chromatography B-Analytical Technologies in the Biomedical and Life Sciences, 2002. **782**(1-2): p. 385-392.
17. Counterman, A.E., et al., *Formation of peptide aggregates during ESI: Size, charge, composition, and contributions to noise*. Journal of the American Society for Mass Spectrometry, 2001. **12**(9): p. 1020-1035.

Dedication

I dedicate this work to my wife, Allyson and unborn son, Cole. You have made this work worth doing and you are both my inspiration. I thank my wife for her patients and willingness to supporting my decisions throughout my graduate career. You have made me a better man. My goal is to provide our family with a comfortable life.

Acknowledgements

I would like to express my deepest gratitude towards every individual who has served as a mentor over my chemistry career: Dr. Matthew Scanlon and Dr. Andreas Baur for introducing me to chemistry and giving me a scientific foundation from which to grow; Ahmad Rhaman for his scientific insight, direction and conversation; Dr. Lisa Holland for her most valued mentorship and high expectations. Your advice and teachings have changed my perception of science and my views on how to be a scientist. Thank you for always taking the time to share your wisdom both scientifically and personally; Dr. Fred King for getting me started with mass spectrometry. Words can't express how thankful I am to have taken your mass spectrometry class. You have undoubtedly introduced me to one of my greatest interests in life – thank you; Dr. Brian Popp for being one of the most knowledgeable scientists I've met. Your scientific understanding is rich and always ignites great discussions and future directions – I truly admire that; Dr. Andrew Shiemke for agreeing to be a part of my graduate career and always offering fruitful discussions about biochemistry and protein structure; and Dr. Stephen Valentine for having to work with my strengths and weakness. Thank you for your willingness to teach me your expertise and the patients to answer every question. I am beyond thankful that I had the opportunity to learn from someone I very much respect. I am most sincerely grateful that you were my academic mentor.

I would also like to thank my peers, Jim Arndt, Brian Nichols, Hossein Maleki, Mahdiar Khakenejad, Samaneh Kondalaji and Megan Maurer. I think we've all grown together and been presented the unique opportunity to learn from one another. I've truly enjoyed my time with you all. I wish each one of you success in all of your challenges and scientific opportunities. I believe my memories in the Valentine group and my graduate career at WVU will last a lifetime.

TABLE OF CONTENTS

Abstract	ii
Dedication	vi
Acknowledgements	vi
Table of Contents	viii
Appendices	xiv
List of Figures	xv
List of Tables	xvii
List of Symbols and Abbreviations	xvii
1. Introduction: Applications of Ion Mobility Spectrometry and Mass Spectrometry in ‘Omic Analyses	1
1.1. Fundamentals of Ion Mobility Spectrometry (IMS)	1
1.2. Fundamentals of Mass Spectrometry (MS) – Linear Ion Traps	8
1.3. Collision Induced Dissociation (CID) in Trapping Mass Analyzers	13
1.3.1. CID of Peptides and Proteins: <i>b</i> – and <i>y</i> – ions	13
1.3.2. CID of Small Molecules: Understanding Fragmentation	14
1.4. IMS-MS Metabolomics and Small Molecule Studies	15
1.5. An Overview of the Metablome and Traditional Techniques	16
1.5.1. Parallel Dissociation Combined with IM-MS for Data Independent Analysis of Small Molecules	18
1.6. Electron Transfer Dissociation (ETD) of Peptides and Proteins	20
1.6.1. ETD Mechanism: <i>c</i> – and <i>z</i> – ions	21
1.6.2. IMS – ETD – MS Techniques	22
1.7. Phosphoproteomics and MS Techniques	23
	viii

1.7.1. Coupling IM-CID-ETD-MS for Determining the Presence and Location of Phosphorylation from Complex Mixtures.	25
1.8. Solution Hydrogen Deuterium Exchange: Fundamentals	26
1.8.1. Bottom – up Hydrogen Deuterium Exchange – Mass Spectrometry (HDX – MS)	28
1.8.2. Top – down HDX – MS	29
1.8.2.1. Pre – residue Deuterium Measurements	30
1.8.3. Solution HDX Coupled with IMS – ETD – MS	31
1.9. Gas Phase Hydrogen Deuterium Exchange Coupled with IMS-MS	32
1.10. Helium Charge Transfer Dissociation	35
1.11. References	37
2. A New Ion Mobility – Linear Ion Trap for Complex Mixture Analysis	47
2.1. Introduction: Complex Mixture Separations Using IMS-MS	47
2.2. Materials and Methods	50
2.2.1. Phosphoproteomic Samples	50
2.2.2. Rat Exposure to TiO ₂ Nanoparticles	50
2.2.2.1. Metabolite Extraction	51
2.2.3. IMS-MS: Instrumental Operation	52
2.2.3.1. Recording Two – Dimensional (2D) $t_D(m/z)$ Distributions	53
2.2.3.2. Parallel Dissociation	53
2.2.4. Mass Spectrometry Measurements	54
2.2.5. Generating IMS-MS Datasets	55
2.2.5.1. Comparing IMS-MS Datasets	55

2.2.6. Detection Limit Sample Preparation	56
2.2.7. Dynamic Range Sample Preparation	56
2.2.8. Principal Component Analysis (PCA)	56
2.2.9. Exact Mass Measurements	57
2.3. Results and Discussion	57
2.3.1. Instrument Figures of Merit	57
2.3.1.1. Detection Limit Studies	58
2.3.1.2. Dynamic Range Studies	59
2.3.2. Phosphopeptide Analysis	60
2.3.2.1. Aligning Extracted Ion Drift Time Distributions (XIDTDs)	61
2.3.2.2. IMS – CID – ETD – MS of Precursor and Fragment ions	61
2.3.3. A Comparative IMS – MS Analysis of Metabolomic Samples	64
2.3.3.1. PCA of Sample Cohorts	66
2.3.3.2. Comparing Extraction Ion Drift Time Distributions (XIDTDs)	67
2.3.3.3. IMS – MS ⁿ Experiments for Metabolomic Analysis	70
2.3.3.4. IMS – CID – MS Measurements	72
2.2.4. Instrumental Implication for Comparative Analyses	77
2.4.. References	78
3. Negative ion IMS-HDX-MS	82
3.1. Introduction: A Base for Studying Anionic Peptides and Proteins	82
3.2. Method and Materials	83
3.2.1. Sample Preparation	83

3.2.2. IMS-MS: Instrumental Operation	84
3.2.2.1. Recording Two – Dimensional (2D) $t_D(m/z)$ Distributions	85
3.2.3. Mass Spectrometry Measurements	85
3.2.4. Generating IMS-MS Datasets	86
3.2.5. Gas Phase HDX Experiment Design	86
3.2.5.1. HDX Levels and Rate Constants	87
3.3. Results and Discussion	87
3.3.1. Protein Anion Collision Cross Sections	87
3.3.2. Gas – Phase Deuterium Uptake as a Function of D ₂ O Pressure	90
3.3.2.1. Anion HDX levels	93
3.3.2.2. HDX Kinetics of Deprotonated Peptides and Proteins	95
3.3.3. Structural Implications of the HDX Results	96
3.3.4.1. Exchange Efficiency and the Protein Fold – Ubiquitin	97
3.3.4. Experimental Limitations	101
3.3.5. Conclusions	102
3.3.6. References	104
4. On – line Deuterium Hydrogen Exchange and Pepsin Digestion Coupled to IMS – MS and Tandem Mass Spectrometry	109
4.1. Introduction: Deuterium Hydrogen Exchange and IMS – MS	109
4.2. Methods and Materials	112
4.2.1. Sample Preparation	112
4.2.2. On – Line DHX – PD – IMS System	112

4.2.3. Scrambling Control On – Line System	114
4.2.3.1. Optimized Parameters	115
4.2.3. IMS-MS: Instrumental Operation	115
4.2.3.1. Recording Two – Dimensional (2D) $t_D(m/z)$ Distributions	116
4.2.4. Mass Spectrometry Measurements	116
4.2.4.1. CID – MS Experiments	117
4.2.4.1.1. Identification of Precursor Ions	117
4.2.4.2. Deuterated Samples and ETD Analysis	117
4.2.4.3. IMS – MS Datasets	118
4.2.4.3. Comparing XIDTDs for Identification	119
4.2.4.4. Per – Residue Deuterium Measurements	119
4.3. Results and Discussion	119
4.3.1. Comparing Peptides and 2D IMS – MS Datasets	121
4.3.2. Generating XIDTDs and Combing CID for Unlabeled Peptide Identification	121
4.3.3. Matching XIDTDs Between Undeuterated and Deuterated Datasets	123
4.3.4. Overall Per – Peptide Deuterium Analysis – Ubiquitin	125
4.3.5. Scrambling Control Peptide Studies	127
4.3.6. IMS – ETD –MS of Deuterated Peptides for Per – Residue Analysis – Ubiquitin	128
4.3.7. Reproducibility of the On – Line DHX–PD–IMS–MS System	132
4.3.8. Assessment of the Effects of ESI Solvent Composition	136
4.3.9. Instrumental Implications and Conclusion	136

5. Helium Charge Transfer Dissociation Combined with Deuterium Hydrogen Exchange Mass Spectrometry	143
5.1. Introduction: Fragmentation Techniques and Hydrogen Deuterium Scrambling	143
5.2. Method and Materials	144
5.2.1. Sample Preparation	145
5.2.2. Modified Instrument	145
5.2.3. HD – Scrambling Peptide	146
5.2.4. Mass Spectrometry Measurements and Parameters	147
5.2.4.1. ETD Measurements	147
5.2.4.2. He-CTD Measurements	148
5.2.5. Per-Residue Deuterium Measurements	148
5.3. Results and Discussion	149
5.3.1. Peptide Control Studies and HD – Scrambling Evaluation	149
5.3.1.1. He-CTD HD-Scrambling Analysis	149
5.3.1. He – CTD Mechanistic Insights for c – ions	151
5.3.2. Ammonia Neutral Loss and N – terminal Scrambling	155
5.3.3. DHX – He – CTD – MS Structural Determinations	158
5.3.3.1. Per – Residue ETD – MS Analysis: Control	160
5.3.3.2. Per – Residue He – CTD – MS Analysis	162
5.4. Conclusion	164
5.5. References	166
6. Future Directions: Applied ‘Omics using IMS-MS Techniques	168

6.1. Post Translational Modifications: Phosphorylation	168
6.1.1. Doubly – Phosphorylated Peptides from Complex Mixtures	168
6.1.2. Conducting IMS-CID-MS on Glycosylated Proteins	169
6.2. Expanding the Usage of IMS-CID-MS in Metabolomic Workflows	170
6.3. Gas Phase HDX of Anionic Proteins	172
6.3.1. Comparing Cationic and Anionic HDX Deuterium Level: Structural Studies	173
6.3.2. Binding Faces of Acidic Proteins Involved in Protein Aggregates	174
6.3.3. Gas Phase HDX and Anionic Glycans: Structural Considerations and Separation Techniques	174
6.4. Solution – Base DHX Coupled with IMS-ETD-MS	175
6.4.1. Constructing a New Micro-fluidic Chip of On – Line Analysis	175
6.4.2. Increasing Sequence Coverage for Per-residue Studies	176
6.4.3. Evaluating Larger Proteins	177
6.4.4. Connecting Rapid Solution Structural Changes with Solution DHX and IMS-MS	177
6.5. Helium Charge Transfer Dissociation : Insights and Future Outlook	178
6.5.1. Using He – CTD for Anionic Peptides and Proteins	178
6.5.2. Evaluating Other Ions for HD-Scrambling	179
6.5.3. Other Potential Usages; IMS – He – CTD – MS	179
6.6. References	181

Appendices

Appendix 1. Optimized Instrumental Parameters for DHX-IMS-ETD-MS	183
Appendix 2. Optimized Instrumental parameters for DHX-He-CTD-MS	185

LIST OF FIGURES

1.1. Schematic of the ion mobility linear ion trap	2
2.1. Mass spectrum of model peptide $[M+3H]^{3+}$	59
2.2. XIDTD of Cytochrom c Tryptic Peptide m/z 806.5	60
2.3. Two-dimensional (2D) $t_D(m/z)$ heat-plot of a cytochrome c tryptic digest containing the phosphorylated peptide standard $[KRP_sQRHGSKY-NH_2]$	62
2.4. (A) Mobility – selected IMS-CID-ETD-MS spectra of $[KRP_sQRHGSKY-NH_2+3H]^{3+}$ precursor and (B) Neutral loss fragment ion	63
2.5. $t_D(m/z)$ heat-plot of the EXP24 metabolite extract	65
2.6. (A) PCA plot of all sample cohorts (B) loadings matrix values for metabolite ions	67
2.7. (A) XIDTDs comparison of m/z 518.3 and (B) 732.2 for Exposed 24 for Control 24 sample cohorts	69
2.8. Multistage tandem mass spectrometry of m/z 518.3 and 542.3	71
2.9. $t_D(m/z)$ heat-plot of the EXP24 sample obtained from an IMS-CID-MS experiment.	73
2.10. Matching XIDTDs of fragment ions to precursor ions	74
2.11. semi-quantitative assessment for matching XIDTDs from IMS-CID-MS experiments	76
3.1. (A) Two-dimensional, $t_D(m/z)$ dot plot of electrosprayed ubiquitin ions and (B) , $t_D(m/z)$ dot plot of electrosprayed ubiquitin ions at a partial pressure of 0.04 torr D_2O	88
3.2. (A) Collision Cross Section for protein and (B) insulin anions	90
3.3. (A) Plot of deuterium uptake and (B) Plot of the natural log of the number of remaining exchanged residues. Both are plotted against the product of the partial pressure D_2O and drift time	91
3.4. Plot of the maximum HDX level for protein anionic conformers	94
3.5. Expanded Two-dimensional, $t_D(m/z)$ heat plot of the $[M-6H]^{6-}$ charge state of	98

ubiquitin after gas phase HDX with D ₂ O at a partial pressure of 0.04 torr.	
3.6. Plot of cross section/maximum exchange level for protein charge states	100
4.1. Schematic representation of the on-line system for DHX-PD-IMS-MS	113
4.2. (A) Two-dimensional (2D) $t_D(m/z)$ raised-relief plot showing the resulting peptide ions generated from DHX-PD-IMS-MS of unlabeled ubiquitin. (B) 2D $t_D(m/z)$ contour-plot of DHX-PD-IMS-MS analysis of unlabeled peptides extracted from the boxed region in Figure A. (C) 2D $t_D(m/z)$ contour-plot the DHX-PD-IMS-MS analysis of labeled peptides over the same $t_D(m/z)$ ranges	120
4.3. Comparing XIDTD between deuterated and undeuterated ions. (B) identification of undeuterated ions using CID. (C) Overlays of ion isotopic distributions	122
4.4. (A) Location of the secondary structural elements of ubiquitin atop the respective regions of primary sequence. (B) Crystal structure of ubiquitin. (C) Histogram of peptide deuterium retention.	126
4.5. H-D scrambling analysis using model peptide KKDDDDDDIIKIIK	127
4.6. Per-residue deuterium content histogram via IMS-ETD-MS for (A) residues 1-15 and (B) 25-42	130
4.7. t_D distributions for the identified peptide ions presented in Table 4.1	133
4.8. Theoretical amide deuterium content per residue	137
5.1. Schematic representation on (A) the on-line system interfaced to (B) the modified quadrupole ion trap. (C) shows the electronic components for pulsed operation during He-CTD-MS	146
5.2. He-CTD-MS spectrum of [KKDDDDDDIIKIIK+3H] ³⁺ precursor ions. (B) [KKDDDDDDIIKIIK+2H] ²⁺ precursor ions	151
5.3. Left and right panels show identified deuterated c-ions resulting from He-CTD-MS and ETD-MS of KKDDDDDDIIKIIK after on-line DHX respectively.	154- 155
5.4. Isotopic distribution of charge reduced ions for deuterated and undeuterated ions using for determining N-terminal HD-scrambling	157
5.5. Full mass spectrum resulting from a single DHX-PD-MS analysis. The two most abundant ions used for per-residue deuterium calculations are labeled.	159

LIST OF TABLES

2.1. Tentative plasma metabolite assignments including those contributing the most to the variation between sample cohorts	68
3.1. Collision cross section, HDX levels and rate constants for all major dataset features	92
4.1. Reproducibility of the online DHX-PD-MS system	134
5.1. HD-Scrambling analysis of [KKDDDDDIKLIK+3H] ³⁺ c-ions generated from ETD-MS and He-CTD-MS	150

LIST OF SYMBOLS AND ABBREVIATIONS

v_d	Drift velocity
K	mobility
E	Electric field
L	Length of drift tube
t_D	Drift time
N	the number density of the buffer gas
m	Ion mass
M	Mass of the buffer gas
Td	Townsend (1 Td = 10^{-16} V·cm ²)
D	Ion diffusion constant
q	elemental charge
k_B	Boltzmann distribution constant
T	temperature
d	sum of the radii between the ion and neutral buffer ga
z	Ion charge
Ω	Collision cross section
K_o	Reduced mobility
P	Pressure
r	Radius of drift tube entrance aperture
C	Constant
$P(t_p)dt_p$	time-dependent shape of the ion packet
$\Phi_2(x,y,t)$	quadrupolar potential
U	Direct current
V_{RF}	Radio frequency voltage
Ω_a	angular frequency of the applied RF
t	time
A_2	constant with respect to the order of the multipoles
a_m	Mathieu parameter (function of U)
q_m	Mathieu parameter (function of V_{RF})

ω	Frequency
$V_{eff}(r)$	effective electric potential
$D_{x,y}$	depth of the potential
r_d	radial distance
r_o	Inner radius between quadrupoles
m/z	Mass-to-charge ratio
E_{cm}	Center of mass energy
V_{p-p}	Voltage peak-to-peak
IMS-MS	Ion mobility spectrometry mass spectrometry
MS	Mass spectrometry
MS/MS	Tandem mass spectrometry
MS^n	Multistage tandem mass spectrometry
CID	Collision induced dissociation
HCD	High energy collision induced dissociation
IMS-CID-MS	Parallel dissociation
XIDTD	Extracted ion drift time distribution
ToF	Time of Flight mass spectrometer
ETD	Electron transfer dissociation
ETnoD	Electron transfer without dissociation
He-CTD	Helium cation charge transfer dissociation
ECD	Electron capture dissociation
UVPD	Ultra-violet photodissociation
CSIT	Charge-sign independent trapping
TWIM	Traveling wave ion mobility spectrometry
HDX	Hydrogen-deuterium exchange (H-to-D exchange)
DHX	Deuterium-hydrogen exchange (D-to-H exchange)
ESI	Electrospray ionization
LIT	Linear ion trap
LTQ	Linear trap quadrupole (same meaning as LIT)
LysoPC	Lysophosphatidylcholine
SP	Synthetic peptide
MP	Model peptide
PD	Pepsin digestion
PTM	Post translational modification
CCS	Collision cross section
F1	Funnel 1
G1	Gate 1
F2	Funnel 2
G2	Gate 2 (selection gate)
IA	Ion activation region
SRIG	Stacked ring ion guide
nCI	Negative chemical ionization
ACN	Acetonitrile
D ₂ O	Deuterium oxide
FA	Formic acid
MeOH	Methanol

NH ₄ OH	Ammonium hydroxide
NMR	Nuclear magnetic resonance spectroscopy
LC-MS	Liquid chromatography mass spectrometry
SCX	Strong cation exchange
GC	Gas chromatography
EX1	Exchange 1 kinetics
EX2	Exchange 2 kinetics
N_{bk}	Backbone amide hydrogen
k_{cl}	Rate of protein closing
k_{op}	Rate of protein opening
ND ₃	Deuterated ammonia
FAB	Fast atom bombardment
EA	Electron affinity
NRMSD	Normalized root mean square of the deviation
CV	Coefficient of variation
N_t	Total number of drift time values

1. Introduction: Expanding the Applications of Ion Mobility Spectrometry-Mass Spectrometry (IMS-MS) for Complex Mixtures Separations and Protein Structural Insights.

Reprinted in part with permission from Analyst: Advances in Ion Mobility-Mass Spectrometry instrumentation and Techniques for Characterizing Structural Heterogeneity. Gregory C. Donohoe, Megan M. Maurer and Stephen J. Valentine, Analyst, 2015. 140(20):p.6782-6798

1.1 Ion Mobility Spectrometry and Linear Ion Trap Mass Spectrometry

Fundamentals

Several new applications have attempted to expand the utility of IMS-MS by implementing a new IMS-linear ion trap (LIT) mass spectrometer. The IMS separation is used in four specific and different fashions: 1) a traditional separation device for small molecule mixtures, 2) a fragmentation cell for high-throughput, data-independent analysis that requires no spectral alignment 3;) a structural gas phase deuterium labeling cell aimed at understanding protein anion structures; and, 4) as a traditional drift cell for calculating an ion's collision cross section (CCS). These four areas are then combined with the ion trapping capabilities of the LIT to perform MSⁿ and ETD on drift-selected ions.

In experiments reported here, the IMS-MS (Figure 1.1) consists of an ion desolvation region that incorporates a dual ion funnel/ ion gate design coupled to a LTQ Velos (Thermo Electron, San Jose, CA, USA) mass spectrometer.[1, 2] A continuous beam of ions, produced via electrospray ionization (ESI), enters into a desolvation region and become focused through an hour-glass funnel (F1).[3, 4] The funnel is composed of a stacked ring ion guide (SRIG) composed for ring electrodes having

different inner diameters. The inner diameter of each electrode changes sequentially such that the cross-sectional view would appear as an hour-glass. Ions entering F1 are desolvated and emerge as a focused beam of ions before becoming trapped at an electrically biased gate (G1). Ion trapping is performed with the use of both RF and DC voltages applied across the ion funnel as well as a repulsive voltage at G1. Using an attractive field applied at the G1, ions are periodically pulsed into the drift tube. The drift tube is constructed of ring electrodes separated by electrical insulators. A resistor chain is connected to each electrode, where the application of voltage produces in a potential drop across the length of the drift tube (~1 meter) resulting in a homogenous electric field (~10 V·cm⁻¹).

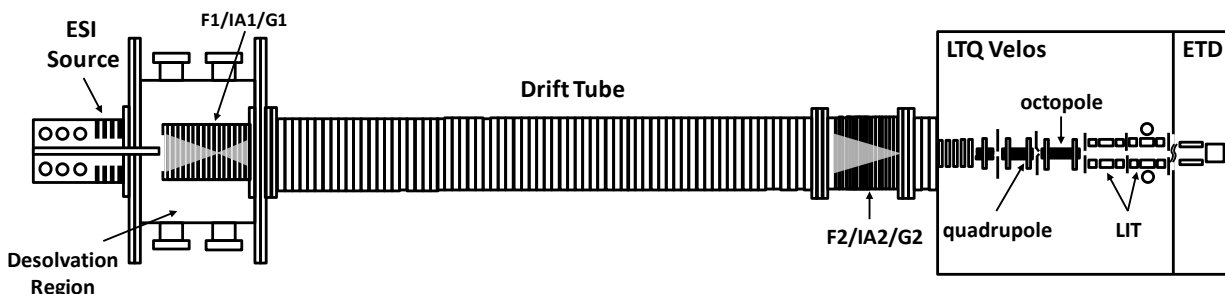


Figure 1.1. Schematic locations of the IMS-MS instrument showing the front and rear funnels (F) and the locations of both gates (G). The boxed portion of the schematic shows the LTQ Velos (ThermoScientific) mass spectrometer consisting of RF focusing devices, the linear ion trap (LIT) mass analyzer and the ETD source.

Ions that enter into the drift region undergo collisions with He gas (~2.50 Torr at 300 K) and separate based on differences in their three dimensional, rotationally averaged structures and overall charge. Upon reaching a selection gate (G2), ions are defined by their mobility (K) as a function of ion drift velocity (v_d) at a defined electric field strength (E) according to:[5]

$$v_d = KE \tag{1.1)}$$

Here, v_d can also be calculated by subtracting the time between a measurable ion signal at the selection gate and the introductory ion pulse. This defines the drift time (t_D), or the transit time, for an ion population that traversed the drift tube. With this, the velocity of an ion is dependent on the pressure within the drift tube. Since L and t_D can be determined precisely determined as:

$$v_d = \frac{L}{t_D} \tag{1.2)}$$

Combining Equation 2 with Equation 1 yields the follow relationship:

$$K = \frac{L}{t_D E} \tag{1.3)}$$

Here, K is inversely proportional to E and proportional to v_d . From Equation 3 it can be seen the terminal velocity that the same ions attain as they tumble through the buffer gas under the influence of a homogenous electrostatic field is dictated by K . It is important to note that these equations reference ion motion under low-field considerations. That is, an ion's internal energy is greater than the energy gained through translational collisions with the buffer gas. Comparatively, under high-field conditions, ion internal energy would significantly increase, such that perturbations in ion shape may alter the v_d measurement or the ions would not project their shape

during the drift measurement. Field limits can be approximated semi-quantitatively at conditions at standard temperature:[5]

$$\frac{E}{N} < \left(\frac{m}{m+M_b} \right)^{\frac{1}{2}} \frac{d^2}{z} \quad 1.4)$$

where N is the number density of the buffer gas at STP, m and M_b are masses of the ion and buffer gas respectively, d is the sum of the radii between the ion and neutral buffer gas (angstrom) and z is the charge of the ion. Equation 4, is denoted in units of Townsend (1 Td = 10^{-16} V·cm²), where traditional measurements, as well as the ones used in the thesis, are ~1 Td. Ions are generalized to move through the drift tube such that their surface area is rotationally averaged through successive and multiple collisions ($>10^6$) with the buffer gas. Ion motion is also influenced by factors such as like-charge proximity, slight pressure gradients and slight differences in velocities or energies. Here, ion diffusion (D) is a measure of ion spread due to Brownian motion, as expressed in the Nernst-Townsend-Einstein relation:[5]

$$K = \frac{q D}{k_B T} \quad 1.5)$$

Where, q and k_B are the elemental charge and the Boltzmann distribution constant, respectively. Notably, K is inversely related to T and proportional to q . This equation gives insight into why ions are not discrete peaks, but broaden to some degree.

Although simple, Equation 5 explains that ion motions will result in a distribution of velocities and, to some degree, the peak-shape of a drifted ion species (see below). As

will be seen in coming chapters, the drift profile of an ion becomes a “fingerprint” and is useful for structural considerations and interrupting heterogeneity in complex mixtures.

Ultimately K depends on collisions between particles. It is important to note that these collisions are influenced by E and thus the forces between the ions and the buffer gas are important. Revercomb and Mason proposed this dependence in the form of a diffusion collision integral assuming ions were hard spheres and that K depends on momentum transfer.[6]

$$K = \frac{3}{16} \frac{ze}{N} \left(\frac{1}{m} + \frac{1}{M_b} \right)^{\frac{1}{2}} \left(\frac{2\pi}{k_B T} \right)^{\frac{1}{2}} \frac{1}{\Omega} \quad 1.6)$$

Here, z and e ($q = z \cdot e$) are the unit charge of the ion and the elemental charge of an electron respectively. The term Ω is the collision cross section (CCS) of an ion. Since the drift measurement can be performed using different parameters, it becomes instructive to report a reduced mobility (K_o). K_o allows comparisons across instrumental platforms, between laboratories or can be used once instrument performance has been optimized for a specific method. The reduced mobility is derived from scaling, calibrating or correcting to standard temperature and pressure according to:

$$K_o = K \left(\frac{273.15}{T} \right) \left(\frac{P}{760} \right) \quad 1.7)$$

Equation 6 can be rearranged to give a CCS calculation based on the ion’s t_D . The equation below has been normalized to standard pressure and temperature as:[7]

$$\Omega = \frac{(18\pi)^{1/2}}{16} \frac{ze}{(k_B T)^{1/2}} \left[\frac{1}{m} + \frac{1}{M_b} \right]^{1/2} \frac{t_D E}{L} \frac{760}{P} \frac{T}{273.2} \frac{1}{N} \quad 1.8)$$

Calculating CCS values for ions allows a direct measure of a physical property. From Equation 8, the CCS calculation is dependent on the charge of the ion and the parameters T , L and P of the drift tube. One consideration for enhancing CCS determinations is that higher resolving power in the mobility dimension significantly enhances structural both small molecule and protein structural studies. An example is the need to adequately resolve the structural heterogeneity associated with complex mixtures such as those encountered in 'omics investigations.[8, 9] This is also true for distinguishing co-existing solution- and gas-phase structures for biomolecular ions. Resolving such fine details affords greater structural insights and more accurate CCS determinations.

The IMS resolving power (R), where ($R=t_D/\Delta t_D$) represents the ratio of the ion's t_D to the width of the peak at half-maximum height is described by Equation 1.9.[6]

$$R = \left(\frac{LEze}{16 k_B T \ln 2} \right)^{1/2} \quad 1.9)$$

In Equation 9, R is dependent on L , E , and T . Shortly after the application of IMS-MS techniques for the characterization of biomolecular ion structure, researchers began to explore the development of instrumentation that would exploit parameters in Equation 9 to achieve high-resolution measurements for biological ions.[10, 11] Maximizing R by changing instrument geometry often reaches a point of diminishing

returns resulting from unmanageable operational conditions and spatial requirements. This is largely attributed to the square-root dependence in Equation 9.

One parameter not shown in Equation 9 is the pressure of the buffer gas. It is noteworthy to mention that changing the pressure of the drift cell can support higher E values. The limit, as given by Paschen's Curve for various gases, defines the maximum voltage a gas can maintain at a pressure and distance before gaseous breakdown occurs. For high-resolution IMS, $300 \text{ V}\cdot\text{cm}^{-1}$ is possible.[12] As stated above, as long as the drift tube is maintained under low-field conditions ($E/N < 3 \text{ Td}$), the above equations are applicable for characterizing ion structures and heterogeneity.

The IMS separation is based on an ion's size-to-charge ratio. Ions exhibiting larger mobilities reach the detector before ions that have smaller mobilities. Often in protein structural studies, ions with similar shapes can exist over several charge states. These structures can be resolved since K is proportional on the charge of an ion (Equation 6). This charge dependence allows similar structures to be resolved if ion charge is different. However in the case of isomeric structures, where K is not dominated by charge, structural resolution becomes harder to predict. For a single isomer, the theoretical shape of the ion packet exiting the drift tube aperture is determined by the ion flux[13] according to:

$$\Phi(t) = \int \frac{C}{(Dt)^{\frac{1}{2}}} \left(v_d + \frac{L}{t} \right) \left[1 - \exp\left(\frac{-r^2}{4Dt}\right) \right] \exp\left[\frac{-(L-v_d t)^2}{4Dt}\right] P(t_p) dt_p \quad 1.10)$$

where r is the radius of the drift tube's entrance aperture, C is a constant and $P(t_p)dt_p$ is the time-dependent shape of the ion packet that is pulsed into the drift tube. Equation

1.10 only describes a single ion conformation contributing to the overall peak shape. It is important to note that the calculated peak shape may be broader if an ion contains more than one structure or interconverts between ion structures on the time scale of the measurement. Often the former, is most instructive in observing both solution and gas phase structures without the presence of bulk solution.

1.2. Fundamentals of Mass Spectrometry (MS) – Linear Ion Traps

Ions that traverse the drift tube reach a selection gate and pass into a second electrodynamic funnel (F2) used to radially focus the ion cloud.[3, 4, 14] The ions subsequently exit the drift tube through a conductance-limiting aperture and are focused in the IMS-MS interface region by quadrupole and octopole RF guides before entering into the higher pressure linear ion trap followed by subsequent mass analysis in the lower pressure-linear ion trap.

In linear ion traps, ions are confined two-dimensionally (2D) by an RF field for radial confinement and DC stopping potentials applied to end electrodes for axial confinement.[15] The motion of ions in a 2D multipole field can be expressed by Newton's Laws of motion according to:

$$F = m \frac{dv}{dt} \quad 1.11)$$

where F is the force on the ion v and t are the velocity of the ion and time respectively.

The F experienced by an ion in a quadrupole potential is[15]

$$F = -ze\nabla\Phi_{2(x,y,t)} \quad 1.12)$$

where $\Phi_2(x,y,t)$ is the quadrupolar potential if applied from alternate electrodes to ground according to:[15]

$$\Phi_2(x,y,t) = \frac{(x^2-y^2)}{r_o^2} (U - V_{RF} \cos \Omega_a t) \quad 1.13)$$

In Equation 13, U and V are the applications of DC and RF potentials applied to symmetric rods, respectively. The term Ω_a is the angular frequency of the applied RF. For linear ion traps in a quadrupolar geometry, 2 pairs of parabolic rods are positioned adjacently one to another. This creates a well a defined inner radius r_o associated with ion trapping. In quadrupole trapping devices, ion acceleration in the x and y dimensions are not coupled and ion motion in these directions are orthogonal to the central axis[15] according to:

$$m \frac{d^2x}{dt^2} = -zeA_2 \frac{\partial \Phi_2(x,y,t)}{\partial x} \quad 1.14)$$

$$m \frac{d^2y}{dt^2} = -zeA_2 \frac{\partial \Phi_2(x,y,t)}{\partial y}$$

here A_2 is constant with respect to the order of the multipoles. These equations show that ion motion in the x direction does not depend on that of the y direction. This relationship is at the basis for why most 2D trapping devices are quadrupolar, as ion oscillation can be more easily manipulated.

In other arrangements, such as hexopoles or octopoles, x and y motions are coupled.

The motion of ions in a quadrupole field as described by the dimensionless stability parameters a and q are:[16]

$$a_x = -a_y = \frac{8eU}{m\Omega_a^2 r_0^2}$$

$$q_x = -q_y = \frac{4eV_{RF}}{m\Omega_a^2 r_0^2}$$
1.15)

in Equation 1.15, term m is the mass of the ion and is inversely related to both a and q . The equations of motion in Equation 13 can be expressed as the Mathieu equations[15]

$$\frac{d^2x}{d\xi^2} + (a_x - 2q_{mx}\cos 2\xi)x = 0$$

$$\frac{d^2y}{d\xi^2} + (a_y - 2q_{my}\cos 2\xi)y = 0$$
1.16)

where a_m and q_m are Mathieu parameters and $\xi = \Omega_a t/2$. These equations give the stability of an ion whose motion is defined as either stable or unstable within the confines of the trapping instrument. Ion trapping can be visualized by a parabolic potential well that oscillates the ions at frequency (ω):[15]

$$\omega = (2n + \beta) \frac{\Omega_a}{2}; 0 \leq \beta \leq 1 \text{ and } n = 0, \pm 1, \pm 2, \dots$$
1.17)

the term β is dependent on both a_m and q_m parameters. When a_m is 0 and q_m approaches 0, β can be approximated:

$$\beta \approx \frac{q_m}{\sqrt{2}} \quad 1.18)$$

when q_m is small and $n = 0$, ion motion becomes harmonic with ω and can be expressed as follows:[15]

$$\omega \approx \frac{q_m \Omega a}{2\sqrt{2}} \quad 1.19)$$

Under these conditions the stability region of the ion trap becomes defined and ion confinement behaves as a function of the effective electric potential $V_{eff}(r)$ as defined by:[15]

$$V_{eff}(r) = D_{x,y} \left(\frac{r_d}{r_0}\right)^2 \quad 1.20)$$

where r_d is the radial distance and $D_{x,y}$ is the depth of the potential well that traps the ions within a defined oscillation.[15]

$$D_{x,y} = \frac{q_m V_{RF}}{4} \quad 1.21)$$

At the center of this well ions are trapped in a specific oscillation across the x and y directions and are harmonic with the periodicity of the potential well. By scanning the effective potential of the trap, ions are preferentially destabilized and ejected from the

trap and detected. In this manner, ions become characterized by their m/z ratio that is dependent on the stability parameters a and q .

Ion traps are well suited for 'omics analysis, offering high efficiency ion trapping and the ability to couple easily with either front-end techniques such as LC or GC, or for proton transfer reactions[17], ultraviolet photodissociation[18] and chemical ionization sources for ETD reactions[19] (typically interfaced at the rear of the instrument). As standalone instruments, they are considered proteomics-grade mass analyzers that operate at relatively high pressure ($\sim 10^{-5}$ torr). This makes them ideal candidates for interfacing to low pressure IMS instruments (1 -4 torr) and eliminates the need for multiple conductance limiting apertures for differential pumping stages. Ion traps also have the advantage of isolating and confining specific m/z ratios for MS/MS or MSⁿ analyses. Isolation is also useful for reducing space charge effects caused from ion trapping. In some cases, sensitivity can even be increased since the ejection of other ions does not destabilize the oscillation of selected ions.

In isolation experiments, all ions of measurable signal are directed into the trap and confined for mass analysis. This stage is known as the MS scan, which measures the m/z of the precursor ions. Mass selection can be performed by using the trapping RF to resonantly excite undesired ions for ejection. In this method, multiple frequencies are scanned sequentially. For broadband waveform isolation, all frequencies are applied except for the frequency that matches the oscillation of the intended ion for isolation.[15] Ions with oscillations that are resonant with all other frequencies are excited and subsequently ejected from the trap. This type of selection is particularly useful, because ion ejection is performed quickly. However, as will be

discussed in the following sections, special attention needs to be given to ion isolation, because waveforms close to the oscillation frequency of the isolated ion can cause unwanted vibrational excitation.

1.3. Collision Induced Dissociation (CID)

Once an ion has been selected within a user-defined m/z isolation window, ions are excited with an RF frequency that is resonant with the oscillation of the ion.[16] In this manner, selected ions achieve extended oscillations, but are still confined by the ion trap. The periphery of ion traps contain He(g) used for ion confinement and cooling, but this gas can also activate the ions that have been translationally excited. The total energy available for transfer of kinetic energy into internal energy is given by the center of mass energy (E_{cm}) and is dependent on the mass of the ion, the mass of the buffer gas and the laboratory frame kinetic energy. Ions increase their kinetic energies from the applied RF and collide with the buffer gas. A portion of the translational energy is transferred and redistributed statistically throughout all internal modes of motions (e.g. vibrational and rotational).[20] As described by the Rice-Ramsperger-Kassel-Marcus (RRKM) theory, the rate of dissociation is slow compared to the redistribution of energy. Unimolecular dissociation follows at a higher rate once the ion has achieved sufficient internal energy. Fragmentation in ion trapping MS results from the gradual heating of precursor ions that produce fragment ions and is termed tandem-in-time CID.

1.3.1. CID of Peptides and Proteins: b – and y – ions

One of the greatest utilities of CID has been found in proteomics analysis for sequencing peptides and proteins. Wysocki and coworker suggest that the CID of peptides promotes the mobilization of protons for cationic ions.[21] In the mobile proton

model, protons are transferred intramolecularly from basic and acidic residues to heteroatoms found along the backbone.[21] Proton transfer from basic residues is thought to occur at the carbonyl that facilitates nucleophilic attack of the electropositive carbon from another carbonyl. This results in a protonated oxazolone *b-ion* and the corresponding *y-ion* fragments. It is noteworthy to mention that fragmentation appears enhanced at aspartic acid residues, presumably due to solvation effects of the backbone carbonyl by the carboxylic acid. In general the N-CO bond is dissociated resulting in *b-* and *y-ions* that are sequenced from the *N*-terminal and *C*-terminal ends respectively.[22] The use of such information can be used in *de novo* sequencing methods for protein primary sequence identification.[23] Newer techniques allow *in-silico* methods, such as Sequest[24] and Mascot, to be employed for bottom-up proteomic sequencing.[25] This is particularly useful since 1000s of peptides are fragmented over the course of a chromatographic separation.

1.3.2. CID of Small Molecules: Understanding Fragmentation

Dissociation of complex organic molecules can be inherently more difficult than sequencing peptides. Small molecules span a diverse array of structures, classes and covalent bonding arrangements (e.g. alkene). A molecule that has obtained sufficient energy for dissociation must be reconstructed according to valence rules.[20] Structural MS of small molecules depends on the internal energy of the molecular ion and the time scale (10^{-6} s) of observation. In CID processes, fragmentation should be performed quickly. If the rate of dissociation is slow, ions may fragment in transit to the detector and are observable as metastable ions. Fragment ions of complex small molecules are complicated by competing fragmentation pathways that are dependent on the

achieved internal energy of the precursor ion. That is, high energy CID (above 100 eV) can yield different spectra than low energy CID.

1.4. IMS-MS Metabolomics and Small Molecule Studies

Shortly after the first protein ion collision cross section measurements, IMS-MS was demonstrated as a means for separating ions within complex mixtures.[26, 27] Here, the mobility measurement was shown to distinguish isobaric ions of similar type based on differences in CCS as well as overall ion charge. Early on it was recognized that, for peptides, factors such as intramolecular interactions, side-chain packing, and overall side-chain length could affect the overall ion CCS leading to efforts aimed at predicting cross sections based on primary sequence.[28] McLean and coworkers demonstrated that many classes of small molecules could be distinguished using IMS-MS techniques.[29] These early efforts laid the ground work for recent developments in small-molecule ion structure characterization/utilization using IMS-MS techniques.

Recent experiments conducted on an IMS-MS instrument that utilizes a linear, high-resolution drift tube, have yielded the most extensive database to date of CCS values for small biomolecules including quaternary ammonium salts, lipids, peptides and carbohydrates.[30] The study demonstrates the potential for observing low-abundance species in the presence of higher-abundance isobaric species including isomers using IMS-MS analysis. Paglia and coworkers have demonstrated the utility of incorporating such mobility information into comparative metabolomics workflows and describe a searchable CCS database for ion identification.[31] Hill and coworkers have utilized high-resolution mobility separations to identify a new dopamine isomer obtained from striatal metabolomic extracts from genetically modified rats.[32] Similarly, experiments

have shown that mobility measurements can be used with other analytical information (LC retention time and precursor and fragment ion masses) to distinguish isomeric species in complex mixtures obtained from natural products [33] as well as to identify potential biomarkers in comparative metabolomics analyses[34].

1.5. An Overview of the Metabolome and Traditional Techniques

Recent research has shown that the analysis of the plasma metabolome provides insight into fundamental metabolic processes, functions, and biomarkers associated with age, disease, and exposure to environmental influences.[35-40] Studies have revealed changes in metabolite profiles that are associated with cardiovascular disease, cancer and neurological disorders. [32, 40-44] Of particular interest, is the fact that metabolites act as signaling entities that influence cellular activity and biofunctions that include changes in protein profiles and gene expression.[37, 45] Because metabolite signaling is often involved in the initial steps of biological activity, characterization of the metabolome may serve as an important discovery tool for determining biopathways associated with transitions from healthy to disease states.[46] With this in mind, the ability to profile and identify metabolites using analytical techniques offers an opportunity for indirectly observing cellular changes associated with disease onset and progression.

According to the Human Metabolome Database, human plasma contains approximately 42,000 metabolites that mainly encompass organic acids, carbohydrates, lipids and peptides.[47, 48] Because the matrices that contain metabolites are extremely complex, analysis of the metabolome has traditionally required the use of extraction and separation techniques. Currently, most untargeted metabolomic analyses are performed

using liquid chromatography mass spectrometry (LC-MS) because the technique routinely enables high detection numbers.[35, 49] A particular limitation of LC-MS is the data-dependent acquisition most commonly employed. Here, the mass analyzer selects the 10 most abundant ions per defined elution window. These mass-selected precursor ions are then fragmented, generating retention time information, a precursor ion m/z measurement and fragment ion m/z ratios. While this combination is a powerful technique, data dependent acquisition limits the amount of ions that are selected for MS/MS analysis, leading to under sampling of often important ions. While some methods employ data-independent LC-MS acquisition, it is noted that these techniques require multiple runs of the same sample (as to generate an exclusion list) that greatly increases analysis and data processing times.

One limitation regarding metabolomic analysis employing LC-MS is the time required for adequate ion identification. Even with mass spectrometers capable of high mass accuracy determinations, m/z database matching can yield numerous isobars associated with a single spectral feature. Added to this difficulty is the identification of isomeric species that may only differ in structural arrangement (e.g., alkene positioning). Tandem mass spectrometry (MS/MS) has proven an indispensable tool for the elucidation of compound structure and thus identification.[50] As explained above, often, MS/MS is not sufficient to identify compounds of interest requiring the use of MS^n . [51, 52] It is noted that MS^n is difficult to perform on a chromatographic time scale, because these operations require ~50 ms/MS scan to complete.

One advantage of the dual gate IMS design is the ability to filter ions of select mobilities. Since the timing of the selection gate is delayed relative to the introductory

pulse, a well-defined distribution of mobilities can be transferred into the LIT. This not only reduces spectral congestion, but also concentrates ion signal prior to MSⁿ.

Because MS ion trapping can be performed up to 1000 ms, >50 IMS-pulses, containing mobility-selected ions, can be accumulated during the precursor MS scan. This is advantageous for increasing the signal of low-intensity ions that may be missed by LC-MS methodologies. The combination of the mobility filtering and accumulation can be followed by MS/MS, or if signal is sufficient, MSⁿ. As will be discussed in Chapter 2, IMS-MSⁿ was performed on metabolite ions and allowed for high confidence identifications.

1.5.1. Parallel Dissociation Combined with IMS-MS for Data Independent Analysis of Small Molecules

The ability to rapidly profile complex mixtures using MS/MS and MSⁿ techniques is particularly useful for identifying high numbers of molecular ions. Here, parallel dissociation stands at the forefront of high throughput methodologies. Other techniques known as data-independent or SWATH[53, 54] (AB Sciex), identify E (Waters) and all ion fragmentation (Thermo) acquisition use the mass spectrometer to fragment all observable precursor ions at each chromatographic elution window. In this manner the fragment ions are matched back to precursor ions containing similar elution profiles or retention times. However, this method is complicated by run-to-run variability caused by differences during the LC separation (e.g. mobile phase composition, pressure fluctuations, temperature, etc.). In these cases even slight changes in chromatographic trace requires sophisticated algorithms for spectral alignment. This is further

complicated when attempting to align fragment ions back to precursor ions based on elution profiles.

Parallel dissociation within a drift tube, (IMS-CID-MS, IMSⁿ-MS) has been previously described and demonstrated for 'omics applications using ToF[55, 56] and ion trapping mass analyzers.[57] As discussed, nested experiments record ion drift times as they are pulsed into the ToF flight tube. It is noteworthy to mention that IMS-CID-ToF instruments perform parallel dissociation at the end of the mobility separation. While the technique has been successful, performing CID directly after the mobility separation can perturb the drift profile due to differences in transit times of fragment and precursor ions.

For the studies reported here, a dual gate IMS-MS is employed and is well suited for IMS-CID-MS techniques. One difference is that the pulse delay applied to the selection gate allows ion filtering, where only a specific mobility is selected. Once selected, the ions contain drift information prior to mass analysis. Fragmentation is performed at the second ion activation region (IA2 in Figure 1.1) after ion selection has been made. Ion activation is achieved by increasing the voltage difference across two adjacent electrodes. This results in energizing collisions with the buffer gas leading to fragmentation. In this manner the region immediately following the drift tube is used as a collision cell. Since the precursor ions were previously selected, they transfer drift information to the fragment ions. All ions are then transferred to the mass analyzer for *m/z* analysis. Although this process increases the complexity of the sample, fragment ions can be matched back to their respective precursor ions based on extracted ion drift time distributions (XIDTDs). Coupling XIDTDs with the high reproducibility of the IMS

separation, requires no dataset alignment in comparative analyses and enhances spectral deconvolution. As will be described in Chapter 2, fragment XIDTDs that have similar spectral features are capable of being matched back to their respective precursor ion drift traces. This high level of specificity is required for such high throughput data independent workflows.

1.6. Electron Transfer Dissociation (ETD) of Peptides and Proteins

Perhaps the first demonstration of radically fragmenting peptides and proteins with low energy electrons was performed by McLafferty and coworkers in the form of electron capture dissociation (ECD).[58] These experiments used a Fourier transform ion cyclotron resonance mass spectrometer (FT-ICR-MS) equipped with an emission cathode and a grid. A voltage applied across the cathode resulted in the emission of thermal electrons (~ 1 eV) that could be trapped in the ICR cell and reacted with peptide cations in the gas phase. Capture of the electron by the peptide cations resulted in the dissociation of the peptide cations into fragment components. Unlike CID, that produces *b* and *y* ions through vibrational activation, ECD causes radical-directed dissociation of the N-C $_{\alpha}$ bond and produces even electron *c*- and odd electron *z*- ions.

Such ECD experiments led to the advent of ETD for peptide/protein fragmentation shortly later. Although ECD must be performed within the low pressure environment of an ICR cell (10^{-10} torr), ETD can be performed in higher pressure mass analyzers, such as the LIT. The process of fragmentation with ETD is much different than that reported for ECD; however the two techniques both produce *c*- and *z*-ions via the same mechanism. Electron transfer dissociation was first reported by Hunt and coworkers using a LIT interfaced to a chemical ionization (CI) tower at the rear of an LIT

instrument.[19] This tower contains a heated cell for the sublimation of fluoranthene that is swept into the negative CI chamber by a flow of N₂(g). The excess flow of N₂(g) into the CI chamber produces free electrons that are captured by sublimated fluoroanthene. In turn, the fluoranthene anions become charged, and their trajectories can be manipulated in the gas phase. Reagent anions are transferred from the ionization chamber to the rear of the LIT via ion guides. It is important to note that the commercial LIT, used in the studies for this thesis, is segmented into high and low pressure regions and is highly suitable for ETD. Here, fluoranthene radicals transferred into the low pressure trap are subsequently isolated, purified and accumulated prior to ion-ion reactions. At the same time, the high pressure trap is accumulating peptide/protein cations. Ions of opposite charge are held in oscillation within their respective trapping regions. Once enough fluoranthene radicals have been generated, ETD is performed by adjusting the RF potential applied to the end lenses or the matching rod sets. This provides charge-sign independent trapping (CSIT), which axially confines both positive and negative ions simultaneously. The ETD reaction generally proceeds for ~100 ms, after which, the LIT scans and detects fragment ions.

1.6.1. ETD Mechanism: c – and z – ions

The collision between anions and cations causes the transfer of an electron from the fluoranthene radical to the peptide. Electron transfer is thought to occur at a protonated basic side chain such as lysine, arginine or histidine, forming a hypervalent radical species.[58] The electron occupies an excited Rydberg state that upon relaxation transfers a hydrogen from the basic sidechain to the backbone carbonyl.[59] This process produces a carbon radical aminoketyl intermediate. This is followed by

radical rearrangement and cleavage, where half of the electron density of the N-C α bond, combines with the carbon radical and the other half is retained on the C α carbon. The rearrangement is radically driven and produces -c and z- fragment ions. Unlike CID, ETD proceeds through a nonergodic mechanism and dissociation occurs before the redistribution of energy ($\sim 10^{-12}$ s). This mechanism is an important consideration, because unlike CID, ETD can preserve post translational modifications (e.g. phosphorylation and glycosylation) and is necessary for per-residue hydrogen deuterium exchange (HDX) measurements. Both subjects are discussed below.

1.6.2. IMS – ETD – MS Techniques

While biomolecular applications of CID combined with IMS occurred almost concurrently, IMS coupled with ETD is a relatively newer concept. Experiments by de Pauw and coworkers use ETD of cysteine containing peptides prior to the mobility separation.[60] Peptide ions involved with charge reduction were shown to have more extended conformations compared to the same ion that was not subjected to ETD reagent. Post mobility the reduced ions were collisionally activated and the site of disulfide bonding was elucidated. Other early studies used ETD followed by traveling wave ion mobility (TWIM) to locate *cis*-platin interactions with methionine containing peptides.[61] After ETD, the fragments were mobility separated and easily identified based on differences in arrival time distributions. Other studies have used the ETD-TWIM instrument for other peptide and protein workflows.[61-63] While these works are interesting, it is also noted that the ETD cell is located before the mobility region,[64, 65] meaning that the mobility separation is not utilized to distinguish precursor ion conformers. To the best of my knowledge, ETD on a mobility separated ion has only

been performed on a field asymmetric ion mobility spectrometry instrument (FAIMS).[66] However FAIMS operates above the low-field limit and cannot be used to determine CCS values. With this in mind, the ability to perform seminal studies using a linear field drift tube coupled with ETD-MS expands the applications of 'Omics analyses into new frontiers.

1.7. Phosphoproteomics and MS Techniques

Protein phosphorylation is a reversible covalent post-translational modification occurring at tyrosine, serine, and threonine residues.[67, 68] This modification is added or removed by kinases and phosphatases, respectively, making phosphorylation a temporally dynamic process. Phosphorylation is the most common PTM for eukaryotic organisms and implies a specific importance in regulating protein activity, cellular function and signaling pathways.[68, 69] A particular challenge of phosphoproteomics is first detecting and then identifying the site of phosphorylation. Simply measuring protein abundance does not correlate with the stoichiometric amount of phosphorylation. That is, residues that are modified are often low abundance, making enrichment and multidimensional separations necessary.

Mass spectrometry has become a powerful tool for identifying and determining the site of phosphorylation. Identification of the phosphate moiety is complicated due to the phosphodiester bond. That is, under CID conditions, the bond is labile and energizing collisions cause the neutral loss of the phosphate moiety.[70, 71] This can be used advantageously for neutral loss scanning approaches employing triple quadrupole (QqQ) mass filters. Here the first quadrupole (Q1) scans precursor ions which undergo CID in the middle quadrupole (q). The last quadrupole (Q2) scans for the neutral loss of

H₃PO₄. An important consideration of this technique is the observable charge state of the precursor ion, as this influences the fragmentation energy and accessible dissociation pathways resulting in observable fragments. Collision induced dissociation of the precursor ion containing the phosphate moiety can induce several neutral losses. These include *m/z* 79 (PO₃⁻), 80 (HPO₃) 98 (H₃PO₄; HPO₃+H₂O), 63 (PO₂⁻) and 97 (H₂PO₄). Because the backbone amide bond dissociation energy is ~40kcal/mol and the phosphodiester linkage is ~20kcal/mol, the collision energy can be tuned such that fragmentation does not produce a significant amount of *b*- or *y*- ions. Here, neutral loss fragment ions can then be scanned by Q2 to detect the presence of phosphorylation.[71] While this technique excels at detecting the presence of phosphorylation, locating the site of phosphorylation requires the use of CID-MSⁿ or ETD-MS.

More recent experiments involve phosphopeptide enrichment using TiO₂ affinity columns, followed by reverse-phase LC-MS. This technique is capable of observing > 36,000 phosphopeptides using a bottom-up approach from a tryptic digest of HeLa cells.[72] Other techniques use strong cation exchange (SCX),[73] and antibody enrichment strategies.[74] With the advent of high resolution ion trap mass analyzers (such as the Orbitrap), targeted MS/MS techniques coupled with *in-silico* database searching can identify the site of phosphorylation using CID or high-energy collision induced dissociation (HCD).[75] The use of powerful software for necessary in predicting and identifying the neutral loss of the phosphate moiety. This information is then related back to the specific residue that contained the modification.

Other fragmentation methods such as ETD have also been used to identify phosphorylation. Compared to CID, ETD can result in extensive backbone cleavage without losing the phosphate moiety.[71, 76, 77] As discussed above, ETD is a nonergodic mechanism that proceeds without excessive vibrational heating. This application makes sequencing much easier than CID, because the spectra are not dominated by neutral loss events. One limitation regarding ETD is that precursor ions must have high charge densities ($\geq +2$) for complete fragmentation. If this requirement is not met, the ion-ion reaction often proceeds through electron transfer without dissociation (ETnoD).[78, 79] Some studies have combined the use of CID with MS-ETD. Here, the CID (in-source dissociation) event results in the neutral loss of the phosphate moiety. The intact neutral loss fragment is then transferred to MS for MSⁿ or MS-ETD. These experiments are referred to as CID triggered MS/MS. In this manner the presence and identify of the phosphopeptide is obtained. As described above, one limitation is identifying the neutral loss event since many combinations of phosphate dissociation are possible.

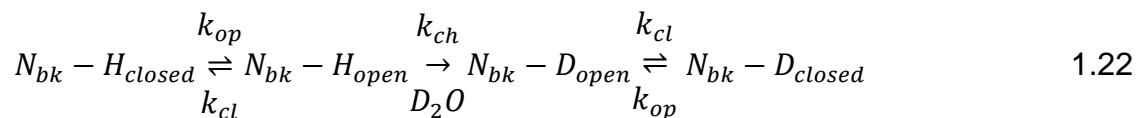
1.7.1. Coupling IMS-CID-ETD-MS for Determining the Presence and Location of Phosphorylation for Peptides Within Complex Mixtures.

Neutral loss scanning and ETD-MS techniques have their limitations and merits. The neutral loss scanning approach can easily identify the presence of phosphorylation events within complex mixtures, but can be limited by its ability to identify modified residues. On the other hand, ETD stands as a capable approach of easily identifying residues that have been post translationally modified. It therefore becomes desirable to create methods that can separate complex mixtures quickly, while detecting

phosphorylation and identifying modified residues. Ion mobility has been used in the past to observe structural aspects of phosphorylation on protein and peptide structure. Additionally, parallel dissociation techniques combined with IMS-MS have been used for observing differences in fragmentation behavior of phosphorylated peptides. In Chapter 2 of this thesis, the capability to rapidly identify phosphorylated peptides in tryptic digests that would be encountered in post-translational modification (PTM) experiments is demonstrated. For these studies, IMS-CID methods show that targets for PTM analysis can rapidly be ascertained and subsequently subjected to ETD to identify phosphorylation sites. To some degree, the approach is similar to proteomics techniques that used triggered CID followed by ETD-MS. A difference is that XIDTD helps to confirm and isolate ions for subsequent tandem MS experiments.

1.8. Solution Hydrogen Deuterium Exchange: Fundamentals

Protein hydrogen deuterium exchange-mass spectrometry (HDX-MS) is an isotopic labeling strategy involving the exchange of heteroatom hydrogens with deuterium over a defined period of time.[80-82] The main focus of HDX-MS methodology is to elucidate protein structural regions[83, 84], folding dynamics[80, 85-91] and protein interactions[92-96] via mass shifts caused by the incorporation of deuterium after the exchange event. Most commonly, these exchange reactions involve the incubation of protein within a buffered solution containing deuterium oxide. The overall exchange mechanism can be described by:[80]



where N_{bk} is a backbone amide along the proteins primary sequence. Due to random vibrations and motions of the protein, temporary conformations allow the protein to open at a rate k_{op} and close back to the initial conformation at a rate of k_{cl} . If k_{op} is such that solvent D_2O is capable of interacting, then $N-H \rightarrow N-D$ exchange occurs at a rate k_{ch} . The term k_{ch} is the intrinsic rate constant and is determined by the flanking side chains, as well as the temperature and pD of the solution. If all rates are favorable, then deuterium is incorporated into the protein before the region closes and is no longer solvent accessible.

The exchange mechanism is base catalyzed, and occurs with hydroxide abstracting a hydrogen from a solvent-accessible hetero-atomic site.[80] Deutration follows and is driven by the free amount of D^+ in the solution. It is easy to see that k_{op} , k_{cl} and k_{ch} can give several combinations of exchange rates. In general exchange has been divided into two separate regimes referred to as EX1 and EX2. In EX1, $k_{ch} \gg k_{cl}$ and suggests that HDX occurs during the initial opening transition.[97, 98] Comparatively, under the EX2 regime, $k_{ch} \ll k_{cl}$ and implies that exchange occurs over many opening and closing cycles before $N-H \rightarrow N-D$ exchange occurs.[99] EX2 suggests that bonding networks found in secondary, tertiary and quaternary scaffolds are less frequented by intermolecular interactions with the aqueous solution, thereby resulting in slower exchange kinetics for structured regions. As is often the case, most systems exhibit EX2 kinetics.

While the above equations reference the exchange from $H \rightarrow D$, it is noted that in the coming chapters $D \rightarrow H$ exchange was used. This is commonly called deuterium hydrogen exchange or backexchange.[80] Here, the protein is first incubated in D_2O to

a level of ~100 % deuterium incorporation. The rate constants and mechanism of action are the same as described above; however, the deuterated protein is exposed to a hydrogen source. In this manner the representation of secondary structure is indicated by regions that will retain deuterium. Comparatively, unstructured regions will backexchange to hydrogen. In this manner, mass shifts directly suggest areas of secondary structure.

1.8.1. Bottom – up Hydrogen Deuterium Exchange – Mass Spectrometry (HDX – MS)

Most common HDX-MS workflows employ a bottom-up technique. Here, the protein is placed into a D₂O rich buffer and exchange occurs over a defined period of time. Kinetic studies can be performed to determine both EX1 and EX2 regimes based on exchange profiles after varying the incubation time. The exchange also gives an idea of the relative protection of a particular area, since unstructured areas will exchange at higher rates (up to some maximum) than structured regions. Exchange events are quenched at low pH (~2.5) and temperatures approaching 0 °C. Under these conditions the protein is digested with pepsin, because the enzyme displays high activity under quench conditions. These conditions are used to limit backexchange, which is a major concern for bottom-up approaches. Because the protein has been digested, the native structure is lost and any further exchange may change the true deuterium content level of the peptide sequence. Many HDX-MS experiments use LC systems consisting of an immobilized pepsin column for online digestion followed by trapping and reverse-phase separation of peptic fragments that are subsequently mass analyzed.[100, 101] Using this "bottom-up" approach, deuterium incorporation at backbone amide locations can be evaluated on a per-peptide basis.

Despite much success,[86, 102, 103] bottom-up HDX-MS is limited by spatial resolution that is dependent upon the number of overlapping peptide fragments. That is, per-residue analysis of deuterium incorporation must contain two peptides that differ by one residue in length. Since many proteolytic peptides increase the overall overlap, and thus spatial resolution, multiple catalytic enzymes have been used; however, this creates a highly complex dataset.[104, 105] Due to the incorporation of deuterium, mass measurements can be made and structural insights can be ascertained based on uptake profiles across a particular identified sequence.

1.8.2. Top – down HDX – MS

Top-down approaches using non-ergodic fragmentation techniques such as electron capture dissociation (ECD) and electron transfer dissociation (ETD) have shown improved spatial resolution without deuterium scrambling (see below).[106-109] These workflows are similar to that described above. That is, the protein is incubated in D₂O over several periods of time. The protein is electrosprayed in positive polarity mode. Here, the low pH environment of the quench solution is highly suitable for positive ESI and mass analysis. Also noteworthy is that under these conditions the protein is denatured and higher charge states can be achieved. In turn, these high charge states are highly suitable for electron-based fragmentation methods, as the reaction cross sections are larger and ECD or ETD can proceed at higher efficiencies (greater sequence coverage). Once fragmented in the gas phase, Top down approaches can determine deuterium incorporation at a per-residue level. This is different than the bottom up approaches that observe the global view based on peptide sequence. However, larger proteins (>20 kDa)[110] and inadequate charge states

remain problematic for electron-based fragmentation. Other groups have coupled LC-MS/MS based techniques for fragmentation of deuterated proteolytic peptides, using a bottom-up workflow.[107, 111]

1.8.2.1. Per – residue Deuterium Measurements

Tandem mass spectrometry (MS/MS) presents a technique that is well suited to site-specific (per-residue) deuterium retention using both top-down[106, 107, 109] and bottom-up[112, 113] approaches. Early HDX-MS/MS studies employed collision-induced dissociation (CID) to elucidate per-residue deuterium incorporation.[114, 115] In general, CID relies on the conversion of translational energy to internal energy via inelastic collisions of selected ions with an inert buffer gas such as helium. Through multiple collisions, the internal energy of the molecular ion increases and fragmentation occurs at the oscillator with the lowest bond dissociation energy. For proteins and peptides, CID predominantly produces *b*- and *y*-type fragment ions.[20]

Although CID combined with HDX has shown some success,[115, 116] one limitation is hydrogen/deuterium (HD)-scrambling. Because CID is an ergodic process, energy is redistributed and CID is accompanied by the mobilization of protons (see above).[21] These mobile protons, found on both acidic and basic residues, are transferred throughout the molecule and participate in the fragmentation process.[21] Because proton mobilization occurs before dissociation in CID, the final location of the proton on the product ion is typically different than the initial location on the precursor ion. Mobilization is obviously problematic when using HDX-MS/MS to target structural areas because redistribution occurs as readily for mobile deuteriums as it does for mobile hydrogens. That is, structured regions expected to contain higher levels of

deuterium will appear lower than the “true” deuterium content value. Conversely, unstructured regions are artificially enriched. In such cases, per-residue measurements provide ambiguous or erroneous data for structural information.

More recently, electron capture dissociation (ECD) and electron transfer dissociation (ETD) have been shown to fragment deuterated precursor ions without HD-scrambling[108, 111, 113, 117-119]. In contrast to CID, electron-based fragmentation of biomolecular ions proceeds through a high energy mechanism. In ECD and ETD, the capture or transfer of a near thermal electron to the biomolecular ion results in short-lived, odd electron intermediates. Fragmentation is radical-driven and occurs rapidly before proton mobilization throughout the molecular ion. ECD and ETD primarily produces *c*- and *z*-ion series with significantly less contribution of *b*- and *y*-ions. Although ECD and ETD can involve the transfer of a proton from a basic side chain to a *c*-ion,[120] such observations can be accounted for and are more predictable than proton mobilization associated with CID. Importantly, because electron excitation occurs before proton randomization, per-residue HDX studies typically proceed without the loss of the initial deuterium label.

1.8.3. Solution HDX Coupled with IMS – ETD – MS

Ion mobility spectrometry-mass spectrometry has emerged as a powerful tool for separating complex mixtures containing biomolecules.[26, 27, 121-126] The gas phase separation is rapid (milliseconds), affording increased peak capacity at no cost to MS analysis times.[127, 128] A particular advantage of IMS is its ability to decrease the lower-detection limit by removing highly-abundant ions from spectral regions containing interfering ions.[47, 125, 129, 130] Thus, by extracting a specific mobility distribution

within the 2D IMS-MS dataset, a better evaluation of precursor ions that may be suppressed during ionization is obtained. It is noteworthy to mention that the IMS separation occurs in the gas phase. This eliminates the process of solution backexchange found in condensed-phase separations.

To date, few studies have explored the potential in coupling ion mobility with solution phase HDX. However, some studies have used commercial TWIM devices coupled with Time-of-flight mass analyzers for bottom-up peptide studies.[131, 132] These studies showed that that incorporation of deuterium did not change the arrival time distributions of deuterated peptides, relative to the corresponding undeuterated peptides. Also noted is the ability of the mobility measurement to separate overlapping deuterated peptides. This is particularly advantageous since deuterium incorporation broadens the isotopic distribution and results in reduced peak capacity. Moreover, isotopic overlap between neighboring ions interferes with deuterium calculations. This is problematic for accurately determining deuterium content for both overlapping species.

1.9. Gas Phase Hydrogen Deuterium Exchange Coupled with IMS-MS

In 2009, Engen and coworkers showed that mobility measurements could be combined with gas-phase HDX using ND_3 as a deuterating reagent.[63] Different conformer types of ubiquitin ions could be distinguished by their unique mobilities and HDX levels. Rand and coworkers later showed that HDX could be accomplished for protein ions in a TWIM instrument with site-specific determination of the label incorporation.[62] Later the research group demonstrated different operational modes for performing gas-phase HDX measurements with IMS-MS techniques using a TWIM instrument.[133] Ashcroft and coworkers monitored changes in protein ion structure

resulting from solution perturbations using gas-phase HDX-MS techniques.[134] The resulting data was shown to correlate to mobility information obtained from IMS-MS measurements. Valentine and coworkers demonstrated the first determination of site-specific deuterium incorporation for mobility-selected biomolecular ion conformations using a drift tube coupled to a linear ion trap outfitted with ETD capabilities.[135] The researchers then showed that the contributions by individual amino acid residues to conformer type exchange rate could be determined.[136] Using the experimental results and a kinetics model, the authors were able to show that multiple ion conformers are likely to comprise many mobility selections.

Early theoretical studies resulted in proposed mechanisms for HDX of protonated peptide ions by a number of deuterating agents.[137, 138] The use of ND_3 and D_2O are the most common deuterating reagents for gas phase HDX employing IMS. In the studies reported here, D_2O is exclusively used for gas phase labeling experiments. For gas phase HDX using D_2O , a relay mechanism has been computationally determined and supported by experimental results.[139] In this model, biomolecular ions collided with D_2O vapour and form a long-lived complex. Upon complexation the free energy of the system is lowered due to hydrogen bonding. Exchange commences as a proton is shuttled from a heteroatomic charge site of the ion to D_2O . A second hydrogen bond results in simultaneous transfer of deuterium to a distant, less basic site or to the site of interaction. Dissociation of the complex results with no net gain or loss to the free energy of the system.

Initial IMS-HDX-MS studies reported the maximum HDX levels as well as rates of exchange for a number of cytochrome *c* ion conformers.[140] These early studies

demonstrated that compact cytochrome c ion conformers exhibited decreased levels of HDX compared with more elongated ions at room temperature. Additionally, the overall HDX levels were compared with those reported for the same ion charge states as measured in a Fourier transform ion cyclotron resonance mass spectrometer. In general the HDX levels recorded for the mobility-resolved conformers was determined to be smaller than those recorded for ions in the FTICR. This was explained as possibly arising from the longer timescale of the latter measurement rendering the observed exchange subject to longer timescale structural fluctuations.

Although the gas-phase HDX characteristics of negatively charged oligonucleotides and small molecules including amino acids have been studied,[141-146] HDX of protein and peptide anions has received considerably less attention.[147] As a consequence, no experiments describing HDX characterization of peptide and protein anions exists. Because many proteins contain a large number of acidic residues, it is useful to develop a sound understanding of the conformational information afforded by gas-phase HDX measurements for select conformers from negatively-charged protein ions. Moreover, the degree of HDX scrambling occurring for activated, negatively-charged peptide ions has recently been reported.[148] Such information begins to lay the foundation for an understanding of intramolecular deuterium migration which can further clarify the structural information obtained from HDX experiments. Finally, it should be noted that with the rapid development of novel ion fragmentation techniques,[19, 58, 149-154] the experiments described here are timely; that is, this work leads to future studies allowing the determination of residue-specific deuterium uptake for select anion conformers.

1.10. Helium Charge Transfer Dissociation

Electron based fragmentation processes like ECD and ETD are dependent on the charge state of the precursor ion. Given that many bottom up workflows produce highly digested peptides of low charge state, per-residue measurements without HD-scrambling can therefore be difficult to obtain. Both ECD and ETD techniques can fragment peptides exhibiting charge states ≥ 2 ; however, complete sequence information is often limited because ETnoD becomes the dominant product ion pathway. With this in mind, it would be highly desirable to have access to a fragmentation technique that could proceed via odd electron or radical-induced pathways for low charge state precursors without proton mobilization

Recently, a new MS/MS technique known as Helium charge transfer dissociation (He-CTD) of peptide and protein ions has been demonstrated using either helium cations[155] or cations from an air plasma.[156] Gaseous ions emitted from a fast atom bombardment (FAB) gun achieve kinetic energies sufficient to overcome the Coulombic barrier with biomolecular cations. These cationic species are directed into an ion trapping instrument, where peptide cations have been previously mass-selected. He-CTD product ions are seen to result from both vibrationally- and radically-driven dissociation pathways that resemble those formed from both CID and ECD/ETD and ultraviolet photodissociation (UVPD) processes.[155, 156] In other cases, ion-ion reactions result in both non-dissociative charge reduction and increase (gas-phase supercharging).[156] Of particular interest is the ability of He-CTD to produce radical fragmentation regardless of precursor ion charge state. Although the processes that influence these observations are currently difficult to pinpoint, the capability of

fragmenting low charge state precursor ions may offer an improvement over traditional techniques (i.e. ETD).

Because of the short interaction times, He-CTD is presumed to follow vertical activation (not adiabatic), and has been shown to fragment neutral molecules with appearance potentials on the order of 30 eV.[155] He-CTD therefore activates precursor ions through electronic and vibration modes. Fragment ions *y*, *b*, *c* and *z* ions were identified. In chapter 5, experiments consider the *c* ion series after He-CTD MS measurements. CTD is performed with He⁺ cations emitted with high kinetic energy (6 KeV) from the saddle field source. The main purpose of kiloelectronvolt energies is to overcome the Coulombic barrier of cation/cation reactions. Perhaps because of inelastic transfer of energy during charge transfer, the activation energy obtained through He⁺ CTD exceeds the electron affinity of the He⁺ cation and is on the order of 30 eV.[155] The formation of *c* ions can result from proximal reagent He⁺ ions abstracting an electron (EA ~24.6 eV) and creating a hole in the precursor ions. In turn, the electron deficient ion undergoes radical fragmentation.

1.11. References

1. Lee, S., et al., *Extracted fragment ion mobility distributions: A new method for complex mixture analysis*. International Journal of Mass Spectrometry, 2012. **309**: p. 154-160.
2. Zucker, S.M., et al., *An Ion Mobility/Ion Trap/Photodissociation Instrument for Characterization of Ion Structure*. Journal of the American Society for Mass Spectrometry, 2011. **22**(9): p. 1477-1485.
3. Kelly, R.T., et al., *The ion funnel: Theory, implementations, and applications*. Mass Spectrometry Reviews, 2010. **29**(2): p. 294-312.
4. Shaffer, S.A., et al., *An ion funnel interface for improved ion focusing and sensitivity using electrospray ionization mass spectrometry*. Analytical Chemistry, 1998. **70**(19): p. 4111-4119.
5. Viehland, L.A. and E.A. Mason, *Transport Properties of Gaseous Ions over a Wide Energy Range, IV*. Atomic Data and Nuclear Data Tables, 1995. **60**(1): p. 37-95.
6. Revercomb, H.E. and E.A. Mason, *THEORY OF PLASMA CHROMATOGRAPHY GASEOUS ELECTROPHORESIS - REVIEW*. Analytical Chemistry, 1975. **47**(7): p. 970-983.
7. Mason, E.A.M., E. W., *Transport Properties of Ions in Gases*. 1988, New York: Wiley.
8. Dwivedi, P., et al., *Metabolic profiling by ion mobility mass spectrometry (IMMS)*. Metabolomics, 2008. **4**(1): p. 63-80.
9. Myung, S., et al., *Development of high-sensitivity ion trap-IMS-TOF techniques: A high-throughput nano-LC/IMS/TOF-separation of the Drosophila melanogaster proteome*. Abstracts of Papers of the American Chemical Society, 2003. **226**: p. U112-U112.
10. Dugourd, P., et al., *High-resolution ion mobility measurements*. Review of Scientific Instruments, 1997. **68**(2): p. 1122-1129.
11. Asbury, G.R. and H.H. Hill, *Evaluation of ultrahigh resolution ion mobility spectrometry as an analytical separation device in chromatographic terms*. Journal of Microcolumn Separations, 2000. **12**(3): p. 172-178.
12. Tang, X., J.E. Bruce, and H.H. Hill, *Design and performance of an atmospheric pressure ion mobility Fourier transform ion cyclotron resonance mass spectrometer*. Rapid Communications in Mass Spectrometry, 2007. **21**(7): p. 1115-1122.
13. Moseley, J.T., et al., *Measurement of Transport Properties of Ions in Gases; Results for K^+ Ions in N_2* . Physical Review, 1969. **178**(1): p. 234-239.
14. Tang, K., et al., *High-sensitivity ion mobility spectrometry/mass spectrometry using electrodynamic ion funnel interfaces*. Analytical Chemistry, 2005. **77**(10): p. 3330-3339.
15. Douglas, D.J., A.J. Frank, and D. Mao, *Linear ion traps in mass spectrometry*. Mass Spectrometry Reviews, 2005. **24**(1): p. 1-29.
16. March, R.E., *An Introduction to Quadrupole Ion Trap Mass Spectrometry*. Journal of Mass Spectrometry, 1997. **32**(4): p. 351-369.

17. Mielke, L.H., et al., *Development of a Proton-Transfer Reaction-Linear Ion Trap Mass Spectrometer for Quantitative Determination of Volatile Organic Compounds*. Analytical Chemistry, 2008. **80**(21): p. 8171-8177.
18. Kim, T.-Y., M.S. Thompson, and J.P. Reilly, *Peptide photodissociation at 157 nm in a linear ion trap mass spectrometer*. Rapid Communications in Mass Spectrometry, 2005. **19**(12): p. 1657-1665.
19. Syka, J.E.P., et al., *Peptide and protein sequence analysis by electron transfer dissociation mass spectrometry*. Proceedings of the National Academy of Sciences of the United States of America, 2004. **101**(26): p. 9528-9533.
20. Shukla, A.K. and J.H. Futrell, *Tandem mass spectrometry: dissociation of ions by collisional activation*. Journal of Mass Spectrometry, 2000. **35**(9): p. 1069-1090.
21. Wysocki, V.H., et al., *Mobile and localized protons: a framework for understanding peptide dissociation*. Journal of Mass Spectrometry, 2000. **35**(12): p. 1399-1406.
22. Roepstorff, P. and J. Fohlman, *Proposal for a common nomenclature for sequence ions in mass spectra of peptides*. Biomed Mass Spectrom, 1984. **11**(11): p. 601.
23. Dancik, V., et al., *De novo peptide sequencing via tandem mass spectrometry*. J Comput Biol, 1999. **6**(3-4): p. 327-42.
24. Eng, J.K., A.L. McCormack, and J.R. Yates, *An approach to correlate tandem mass spectral data of peptides with amino acid sequences in a protein database*. Journal of the American Society for Mass Spectrometry. **5**(11): p. 976-989.
25. Boyd, R. and Á. Somogyi, *The Mobile Proton Hypothesis in Fragmentation of Protonated Peptides: A Perspective*. Journal of the American Society for Mass Spectrometry, 2010. **21**(8): p. 1275-1278.
26. Valentine, S.J., et al., *Gas-phase separations of protease digests*. Journal of the American Society for Mass Spectrometry, 1998. **9**(11): p. 1213-1216.
27. Gillig, K.J., et al., *Coupling high-pressure MALDI with ion mobility/orthogonal time-of flight mass spectrometry*. Analytical Chemistry, 2000. **72**(17): p. 3965-3971.
28. Valentine, S.J., et al., *Intrinsic amino acid size parameters from a series of 113 lysine-terminated tryptic digest peptide ions*. Journal of Physical Chemistry B, 1999. **103**(8): p. 1203-1207.
29. Fenn, L.S. and J.A. McLean, *Biomolecular structural separations by ion mobility-mass spectrometry*. Analytical and Bioanalytical Chemistry, 2008. **391**(3): p. 905-909.
30. May, J.C., et al., *Conformational Ordering of Biomolecules in the Gas Phase: Nitrogen Collision Cross Sections Measured on a Prototype High Resolution Drift Tube Ion Mobility-Mass Spectrometer*. Analytical Chemistry, 2014. **86**(4): p. 2107-2116.
31. Paglia, G., et al., *Ion Mobility Derived Collision Cross Sections to Support Metabolomics Applications*. Analytical Chemistry, 2014. **86**(8): p. 3985-3993.
32. Zhang, X., et al., *Metabolic Analysis of Striatal Tissues from Parkinson's Disease-like Rats by Electrospray Ionization Ion Mobility Mass Spectrometry*. Analytical Chemistry, 2014.

33. Yassin, G.H., et al., *Investigation of isomeric flavanol structures in black tea thearubigins using ultraperformance liquid chromatography coupled to hybrid quadrupole/ion mobility/time of flight mass spectrometry*. Journal of Mass Spectrometry, 2014. **49**(11): p. 1086-1095.
34. Malkar, A., et al., *Metabolic profiling of human saliva before and after induced physiological stress by ultra-high performance liquid chromatography-ion mobility-mass spectrometry*. Metabolomics, 2013. **9**(6): p. 1192-1201.
35. Patti, G.J., O. Yanes, and G. Siuzdak, *Metabolomics: the apogee of the omics trilogy*. Nature Reviews Molecular Cell Biology, 2012. **13**(4): p. 263-269.
36. Rappaport, S.M., *Implications of the exposome for exposure science*. Journal of Exposure Science and Environmental Epidemiology, 2011. **21**(1): p. 5-9.
37. Weckwerth, W., *Metabolomics in systems biology*. Annual Review of Plant Biology, 2003. **54**: p. 669-689.
38. Lawton, K.A., et al., *Analysis of the adult human plasma metabolome*. Pharmacogenomics, 2008. **9**(4): p. 383-97.
39. Czene, K., P. Lichtenstein, and K. Hemminki, *Environmental and heritable causes of cancer among 9.6 million individuals in the Swedish family-cancer database*. International Journal of Cancer, 2002. **99**(2): p. 260-266.
40. Menni, C., et al., *Metabolomic markers reveal novel pathways of ageing and early development in human populations*. International Journal of Epidemiology, 2013. **42**(4): p. 1111-1119.
41. Rhee, E.P. and R.E. Gerszten, *Metabolomics and Cardiovascular Biomarker Discovery*. Clinical Chemistry, 2012. **58**(1): p. 139-147.
42. Spratlin, J.L., N.J. Serkova, and S.G. Eckhardt, *Clinical Applications of Metabolomics in Oncology: A Review*. Clinical Cancer Research, 2009. **15**(2): p. 431-440.
43. Underwood, B.R., et al., *Huntington disease patients and transgenic mice have similar pro-catabolic serum metabolite profiles*. Brain, 2006. **129**: p. 877-886.
44. Bogdanov, M., et al., *Metabolomic profiling to develop blood biomarkers for Parkinson's disease*. Brain, 2008. **131**: p. 389-396.
45. Li, F., W. Xu, and S.M. Zhao, *Regulatory Roles of Metabolites in Cell Signaling Networks*. Journal of Genetics and Genomics, 2013. **40**(7): p. 367-374.
46. Cheng, S.S., et al., *Metabolite Profiling Identifies Pathways Associated With Metabolic Risk in Humans*. Circulation, 2012. **125**(18): p. 2222-U132.
47. Dwivedi, P., A.J. Schultz, and H.H. Hill, *Metabolic profiling of human blood by high-resolution ion mobility mass spectrometry (IM-MS)*. International Journal of Mass Spectrometry, 2010. **298**(1-3): p. 78-90.
48. Wishart, D.S., et al., *HMDB: the Human Metabolome Database*. Nucleic Acids Res, 2007. **35**(Database issue): p. D521-6.
49. Patti, G.J., R. Tautenhahn, and G. Siuzdak, *Meta-analysis of untargeted metabolomic data from multiple profiling experiments*. Nature Protocols, 2012. **7**(3): p. 508-516.
50. Bocker, S. and F. Rasche, *Towards de novo identification of metabolites by analyzing tandem mass spectra*. Bioinformatics, 2008. **24**(16): p. 149-155.
51. Scheubert, K., et al., *Computing fragmentation trees from metabolite multiple mass spectrometry data*. J Comput Biol, 2011. **18**(11): p. 1383-97.

52. Cao, M., K. Fraser, and S. Rasmussen, *Computational Analyses of Spectral Trees from Electrospray Multi-Stage Mass Spectrometry to Aid Metabolite Identification*. *Metabolites*, 2013. **3**(4): p. 1036-1050.
53. Peterson, A.C., et al., *Parallel reaction monitoring for high resolution and high mass accuracy quantitative, targeted proteomics*. *Mol Cell Proteomics*, 2012. **11**(11): p. 1475-88.
54. Gillet, L.C., et al., *Targeted data extraction of the MS/MS spectra generated by data-independent acquisition: a new concept for consistent and accurate proteome analysis*. *Mol Cell Proteomics*, 2012. **11**(6): p. O111.016717.
55. Hoadlund-Hyzer, C.S., J.W. Li, and D.E. Clemmer, *Mobility labeling for parallel CID of ion mixtures*. *Analytical Chemistry*, 2000. **72**(13): p. 2737-2740.
56. Koeniger, S.L., et al., *An IMS-IMS analogue of MS-MS*. *Analytical Chemistry*, 2006. **78**(12): p. 4161-4174.
57. Lee, S., et al., *Extracted Fragment Ion Mobility Distributions: A New Method for Complex Mixture Analysis*. *Int J Mass Spectrom*, 2012. **309**: p. 154-160.
58. Zubarev, R.A., N.L. Kelleher, and F.W. McLafferty, *Electron Capture Dissociation of Multiply Charged Protein Cations. A Nonergodic Process*. *Journal of the American Chemical Society*, 1998. **120**(13): p. 3265-3266.
59. Zhurov, K.O., et al., *Principles of electron capture and transfer dissociation mass spectrometry applied to peptide and protein structure analysis*. *Chemical Society Reviews*, 2013. **42**(12): p. 5014-5030.
60. Massonnet, P., et al., *Combined use of ion mobility and collision-induced dissociation to investigate the opening of disulfide bridges by electron-transfer dissociation in peptides bearing two disulfide bonds*. *Anal Chem*, 2015. **87**(10): p. 5240-6.
61. Williams, J.P., et al., *Identifying drug metallation sites on peptides using electron transfer dissociation (ETD), collision induced dissociation (CID) and ion mobility-mass spectrometry (IM-MS)*. *Chemical Communications*, 2010. **46**(30): p. 5458-5460.
62. Rand, K.D., et al., *Site-Specific Analysis of Gas-Phase Hydrogen/Deuterium Exchange of Peptides and Proteins by Electron Transfer Dissociation*. *Analytical Chemistry*, 2012. **84**(4): p. 1931-1940.
63. Rand, K.D., et al., *Gas-phase hydrogen/deuterium exchange in a traveling wave ion guide for the examination of protein conformations*. *Anal Chem*, 2009. **81**(24): p. 10019-28.
64. Waters. *SYNAPT G2-Si High Definition Mass Spectrometry*. 2014 [cited 2014 7/1]; Available from: http://www.waters.com/waters/en_US/SYNAPT-G2-Si-High-Definition-Mass-Spectrometry/nav.htm?cid=134740622&locale=en_US.
65. May, J.C. and J.A. McLean, *Ion Mobility-Mass Spectrometry: Time-Dispersive Instrumentation*. *Analytical Chemistry*, 2014.
66. Xuan, Y., et al., *High-field asymmetric waveform ion mobility spectrometry (FAIMS) coupled with high-resolution electron transfer dissociation mass spectrometry for the analysis of isobaric phosphopeptides*. *Rapid Commun Mass Spectrom*, 2009. **23**(13): p. 1963-9.
67. Cohen, P., *The regulation of protein function by multisite phosphorylation--a 25 year update*. *Trends Biochem Sci*, 2000. **25**(12): p. 596-601.

68. Johnson, L.N., *The regulation of protein phosphorylation*. Biochem Soc Trans, 2009. **37**(Pt 4): p. 627-41.
69. Thorner, J., et al., *Signal transduction: From the atomic age to the post-genomic era*. Cold Spring Harb Perspect Biol, 2014. **6**(12): p. a022913.
70. Riley, N.M. and J.J. Coon, *Phosphoproteomics in the Age of Rapid and Deep Proteome Profiling*. Analytical Chemistry, 2016. **88**(1): p. 74-94.
71. Palumbo, A.M., et al., *Tandem mass spectrometry strategies for phosphoproteome analysis*. Mass Spectrometry Reviews, 2011. **30**(4): p. 600-625.
72. Sharma, K., et al., *Ultradeep Human Phosphoproteome Reveals a Distinct Regulatory Nature of Tyr and Ser/Thr-Based Signaling*. Cell Reports, 2014. **8**(5): p. 1583-1594.
73. Huttlin, E.L., et al., *A tissue-specific atlas of mouse protein phosphorylation and expression*. Cell, 2010. **143**(7): p. 1174-89.
74. Mertins, P., et al., *iTRAQ labeling is superior to mTRAQ for quantitative global proteomics and phosphoproteomics*. Mol Cell Proteomics, 2012. **11**(6): p. M111.014423.
75. Jedrychowski, M.P., et al., *Evaluation of HCD- and CID-type fragmentation within their respective detection platforms for murine phosphoproteomics*. Mol Cell Proteomics, 2011. **10**(12): p. M111.009910.
76. Collins, M.O., et al., *Confident and sensitive phosphoproteomics using combinations of collision induced dissociation and electron transfer dissociation*. J Proteomics, 2014. **103**: p. 1-14.
77. Wiese, H., et al., *Comparison of Alternative MS/MS and Bioinformatics Approaches for Confident Phosphorylation Site Localization*. Journal of Proteome Research, 2014. **13**(2): p. 1128-1137.
78. Good, D.M., et al., *Performance characteristics of electron transfer dissociation mass spectrometry*. Mol Cell Proteomics, 2007. **6**(11): p. 1942-51.
79. Hunt, D.F., J. Shabanowitz, and D.L. Bai, *Peptide Sequence Analysis by Electron Transfer Dissociation Mass Spectrometry: A Web-Based Tutorial*. J Am Soc Mass Spectrom, 2015. **26**(7): p. 1256-8.
80. Konermann, L., J. Pan, and Y.-H. Liu, *Hydrogen exchange mass spectrometry for studying protein structure and dynamics*. Chemical Society Reviews, 2011. **40**(3): p. 1224-1234.
81. Wales, T.E. and J.R. Engen, *Hydrogen exchange mass spectrometry for the analysis of protein dynamics*. Mass Spectrometry Reviews, 2006. **25**(1): p. 158-170.
82. Englander, S.W., *Hydrogen Exchange and Mass Spectrometry: A Historical Perspective*. Journal of the American Society for Mass Spectrometry, 2006. **17**(11): p. 1481-1489.
83. Zhang, Z.Q. and D.L. Smith, *DETERMINATION OF AMIDE HYDROGEN-EXCHANGE BY MASS-SPECTROMETRY - A NEW TOOL FOR PROTEIN-STRUCTURE ELUCIDATION*. Protein Science, 1993. **2**(4): p. 522-531.
84. Hamuro, Y., et al., *Rapid analysis of protein structure and dynamics by hydrogen/deuterium exchange mass spectrometry*. Journal of biomolecular techniques : JBT, 2003. **14**(3): p. 171-82.

85. Englander, S.W., et al., *Mechanisms and uses of hydrogen exchange*. Current Opinion in Structural Biology, 1996. **6**(1): p. 18-23.
86. Engen, J.R., *Analysis of Protein Conformation and Dynamics by Hydrogen/Deuterium Exchange MS*. Analytical Chemistry, 2009. **81**(19): p. 7870-7875.
87. Kaltashov, I.A., C.E. Bobst, and R.R. Abzalimov, *H/D Exchange and Mass Spectrometry in the Studies of Protein Conformation and Dynamics: Is There a Need for a Top-Down Approach?* Analytical Chemistry, 2009. **81**(19): p. 7892-7899.
88. Kaltashov, I.A., C.E. Bobst, and R.R. Abzalimov, *Mass spectrometry-based methods to study protein architecture and dynamics*. Protein Science, 2013. **22**(5): p. 530-544.
89. Keppel, T.R. and D.D. Weis, *Analysis of Disordered Proteins Using a Simple Apparatus for Millisecond Quench-Flow H/D Exchange*. Analytical Chemistry, 2013. **85**(10): p. 5161-5168.
90. Skinner, J.J., et al., *Protein dynamics viewed by hydrogen exchange*. Protein Sci, 2012. **21**(7): p. 996-1005.
91. Katta, V. and B.T. Chait, *CONFORMATIONAL-CHANGES IN PROTEINS PROBED BY HYDROGEN-EXCHANGE ELECTROSPRAY-IONIZATION MASS-SPECTROMETRY*. Rapid Communications in Mass Spectrometry, 1991. **5**(4): p. 214-217.
92. Lee, T., et al., *Docking Motif Interactions in MAP Kinases Revealed by Hydrogen Exchange Mass Spectrometry*. Molecular Cell, 2004. **14**(1): p. 43-55.
93. Ehring, H., *Hydrogen Exchange/Electrospray Ionization Mass Spectrometry Studies of Structural Features of Proteins and Protein/Protein Interactions*. Analytical Biochemistry, 1999. **267**(2): p. 252-259.
94. Sowole, M.A., et al., *Noncovalent binding of a cyclic peptide inhibitor to the peptidyl-prolyl isomerase Pin1, explored by hydrogen exchange mass spectrometry*. Canadian Journal of Chemistry, 2014. **93**(1): p. 44-50.
95. Sowole, M.A. and L. Konermann, *Effects of Protein–Ligand Interactions on Hydrogen/Deuterium Exchange Kinetics: Canonical and Noncanonical Scenarios*. Analytical Chemistry, 2014. **86**(13): p. 6715-6722.
96. Arndt, J.R., et al., *Lysine residues in the N-terminal huntingtin amphipathic α -helix play a key role in peptide aggregation*. Journal of Mass Spectrometry, 2015. **50**(1): p. 117-126.
97. Weis, D.D., et al., *Identification and Characterization of EX1 Kinetics in H/D Exchange Mass Spectrometry by Peak Width Analysis*. Journal of the American Society for Mass Spectrometry, 2006. **17**(11): p. 1498-1509.
98. Sivaraman, T. and A. Robertson, *Kinetics of Conformational Fluctuations by EX1 Hydrogen Exchange in Native Proteins*, in *Protein Structure, Stability, and Folding*, K. Murphy, Editor. 2001, Humana Press. p. 193-214.
99. Krishna, M.M., et al., *Hydrogen exchange methods to study protein folding*. Methods, 2004. **34**(1): p. 51-64.
100. Mayne, L., et al., *Many Overlapping Peptides for Protein Hydrogen Exchange Experiments by the Fragment Separation-Mass Spectrometry Method*. Journal of The American Society for Mass Spectrometry, 2011. **22**(11): p. 1898-1905.

101. Zhang, H.M., et al., *Fast reversed-phase liquid chromatography to reduce back exchange and increase throughput in H/D exchange monitored by FT-ICR mass spectrometry*. J Am Soc Mass Spectrom, 2009. **20**(3): p. 520-4.
102. Jones, L.M., et al., *Online, High-Pressure Digestion System for Protein Characterization by Hydrogen/Deuterium Exchange and Mass Spectrometry*. Analytical Chemistry, 2010. **82**(4): p. 1171-1174.
103. Engen, J.R. and D.L. Smith, *Investigating protein structure and dynamics by hydrogen exchange MS*. Anal Chem, 2001. **73**(9): p. 256a-265a.
104. Ahn, J., et al., *Assessing the reproducibility and specificity of pepsin and other aspartic proteases*. Biochim Biophys Acta, 2013. **1834**(6): p. 1222-9.
105. Ahn, J., et al., *Pepsin immobilized on high-strength hybrid particles for continuous flow online digestion at 10,000 psi*. Anal Chem, 2012. **84**(16): p. 7256-62.
106. Pan, J., et al., *Electron Capture Dissociation of Electrosprayed Protein Ions for Spatially Resolved Hydrogen Exchange Measurements*. Journal of the American Chemical Society, 2008. **130**(35): p. 11574-11575.
107. Huang, R.Y.C., et al., *Hydrogen/Deuterium Exchange and Electron-Transfer Dissociation Mass Spectrometry Determine the Interface and Dynamics of Apolipoprotein E Oligomerization*. Biochemistry, 2011. **50**(43): p. 9273-9282.
108. Zehl, M., et al., *Electron Transfer Dissociation Facilitates the Measurement of Deuterium Incorporation into Selectively Labeled Peptides with Single Residue Resolution*. Journal of the American Chemical Society, 2008. **130**(51): p. 17453-17459.
109. Pan, J. and C.H. Borchers, *Top-down structural analysis of posttranslationally modified proteins by Fourier transform ion cyclotron resonance-MS with hydrogen/deuterium exchange and electron capture dissociation*. Proteomics, 2013. **13**(6): p. 974-81.
110. Abzalimov, R.R., C.E. Bobst, and I.A. Kaltashov, *A New Approach to Measuring Protein Backbone Protection with High Spatial Resolution Using H/D Exchange and Electron Capture Dissociation*. Analytical Chemistry, 2013. **85**(19): p. 9173-9180.
111. Rand, K.D., et al., *Protein hydrogen exchange measured at single-residue resolution by electron transfer dissociation mass spectrometry*. Anal Chem, 2009. **81**(14): p. 5577-84.
112. Landgraf, R., M. Chalmers, and P. Griffin, *Automated Hydrogen/Deuterium Exchange Electron Transfer Dissociation High Resolution Mass Spectrometry Measured at Single-Amide Resolution*. Journal of The American Society for Mass Spectrometry, 2012. **23**(2): p. 301-309.
113. Rand, K.D., et al., *Protein Hydrogen Exchange Measured at Single-Residue Resolution by Electron Transfer Dissociation Mass Spectrometry*. Analytical Chemistry, 2009. **81**(14): p. 5577-5584.
114. Deng, Y., H. Pan, and D.L. Smith, *Selective isotope labeling demonstrates that hydrogen exchange at individual peptide amide linkages can be determined by collision-induced dissociation mass spectrometry*. Journal of the American Chemical Society, 1999. **121**(9): p. 1966-1967.

115. Abzalimov, R.R. and I.A. Kaltashov, *Controlling Hydrogen Scrambling in Multiply Charged Protein Ions during Collisional Activation: Implications for Top-Down Hydrogen/Deuterium Exchange MS Utilizing Collisional Activation in the Gas Phase*. Analytical Chemistry, 2010. **82**(3): p. 942-950.
116. Hoerner, J.K., H. Xiao, and I.A. Kaltashov, *Structural and Dynamic Characteristics of a Partially Folded State of Ubiquitin Revealed by Hydrogen Exchange Mass Spectrometry*. Biochemistry, 2005. **44**(33): p. 11286-11294.
117. Abzalimov, R.R., et al., *Protein conformations can be probed in top-down HDX MS experiments utilizing electron transfer dissociation of protein ions without hydrogen scrambling*. Journal of the American Society for Mass Spectrometry, 2009. **20**(8): p. 1514-1517.
118. Rand, K.D., et al., *Electron capture dissociation proceeds with a low degree of intramolecular migration of peptide amide hydrogens*. J Am Chem Soc, 2008. **130**(4): p. 1341-9.
119. Rand, K.D., M. Zehl, and T.J. Jorgensen, *Measuring the hydrogen/deuterium exchange of proteins at high spatial resolution by mass spectrometry: overcoming gas-phase hydrogen/deuterium scrambling*. Acc Chem Res, 2014. **47**(10): p. 3018-27.
120. Syka, J.E., et al., *Peptide and protein sequence analysis by electron transfer dissociation mass spectrometry*. Proceedings of the National Academy of Sciences of the United States of America, 2004. **101**(26): p. 9528-9533.
121. Baker, E.S., et al., *Ion mobility spectrometry-mass spectrometry performance using electrodynamic ion funnels and elevated drift gas pressures*. J Am Soc Mass Spectrom, 2007. **18**(7): p. 1176-87.
122. Becker, C., F.A. Fernandez-Lima, and D.H. Russell, *Ion Mobility-Mass Spectrometry: A Tool for Characterizing the Petroleome*. Spectroscopy, 2009. **24**(4): p. 38-42.
123. Clowers, B.H., et al., *Separation of sodiated isobaric disaccharides and trisaccharides using electrospray ionization-atmospheric pressure ion mobility-time of flight mass spectrometry*. Journal of the American Society for Mass Spectrometry, 2005. **16**(5): p. 660-669.
124. Ruotolo, B.T., et al., *Peak capacity of ion mobility mass spectrometry: Separation of peptides in helium buffer gas*. Journal of Chromatography B-Analytical Technologies in the Biomedical and Life Sciences, 2002. **782**(1-2): p. 385-392.
125. Valentine, S.J., et al., *Toward Plasma Proteome Profiling with Ion Mobility-Mass Spectrometry*. Journal of Proteome Research, 2006. **5**(11): p. 2977-2984.
126. Wu, C., et al., *Separation of isomeric peptides using electrospray ionization/high-resolution ion mobility spectrometry*. Anal Chem, 2000. **72**(2): p. 391-5.
127. Bohrer, B.C., et al., *Biomolecule Analysis by Ion Mobility Spectrometry*, in *Annual Review of Analytical Chemistry*. 2008. p. 293-327.
128. Clemmer, D.E. and M.F. Jarrold, *Ion mobility measurements and their applications to clusters and biomolecules*. Journal of Mass Spectrometry, 1997. **32**(6): p. 577-592.
129. Counterman, A.E., et al., *Formation of peptide aggregates during ESI: Size, charge, composition, and contributions to noise*. Journal of the American Society for Mass Spectrometry, 2001. **12**(9): p. 1020-1035.

130. Zinnel, N.F., P.J. Pai, and D.H. Russell, *Ion Mobility-Mass Spectrometry (IM-MS) for Top-Down Proteomics: Increased Dynamic Range Affords Increased Sequence Coverage*. Analytical Chemistry, 2012. **84**(7): p. 3390-3397.
131. Rand, K., et al., *ETD in a Traveling Wave Ion Guide at Tuned Z-Spray Ion Source Conditions Allows for Site-Specific Hydrogen/Deuterium Exchange Measurements*. Journal of The American Society for Mass Spectrometry, 2011. **22**(10): p. 1784-1793.
132. Iacob, R.E., J.P. Murphy, and J.R. Engen, *Ion mobility adds an additional dimension to mass spectrometric analysis of solution-phase hydrogen/deuterium exchange*. Rapid Communications in Mass Spectrometry, 2008. **22**(18): p. 2898-2904.
133. Mistarz, U.H., et al., *Simple Setup for Gas-Phase H/D Exchange Mass Spectrometry Coupled to Electron Transfer Dissociation and Ion Mobility for Analysis of Polypeptide Structure on a Liquid Chromatographic Time Scale*. Analytical Chemistry, 2014. **86**(23): p. 11868-11876.
134. Beeston, H.S., et al., *Changes in protein structure monitored by use of gas-phase hydrogen/deuterium exchange*. Proteomics, 2015.
135. Khakinejad, M., et al., *Combining ion mobility spectrometry with hydrogen-deuterium exchange and top-down MS for peptide ion structure analysis*. J Am Soc Mass Spectrom, 2014. **25**(12): p. 2103-15.
136. Khakinejad, M., et al., *Gas-Phase Hydrogen-Deuterium Exchange Labeling of Select Peptide Ion Conformer Types: a Per-Residue Kinetics Analysis*. J Am Soc Mass Spectrom, 2015.
137. Campbell, S., et al., *Deuterium exchange reactions as a probe of biomolecule structure. Fundamental studies of gas phase H/D exchange reactions of protonated glycine oligomers with D₂O, CD₃OD, CD₃CO₂D, and ND₃*. Journal of the American Chemical Society, 1995. **117**(51): p. 12840-12854.
138. Gard, E., et al., *Gas-phase hydrogen/deuterium exchange as a molecular probe for the interaction of methanol and protonated peptides*. J Am Soc Mass Spectrom, 1994. **5**(7): p. 623-31.
139. Campbell, S., et al., *Deuterium Exchange Reactions as a Probe of Biomolecule Structure. Fundamental Studies of Gas Phase H/D Exchange Reactions of Protonated Glycine Oligomers with D₂O, CD₃OD, CD₃CO₂D, and ND₃*. Journal of the American Chemical Society, 1995. **117**(51): p. 12840-12854.
140. Suckau, D., et al., *Coexisting stable conformations of gaseous protein ions*. Proceedings of the National Academy of Sciences of the United States of America, 1993. **90**(3): p. 790-793.
141. Chan, S. and C.G. Enke, *Mechanistic study of hydrogen/deuterium exchange between [M - 1]⁻ ions of chlorinated benzenes and D₂O or ND₃*. Journal of the American Society for Mass Spectrometry, 1994. **5**(4): p. 282-291.
142. Robinson, J.M., et al., *Hydrogen/deuterium exchange of nucleotides in the gas phase*. Analytical Chemistry, 1998. **70**(17): p. 3566-3571.
143. Freitas, M.A., et al., *Gas-phase RNA and DNA ions. 1. H/D exchange of the M-H (-) anions of nucleoside 5'-monophosphates (GMP, dGMP, AMP, dAMP, CMP, dCMP, UMP, dTMP), ribose 5-monophosphate, and 2-deoxyribose 5-*

- monophosphate with D2O and D2S*. Journal of the American Chemical Society, 1998. **120**(39): p. 10187-10193.
144. Chipuk, J.E. and J.S. Brodbelt, *Gas-phase hydrogen/deuterium exchange of 5'- and 3'-mononucleotides in a quadrupole ion trap: Exploring the role of conformation and system energy*. Journal of the American Society for Mass Spectrometry, 2007. **18**(4): p. 724-736.
 145. Freitas, M.A. and A.G. Marshall, *Gas phase RNA and DNA ions 2. Conformational dependence of the gas-phase H/D exchange of nucleotide-5'-monophosphates*. Journal of the American Society for Mass Spectrometry, 2001. **12**(7): p. 780-785.
 146. Crestoni, M.E. and S. Fornarini, *Gas-phase hydrogen/deuterium exchange of adenine nucleotides*. Journal of Mass Spectrometry, 2003. **38**(8): p. 854-861.
 147. Tian, Z., L. Lis, and S.R. Kass, *Hydrogen-deuterium exchange and selective labeling of deprotonated amino acids and peptides in the gas phase*. J Am Chem Soc, 2008. **130**(1): p. 8-9.
 148. Bache, N., et al., *Hydrogen atom scrambling in selectively labeled anionic peptides upon collisional activation by MALDI tandem time-of-flight mass spectrometry*. J Am Soc Mass Spectrom, 2008. **19**(12): p. 1719-25.
 149. Yoo, H.J., et al., *Negative-ion electron capture dissociation: radical-driven fragmentation of charge-increased gaseous peptide anions*. J Am Chem Soc, 2011. **133**(42): p. 16790-3.
 150. Hersberger, K.E. and K. Hakansson, *Characterization of O-Sulfopeptides by Negative Ion Mode Tandem Mass Spectrometry: Superior Performance of Negative Ion Electron Capture Dissociation*. Analytical Chemistry, 2012. **84**(15): p. 6370-6377.
 151. Cook, S.L., et al., *Comparison of CID, ETD and metastable atom-activated dissociation (MAD) of doubly and triply charged phosphorylated tau peptides*. Journal of Mass Spectrometry, 2012. **47**(6): p. 786-794.
 152. Cook, S.L., O.L. Collin, and G.P. Jackson, *Metastable atom-activated dissociation mass spectrometry: leucine/isoleucine differentiation and ring cleavage of proline residues*. Journal of Mass Spectrometry, 2009. **44**(8): p. 1211-1223.
 153. Zhou, M.W. and V.H. Wysocki, *Surface Induced Dissociation: Dissecting Noncovalent Protein Complexes in the Gas phase*. Accounts of Chemical Research, 2014. **47**(4): p. 1010-1018.
 154. Zhou, M.W., C.S. Huang, and V.H. Wysocki, *Surface-Induced Dissociation of Ion Mobility-Separated Noncovalent Complexes in a Quadrupole/Time-of-Flight Mass Spectrometer*. Analytical Chemistry, 2012. **84**(14): p. 6016-6023.
 155. Hoffmann, W. and G. Jackson, *Charge Transfer Dissociation (CTD) Mass Spectrometry of Peptide Cations Using Kiloelectronvolt Helium Cations*. Journal of The American Society for Mass Spectrometry, 2014. **25**(11): p. 1939-1943.
 156. Chingin, K., et al., *Fragmentation of Positively-Charged Biological Ions Activated with a Beam of High-Energy Cations*. Analytical Chemistry, 2014. **86**(1): p. 372-379.

2. A New Ion Mobility – Linear Ion Trap Instrument for Complex Mixture Analysis¹

¹Reprinted in part with permission from *Analytical Chemistry: A New Ion Mobility – Linear Ion Trap for Complex Mixture Analysis*. Gregory C. Donohoe, Hossein Maleki, James R. Arndt, Mahdiar Khakinejad, Jinghai Yi, Carroll McBride, Timothy Nurkiewicz, and Stephen J. Valentine. *Anal. Chem.*, 2014, 86 (16), pp 8121–8128.

2.1. Introduction: Complex Mixture Separations Using IMS-MS

Over the last two decades, the use of ion mobility spectrometry (IMS) coupled with mass spectrometry (MS) as a means for biomolecular ion separation has grown dramatically.[1-13] The added peak capacity afforded by the gas-phase separation (IMS) enhances the detection of lower-signal species by removing them from spectral regions containing interfering features from higher-signal ions.[7, 14-16] This advantage has driven technological development in the private sector as an increasing number of MS-based instrument platforms are adopting/developing IMS separation steps.[17-19]

Much of the IMS-MS instrumentation demonstrated for complex mixture analysis has employed the use of time-of-flight (TOF) mass analyzers.[1, 2, 20] The advantage of coupling IMS with TOFMS is that individual TOF spectra can be “nested” within the drift time (t_D) measurement.[21] Although this instrument configuration allows the mass determination of all mobility-dispersed ions, the inability to trap ions precludes the use of multi-stage tandem mass spectrometry (MS^n) as a means for identifying complex mixture components. This is problematic for identifying intractable molecules for which MS/MS analysis is insufficient.[22-25]

IMS-MS instrumentation development has also yielded instruments combining drift tubes with mass spectrometers that employ ion trapping.[26-28][29, 30] Featured designs include those utilizing high-resolution drift tubes operated at atmospheric

pressure and elevated drift voltages.[27, 28] Two challenges became evident with this type of instrument design that relate to the overall measurement sensitivity. The first challenge was associated with the low duty cycle of the measurement. The second was that the addition of the required mobility-selection ion gate essentially resulted in a scanning/filtering operational mode. That is, only ions of select mobilities were transferred into the mass spectrometer. These problems may be addressed in the future using ideas presented in seminal studies demonstrating the use of Fourier Transform and Hadamard Transform IMS.[31-33]

One problem that persists with instruments coupling high-pressure IMS and ion trap mass spectrometers is the decrease in ion transmission across the drift tube-mass spectrometer interface region. That is, ions can be lost in conductance-limiting regions as there are no means currently available to focus diffuse ion clouds at elevated pressures. The ability to compress ion packets in low-pressure drift tubes[34, 35] was one of the motivating factors for pursuing the instrumentation design described here. Additionally, the low-pressure drift tube can not only serve as the device to achieve gas-phase separation but also as an ion fragmentation cell employing collision-induced dissociation (CID).[36] Indeed, the higher-pressure fragmentation process (hereafter referred to as IMS-CID) has been demonstrated to be efficient and highly tunable.[7, 36-38] The combination of the IMS-CID capabilities of the drift tube with the MSⁿ capabilities of the linear ion trap further distinguish the instrument described here.

The new analytical capabilities of the instrument are here demonstrated with the analysis of two model mixture samples. The first sample analysis represents the capability to rapidly identify phosphorylated peptides in tryptic digests such as would be

encountered in post-translational modification (PTM) experiments. For these studies, IMS-CID methods show that targets for PTM analysis can rapidly be ascertained and subsequently subjected to electron transfer dissociation (ETD)[39] to identify phosphorylation sites. To some degree, the approach is similar to proteomics techniques that scan for neutral loss of H_3PO_4 and subject target ions to further tandem MS experiments.[40, 41] A difference is that extracted ion drift time distributions (XIDTD)[42] help to confirm and isolate ions for subsequent tandem MS experiments. Although several instruments demonstrating fragmentation of mobility-selected ions have been described,[7, 36, 37, 43, 44] this work presents the first combination of IMS-CID[36, 38] and ETD-MS. The second experimental example using the IM-MS to profile the plasma metabolome of rats exposed to engineered nanomaterials (ENM) via inhalation. For these studies organisms are exposed to TiO_2 nanoparticles (NP). Here NP can be described as species exhibiting less than 100 nm in length in any dimension. Two-dimensional (2D) IMS-MS datasets are generated for samples from organisms for different post exposure times (directly after and 24 hours post exposure). Comparisons of the 2D datasets show the enhancement provided by the IMS separation for distinguishing samples. Instrumental aspects facilitating ion identification and relative quantitation including IMS coupled with MS^n and IM-collision-induced dissociation (CID)-MS[36, 43] are discussed. This study is unique in that it presents the first demonstration of IMS- MS^n to putatively identify plasma metabolites in comparative analyses. Both 'omic analyses demonstrate the ability of the IM-MS separation compare all spectra without dataset alignment.

The described instrument is similar to that coupling IMS-LIT analysis with photodissociation capabilities;[29, 42] however, this work describes unique ion fragmentation techniques such as the combination of two different methods (IMS-CID and ETD-MS) as well as MS⁴ of mobility-selected ions. The direction of future instrumentation development is discussed while considering improvements for complex mixture analysis.

2.2. Materials and Methods

Cytochrome c (Equine, 95%) was purchased from Sigma Aldrich (St. Louis, MO) and used without further purification. Phosphorylated peptide standards (95% purity) with sequences of KRPsQRHGSKY-NH₂ and SFVLNPTNIGMsKSSQGHVTK were purchased from AnaSpec (Fenton CA) and used without further purification. The peptide, KKDDDDDIKIIK (~90%) was purchased from Genscript. Ultra-pure (chromatography grade) deionized water, methanol, and formic acid (Fisher Scientific, Fair Lawn, NJ, USA) were used to generate stock and ESI solutions of the peptide and proteins.

2.2.1. Phosphoproteomic Samples

Cytochrome c (1.0 mg) was diluted in 1.0 mL of deionized water. Urea was added to a final concentration of 1.5 M. TPCK-treated trypsin was added at a ratio of 1:20 (trypsin:cytochrome c) and the sample was incubated overnight. The tryptic digest (100 μ L) was diluted 10 fold in ESI solution (1:1 water:methanol and 1% formic acid) and 10 μ g (0.01 μ g \cdot μ L⁻¹) of the phosphorylated peptide standard (KRPsQRHGSKY-NH₂) was added to the solution.

2.2.2. Rat Exposure to TiO₂ Nanoparticles

Rat plasma samples were obtained from the West Virginia University Center for Cardiovascular and Respiratory Sciences, School of Medicine, Morgantown, WV. The ENM exposure apparatus and organism handling were described in detail previously.[45, 46] Briefly, Male Sprague Dawley rats (175 - 250 g) were purchased from Hilltop Laboratories (Scottsdale, PA), and housed in laminar flow cages under controlled temperature and humidity conditions and a 12 hr light/12 hr dark cycle at the West Virginia University Health Sciences Center vivarium. Food and water were provided ad libitum. All animals were acclimated for 72-hours before nanomaterial inhalation exposure. To ensure that all methods were performed humanely and with regard to alleviation of suffering, all procedures were approved by the Institutional Animal Care and Use Committee of West Virginia University.

To profile the metabolomes at different post-exposure times, blood was collected directly after exposure to TiO_2 nanoparticles and 24 hours post exposure for control (filtered air) and exposed animals. During exposure, rats were placed into a home-built chamber specifically designed to deliver the nanoparticles. An aerosolized stream of TiO_2 was introduced into the chamber for three hours to deliver an estimated pulmonary load of 30 μg per animal. Blood samples were immediately centrifuged for 10 minutes at 2500 g to produce plasma. The plasma was stored at $-80\text{ }^\circ\text{C}$ until preparation. Hereafter, plasma samples generated directly after exposure and 24 hours post exposure is referred to as EXP0 and EXP24, respectively. For control animals, the same time point samples are referred to as CNTRL0 and CNTRL24.

2.2.2.1. Metabolite Extraction

Pooled plasma samples were prepared from the 40 individual samples by combining 25- μL aliquots. Using a temperature-controlled micro-centrifuge digital dry bath (Lanbnet International, Inc, Edison, NJ, USA), 400 μL of 80°C methanol is added to 100 μL of pooled sample. The samples were vortexed and incubated first at 80 °C (5 minutes) and immediately transferred to ice (5 minutes). Proteins were pelleted using centrifugation (ThermoScientific, San Jose, CA, USA) at 13,000 g for 20 minutes at 4 °C. The supernatant (~375 μL) was combined with 300 μL 18 M Ω H_2O :5% formic acid. Samples were delivered by a syringe pump (KD scientific Holliston, MA, USA) using a 500- μL syringe (Hamilton, Reno, NV, USA) to a pulled-tip nano-electrospray emitter (350 μm o.d. \times 75 μm i.d.). The sample flow was maintained at 300 $\text{nL}\cdot\text{min}^{-1}$ and a bias of 2.2 kV was used to perform electrospray ionization (ESI)[47] of the metabolite mixture.

2.2.3. IMS-MS: Instrumental Operation

IMS theory,[48-51] instrumentation[32, 52-58] and techniques[43, 59-62] are described elsewhere in great detail. For these experiments, the IMS-MS instrument consists of a dual ion funnel/ ion gate design coupled to a LTQ Velos (Thermo Electron, San Jose, CA, USA) mass spectrometer similar to that reported previously.[29, 42] Figure 1.1 shows the instrument schematic designating the locations of the ion funnels, ion gates and ion activation regions within the drift tube. The mass spectrometer has been modified by replacing the ion source and s-lens assembly with a stacked-ring ion drift region (Figure 1.1). Briefly, electrosprayed ions enter into a desolvation region and are focused through an hour-glass ion funnel (F1 in Figure 1.1).[13, 63] Ions are trapped in F1 and periodically pulsed into the drift tube. The drift tube is filled with He buffer gas

(~2.5 Torr at 300 K). Ions traverse the drift tube under the influence of a uniform electric field ($\sim 11 \text{ V}\cdot\text{cm}^{-1}$) and separate based on differences in their mobilities. Upon reaching a selection gate (G2 in Figure 1.1) ions pass into a second ion funnel (F2) used to radially focus the ion cloud.[34, 35] The ions subsequently exit the drift tube through a conductance-limiting aperture and are focused by quadrupole and octopole rf guides before entering into the higher pressure linear ion trap followed by subsequent mass analysis in the lower pressure trap.

2.2.3.1. Recording Two-Dimensional (2D) $t_D(m/z)$ Distributions.

Ion gates (Figure 1.1) are constructed using Ni gridded lens (90% transmittance mesh; Precision Eforming, Cortland, NY, USA). A single, gridded lens located immediately after the first funnel (F1 in Figure 1.1) serves as the first ion gate (G1 in Figure 1). Ions are pulsed into the drift region at G1 (-40 V) for 150 μs every 20 to 30 ms. Data used to construct ion t_D distributions are collected using a time-delayed voltage drop (-3 V) applied to G2. The time delay for opening G2 relative to the initiation pulse at G1 using a step resolution of 0.15 ms (tryptic digest sample) and 0.2 ms (metabolite extract sample) was scanned across the mobility distribution range. For the tryptic digest this range was 4 ms to 12 ms resulting in 41 mobility-resolved mass spectra. For the metabolite sample, the range was 3.4 ms to 15 ms yielding 59 mobility-resolved mass spectra. The mass spectra are combined to create 2D $t_D(m/z)$ datasets (see below). The introduction pulse at G1 and variable delay settings at G2 are controlled by 2 four-channel digital pulse generators (Stanford Research Systems, Sunnyvale, CA, USA).

2.2.3.2. Parallel Dissociation Methods.

Parallel dissociation within a drift tube, (IMS-CID-MS, IMSⁿ-MS) has been previously described in detail[36, 38] and demonstrated for 'omics applications[7]. Briefly, mobility separated ions are subjected to energizing collisions at the second ion activation region (IA2 in Figure 1.1). For dissociation, the voltage between the last two electrodes of the F2/IA2/G2 assembly (Figure 1.1) is elevated to ~220 V over a length of ~0.3 cm. This produces a field of ~700 V·cm⁻¹ to induce ion fragmentation prior to entering the mass analyzer. Thus low-field settings (~11 V·cm⁻¹) and high-field settings (~700 V·cm⁻¹) are employed to transmit precursor and fragment ions, respectively. For neutral loss experiments (see below), more gentle activation conditions (~453 V·cm⁻¹) are employed in the collisional activation region.

2.2.4. Mass Spectrometry Measurements

Mass spectra are generated for all ions by deactivating the dual drift tube gates and setting the mass analyzer scan parameters over a m/z range of 80 to 2000 while enabling the automatic gain control (AGC). The AGC threshold is 1×10^6 ions. In this operational mode, the drift tube acts to transmit all ions into the mass analyzer. During t_D distribution generation, the gates are activated to transmit a specific mobility into the linear trap. For these analyses, the AGC is disabled and sample injection times of 400 ms (4 microscans) for the tryptic digest and 100 ms (1 microscan) for the metabolites are employed.

MSⁿ analysis is conducted by mobility-selecting and isolating (m/z) a precursor ion. For experiments employing CID in the ion trap, a m/z isolation window of ± 1.0 Da relative to the centroid m/z value results in the ejection of all other ions within the t_D window. Selected ions are collisionally activated by a resonant rf excitation waveform

for 10 ms using a normalized activation energy of 35.0%. Fragment ions displaying sufficient signal-to-noise (S/N) levels are isolated in the linear ion trap and subsequently fragmented. For experiments employing ETD, a m/z isolation window of ± 1.0 Da relative to the centroid m/z value was utilized. The acquisition time was set at 100 ms. All precursor and fragment ion spectra were recorded using the XCalibur 2.2 software suite (ThermoScientific, San Jose, CA).

2.2.5. Generating IMS-MS Datasets

Two-dimensional IMS-MS datasets are generated by converting each t_D -selected mass spectrum (.RAW file) to a separate text file. Using software developed in house, the m/z values and intensities from all of the text files are then associated with the respective t_D selection time generating a three-column array text file containing (t_D , m/z , and intensity values). Intensity filters are applied to generate three-column array files of manageable sizes. To generate t_D distributions for specific ions (including fragment ions from parallel dissociation), a separate program (in house) integrates all intensities within a user-defined m/z range for each t_D window. As mentioned above, this is termed a XIDTD.[42]

2.2.5.1. Comparing of IMS-MS Datasets.

IMS-MS [$t_D(m/z)$] datasets (triplicate measurements) were compared across the four metabolite samples using intensity integration for user-defined pixels over a designated range in the $t_D(m/z)$ distribution. For these comparisons, each pixel represented m/z and t_D windows of 2 m/z units and 500 μs , respectively. Data normalization is performed by dividing all integrated pixels in the IMS-MS dataset by the

total ion intensity. Because of the high-reproducibility of the IMS measurements, alignment of dataset pixels was not performed.

2.2.6. Detection Limit Sample Preparation

A model peptide of sequence KKDDDDIIKIHK (Genscript, ~90%) was prepared in 1:1 18 MΩ H₂O:methanol containing 1% formic acid at a stock concentration of 1mg·mL⁻¹. Using a serial dilution method, a working sample (0.1 μg·mL⁻¹) was prepared for sensitivity studies. The working sample was delivered by a syringe pump (KD scientific Holliston, MA, USA) using a 500-μL syringe (Hamilton, Reno, NV, USA) to a pulled-tip nano-electrospray emitter (350 μm o.d.x75 μm i.d.). The sample flow was maintained at 60 nL·min⁻¹ and a bias of 1.7 kV was used during direct infusion of the sample solution.

2.3.1.2. Dynamic Range Studies

A phosphopeptide standard (Anaspec, Fenton , CA) having a sequence of SFVLNPTNIGMsKSSQGHVTK (M.W. 2316.6) was added to the tryptic digest solution at a concentration of 0.01 μg·μL⁻¹. The standard was chosen due to efficient ionization properties. During IMS-MS dataset generation of the tryptic digest, the [SFVLNPTNIGMsKSSQGHVTK +3]³⁺ ion (*m/z* 771.9) was evaluated (XIDTD) for maximum intensity because it produced the largest signal. In addition to this ion, the signal level for the low-intensity [KYIPGTK+1H]¹⁺ peptide ion from the cytochrome c digest was also evaluated from a XIDTD.

2.2.8. Principal Component Analysis (PCA)

Using the JMP statistical software package (JMP, Version 7. SAS Institute Inc., Cary, NC, 1989-2007) PCA has been performed for the triplicate analyses of each

cohort. For PCA, inputs included the normalized pixel intensities (see above). A comparison of dataset features providing the greatest contribution to distinguishing the datasets by PCA is performed using the loadings matrix (LM) values for all pixel inputs. High LM scores (≥ 0.90 in absolute value) along principal component one (PC 1) result in the determination of pixels for which dataset features exhibit large differences in intensity.

2.2.9. Exact Mass Measurements.

A Q-Exactive Orbitrap mass spectrometer (Thermo Scientific, San Jose, CA, USA) has been used for exact mass measurements. Briefly, the EXP24 sample is introduced by direct infusion through a heated electrospray source inlet (HESI) using a 2.5 kV spray voltage bias relative to the entrance orifice and a capillary temperature of 250 °C. The generated ions pass through the S-lens ion guide (60.0 V) and are subsequently transferred into an Orbitrap mass analyzer. The Orbitrap is scanned from m/z 100.0 to 1000.0 with a resolving power of 140,000. A target AGC of 1.0×10^6 with a 200 ms injection time has been used for the analysis.

2.3. Results and Discussion

2.3.1. Instrument Figures of Merit

Instrument figures of merit. A number of the measurement capabilities of the instrument are here reported to provide context for its utility in complex mixture analysis. The resolving power ($t_D/\Delta t_D$ FWHM) capabilities of the instrument can be provided from the XIDTDs of a number of singly-charged peptide ions. The singly-charged ions are used because they are observed in a less congested area of the two-dimensional (2D) IMS-MS dataset and therefore are less influenced by overlapping ions. For the peptides

[MIFAGIK+H]⁺ , [YIPGTK+H]⁺ , and [GITWK+H]⁺ resolving power values of 36, 46, and 40 have been computed. It is noted that for this 1-m long drift tube, the resolving power is somewhat limited by the gate width of the second ion gate (G2 in Figure 1.1) Because of the finite distance (3 mm) of the Tyndall gate, a relatively large “open” time is required to transmit the ions of interest. This will limit the achievable resolving power. Increasing the drift tube length to 2 m and 3 m would lessen the effect of this drift time (t_D) bin size.

2.3.1.1. Detection Limit Studies

The detection limits of the instrument have been determined for individual peptide ions. This is accomplished by serial dilution of a given peptide in ESI solution until ion signals are just perceptible for mobility-selected species. Figure 2.1 shows the mass spectral peak for mobility-selected [M+3H]³⁺ ions of the model peptide KKDDDDDIKLIK. Here, the concentration of the peptide was 0.1 $\mu\text{g}\cdot\text{mL}^{-1}$. The spectrum represents a 1.0 second signal averaging from a 6 second data acquisition. The signal-to-noise ratio (S/N) of 31 suggests that detection limits (S/N = 3) for this peptide are 64 attomoles. Based on signal levels for other peptides, it is estimated that the detection limits for mobility-selected ions (dominant charge states) are generally tens of attomoles.

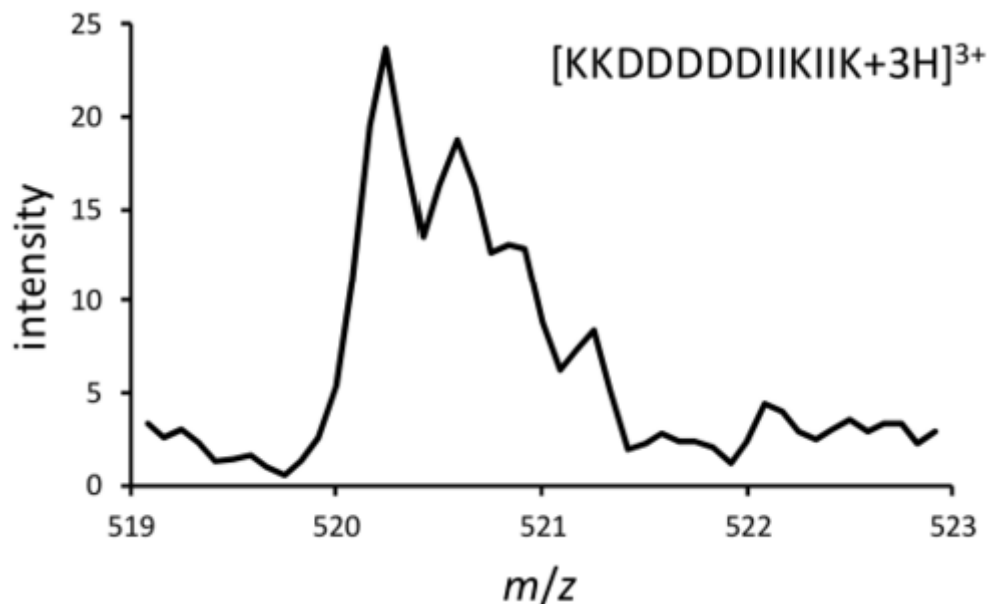


Figure 2.1. Mass spectrum showing the $[M+3H]^{3+}$ ions of the KKDDDDDDIIKIIK model peptide. Parameters for spectrum collection included a 1000 ms trap injection time. The ion current was averaged over 1 second.

2.3.1.2. Dynamic Range Studies

The dynamic range of the instrument can be estimated by comparisons of peak intensities from IMS-MS datasets. An example comparison of XIDTDs for two different ions is shown in Figure 2.2. Only peptides having a m/z that could be used for identification were used for dynamic range determination. Figure 2.2A shows the XIDTD for the cytochrome c tryptic peptide, $[KYIPGTK+1H]^+$ having m/z 806.5. The low-intensity feature at $t_D \sim 11.2$ ms is observed to fall within the singly-charged trend line shown in Figure 2.3A (see below). The integrated intensity for m/z 806.5 is ~ 37 . Figure 2.2B shows data for a phosphorylated peptide standard having a m/z 771.9. The XIDTD shows a dominant conformation at 7.4 ms followed by unresolved larger conformations. Here, the integrated area is 43764. These numbers demonstrate a dynamic range of $>1.0 \times 10^3$. Here we note that a higher dynamic range is observed when using lower-signal species (integrated intensities of ~ 5 counts – above the S/N threshold of 3). Such

ions cannot be identified as cytochrome c digest ions however, and therefore the dynamic range is presented as $>10^4$.

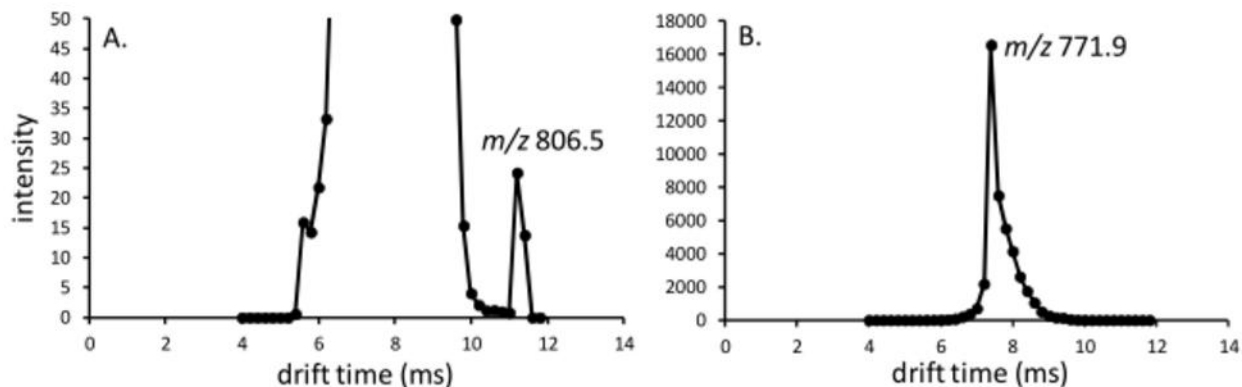


Figure 2.2. (A) XIDTD of the cytochrome c tryptic peptide ion, $[KYPIGTK+H]^+$, of m/z 806.5. That dataset feature corresponding to these ions is centered at $t_D = 11.2$ ms. (B) XIDTD of the $[SFVLNPTNIGMsKSSQGHVTK+3H]^{3+}$ ions of m/z 771.9. The entire t_D distribution corresponds to these ions

2.3.2. Phosphopeptide Analysis

Figure 2.3A shows a heat plot of the 2D $t_D(m/z)$ dataset of the cytochrome c digest containing the phosphorylated peptide standards. Tryptic peptide ions are observed to exist predominately as $[M+2H]^{2+}$ and $[M+3H]^{3+}$ ions exhibiting similar $t_D(m/z)$ trends as reported previously.[1] Most spectral features appear between ~ 5 ms to ~ 9 ms and are observed within the 400 to 1000 m/z range. The data in Figure 2.3A represents a number of ions exhibiting an intensity range of 10^3 .

The highly-tunable nature of the IMS-CID process[36, 37] can be combined with the efficient mobility separations[64, 65] to characterize phosphorylated peptides in tryptic digests. Because the bond dissociation energy of the phosphate modification is lower than that of backbone amide fragmentation, an IMS-CID approach that employs gentle activation ($\sim 450 \text{ V}\cdot\text{cm}^{-1}$) can be utilized. Here a goal is to increase the activation

voltage in IA2 (Figure 1.1) until neutral loss (H_3PO_4) is observed while preserving much of the other tryptic digest peptide ions. This allows for a more straightforward analysis of precursor and product ions similar to ion trap experiments described previously.[40, 41]

2.3.2.1. Aligning Extracted Ion Drift Time Distributions (XIDTDs)

For matching the precursor and neutral loss fragment ions, it is useful to evaluate the XIDTDs. Figure 2.3A shows the XIDTD of the $[\text{KRP}\text{sQRHGSKY-NH}_2 + 3\text{H}]^{3+}$ (m/z 475.2) ions as an inset. This peptide exhibits a broad mobility profile containing more compact ($t_D = 5.2$ ms) and more elongated ($t_D = 6.4$ ms) species. Figure 2.3B shows $t_D(m/z)$ data generated from IMS-CID of the digest mixture. The m/z difference between the precursor ion and the neutral loss product ion is 32.6, which is consistent with the loss of H_3PO_4 for the triply-charged ion. The XIDTD of the neutral loss product ion is shown as an inset in Figure 2.3B revealing a slightly broader distribution with conformational maxima matching the precursor XIDTD profile (5.2 ms and 6.4 ms). A difference in the distributions is the higher intensities observed for more elongated species in the IMS-CID dataset. That said, the t_D matching of the dominant features in the XIDTDs helps confirm the origin for much of the ions. The differences in the distributions may arise from the presence of overlapping lower-intensity fragment ions.

2.3.2.2. IMS – CID – ETD – MS of Precursor and Fragment ions

Both the intact precursor and neutral loss ions are present in the same $t_D(m/z)$ distribution (Figure 2.3) and either can be mobility-selected and m/z isolated for further characterization by ETD. Figure 2.4A and B show the ETD spectra for the intact precursor and neutral loss fragment ions, respectively. Here the z -ion series is most informative for observing the site of phosphorylation. That is, for the precursor ETD

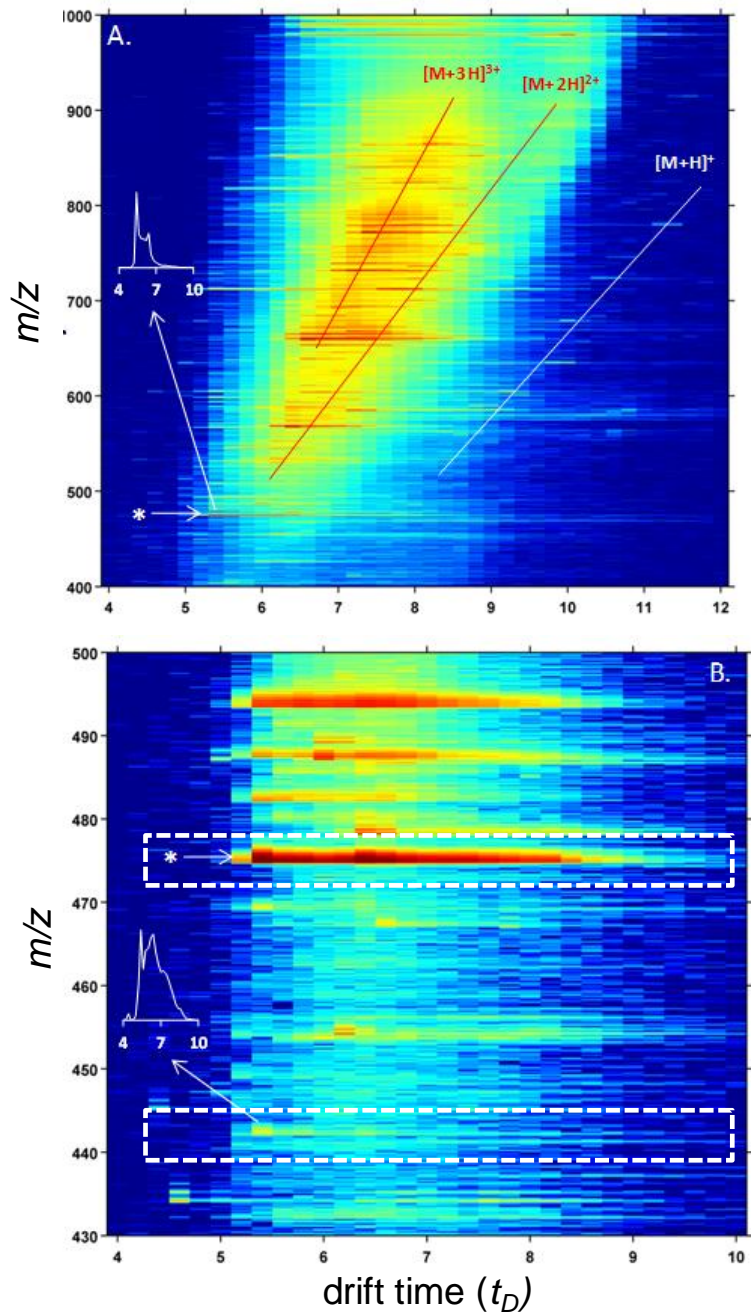


Figure 2.3 (A) Two-dimensional (2D) $t_D(m/z)$ heat-plot of a cytochrome *c* tryptic digest containing the phosphorylated peptide standard [KRP_sQRHGSKY-NH₂ (m/z 475.2)]. The color map for the plot is shown on a logarithmic scale ranging from -2 to 3 in order to show the low-intensity [M+H]⁺ ions. (B) Expanded region of a 2D $t_D(m/z)$ heat-plot for the same digest sample upon performing IMS-CID. The same color scale is used. The XIDTDS of the precursor and neutral loss product ions are shown as insets on the respective 2D plots. An asterisk denotes the location of the precursor ion both 2D plots.

fragments, the z_8 ion at m/z 1025.4 reveals residue-specific phosphorylation. Comparatively, in the neutral loss product ion spectrum, the same z_8 ion has a m/z value of 946.4. As expected, lower z -series ions for both the precursor and neutral loss ions demonstrate the same m/z values. For larger ions ($> z_8$ ion), those originating from the precursor species are higher in m/z due to the addition of the phosphate moiety. Also noticeable in the spectra are the ETD charge-reduced species that further confirm the neutral loss product ion. In the case of the $[M+3H]^{2+}$ ions, the precursor m/z is 712.4, while the product ion m/z is 663.4. The m/z difference (49) is consistent with the neutral loss of H_3PO_4 for the doubly-charged ion.

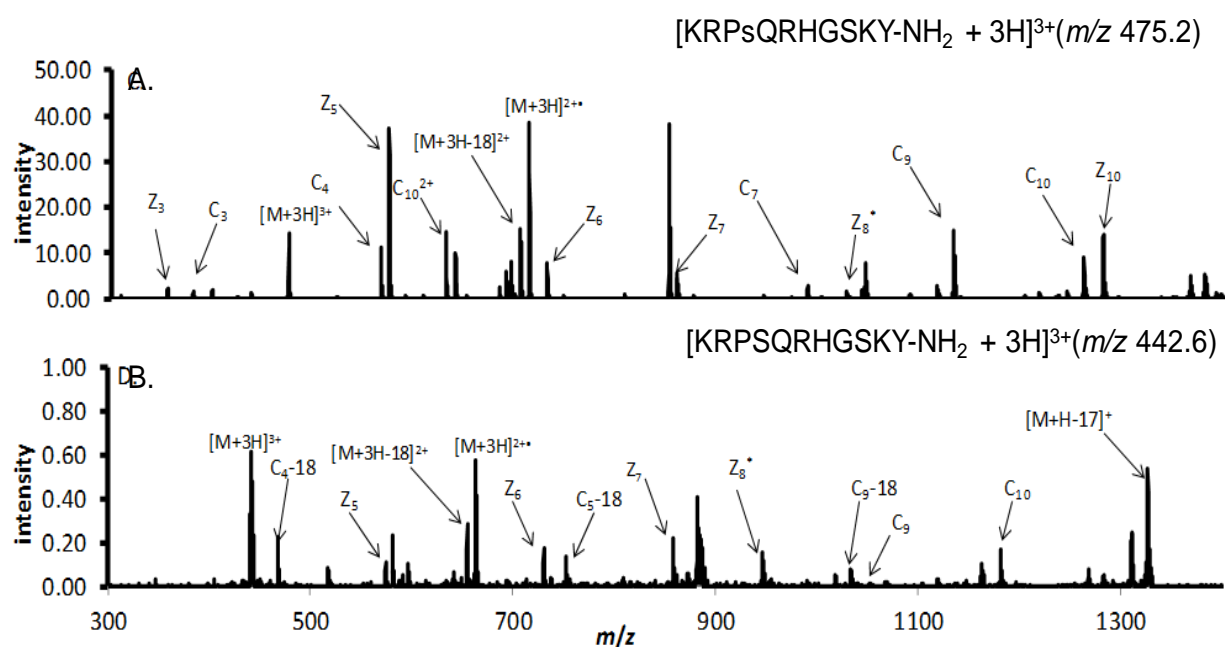


Figure 2.4 (A) and (B) Mobility-selected ETD spectra of the precursor and neutral loss ions, respectively. Identified fragment ions are labeled. Several identified c - and z -ions are labeled as well as the charged reduced molecular species. The z_8^* fragment ion denotes the neutral loss of H_3PO_4 by IMS-CID. This fragment ion corresponds with the S^4 residue for the model phosphopeptide.

The use of ion trapping instruments without ETD capabilities often requires at least MS³ to determine the site of phosphorylation.[66, 67] As a result, the technique requires relatively higher ion signal levels for informative higher-order MSⁿ results. The use of IMS-CID-ETD-MS for PTM peptide precursor scans is unique in that neutral loss ions can be uniquely matched back to the precursor based on XIDTDs; this can be followed by ETD-MS of the intact precursor for site specific PTM determination. Such a technique also represents an enhanced scanning approach compared to that employing CID and ETD in an ion trap[40, 41] as the mobility matching and selection would help to identify precursor ions and improve their isolation for PTM site determination.

It is also noted that the IMS-CID technique is data independent. That, is fragmentation of the precursor ions are signal dependent to trigger CID. Instead, IA2 is used to preferentially fragment the phosphodiester bond. In turn any produced fragment ions are matched based on XIDTDs for ETD-MS analysis. This further differentiates the technique from other MS/MS methods.

2.3.3. A Comparative IMS – MS Analysis of Metabolomic Samples

2D IMS-MS datasets have been recorded in triplicate for the four metabolite extract samples. Figure 2.5, shows the $t_D(m/z)$ heat plot of metabolites obtained from a single IMS-MS analysis of the EXP24 pooled sample. For all datasets, spectral features are first observed at ~3.4 ms and extend to ~15.0 ms; the highest intensity metabolite features exist between ~8.0 ms to ~9.0 ms. In general, dataset features are observed over a wide m/z range from ~80 to ~1200 with the ions exhibiting the greatest intensity being observed over a m/z range of ~500 to ~650. Using the pixel integration sizes

mentioned above, dataset pixel intensities for 19,000 separate $t_D(m/z)$ regions range from 0 to $>10^4$.

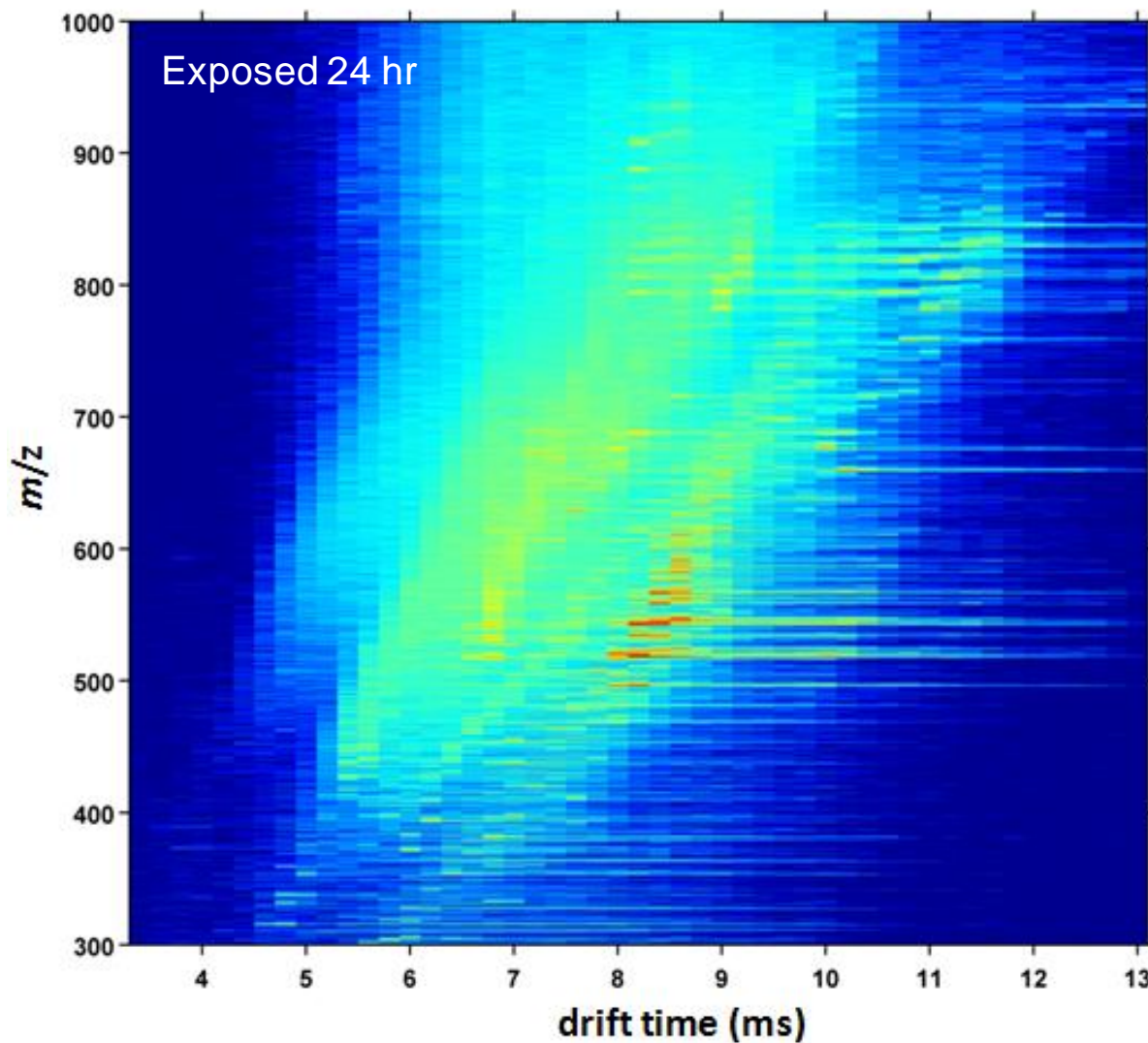


Figure 2.5 (A) 2D $t_D(m/z)$ heat-plot of one replicate analysis of the EXP24 metabolite sample. The color map for the plot is shown on a logarithmic scale ranging from -2 to 3 in order to show low-intensity features.

2.3.3.1. PCA of Sample Cohorts

The two-dimensional PCA plot obtained from triplicate measurements of the samples is shown in Figure 2B. Overall PC 1 contributes the greatest to the differentiation of all samples, with only a small degree of variation along PC 2. Data

points for triplicate measurements for both CNTRL0 and CNTRL24 are observed to cluster more toward the center of the PCA plot (Figure 2.6A). Comparatively, points for the EXP24 and EXP0 samples show a slightly higher degree of variation associated with PC 1. Therefore, the separation along PC 1, to a greater degree, is related to differences in dataset features associated with organism post exposure time. PC 1 then becomes a factor for focusing the analysis to a select number of spectral features (see below). It is worth noting that, compared to triplicate LC-MS experiments (data not shown), replicate dataset similarity is increased for the IMS-MS datasets.

Dataset features with the greatest contributions to distinguishing the pooled samples via PCA can be identified from the loadings matrix (LM) as shown in Figure 2.6B. Comparing data recorded for the EXP24 and EXP0 samples, LM values that exhibit high positive x-values correspond to a direct correlation for the EXP0 sample; that is, these $t_D(m/z)$ regions exhibit higher intensities, in general, for this sample. Conversely, the pixel intensities associated with the largest negative LM values correspond to an inverse correlation for the EXP0 samples. The absolute value of LM scores for dataset features exhibiting m/z values of 542.3 ($t_D = 7.4$ ms) and 518.3 ($t_D = 7.4$ ms) are 0.98 and 0.97 respectively, representing the greatest contributions to the PCA. These dataset features as well as those for several other metabolites having LM values ≥ 0.90 in magnitude are considered for further analysis and tentative metabolite identification. Although somewhat arbitrary, this threshold provides a stringent filter for focusing the analysis on a select few dataset features (35) from hundreds of potential candidates.

The dataset features along with tentative assignments obtained from accurate mass matching and precursor ion fragmentation are listed in Table 2.1.

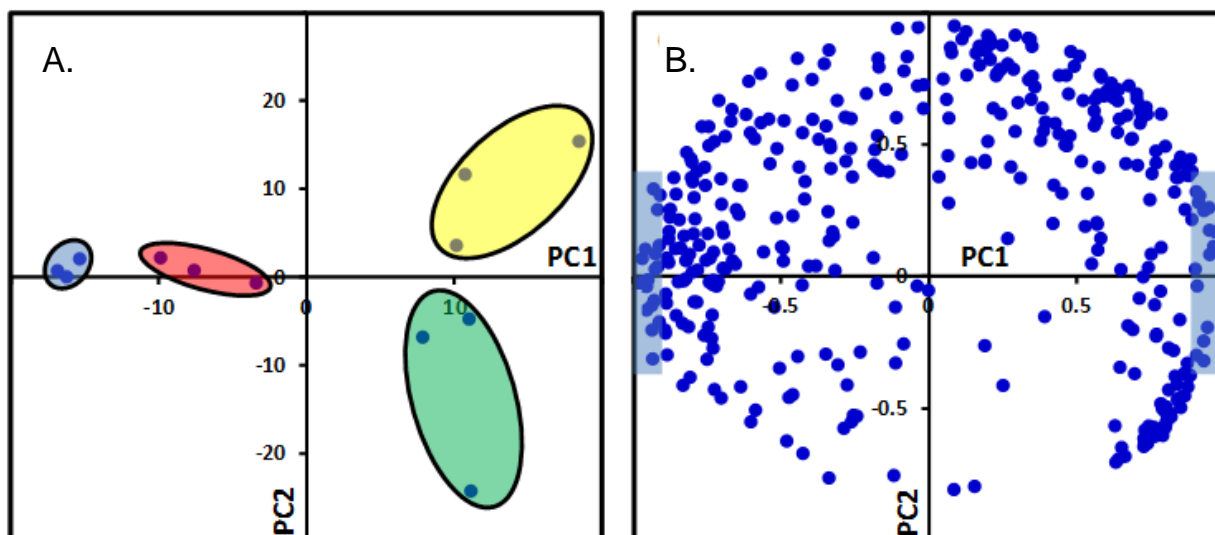


Figure 2.6(A) PCA of the triplicate measurements for all sample cohorts including, Blue: CNTRL24; Red: CNTRL0; Yellow: EXP24; Green: EXP24. The PCA plot was generating using normalized intensities for $t_D(m/z)$ pixels from the IMS-MS datasets. (B) Loadings matrix (LM) values showing the degree of contribution to PCA separation by specific pixels across all sample cohorts along PC 1 and 2. Shaded areas represent those having $|LM \text{ value}| \geq 0.90$.

2.3.3.2. Comparing Extraction Ion Drift Time Distributions (XIDTDs)

Rapid comparisons of percent differences in pixel intensity across multiple datasets can reveal features that are significantly different even when they are of much lower intensity. Figure 2.7A and B shows the XIDTDs of ions of m/z 518.3 for the EXP24 and CNTRL24 samples. Dataset replicates of the EXP24 sample show the

Table 2.1. Tentative plasma metabolite assignments including those contributing the most to the variation between sample cohorts

Searched database ^a	m/z ^b	Metabolite	Error (ppm) ^c	Adduct ^d	m/z Precursor ^e	MS ^f	Dominant productions ^g
HMDB	518.3217	LysPQC(16:0)	0.00579	[M+Na] ⁺	518.3	MS ²	459.3
					459.3	MS ³	313.2, 335.2, 415.2, 146.8, 257.2, 176.9, 460.2
					313.2	MS ⁴	257.2, 239.2, 221.1, 151.0, 137.0, 123.0, 109.0, 95.0
HMDB	542.3217	LysPQC(18:2(9Z, 12Z))	0.04979	[M+Na] ⁺	542.3	MS ²	483.2
					483.2	MS ³	146.8, 176.9, 337.2, 359.2, 439.2
HMDB	496.3397	LysPQC(16:0)	0.19140	[M+H] ⁺	496.4	MS	
HMDB	534.2957	LysPQC(16:0)	0.13663	[M+K] ⁺	534.3	MS	
HMDB	302.2329	Nonanoylcarnitine	1.04565	[M+H] ⁺	302.2	MS	
HMDB	588.3423	PC(18:1(9Z)/e(2:0))	0.50661	[M+K] ⁺	588.3	MS	
HMDB	676.4187	PS(14:1(9Z)/14:1(9Z)) ^h	0.42873	[M+H] ⁺	676.3	MS	
Metlin	566.3215	LysPQC(20:4)	0.35316	[M+Na] ⁺	566.3	MS	
Metlin	520.2440	Malnygamide C acetate	0.74965	[M+Na] ⁺	520.3	MS	
Metlin	732.5990	Unassigned	N/A	N/A	N/A	MS	

^aHMDB refers to the Human Metabolome Database (<http://www.hmdb.ca/>)

^bMetlin metabolite database generated from Scipos Metabolomics Center (<http://metlin.scipos.edu/index.php>)

^cError is reported from the Q.Exactive monoisotopic exact mass analysis and the theoretical m/z value from the searched database

^dDetermined adduct generated from the respective searched database

^ePrecursor m/z values obtained from the IMS-MS analysis

^fDominant product ions generated from MSⁿ experiments during IMS-MS analysis

^gSPS refers to phosphatylserine

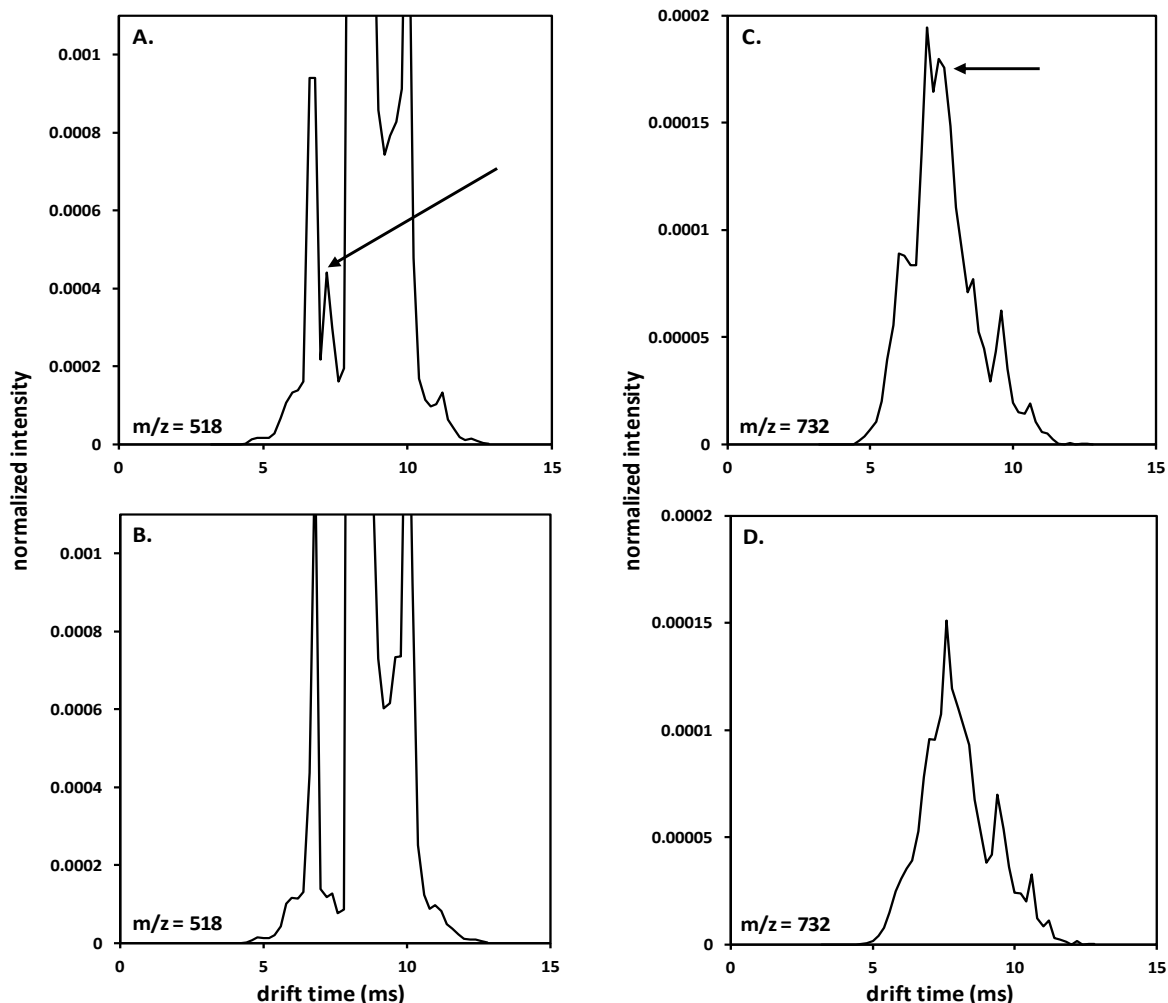


Figure 2.7 (A) Extracted ion drift time distribution (XIDTD) of the ion of m/z 518.3 for the CNTRL24 sample (single replicate). (B) XIDTD of the ion of m/z 518.3 for the EXP24 sample (single replicate). The XIDTD is obtained by integrating all intensities over m/z range of 6 (centered about the average m/z of the ion) across all drift times. (C) XIDTD for m/z 732.2 for EXP24 and (D) CNTRL 24, respectively. Each distribution is normalized such that the total area under the curve is unity. The arrow indicates a difference in spectral features between the two samples that have been recognized originally in the pixel-by-pixel intensity comparison of the

presence of a higher abundance feature at ~ 7.2 ms. The average normalized pixel intensities for this region in the EXP24 replicates is 0.64 ± 0.02 compared to 0.11 ± 0.01 for the CNTRL24 replicates. Similar spectral comparisons can be made for other ions. Figure 2.7C and D show that for m/z 732.2, several differences are observed. For example the peak intensities for ions with $t_D \sim 7.4$ ms and ~ 7.6 ms are greater for EXP

24 relative to the CNTRL 24 sample cohorts. Although the features in the XIDTD cannot be ascribed to different gas-phase conformers or isobaric ions, Figure 2.7 shows the ability to rapidly compare distinguishing dataset features that may otherwise not be considered to be significantly different between samples by MS analysis alone. Additionally, the comparison reveals the high-reproducibility of the measurement. Without having to employ peak (pixel) alignment techniques, the coefficients of variation for the low-intensity m/z 518.3 feature are ~3% (EXP24 replicates) and ~9% (CNTRL24 replicates).

2.3.3.3. IMS – MSⁿ Experiments for Metabolomic Analysis

The low-pressure drift tube allows trapping of electrosprayed ions increasing the overall sensitivity and enabling MSⁿ experiments for mobility-selected ions. To demonstrate this capability, metabolite ions exhibiting a t_D of ~8.2 ms and having m/z 518.3 have been selected for MSⁿ analysis. A precursor mass search of the Human Metabolome Database (HMDB)[68] presented the sodiated lysophosphatidylcholines LysoPC(16:0) as the top match. MS² of this ion yields essentially one fragment ion at m/z 459.2 as shown in Figure 2.8A. This ion could indicate the loss of a methylated ammonium head group (m/z 59) that is characteristic to many LysoPC.[69, 70] Fragments that displayed the highest S/N ratios have been used in subsequent fragmentation experiments. For example, activation of the m/z 459.2 ion produced from the mobility-selected m/z 518.3 precursor yields several peaks including those at m/z

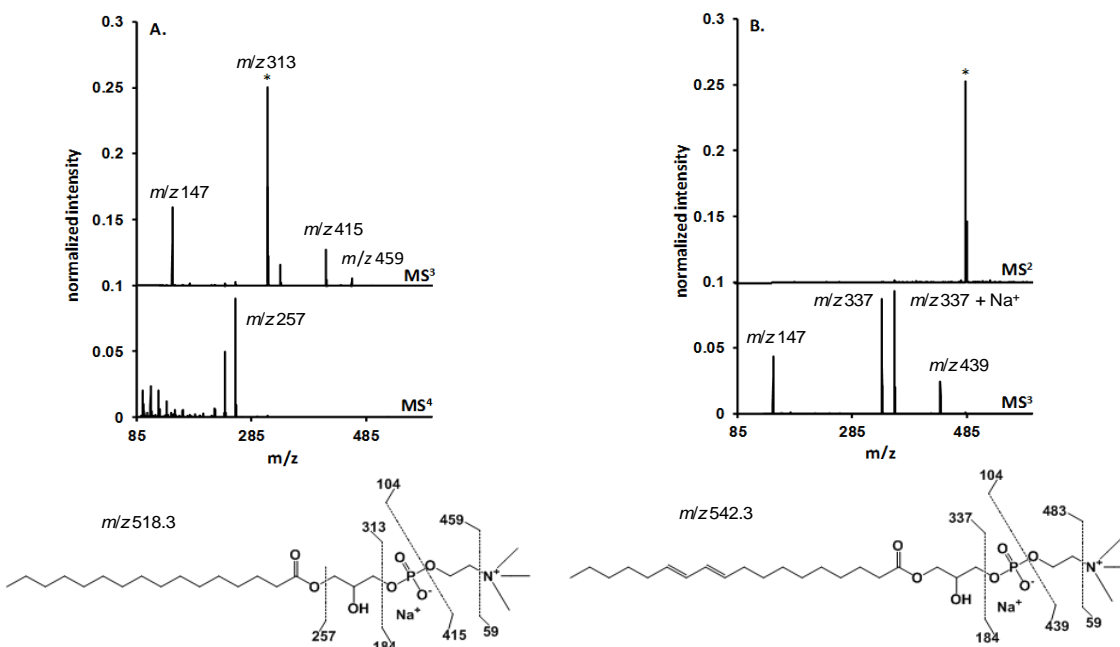


Figure 2.8 (A) Multistage tandem mass spectrometry (MS^n) of the drift selected (t_D 8.2 ms) precursor ion of m/z 518.3. The top spectrum shows the MS^3 spectrum obtained upon activation of the major product ion (m/z 459.2) generated during MS/MS (spectrum not shown). The bottom spectrum shows MS^4 fragments produced by selecting the ion of m/z 313.2 from MS^3 experiments. (B) MS^n of the drift selected (t_D 8.2 ms) precursor ion m/z 542.3. The top panel shows the MS/MS spectrum resulting in the dominate fragment ion m/z 483.2. The bottom spectrum shows the MS^3 upon collisionally activated of m/z 483.2. Several identified fragment ions are labeled in each respective panel and referenced back to the tentative structures (below respective spectrum). The peak marked with an asterisk indicates the m/z selected for subsequent MS analysis.

313.2, 335.2, and 415.2. Isolation of m/z 313.2 ions allows for MS^4 analysis that produces several features. Although not possible to assign all fragment ions, the peak at m/z 257.2 is consistent with the alkyl chain and ester region of a LysoPC molecule. When compared to the feature at m/z 257.2, the product ion with m/z 239.2 indicates a loss of water. Additionally, a number of low m/z fragments differing by 14 Da is consistent with fragmentation of the aliphatic chain of a LysoPC molecule. The inset in Figure 2.8A shows a schematic representation of the sodiated LysoPC(16:0) molecule and the observed fragments that are consistent with those obtained from the precursor ion of m/z 518.3.

Similar fragmentation is also observed for the mobility selected ion of m/z 542.3. Figure 2.8B shows the MS² spectrum from m/z 542.3 where a dominate ion of m/z 483.2 was observed. This fragment ion is indicative of the choline head region (m/z ~59). For the MS³ scan, the fragment ion of m/z 483.2 was selected and collisionally activated. Several fragments ions are observed and are consistent with a LysoPC. For example, m/z 125.3 is consistent with the loss of the phosphate region minus to the MS² loss of the choline. The fragment ion m/z 337.1 may indicate that the alkyl chain may contain two alkene regions. However, the exact locations of these regions were not capable of being identified do to signal restraints.

The tentative molecular assignment obtained from the MS⁴ and MS³ spectra from both ion experiments is further supported by accurate mass matches (± 0.5 ppm) obtained by direct electrospray of the sample into a Q-Exactive Orbitrap (ThermoScientific) mass spectrometer. Such assignments are presented as tentative as biomarker discovery efforts would require exact mass and ion fragmentation matches to molecular standards. That said, the IMS-MS instrumental approach is presented here as a means to rapidly provide candidate molecules for which confirmatory experiments can be conducted.

2.3.3.4. IMS – CID – MS Measurements

Not requiring user defined isolation and fragmentation of each individual ion, shotgun proteomics experiments have demonstrated that parallel dissociation[43] of ions in a drift tube offers significant advantages in terms of speed.[7, 71] Such a speed increase using the current IMS-MS instrument can be advantageous for rapid comparative metabolomics analyses as well. Figure 2.9A shows a 2D IMS-CID-MS

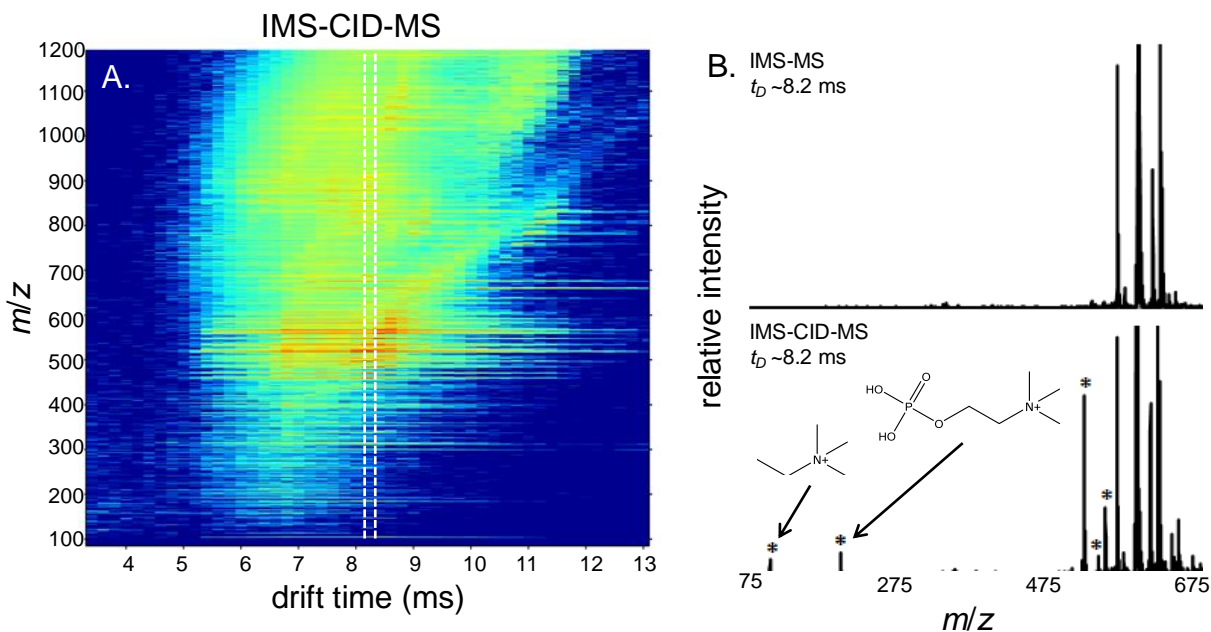


Figure 2.9 (A) Two-dimensional (2D) $t_D(m/z)$ heat-plot of the EXP24 sample obtained from an IMS-CID-MS experiment. The color map for the plot is shown on the same scale as described in Figure 1. (B) Comparison of the mass spectra produced after IMS-MS (top) and IMS-CID-MS (bottom). The white dashed line in panel A denotes the mass spectra extracted in the bottom panel B. the starred peaks indicate new spectral features not observed in IMS-MS experiments of thsame sample. Several new spectral features have been identified.

dataset for the EXP24 metabolite extract sample. Here, increased ion intensity is observed in high- and low- m/z regions indicating ion dissociation. A comparison of the mass spectra extracted at $t_D \sim 8.2$ ms is shown in Figure 2.9B and C. The top panel in Figure 2.9B shows that the extracted mass spectrum ($t_D \sim 8.2$ ms) is mostly void of detectable spectral features below $m/z \sim 350$. Because of the mobility separation, increase analytical space is afforded and is advantageous during IMS-CID experiments. For example, IMS-CID-MS of the EXP24 sample resulted in new spectral features observed in the lower mass spectrum (Figure 2.9C), which are free of spectral interferences at $t_D \sim 8.2$ ms. It therefore becomes instructive to identify the fragment ions and their origin.

A particular advantage of IMS is the ability to separate ions based on molecular class. McLean and coworkers showed that lipid classes share similar functionality and thus intrinsic gas phase conformations.[72] With this in mind, Figure 2.9C shows that several spectral features are consistent with LysoPC molecules at $t_D \sim 8.2$ ms. Here, m/z values consistent with dissociation of the choline head region and phosphodiester bond are observed in Figure 2.9. Notably, these ions also observed during MS^n experiments (see above) on mobility selected ($t_D \sim 8.2$ ms) and tentatively identified LysoPC molecules (Table 2.1). Taken collectively, these results suggest that the IMS-CID-MS approach can be utilized to aid in identifying molecular classes not only on intrinsic structural packing, but also through fragmentation characteristics using IMS-CID.

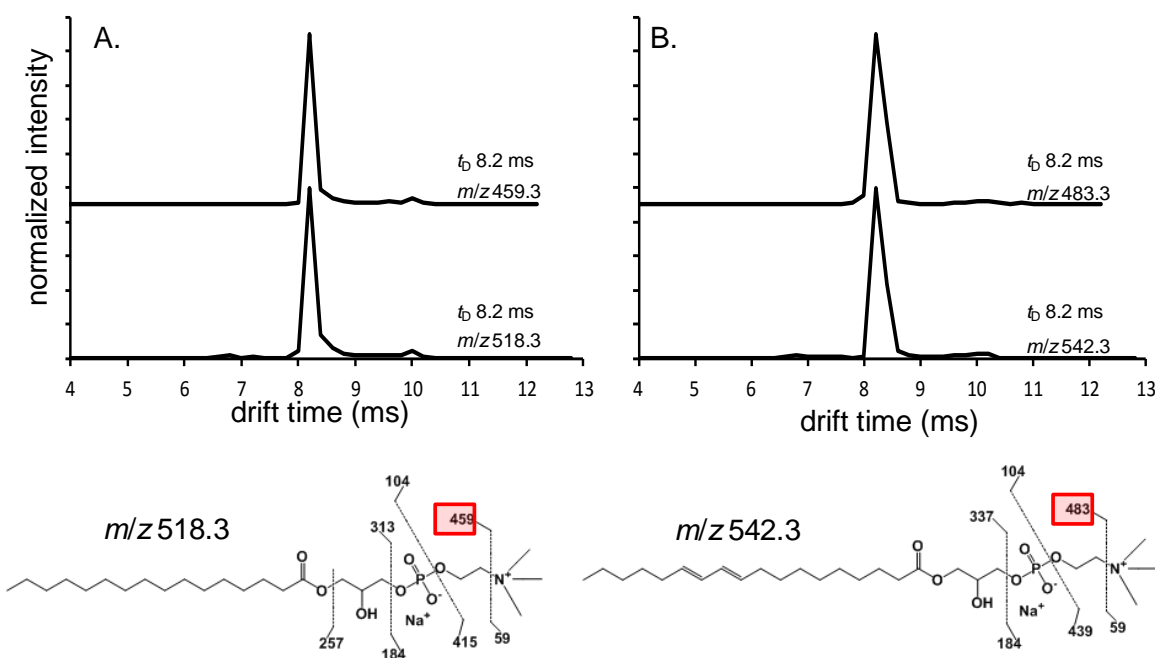


Figure 2.10 (A) XIDTD for the fragment ion m/z 459.3 (top) and precursor ion m/z 518.3 (bottom). (B) XIDTD for the fragment ion m/z 483.3 and precursor ion m/z 542.3 for top and bottom panels respectively. All XIDTDs were collected during from IMS-CID-MS of a single EXP24 replicate

For complex mixtures, the data in Figure 2.9A show the challenge in associating fragment and precursor ions by IMS-CID due to increased spectral complexity. While

some ions can be identified as unique to a particular lipid class, assigning the origin of fragment ions is more difficult. One method that may help alleviate this problem is comparison of XIDTDs. The utility of this approach for distinguishing precursor ions with overlapping mobilities has been shown previously in IMS-photodissociation (PD)-MS experiments.[42] Figure 2.10A shows an example comparison of the XIDTD for the precursor ion of m/z 518.3 (bottom panel) and the XIDTD for the fragment ion of m/z 459.3 (top panel). Overall the two distributions are very similar. Each exhibits a major peak maximum at a t_D value of ~ 8.2 ms. In each XIDTD a second peak a t_D of ~ 10.0 ms is also observed. Differences are observed in that the XIDTD of the precursor ion exhibits a small feature at a $t_D \sim 6.8$ ms. Another example of XIDTD matching is shown in Figure 2.10 B. Here, the XIDTD for the fragment ion m/z 483.3 is matched with the precursor XIDTD for m/z 542.2. Overall, the XIDTDs for m/z 483.3 and m/z 542.3 are also very similar. For example, the maximum peak intensity is observed at $t_D \sim 8.2$ ms, followed by a smaller spectral feature at $t_D \sim 10.0$ ms. Also noted is the slightly broader distribution observed for these XIDTDs (Figure 2.10B).

It is instructive to compare panels A and B in Figure 2.10 since both precursor ions display similar spectral features (t_D values ~ 8.2 ms and ~ 10.0 ms). Here, both fragment ions are show similar features; however, the overall XIDTDs for each fragment ion appears to correctly reflect the drift profile of the corresponding precursor ion. This is largely attributed to the dual gate design, where mobility information is passed from the precursor ion to the fragment ion before mass analysis. Using the IMS-CID-MS in a high throughput fashion, the method appears specific. That is, XIDTDs between precursor and fragment ion are capable of being match base on coincidence in drift time. It is also

noted that no spectral alignment was made between these datasets (Figure 2.10A and B). Another observation is that for each panel in Figure 2.10A and B, the same fragment ions were generated during MS/MS (Figure 2.8A and 2.8B) of the respective precursors ions. This adds a layer of confidence in the XIDTD assignments.

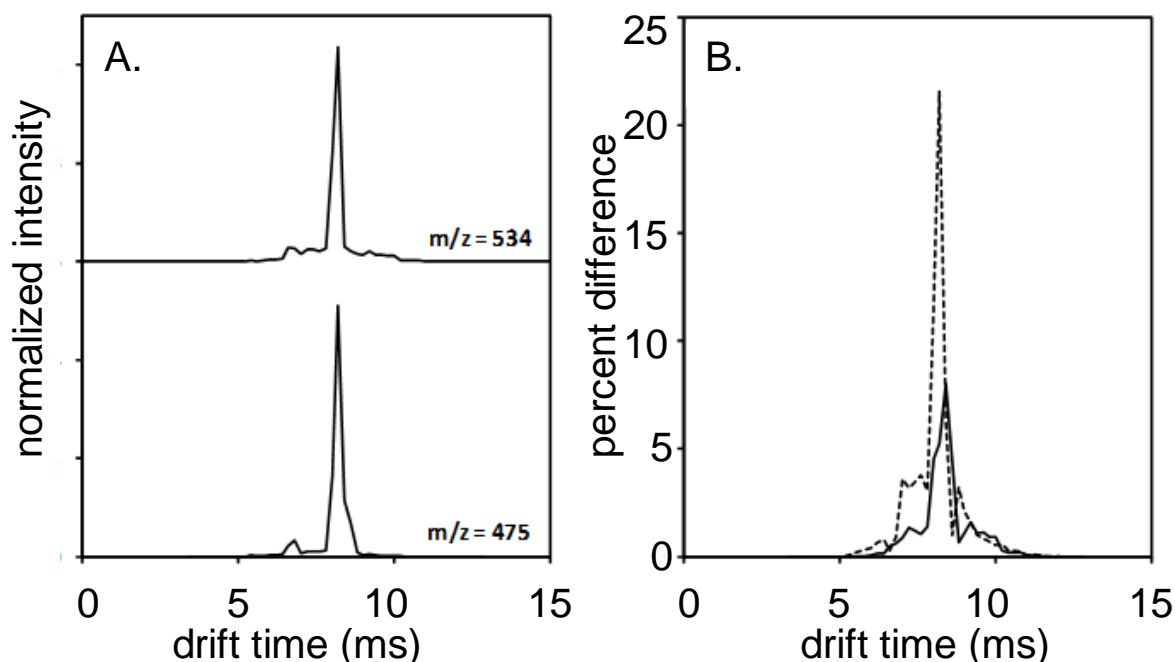


Figure 2.11 (A) XIDTD (top trace) and XIDTD (bottom trace) for the precursor and fragment ions of m/z 534.2 and 475.0, respectively. (B) Percent difference plots obtained upon comparison of the XIDTD for the fragment ion of m/z 475.0 and the XIDTDs of the precursor ions of m/z 534.2 (solid trace) and 496.3 (dashed-line trace). Each distribution is normalized such that the total area under the curve is unity.

A semi-quantitative assessment can be performed to rank the comparison of two XIDTDs. As a proof-of-principle study, Figure 2.11A shows the fragment ion of m/z 475.2 that has been matched to m/z 534.2 precursor ions in a similar manner as described above. Figure 2.11B shows the percent difference in XIDTDs for two different precursor ions (m/z 496.3 and 534.2) relative to the XIDTD of the fragment ion (m/z 475.2). The percent difference in Figure 2.11B for m/z 534.2 (solid trace) has a smaller integrated intensity (~3 times) relative to m/z 496.3 (dashed trace). Accurate mass matching in Table 2.1 show the precursor ion of m/z 534.2 is consistent with potassiumated

LysoPC(16:0). The IMS-CID-MS product ion of m/z 475.2 suggests the loss of the methylated ammonium in the choline head group for this tentative assignment.

2.2.4. Instrumental Implication for Comparative Analyses

Although the data provided here present a proof-of-principle demonstration of instrumentation capabilities, several improvements are envisioned to yield more effective comparative analyses. Increased IMS resolving power would better disperse the overlapping (t_D dimension) precursor ions (Figure 2.10) and allow for higher accuracy association of fragment ions to precursor ions in parallel dissociation experiments. Additionally, adaptations in drift tube design would allow for fragmentation of mobility-selected precursor ions followed by parallel dissociation and mobility resolution of fragment ions as demonstrated previously.[30, 38] An additional enhancement can be obtained by coupling off-line LC fractionation with the IMS-MS analysis. Because the IMS separation occurs after the ionization step, ion suppression contributes to the observation of the very high-signal LysoPC species observed in the middle range of the mass spectrum (Figure 2.5) along with the observation of much lower intensity species in other spectral regions.

2.4. References

1. Valentine, S.J., et al., *Gas-phase separations of protease digests*. Journal of the American Society for Mass Spectrometry, 1998. **9**(11): p. 1213-1216.
2. Gillig, K.J., et al., *Coupling high-pressure MALDI with ion mobility/orthogonal time-of flight mass spectrometry*. Analytical Chemistry, 2000. **72**(17): p. 3965-3971.
3. Ruotolo, B.T., et al., *Peak capacity of ion mobility mass spectrometry: Separation of peptides in helium buffer gas*. Journal of Chromatography B-Analytical Technologies in the Biomedical and Life Sciences, 2002. **782**(1-2): p. 385-392.
4. Wu, C., et al., *Separation of isomeric peptides using electrospray ionization/high-resolution ion mobility spectrometry*. Anal Chem, 2000. **72**(2): p. 391-5.
5. Clowers, B.H., et al., *Separation of sodiated isobaric disaccharides and trisaccharides using electrospray ionization-atmospheric pressure ion mobility-time of flight mass spectrometry*. Journal of the American Society for Mass Spectrometry, 2005. **16**(5): p. 660-669.
6. McLean, J.A., et al., *Ion mobility-mass spectrometry: a new paradigm for proteomics*. International Journal of Mass Spectrometry, 2005. **240**(3): p. 301-315.
7. Valentine, S.J., et al., *Toward Plasma Proteome Profiling with Ion Mobility-Mass Spectrometry*. Journal of Proteome Research, 2006. **5**(11): p. 2977-2984.
8. Becker, C., F.A. Fernandez-Lima, and D.H. Russell, *Ion Mobility-Mass Spectrometry: A Tool for Characterizing the Petroleome*. Spectroscopy, 2009. **24**(4): p. 38-42.
9. Dwivedi, P., et al., *Metabolic profiling by ion mobility mass spectrometry (IMMS)*. Metabolomics, 2008. **4**(1): p. 63-80.
10. Isailovic, D., et al., *Profiling of human serum glycans associated with liver cancer and cirrhosis by IMS-MS*. Journal of Proteome Research, 2008. **7**(3): p. 1109-1117.
11. McLean, J.A., *The Mass-Mobility Correlation Redux: The Conformational Landscape of Anhydrous Biomolecules*. Journal of the American Society for Mass Spectrometry, 2009. **20**(10): p. 1775-1781.
12. Kliman, M., J.C. May, and J.A. McLean, *Lipid analysis and lipidomics by structurally selective ion mobility-mass spectrometry*. Biochimica Et Biophysica Acta-Molecular and Cell Biology of Lipids, 2011. **1811**(11): p. 935-945.
13. Baker, E.S., et al., *Ion mobility spectrometry-mass spectrometry performance using electrodynamic ion funnels and elevated drift gas pressures*. J Am Soc Mass Spectrom, 2007. **18**(7): p. 1176-87.
14. Dwivedi, P., A.J. Schultz, and H.H. Hill, *Metabolic profiling of human blood by high-resolution ion mobility mass spectrometry (IM-MS)*. International Journal of Mass Spectrometry, 2010. **298**(1-3): p. 78-90.
15. Zinnel, N.F., P.J. Pai, and D.H. Russell, *Ion Mobility-Mass Spectrometry (IM-MS) for Top-Down Proteomics: Increased Dynamic Range Affords Increased Sequence Coverage*. Analytical Chemistry, 2012. **84**(7): p. 3390-3397.
16. Counterman, A.E., et al., *Formation of peptide aggregates during ESI: Size, charge, composition, and contributions to noise*. Journal of the American Society for Mass Spectrometry, 2001. **12**(9): p. 1020-1035.
17. Kurulugama, R.T.I., K; Taylor, L. *The Agilent Ion Mobility Q-TOF Mass Spectrometer System*. 2014 [cited 2014 May 23,]; Available from: <http://www.chem.agilent.com/Library/technicaloverviews/Public/5991-3244EN.pdf>.
18. Hernandez, D.R., et al., *Ion dynamics in a trapped ion mobility spectrometer*. Analyst, 2014. **139**(8): p. 1913-1921.

19. Waters. *SYNAPT G2-Si High Definition Mass Spectrometry*. 2014 [cited 2014 7/1]; Available from: http://www.waters.com/waters/en_US/SYNAPT-G2-Si-High-Definition-Mass-Spectrometry/nav.htm?cid=134740622&locale=en_US.
20. Steiner, W.E., et al., *Atmospheric pressure matrix-assisted laser desorption/ionization with analysis by ion mobility time-of-flight mass spectrometry*. *Rapid Communications in Mass Spectrometry*, 2004. **18**(8): p. 882-888.
21. Hoaglund, C.S., et al., *Three-dimensional ion mobility TOFMS analysis of electrosprayed biomolecules*. *Analytical Chemistry*, 1998. **70**(11): p. 2236-2242.
22. Scheubert, K., et al., *Computing fragmentation trees from metabolite multiple mass spectrometry data*. *J Comput Biol*, 2011. **18**(11): p. 1383-97.
23. Cao, M., K. Fraser, and S. Rasmussen, *Computational Analyses of Spectral Trees from Electrospray Multi-Stage Mass Spectrometry to Aid Metabolite Identification*. *Metabolites*, 2013. **3**(4): p. 1036-1050.
24. Prien, J.M., et al., *The high mannose glycans from bovine ribonuclease B isomer characterization by ion trap MS*. *J Am Soc Mass Spectrom*, 2009. **20**(4): p. 539-56.
25. Jiao, J., H. Zhang, and V.N. Reinhold, *High Performance IT-MS Sequencing of Glycans (Spatial Resolution of Ovalbumin Isomers)*. *Int J Mass Spectrom*, 2011. **303**(2-3): p. 109-117.
26. Bluhm, B.K., K.J. Gillig, and D.H. Russell, *Development of a Fourier-transform ion cyclotron resonance mass spectrometer-ion mobility spectrometer*. *Review of Scientific Instruments*, 2000. **71**(11): p. 4078-4086.
27. Clowers, B.H. and H.H. Hill, *Mass analysis of mobility-selected ion populations using dual gate, ion mobility, quadrupole ion trap mass spectrometry*. *Analytical Chemistry*, 2005. **77**(18): p. 5877-5885.
28. Tang, X., J.E. Bruce, and H.H. Hill, Jr., *Design and performance of an atmospheric pressure ion mobility Fourier transform ion cyclotron resonance mass spectrometer*. *Rapid Commun Mass Spectrom*, 2007. **21**(7): p. 1115-22.
29. Zucker, S.M., et al., *An Ion Mobility/Ion Trap/Photodissociation Instrument for Characterization of Ion Structure*. *Journal of the American Society for Mass Spectrometry*, 2011. **22**(9): p. 1477-1485.
30. Li, H.L., et al., *Carbohydrate Structure Characterization by Tandem Ion Mobility Mass Spectrometry (IMMS)(2)*. *Analytical Chemistry*, 2013. **85**(5): p. 2760-2769.
31. Knorr, F.J., et al., *FOURIER-TRANSFORM ION MOBILITY SPECTROMETRY*. *Analytical Chemistry*, 1985. **57**(2): p. 402-406.
32. Clowers, B.H., et al., *Hadamard transform ion mobility spectrometry*. *Anal Chem*, 2006. **78**(1): p. 44-51.
33. Szumilas, A.W., S.J. Ray, and G.M. Hieftje, *Hadamard transform ion mobility spectrometry*. *Anal Chem*, 2006. **78**(13): p. 4474-81.
34. Tang, K., et al., *High-sensitivity ion mobility spectrometry/mass spectrometry using electrodynamic ion funnel interfaces*. *Analytical Chemistry*, 2005. **77**(10): p. 3330-3339.
35. Koeniger, S.L., et al., *An IMS-IMS analogue of MS-MS*. *Analytical Chemistry*, 2006. **78**(12): p. 4161-4174.
36. Valentine, S.J., S.L. Koeniger, and D.E. Clemmer, *A split-field drift tube for separation and efficient fragmentation of biomolecular ions*. *Analytical Chemistry*, 2003. **75**(22): p. 6202-6208.
37. Koeniger, S.L., et al., *Development of field modulation in a split-field drift tube for high-throughput multidimensional separations*. *Journal of Proteome Research*, 2005. **4**(1): p. 25-35.
38. Merenbloom, S.I., et al., *IMS-IMS and IMS-IMS-IMS/MS for separating peptide and protein fragment ions*. *Analytical Chemistry*, 2006. **78**(8): p. 2802-2809.

39. Syka, J.E.P., et al., *Peptide and protein sequence analysis by electron transfer dissociation mass spectrometry*. Proceedings of the National Academy of Sciences of the United States of America, 2004. **101**(26): p. 9528-9533.
40. Beausoleil, S.A., et al., *Large-scale characterization of HeLa cell nuclear phosphoproteins*. Proc Natl Acad Sci U S A, 2004. **101**(33): p. 12130-5.
41. Schroeder, M.J., et al., *A neutral loss activation method for improved phosphopeptide sequence analysis by quadrupole ion trap mass spectrometry*. Anal Chem, 2004. **76**(13): p. 3590-8.
42. Lee, S., et al., *Extracted fragment ion mobility distributions: A new method for complex mixture analysis*. International Journal of Mass Spectrometry, 2012. **309**: p. 154-160.
43. Hoadlund-Hyzer, C.S., J.W. Li, and D.E. Clemmer, *Mobility labeling for parallel CID of ion mixtures*. Analytical Chemistry, 2000. **72**(13): p. 2737-2740.
44. Stone, E., et al., *Surface-induced dissociation on a MALDI-ion mobility-orthogonal time-of-flight mass spectrometer: Sequencing peptides from an "in-solution" protein digest*. Analytical Chemistry, 2001. **73**(10): p. 2233-2238.
45. Nurkiewicz, T., et al., *Nanoparticle inhalation augments particle-dependent systemic microvascular dysfunction*. Particle and Fibre Toxicology, 2008. **5**(1): p. 1.
46. Knuckles, T.L., et al., *Nanoparticle inhalation alters systemic arteriolar vasoreactivity through sympathetic and cyclooxygenase-mediated pathways*. Nanotoxicology, 2012. **6**(7): p. 724-735.
47. Fenn, J.B., et al., *ELECTROSPRAY IONIZATION FOR MASS-SPECTROMETRY OF LARGE BIOMOLECULES*. Science, 1989. **246**(4926): p. 64-71.
48. Revercomb, H.E. and E.A. Mason, *THEORY OF PLASMA CHROMATOGRAPHY GASEOUS ELECTROPHORESIS - REVIEW*. Analytical Chemistry, 1975. **47**(7): p. 970-983.
49. Shvartsburg, A.A. and M.F. Jarrold, *An exact hard-spheres scattering model for the mobilities of polyatomic ions*. Chemical Physics Letters, 1996. **261**(1-2): p. 86-91.
50. Mesleh, M.F., et al., *Structural Information from Ion Mobility Measurements: Effects of the Long-Range Potential*. The Journal of Physical Chemistry, 1996. **100**(40): p. 16082-16086.
51. Wyttenbach, T., et al., *Effect of the long-range potential on ion mobility measurements*. Journal of the American Society for Mass Spectrometry, 1997. **8**(3): p. 275-282.
52. Wittmer, D., et al., *ELECTROSPRAY-IONIZATION ION MOBILITY SPECTROMETRY*. Analytical Chemistry, 1994. **66**(14): p. 2348-2355.
53. Clemmer, D.E., R.R. Hudgins, and M.F. Jarrold, *NAKED PROTEIN CONFORMATIONS - CYTOCHROME-C IN THE GAS-PHASE*. Journal of the American Chemical Society, 1995. **117**(40): p. 10141-10142.
54. von Helden, G., T. Wyttenbach, and M.T. Bowers, *Conformation of macromolecules in the gas phase: use of matrix-assisted laser desorption methods in ion chromatography*. Science, 1995. **267**(5203): p. 1483-5.
55. Hoaglund-Hyzer, C.S. and D.E. Clemmer, *Ion trap/ion mobility/quadrupole/time-of-flight mass spectrometry for peptide mixture analysis*. Anal Chem, 2001. **73**(2): p. 177-84.
56. Merenbloom, S.I., et al., *High-resolution ion cyclotron mobility spectrometry*. Anal Chem, 2009. **81**(4): p. 1482-7.
57. Kurulugama, R.T., et al., *Overtone Mobility Spectrometry: Part 1. Experimental Observations*. Journal of the American Society for Mass Spectrometry, 2009. **20**(5): p. 729-737.
58. Blase, R.C., et al., *Increased ion transmission in IMS: A high resolution, periodic-focusing DC ion guide ion mobility spectrometer*. International Journal of Mass Spectrometry, 2011. **301**(1-3): p. 166-173.
59. Stlouis, R.H. and H.H. Hill, *ION MOBILITY SPECTROMETRY IN ANALYTICAL-CHEMISTRY*. Critical Reviews in Analytical Chemistry, 1990. **21**(5): p. 321-355.

60. Clemmer, D.E. and M.F. Jarrold, *Ion mobility measurements and their applications to clusters and biomolecules*. Journal of Mass Spectrometry, 1997. **32**(6): p. 577-592.
61. Collins, D.C. and M.L. Lee, *Developments in ion mobility spectrometry-mass spectrometry*. Analytical and Bioanalytical Chemistry, 2002. **372**(1): p. 66-73.
62. Bohrer, B.C., et al., *Biomolecule Analysis by Ion Mobility Spectrometry*, in *Annual Review of Analytical Chemistry*. 2008. p. 293-327.
63. Shaffer, S.A., et al., *A novel ion funnel for focusing ions at elevated pressure using electrospray ionization mass spectrometry*. Rapid Communications in Mass Spectrometry, 1997. **11**(16): p. 1813-1817.
64. Ruotolo, B.T., et al., *Distinguishing between phosphorylated and nonphosphorylated peptides with ion mobility-mass spectrometry*. J Proteome Res, 2002. **1**(4): p. 303-6.
65. Ruotolo, B.T., et al., *Analysis of phosphorylated peptides by ion mobility-mass spectrometry*. Anal Chem, 2004. **76**(22): p. 6727-33.
66. Palumbo, A.M., J.J. Tepe, and G.E. Reid, *Mechanistic insights into the multistage gas-phase fragmentation behavior of phosphoserine- and phosphothreonine-containing peptides*. J Proteome Res, 2008. **7**(2): p. 771-9.
67. Palumbo, A.M., et al., *Tandem mass spectrometry strategies for phosphoproteome analysis*. Mass Spectrom Rev, 2011. **30**(4): p. 600-25.
68. Wishart, D.S., et al., *HMDB 3.0-The Human Metabolome Database in 2013*. Nucleic Acids Research, 2013. **41**(D1): p. D801-D807.
69. Fang, N., S. Yu, and T.M. Badger, *LC-MS/MS Analysis of Lysophospholipids Associated with Soy Protein Isolate*. Journal of Agricultural and Food Chemistry, 2003. **51**(23): p. 6676-6682.
70. Barroso, B. and R. Bischoff, *LC-MS analysis of phospholipids and lysophospholipids in human bronchoalveolar lavage fluid*. Journal of Chromatography B, 2005. **814**(1): p. 21-28.
71. Liu, X.Y., et al., *Mapping the human plasma proteome by SCX-LC-IMS-MS*. Journal of the American Society for Mass Spectrometry, 2007. **18**(7): p. 1249-1264.
72. May, J.C., et al., *Conformational Ordering of Biomolecules in the Gas Phase: Nitrogen Collision Cross Sections Measured on a Prototype High Resolution Drift Tube Ion Mobility-Mass Spectrometer*. Analytical Chemistry, 2014. **86**(4): p. 2107-2116.

3. Negative Ion IMS-HDX-MS¹

¹Reprinted with permission from the *Journal of the American Society for Mass Spectrometry: Ion Mobility Spectrometry-Hydrogen Deuterium Exchange Mass Spectrometry of Anions: Part 1 Peptides to Proteins*. Gregory C. Donohoe, Mahdiar Khakinejad, Stephen J. Valentine, *J. Am. Soc. Mass Spectrom.*, 2015, 26 (4), 564-576.

3.1. Introduction: A Base for Studying Anionic Proteins

The development of soft ionization methods such as electrospray ionization (ESI)[1] and matrix-assisted laser desorption (MALDI)[2, 3] presented the unique opportunity to study the gas-phase conformations of large biomolecular ions. Within a short time a variety of mass spectrometry (MS)-based techniques were developed for the structural characterization of these ions as well as to relate gas-phase conformers to antecedent solution structures.[4-20] One early technique determined the gas-phase hydrogen-deuterium exchange (HDX) reactivities of ions comprising different charge states of proteins.[6, 21-24] The observation of different HDX rates and maximum HDX levels indicated the presence of coexisting gas-phase conformations. Early theoretical studies resulted in proposed mechanisms for HDX of protonated peptide ions by a number of deuterating agents.[8, 22]

Concurrent to the development of HDX techniques, experimental efforts were directed at utilizing ion mobility spectrometry (IMS) coupled with MS for the determination of collision cross sections for peptide and protein ions.[9, 19, 20, 25] Shortly later, IMS-MS was combined with HDX in order to determine the reactivities of specific gas-phase conformers of protein ions. These early IMS-HDX-MS experiments provided information about the degree of protection afforded by the protein fold

associated with elongated and compact conformations for positively charged biomolecules.

Relative to positive ions, anionic peptides and proteins have received considerably less attention.[26] As a consequence, very few studies have been performed on negation ions. Because many proteins contain a large number of acidic residues, it is useful to develop a sound understanding of the conformational information afforded by gas-phase HDX measurements for select conformers from negatively-charged protein ions. Similarly the combined IMS-HDX-MS studies described here present the first conformer specific analysis of peptide and protein anions. That said, the methods utilized in these studies are similar to those employed previously for the characterization of conformers of positively-charged protein ions.[27, 28]

3.2. Method and Materials

3.2.1. Sample Preparation

Samples were selected to allow comparisons of a variety of gas-phase ion conformers including those formed from a conformationally-restricted protein (disulfide bonds) and globular proteins of increasing size. The proteins bovine insulin (90%), ubiquitin (95%), and equine cytochrome c (95%) were purchased (Sigma Aldrich, St. Louis, MO, USA) and used without further purification. Ultra-pure (chromatography grade) deionized water, acetonitrile, and ammonium hydroxide (Fisher Scientific, Fair Lawn, NJ, USA) were used to generate stock and ESI solutions of the peptide and proteins. The stock solutions were prepared by dissolving 1.0 mg of analyte in 1.0 mL of ultra-pure water and were capped in glass vials while being maintained in a refrigerator (4 °C); no stock solution was used a week after preparation. ESI solutions (0.1 mg·mL⁻¹

¹) were prepared fresh by diluting 0.1 mL of stock solution with the addition of 0.4 mL of ammonium hydroxide and 0.5 mL of acetonitrile. Samples were infused through a pulled-tip capillary using a flow rate of 300 nL·min⁻¹.

3.2.2. IMS-MS: Instrumental Operation

The use of ion mobility spectrometry for the characterization of biomolecules has an extensive history; the development of IMS instrumentation,[19, 25, 29-45] theory[46-57] and applications[58-62] have been discussed in detail. The IMS-MS instrument used in these studies has also been described previously.[63] A brief description of the instrument and data collection and analysis is presented here. Figure 1.1 shows a schematic diagram of the drift tube, linear ion trap instrument used to conduct these experiments. Peptide/Protein ions are generated by electrospraying the ESI solution through a pulled-tip capillary. The capillary is biased at ~-2200 V above the entrance aperture of the desolvation region (Figure 1.1). Here ions are desolvated and focused into an “hour-glass” ion funnel [64] (F1/IA1/G1 in Figure 1.1). Ions are trapped near the exit region of the ion funnel and periodically (typically 50 Hz) pulsed into the drift tube. The drift tube is filled with He buffer gas (300 K) and supports a drift field of ~10 V·cm⁻¹. Ions separate in the drift tube based on differences in their mobilities through the buffer gas. The second ion gate (G2 in Figure 1.1) is employed to select ions of specific mobilities for transmission into the LTQ Velos linear ion trap (ThermoScientific, San Jose, CA, USA) for mass analysis.

3.2.2.1. Recording Two – Dimensional (2D) $t_D(m/z)$ Distributions

Delay times between the high-voltage pulse applied to the drift tube entrance gate (G1) and the mobility selection gate (G2) are scanned in order to generate IMS-MS

datasets. In the current instrument G1 is a single gridded lens and G2 is a Tyndall gate located directly in front of the second ion funnel. G1 prevents ions from entering the drift tube using an ~ 40 V bias relative to first ion funnel exit. Periodically, a 150 μ s-long voltage pulse is applied to G1 to allow ions to enter the drift tube. The Tyndall gate, with a bias of ~ 10 V, neutralizes all ions with the exception of those selected for transmission by the time delay of the voltage pulse applied to G2 relative to G1. The timing of G1 and G2 is synchronized by two four channel digital/delay pulse generators (Stanford Research Systems, Sunnyvale, CA, USA). Drift time (t_D) delays are scanned from ~ 3 ms to ~ 15 ms (200 μ s increments) to encompass the entire t_D range of all ions produced by ESI.

3.2.3. Mass Spectrometry Measurements

Total ion mass spectra are generated by setting the drift tube gates to pass all ions. In this operational mode, all ions pass into the mass analyzer. The mass analyzer scan parameters include a m/z range of 80 to 2000 as well as automatic gain control (AGC) with a threshold of 1×10^6 ions. For these analyses, sample injection times of 200 ms (5 microscans) have been utilized. During t_D distribution generation, the ion gates in the drift tube are activated as mentioned above to transmit ions of a specific mobility into the linear trap. Data acquisition is accomplished by collecting a mass spectrum (0.5 min) for each t_D selection setting. For IMS data generation, the AGC is disabled and a sample injection time of 200 ms (5 microscans) is also employed.

3.2.4. Generating IMS-MS Datasets

To generate the two-dimensional IMS-MS dataset, each t_D selected mass spectrum (.RAW file) is converted to a separate text file. All x and y data points (m/z

values and intensities) are then associated with the respective mobility selection time (t_D) using software developed in house. This process creates a three-column array text file containing t_D , m/z , and intensity values. Intensity filters can be applied to control the size of the three-column array file. To generate t_D distributions for ions of specific m/z values, a separate program developed in house integrates all intensities within a user-defined m/z range for each t_D . In accordance with previous studies, this is called an extracted ion drift time distribution (XIDTD).[65]

3.2.5. Gas Phase HDX Experiment Design

Gas-phase HDX is accomplished by introducing D_2O (>99%, Sigma Aldrich, St. Louis, MO, USA) into the drift tube buffer gas system. First, the D_2O was purified by several freezing and melting cycles under vacuum. The pressures of D_2O and helium are adjusted with two separate leak valves, (Granville Philips, Longmont, CO, USA) and monitored using a Baratron capacitance manometer (MKS, Andover, MA, USA). For these experiments, the helium pressure is set at 2.50 ± 0.01 Torr. The partial pressure of D_2O is varied from ~ 0.05 Torr to ~ 0.20 Torr. t_D distributions are first recorded in pure He to allow the determination of accurate collision cross sections. To ensure no conformational transitions occur, the t_D distributions are monitored upon adding D_2O as demonstrated previously [23]. Additionally, the D_2O uptake for the different ions is recorded at different D_2O pressures. The partial pressures of the components of the buffer gas system are stable differing by less than ± 0.01 Torr during the course of the mass spectral characterization as well and upon removal of the D_2O , the total pressure quickly re-equilibrates to 2.50 Torr.

3.2.5.1. HDX Levels and Rate Constants

The number of deuteriums incorporated into specific ion conformers is determined by subtracting their average m/z value after passing through the pure He buffer gas from their average m/z value after passing through a He/D₂O mixture. Average values are determined using a simple algorithm developed in house that weights each m/z point in the isotopic distribution by its intensity.

HDX rate constants have been determined for a number of different ion conformers assuming pseudo first order kinetics as described previously.[6, 21, 27, 28] Briefly, the partial pressure of D₂O is adjusted in small increments (as little as 0.01 Torr) from 0 to 0.20 Torr and the t_D s and HDX levels of different ion conformers are determined. A semi-log plot of the number of remaining exchangeable hydrogens as a function of the product of the D₂O pressure and t_D provides a means for determining the rate constant; the slopes of best linear fits to the data on the semi-log plot are used for this determination.

3.3. Results and Discussion

3.3.1. Protein Anion Collision Cross Sections

Figure 3.1 shows the two-dimensional $t_D, m/z$ distribution obtained for negatively-charged ubiquitin ions. Ions produced from the ubiquitin sample range from the [M-5H]⁵⁻ to the [M-9H]⁹⁻ species. The drift times for these same ions range from ~7.5 to 13 ms. The data indicate a transition from a more elongated structural conformation type to a more compact structural type for the [M-7H]⁷⁻ and [M-6]⁶⁻ ions, respectively. This is evidenced by the higher mobility of the dominate conformer type for the latter ions

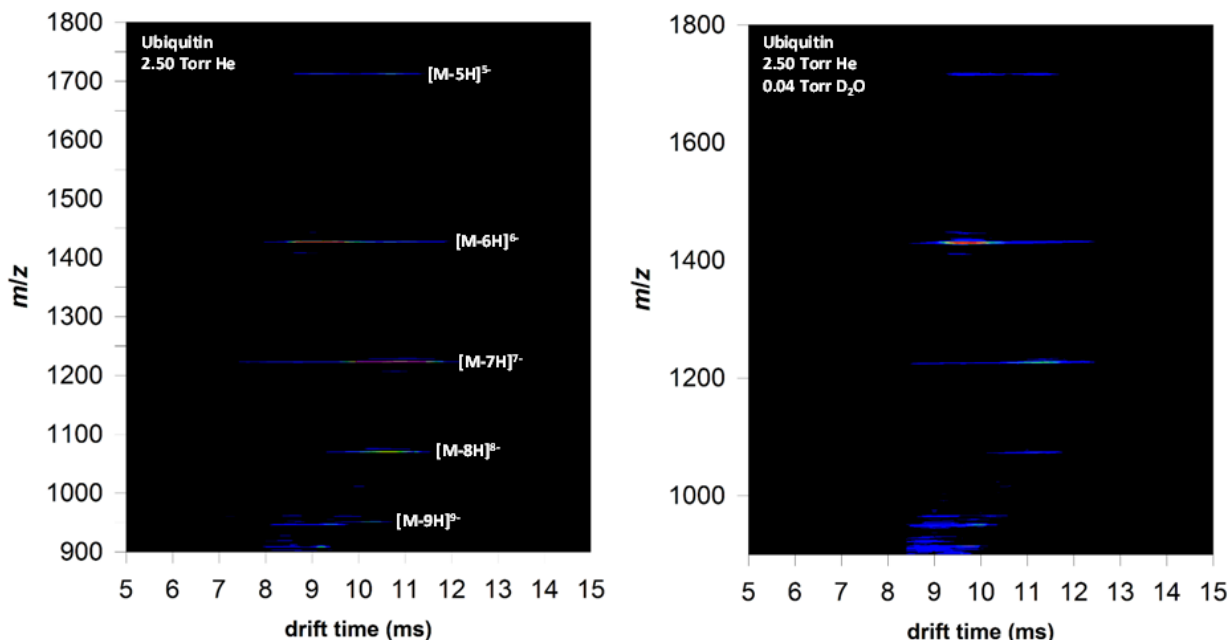


Figure 3.1 Two-dimensional, $t_D(m/z)$ dot plot of electro sprayed ubiquitin ions. The intensity is represented with a color scale using logarithmic cutoff thresholds. The maximum intensity cutoff is 10^2 . The ions of different charge are labeled on the two-dimensional plot.

(shorter t_D in Figure 3.1). Ion elongation resulting from increased coulomb repulsion has been described for a number of protonated and deprotonated protein ions.[59, 66-68] Figure 3.1 also shows the $t_D, m/z$ distribution obtained for negatively-charged ubiquitin ions upon addition of ~ 0.04 Torr of D_2O into the drift tube buffer gas. In general the m/z peaks become broader due to the incorporation of deuteriums at heteroatom exchange sites. On average, the t_D values of ion conformers increase by ~ 0.5 ms. At this D_2O pressure it is expected that the more highly accessible exchange sites have incorporated deuteriums (see HDX kinetics discussion below). Although the addition of D_2O does not appear to alter the conformations of the observed ions as evidenced by the similar t_D distributions, at higher D_2O pressures, the overall ion signal level decreases and maximum HDX levels and rate constants cannot be determined for some ion conformers of lower abundance (see below).

Figure 3.2A shows that collision cross section distributions indicate that several $[M-nH]^{n-}$ ions yield two conformations (i.e., two dominant features are observed in the t_D distribution). These collision cross sections are also summarized in Table 3.1. The collision cross sections of ions produced from bovine insulin are listed in Table 3.1 and shown in Figure 3.2B. For illustrative purposes the collision cross sections of ions from bovine insulin are depicted separately from those formed by the larger proteins (ubiquitin and cytochrome *c*). Insulin is observed to produce a single dimer, $[2M-7H]^{7-}$, having a cross section of 1260 \AA^2 . It is likely that the largest contributing factor to the relatively decreased size of the insulin ions is the presence of the four disulfide bonds which serve to tether the molecule in more compact conformations even at higher charge states. This phenomenon has been described previously.[68]

The collision cross sections for the ions formed from the larger proteins are shown in Figure 3.2A. For these ions, cross sections range in size from 862 \AA^2 to 2615 \AA^2 corresponding to $[M-5H]^{5-}$ ubiquitin and $[M-13H]^{13-}$ cytochrome *c* ions, respectively. Ubiquitin ions show both compact and more elongated conformations across the observed charge state distribution. A transition from the dominant species being comprised of more compact ions to more elongated ions is observed from the $[M-6H]^{6-}$ to the $[M-7H]^{7-}$ species as evidenced in Figure 3.1 (see discussion above). The dataset features observed for cytochrome *c* show only single conformer types across the charge state range (from the $[M-7H]^{7-}$ to the $[M-12H]^{12-}$ ions). The overlapping charge states for cytochrome *c* and ubiquitin reflect the difference in size of the two proteins. That is,

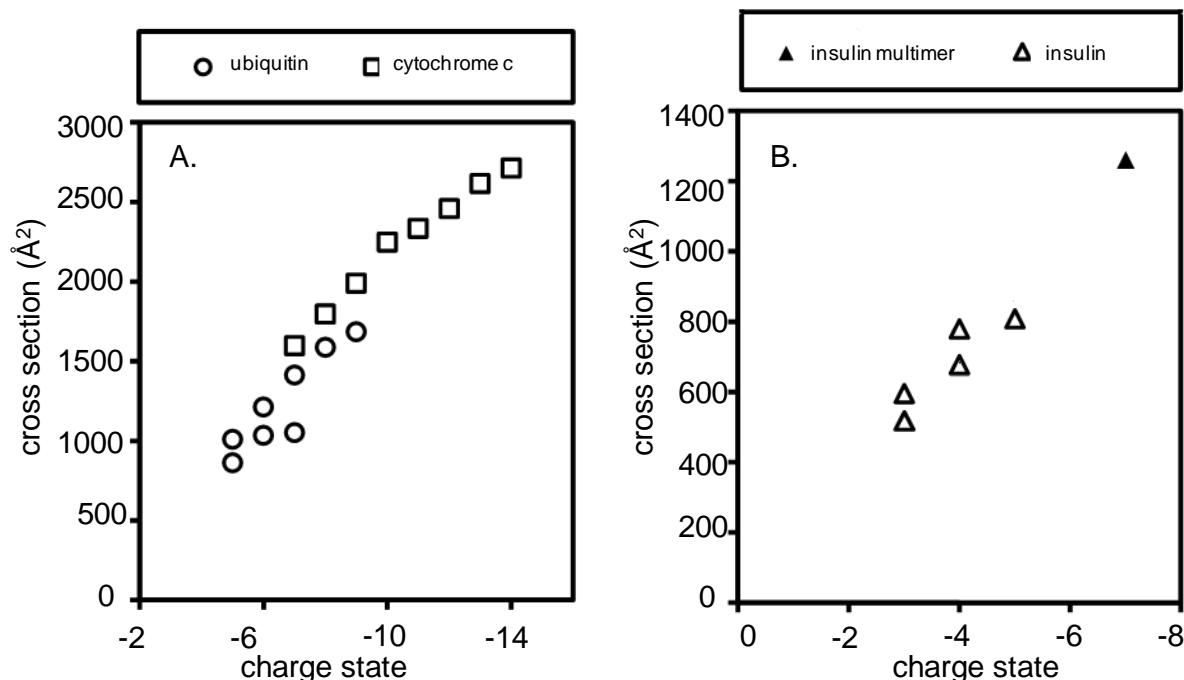


Figure 3.2. Collision cross sections for protein (panel A) and insulin (panel B) conformers. Triangle, circle and square symbols represent negatively-charged ions of the model peptide, bovine insulin, ubiquitin, and equine cytochrome c, respectively. Solid and open symbols represent monomeric and multimeric species, respectively. The number of individual monomers within multimeric species precedes the symbol.

cytochrome c contains ~37% more amino acid residues than ubiquitin. Additionally, no more compact ions are observed for these charge states of cytochrome c. The collision cross sections of the elongated cytochrome c protein ions have been compared to values reported in an online database obtained from separate IMS measurements and the average percent difference is determined to be $1.7 \pm 0.3 \text{ \AA}^2$.

3.3.2. Gas – Phase Deuterium Uptake as a Function of D_2O Pressure

The addition of D_2O to the drift tube, results in shifts of the m/z values of the various ions to higher values indicating the incorporation of deuterium. Figure 3.3A shows the increase in m/z of the more compact conformer of $[M-5H]^{5-}$ ubiquitin ions as a

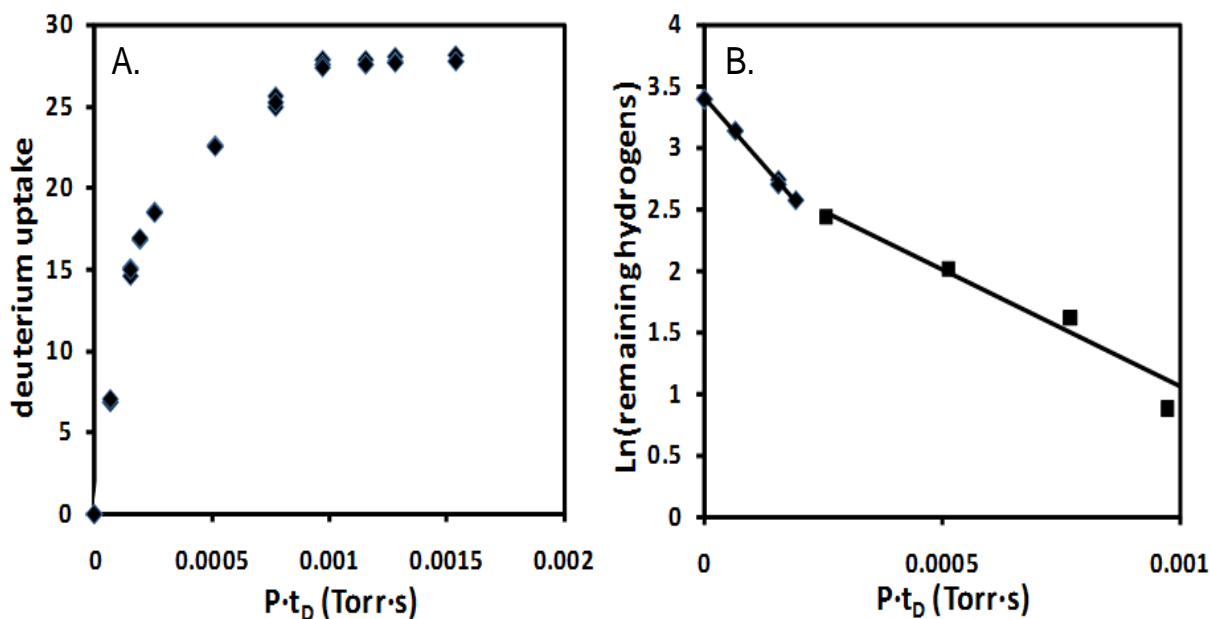


Figure 3.3. (A) Plot of deuterium uptake as a function of the partial pressure of D_2O multiplied by t_D . This data was recorded for $[M-5H]^{5-}$ ubiquitin ions. (B) Plot of the natural log of the number of remaining exchangeable hydrogens as a function of the product of D_2O partial pressure and t_D . Linear fits of fast- and slow-exchanging hydrogens are shown.

function of the product of ion t_D and pressure of D_2O . Initially, small increases in D_2O pressure are associated with large increases in HDX levels while at higher D_2O pressures the HDX level reaches a near maximum value corresponding to uptake of ~28 deuteriums. Using this deuterium uptake data it is possible to generate a semilog plot of the remaining hydrogens as a function of the product of pressure and ion residence time in the drift tube as shown in Figure 3.3B. A linear relation for the first 3 to 4 datapoints is observed; however, beyond this point, the data deviate from linearity. The observation of a linear region for the uptake of the first deuteriums has been observed in studies of positively-charged protein ions and has been ascribed to fast-exchanging sites near the charge sites.[27, 28] Using a linear fit to the first data points

Table 3.1. Collision Cross Section, HDX levels and rate constants for all major dataset features

Sample	Ion	Cross Section ^a	HDX Level ^b	Rate Constants ^c		Correlation Coefficient ^d	
				Fast	Slow	Fast	Slow
Insulin	[M-3H] ⁺	528±2	14.8±0.3	8.3×10^{-14}	1.87×10^{-14}	0.956	0.993
	[M-3H] ²⁺	595±2	NA	NA	NA	NA	NA
	[M-4H] ⁺	676±3	NA	NA	NA	NA	NA
	[M-4H] ²⁺	779±3	14.2±0.4	1.0×10^{-13}	1.8×10^{-14}	0.952	0.973
	[M-5H] ⁺	808±4	14.1±0.5	1.3×10^{-13}	3.2×10^{-14}	0.971	0.988
	[2M-7H] ⁺	1260±5	26.8±0.7	NA	NA	NA	NA
Ubiquitin	[M-5H] ²⁺	862±4	NA	NA	NA	NA	NA
	[M-5H] ³⁺	1010±4	27.8±0.5	1.3×10^{-13}	6.5×10^{-14}	0.998	0.964
	[M-6H] ²⁺	1035±4	28.32±0.6	1.4×10^{-13}	5.4×10^{-14}	0.994	0.991
	[M-6H] ³⁺	1212±4	NA	NA	NA	NA	NA
	[M-7H] ²⁺	1052±5	NA	NA	NA	NA	NA
	[M-7H] ³⁺	1414±5	39.4±0.7	1.3×10^{-13}	5.9×10^{-14}	0.993	0.985
Cytochrome c	[M-9H] ²⁺	1587±6	47.7±0.8	1.1×10^{-13}	3.9×10^{-14}	0.992	0.992
	[M-9H] ³⁺	1686±7	46.4±0.9	1.2×10^{-13}	3.6×10^{-14}	0.994	0.955
	[M-7H] ²⁺	1598±5	56.8±0.7	2.1×10^{-13}	4.2×10^{-14}	0.981	0.947
	[M-9H] ³⁺	1797±6	62.8±0.8	1.9×10^{-13}	6.2×10^{-14}	0.977	0.969
	[M-9H] ⁴⁺	1990±7	67.1±0.9	2.0×10^{-13}	2.9×10^{-14}	0.996	0.998
	[M-10H] ³⁺	2247±7	72±1	2.1×10^{-13}	5.2×10^{-14}	0.998	0.968
Cytochrome c	[M-11H] ³⁺	2334±8	80±1	3.2×10^{-13}	3.3×10^{-14}	0.970	0.969
	[M-12H] ³⁺	2458±9	84±1	3.9×10^{-13}	5.0×10^{-14}	0.999	0.820
	[M-13H] ³⁺	2615±10	105±1	2.6×10^{-13}	5.6×10^{-14}	0.937	0.999
	[M-14H] ³⁺	2713±10	NA	NA	NA	NA	NA

^aCollision cross sections reported as Å².^bHDX levels reported as average±standard deviation for triplicate measurements^cRate constants reported as cm³·s⁻¹·cm⁻¹.^dCorrelation coefficient for a linear fit to the rate constant data. See figure 3 and text for details.

(Figure 3.3B) allows the determination of an HDX rate constant for the fast-exchanging sites. For the $[M-5H]^{5-}$ ions, this rate constant is determined to be $1.3 \times 10^{-13} \text{ cm}^3 \cdot \text{s}^{-1} \cdot \text{molecule}^{-1}$. The data in Figure 3.3B also suggest that some hydrogens exchange at a slower rate. Using the remaining data points up to those representing complete exchange, a second linear correlation provides a slower rate constant of $6.5 \times 10^{-14} \text{ cm}^3 \cdot \text{s}^{-1} \cdot \text{molecule}^{-1}$.

The maximum HDX levels and rate constants for all dominant ion conformations are listed in Table 3.1. For many conformations, both faster- and slower-exchanging hydrogens can be determined and therefore both rate constants are reported in Table 3.1. Comparatively, the reported rate constants are similar to those reported previously for positively-charged protein ions exposed to D_2O in a drift tube.[27, 28] This determination is of interest indicating that a similar charge-mediated exchange process (see below) could account for the observed HDX.

3.3.2.1. Anion HDX levels

Figure 3.4 shows the maximum HDX levels of the predominant ion conformers (Table 3.1) from bovine insulin, globular proteins ubiquitin and cytochrome *c*. Interestingly, insulin exchange appear similar across the charge state distribution (-3 to -5). As mentioned above, this may be attributed to the 4 disulfide bonds that act to restrict the protein for forming extended conformation. Insulin CCS values are similar across the proteins charge state distribution (Table 3.1). This may account for similar HDX uptake values shown in Figure 3.4. For ubiquitin, the HDX levels for the $[M-5H]^{5-}$ and $[M-6H]^{6-}$ ions increase only slightly. Notably, the two ions have similar collision

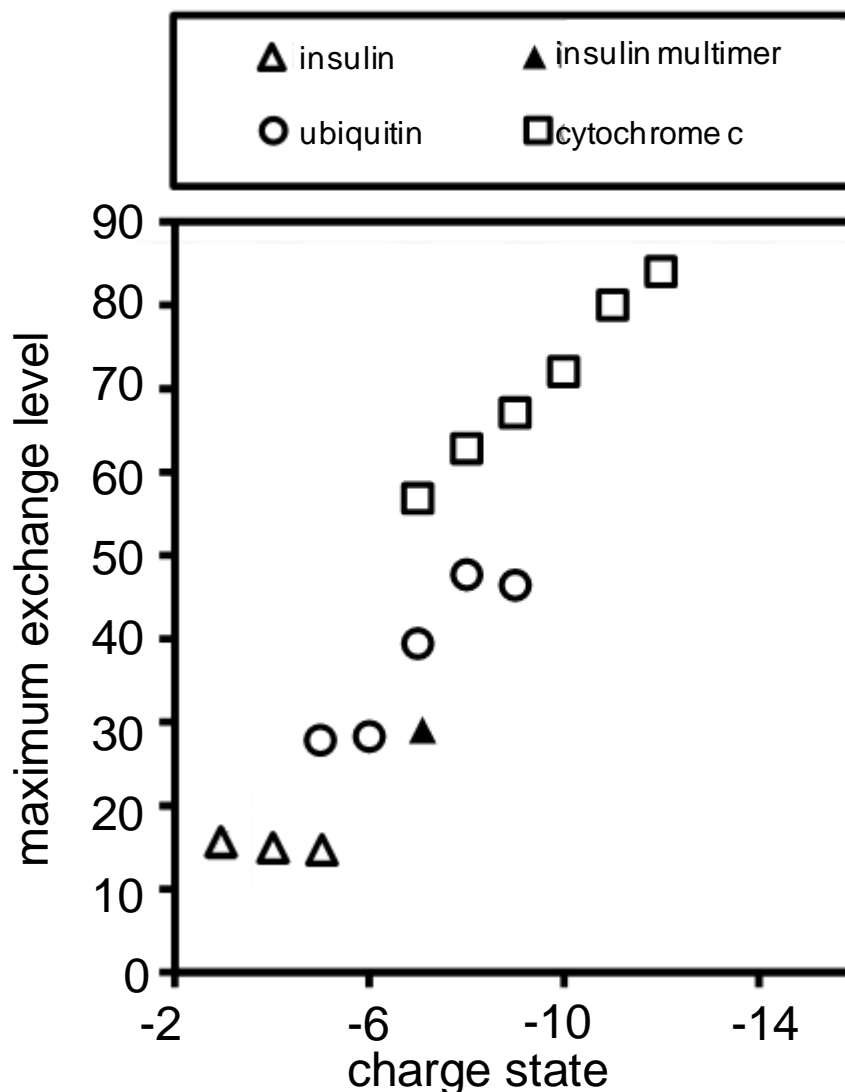


Figure 3.4. Plots of the maximum HDX levels for the dominant protein conformers. Diamond, circle and square symbols represent negatively-charged ions of the model peptide, bovine insulin, ubiquitin, and equine cytochrome c, respectively. Solid and open symbols represent monomeric and multimeric species, respectively. The number of individual monomers within multimeric species precedes the symbol.

cross sections (1010 \AA^2 and 1035 \AA^2 , respectively). The HDX level of the $[\text{M-7H}]^{7-}$ ions increases by nearly $\sim 40\%$ relative to that of the $[\text{M-6H}]^{6-}$ ions. Similarly, the collision cross section for these ions is observed to be $\sim 37\%$ larger than that of the more compact $[\text{M-6H}]^{6-}$ ions representing the largest conformational change between any ions observed in the charge state distribution for ubiquitin. An increase in HDX level

(~20%) is also observed for the $[M-8H]^{8-}$ ions relative to that of the $[M-7H]^{7-}$ ions while the change in collision cross section is smaller (~12%). The HDX levels of the $[M-8H]^{8-}$ and $[M-9H]^{9-}$ ions are similar and the latter ions exhibit only a slightly larger collision cross section (~6%). In general, the collision cross section data show a transition for dominant dataset features going from compact conformations for the $[M-6H]^{6-}$ ions to more elongated conformations for the $[M-8H]^{8-}$ ions. The HDX levels reflect this transition as well; the more elongated species are observed to have greater deuterium incorporation.

Cytochrome *c* is the largest biomolecule examined in this study. Figure 3.4 shows the HDX levels for the ion conformations of cytochrome *c*. Overall, higher charge states are associated with increased HDX levels across the distribution and deuterium exchange proceeds in a nearly linear relationship with respect to increasing charge state. For example, exchange levels increase in a uniform manner from the $[M-8H]^{8-}$ ions to the $[M-12H]^{12-}$ ions and correspond to an overall increase of ~50% (~57 to ~85). Collision cross sections increase by a nearly identical 53% (1599 \AA^2 to 2459 \AA^2) across this charge state range.

3.3.2.2. HDX Kinetics of Deprotonated Peptides and Proteins

Table 3.1 lists fast- and slow-exchanging rate constants for the various ion conformers. As mentioned above, for many ions, two rate constants have been determined. On average, the larger rate constants are ~6 times larger than the smaller rate constants. Of the larger rate constants, the fastest ($k = 6.4 \times 10^{-13} \text{ cm}^3 \cdot \text{s}^{-1} \cdot \text{molecule}^{-1}$) and slowest ($k = 3.9 \times 10^{-13} \text{ cm}^3 \cdot \text{s}^{-1} \cdot \text{molecule}^{-1}$) exchanging hydrogens are observed for $[M-11H]^{11-}$ ions from cytochrome *c* and bovine insulin, respectively. For the smaller

rate constants the fastest ($k = 6.5 \times 10^{-14} \text{ cm}^3 \cdot \text{s}^{-1} \cdot \text{molecule}^{-1}$) and slowest ($k = 1.8 \times 10^{-14} \text{ cm}^3 \cdot \text{s}^{-1} \cdot \text{molecule}^{-1}$) exchanging hydrogens are observed for $[\text{M}-5\text{H}]^{5-}$ ubiquitin and $[\text{M}-4\text{H}]^{4-}$ insulin ions, respectively.

3.3.3. Structural Implications of the HDX Results

To discuss the IMS and HDX information with regard to ion structure, it is useful to consider the process of HDX for negative ions. Although a mechanism for HDX with peptide anions and D_2O has not been presented in the literature, studies with other anion systems suggest the possibility of a relay mechanism.[26, 69, 70] For peptides, the exchange would occur via a long-lived reaction intermediate involving interaction of the D_2O molecule at the deprotonated site as well as a less acidic site (e.g., the neutral carboxylic acid moiety of a neighboring acidic amino acid residue). Exchange would proceed with deuterium transfer to the charge site and abstraction of the proton from the less acidic site. In this regard, the accessibility of a given hetero-atom site could be described with regard to its accessibility or proximity to a charge site as described previously for positively charged ions.[23, 27] An additional factor would be the conformational flexibility of the specific ions;[70, 71] that is, molecular motions that can position charge sites within an accessible range of exchange sites should also be considered. Finally, accessibility of exchange sites to collision events is also required. Further discussion of structural interpretation of the data is presented with respect to such processes.

The insulin ions exhibit the smallest HDX levels and the slowest exchange rates. The observation of decreased HDX levels for ions formed from proteins with disulfide bonds has been reported previously for positively charged ions.[71] As before, it is

proposed that conformational rigidity of insulin ions results in the decreased exchange. That is, limitations in molecular motion result in decreased access to exchange sites by charge sites. For ubiquitin ions, conformational rigidity and accessibility to D₂O can explain the observed HDX levels. For example, the compact nature of the [M-5H]⁵⁻ and [M-6H]⁶⁻ ions may prevent access of specific exchange hydrogens to D₂O; protection by compact structures for positively-charged cytochrome c ions has been presented previously.[28] It is also noted that the compact nature can also provide conformational rigidity as demonstrated in previous molecular modeling studies.[27] For the more elongated, higher charge states of ubiquitin, the increased accessibility of exchange sites to D₂O and increased conformational flexibility could account for the increased HDX levels. Finally, for the multiply-charged cytochrome c ions, the relatively elongated nature of the ions would also expose more exchange sites to the D₂O and the charge sites. The exposure to charge sites would increase with increasing charge and result in the observed higher HDX levels of these ions.

3.3.4.1. Exchange Efficiency and the Protein Fold – Ubiquitin

The discussion above of the maximum HDX levels for ubiquitin ion conformers demonstrates that HDX levels correlate to a conformational transformation occurring for the [M-6H]⁶⁻ and [M-7H]⁷⁻ ions. However, these maximum HDX levels do not reveal the degree to which increased exchange can be ascribed to protein fold versus an increase in the number of charge sites. To investigate this issue, HDX levels were recorded for compact and more elongated species for ions of both charge states at reduced D₂O pressures (0.04 Torr). The lower pressure was utilized to ensure sufficient signal of lower abundance conformers while at the same time determining differences in the

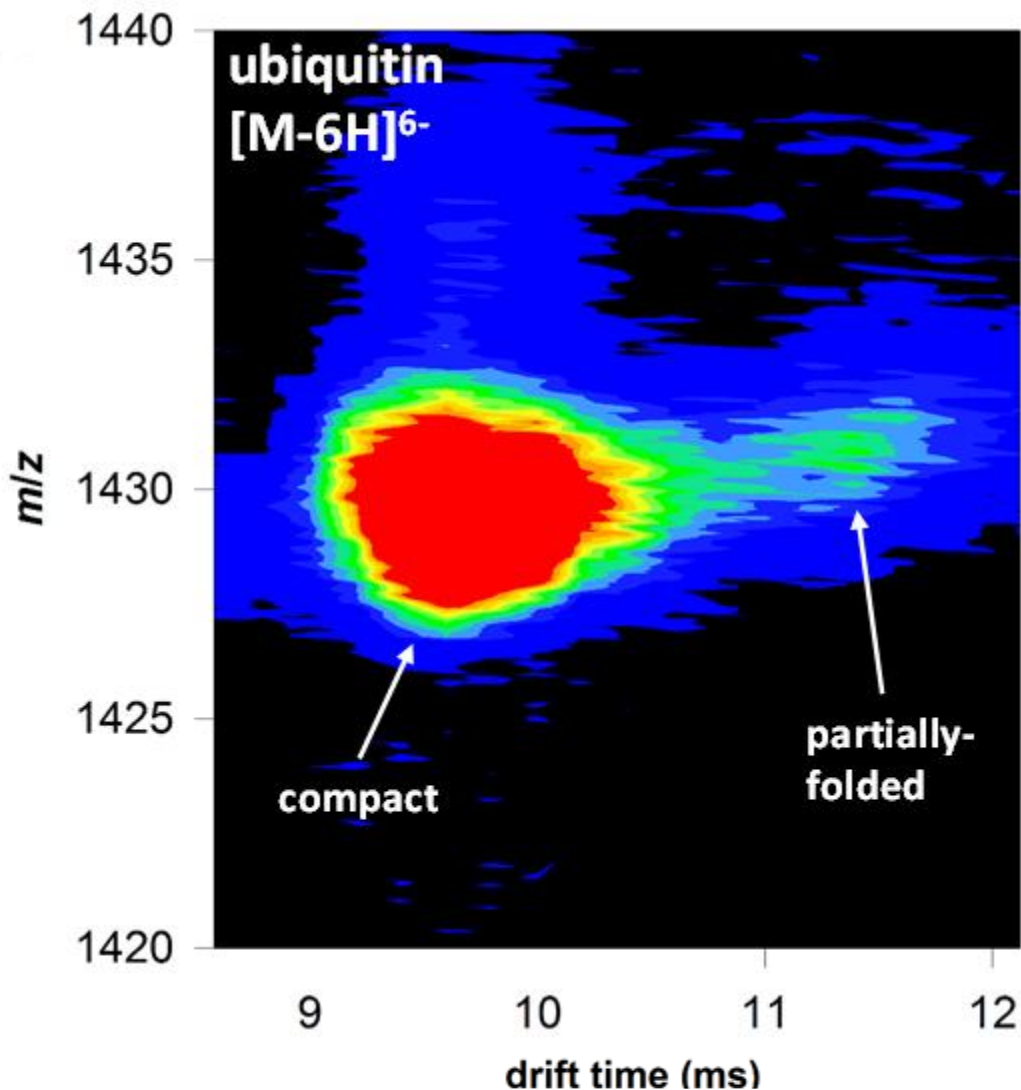


Figure 3.5. Two-dimensional, $t_D(m/z)$ heat plot of the $[M-6H]6^-$ charge state of ubiquitin after gas phase HDX with D₂O at a partial pressure of 0.04 torr. Compact and partially folded anionic species are observed and are observed to exchange different amounts of deuterium (see text for details).

levels of rapidly exchanging hydrogens (see Figure 3.3). Figure 3.5 shows an expanded region of a $t_D, m/z$ distribution for ubiquitin ions centered on compact and more elongated states of $[M-6H]6^-$ conformers. On average, for the rapidly exchanging hydrogens, the more elongated conformer exhibits a m/z value that is ~ 1.0 unit higher than the more compact conformer indicating an increased level of exchange corresponding to ~ 6 deuteriums. This same increase is also observed for more

elongated $[M-7H]^{7-}$ ions when compared with more compact species of the same charge. These observations suggest that roughly half of the increase in deuterium incorporation (~11 deuteriums) from the compact $[M-6H]^{6-}$ ions to the $[M-7H]^{7-}$ ions can be attributed to the protein fold while the remaining difference can be accounted for by the addition of a charge site.

A more subtle contribution of exchange site protection provided by protein fold (i.e., locating exchange sites in interior regions) may be explained upon examining exchange efficiency. Exchange efficiency can be represented as the ratio of ion collision cross section to maximum HDX level. Figure 3.6 shows these ratios for all ions for which maximum HDX levels could be determined. A comparison of values determined for ubiquitin ions with those of cytochrome c ions suggests that the former ions exhibit slightly increased protection due to protein fold. That is, lower exchange efficiency is observed for the ubiquitin ions even though, on average, they exhibit a higher (~14%) charge site density. This lower exchange efficiency could result from less accessibility to buried exchange sites. Insulin ions yield an exchange efficiency that is similar to the monomeric insulin ions suggesting that the conformational rigidity afforded by the disulfide bonds, also affects the maximum exchange level that can be achieved by these ions.

Having described the HDX levels and rates with regard to protein fold and conformational flexibility, it is instructive to present an alternative explanation for the experimental results. Over the last two decades, seminal research has indicated a propensity for gas-phase peptide and protein ions as well as ion complexes to form salt bridges in the gas-phase. Arguably, such salt-bridge structures impose a degree of

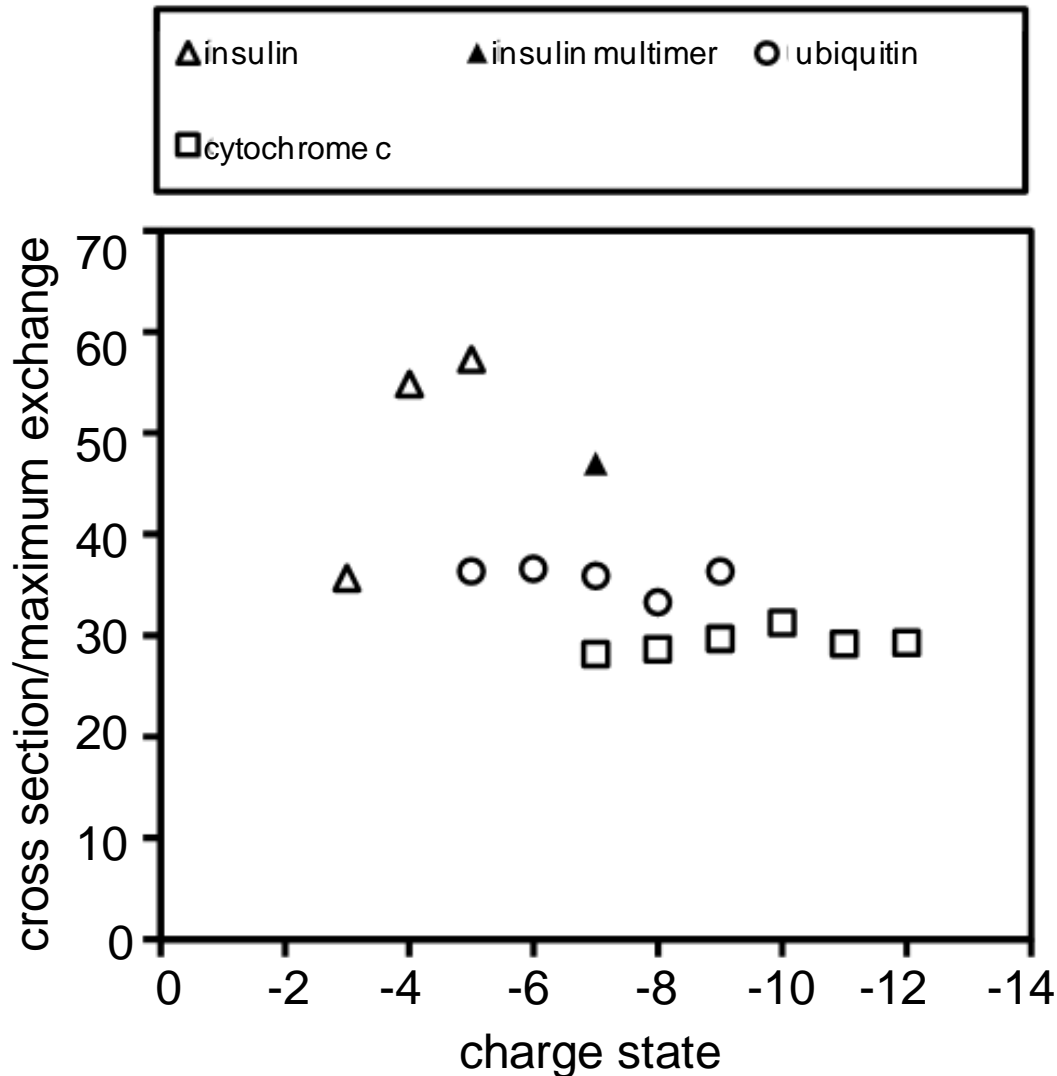


Figure 3.6. Plots of cross section/maximum HDX levels for the dominant protein conformers. Diamond, circle and square symbols represent negatively-charged ions of the model peptide, bovine insulin, ubiquitin, and equine cytochrome c, respectively. Solid and open symbols represent monomeric and multimeric species, respectively. The number of individual monomers within multimeric species precedes the symbol.

conformational inflexibility which could prevent exchange even at sites more proximal to charge sites. Here the argument of the necessity of charge site and exchange site proximity has been advanced based on the explanations provided for the observed maximum exchange levels and exchange efficiencies. The uniform increase in exchange levels for extended conformations of cytochrome c with additional charge as

well as the differences in efficiencies between ubiquitin and cytochrome c suggest deuterium uptake near charge sites. This occurs even though acidic and basic residues are observed in flanking regions of the peptide; that is, even with the possibility of forming ion conformers with salt-bridges, increased exchange is observed. That said, other factors associated with the fast- and slow-exchanging sites cannot be ruled out. Indeed the work presented here lays the foundation for testing different exchange models as initiated in recent peptide ion conformer studies.

3.3.4. Experimental limitations.

The combination of IMS with HDX-MS demonstrates a powerful approach for characterizing the ion structures of negatively-charged biomolecular ions. The use of non-ergodic ion fragmentation techniques with MS analysis has proven useful in the localization of HDX sites.[72, 73] More recently, IMS-HDX experiments have been coupled with ETD-MS to determine deuterium uptake sites for specific conformations of positively-charged ions for the model peptide described here.[74] The addition of a suitable, non-ergodic ion fragmentation technique with IMS-HDX characterization of specific peptide and protein anions would allow similar determinations for the specific peptide and protein ions presented here. The development of new ion fragmentation methods offers promise for these experiments.[75-79]

Previously, molecular dynamics simulations have been used with IMS-HDX-MS results to help explain the HDX levels observed for positively-charged peptide and protein ions.[23, 27] The recent experiments combining IMS-HDX and ETD-MS with molecular dynamics simulations suggest a need for a refinement of the previous models for deuterium incorporation (i.e., those considering only the distance between exchange

sites and charge sites). The observation that many of exchangeable hydrogens on charge sites do not undergo exchange necessitated the consideration of other models to be explored by molecular dynamics simulations. Indeed a model that incorporated distances to the charge site as well as to less basic sites using computer-generated peptide ion structures provide a better fit to experimentally determined deuterium uptake by individual amino acid residues.[74] Extending the experimental capabilities to allow determination of deuterium uptake at individual residues and the development of models from molecular dynamics simulations to explain these uptake levels will be pursued in future studies.

3.3.5. Conclusions

The HDX characteristics of negatively-charged ion conformers for peptides and proteins have been studied with IMS-MS techniques. Electrosprayed insulin ions exhibit the lowest HDX levels which can be attributed to decreased conformational flexibility resulting from the restraining disulfide bonds. This is further supported by the observation of the low exchange rates for these ions. HDX levels of larger proteins are observed to increase with charge state and ion size consistent with a charge-mediated exchange process. Of note, the HDX levels for ubiquitin ions scale with a conformational transition from more compact species to more elongated species. Based on comparisons to exchange protection for compact and elongated ion conformers, it is proposed that the exchange level transition results in part from protein fold exchange site protection and decreased access to charge sites for these ubiquitin ions. Finally, exchange efficiency comparisons suggest that ubiquitin ion conformers provide increased protection of interior sites relative to cytochrome *c* ions. Together the

results demonstrate the utility of the combined IMS and HDX conformational probes for obtaining structural information. Moreover, these studies lay the groundwork for powerful new approaches where additional tools including the incorporation of novel ion fragmentation techniques and the use of molecular dynamics simulations can be used to refine the structural information afforded by IMS-HDX measurements.

3.3.6. References

1. Fenn, J.B., et al., *ELECTROSPRAY IONIZATION FOR MASS-SPECTROMETRY OF LARGE BIOMOLECULES*. Science, 1989. **246**(4926): p. 64-71.
2. Hillenkamp, F., et al., *MATRIX-ASSISTED LASER DESORPTION IONIZATION MASS-SPECTROMETRY OF BIOPOLYMERS*. Analytical Chemistry, 1991. **63**(24): p. A1193-A1202.
3. Tanaka, K., et al., *Protein and polymer analyses up to m/z 100 000 by laser ionization time-of-flight mass spectrometry*. Rapid Communications in Mass Spectrometry, 1988. **2**(8): p. 151-153.
4. Loo, J.A., C.G. Edmonds, and R.D. Smith, *Primary sequence information from intact proteins by electrospray ionization tandem mass spectrometry*. Science, 1990. **248**(4952): p. 201-4.
5. Cheng, X.H. and C. Fenselau, *HYDROGEN-DEUTERIUM EXCHANGE OF MASS-SELECTED PEPTIDE IONS WITH ND₃ IN A TANDEM SECTOR MASS-SPECTROMETER*. International Journal of Mass Spectrometry and Ion Processes, 1992. **122**: p. 109-119.
6. Suckau, D., et al., *Coexisting stable conformations of gaseous protein ions*. Proceedings of the National Academy of Sciences of the United States of America, 1993. **90**(3): p. 790-793.
7. Covey, T. and D.J. Douglas, *Collision cross sections for protein ions*. J Am Soc Mass Spectrom, 1993. **4**(8): p. 616-23.
8. Campbell, S., et al., *Deuterium exchange reactions as a probe of biomolecule structure. Fundamental studies of gas phase H/D exchange reactions of protonated glycine oligomers with D₂O, CD₃OD, CD₃CO₂D, and ND₃*. Journal of the American Chemical Society, 1995. **117**(51): p. 12840-12854.
9. Clemmer, D.E., R.R. Hudgins, and M.F. Jarrold, *Naked Protein Conformations: Cytochrome c in the Gas Phase*. Journal of the American Chemical Society, 1995. **117**(40): p. 10141-10142.
10. Meot-Ner, M., et al., *Thermal decomposition kinetics of protonated peptides and peptide dimers, and comparison with surface-induced dissociation*. Rapid Commun Mass Spectrom, 1995. **9**(9): p. 829-36.
11. Kaltashov, I.A., D. Fabris, and C.C. Fenselau, *ASSESSMENT OF GAS-PHASE BASICITIES OF PROTONATED PEPTIDES BY THE KINETIC METHOD*. Journal of Physical Chemistry, 1995. **99**(24): p. 10046-10051.
12. Williams, E.R., *Proton transfer reactivity of large multiply charged ions*. J Mass Spectrom, 1996. **31**(8): p. 831-42.
13. Dongre, A.R., et al., *Influence of peptide composition, gas-phase basicity, and chemical modification on fragmentation efficiency: Evidence for the mobile proton model*. Journal of the American Chemical Society, 1996. **118**(35): p. 8365-8374.
14. Schnier, P.D., et al., *Blackbody infrared radiative dissociation of bradykinin and its analogues: energetics, dynamics, and evidence for salt-bridge structures in the gas phase*. J Am Chem Soc, 1996. **118**(30): p. 7178-89.
15. Green, M.K. and C.B. Lebrilla, *Ion-molecule reactions as probes of gas-phase structures of peptides and proteins*. Mass Spectrom Rev, 1997. **16**(2): p. 53-71.
16. Rodriguez-Cruz, S.E., J.S. Klassen, and E.R. Williams, *Hydration of Gas-Phase Gramicidin S (M + 2H)²⁺ Ions Formed by Electrospray: The Transition From Solution to Gas-Phase Structure*. Journal of the American Society for Mass Spectrometry, 1997. **8**(5): p. 565-568.
17. Stephenson, J.L. and S.A. McLuckey, *Gaseous protein cations are amphoteric*. Journal of the American Chemical Society, 1997. **119**(7): p. 1688-1696.
18. Javahery, G. and B. Thomson, *A segmented radiofrequency-only quadrupole collision cell for measurements of ion collision cross section on a triple quadrupole mass spectrometer*. Journal of the American Society for Mass Spectrometry, 1997. **8**(7): p. 697-702.

19. Dugourd, P., et al., *High-resolution ion mobility measurements*. Review of Scientific Instruments, 1997. **68**(2): p. 1122-1129.
20. Valentine, S.J., A.E. Counterman, and D.E. Clemmer, *Conformer-dependent proton-transfer reactions of ubiquitin ions*. Journal of the American Society for Mass Spectrometry, 1997. **8**(9): p. 954-961.
21. Wood, T.D., et al., *GAS-PHASE FOLDING AND UNFOLDING OF CYTOCHROME-C CATIONS*. Proceedings of the National Academy of Sciences of the United States of America, 1995. **92**(7): p. 2451-2454.
22. Gard, E., et al., *Gas-phase hydrogen/deuterium exchange as a molecular probe for the interaction of methanol and protonated peptides*. J Am Soc Mass Spectrom, 1994. **5**(7): p. 623-31.
23. Wyttenbach, T. and M.T. Bowers, *Gas phase conformations of biological molecules: The hydrogen/deuterium exchange mechanism*. Journal of the American Society for Mass Spectrometry, 1999. **10**(1): p. 9-14.
24. Freitas, M.A., et al., *Gas-phase bovine ubiquitin cation conformations resolved by gas-phase hydrogen/deuterium exchange rate and extent*. International Journal of Mass Spectrometry, 1999. **185**: p. 565-575.
25. Wyttenbach, T., G. vonHelden, and M.T. Bowers, *Gas-phase conformation of biological molecules: Bradykinin*. Journal of the American Chemical Society, 1996. **118**(35): p. 8355-8364.
26. Tian, Z., L. Lis, and S.R. Kass, *Hydrogen-deuterium exchange and selective labeling of deprotonated amino acids and peptides in the gas phase*. J Am Chem Soc, 2008. **130**(1): p. 8-9.
27. Valentine, S.J. and D.E. Clemmer, *Temperature-dependent H/D exchange of compact and elongated cytochrome c ions in the gas phase*. Journal of the American Society for Mass Spectrometry, 2002. **13**(5): p. 506-517.
28. Valentine, S.J. and D.E. Clemmer, *H/D exchange levels of shape-resolved cytochrome c conformers in the gas phase*. Journal of the American Chemical Society, 1997. **119**(15): p. 3558-3566.
29. Hoaglund, C.S., et al., *Three-dimensional ion mobility TOFMS analysis of electrosprayed biomolecules*. Analytical Chemistry, 1998. **70**(11): p. 2236-2242.
30. Hoaglund, C.S., S.J. Valentine, and D.E. Clemmer, *An ion trap interface for ESI-ion mobility experiments*. Analytical Chemistry, 1997. **69**(20): p. 4156-4161.
31. Valentine, S.J., S.L. Koeniger, and D.E. Clemmer, *A split-field drift tube for separation and efficient fragmentation of biomolecular ions*. Analytical Chemistry, 2003. **75**(22): p. 6202-6208.
32. Merenbloom, S.I., et al., *IMS-IMS and IMS-IMS-IMS/MS for separating peptide and protein fragment ions*. Analytical Chemistry, 2006. **78**(8): p. 2802-2809.
33. Wittmer, D., et al., *ELECTROSPRAY-IONIZATION ION MOBILITY SPECTROMETRY*. Analytical Chemistry, 1994. **66**(14): p. 2348-2355.
34. Clemmer, D.E., R.R. Hudgins, and M.F. Jarrold, *NAKED PROTEIN CONFORMATIONS - CYTOCHROME-C IN THE GAS-PHASE*. Journal of the American Chemical Society, 1995. **117**(40): p. 10141-10142.
35. Hoadlund-Hyzer, C.S., J.W. Li, and D.E. Clemmer, *Mobility labeling for parallel CID of ion mixtures*. Analytical Chemistry, 2000. **72**(13): p. 2737-2740.
36. Wu, C., et al., *Electrospray ionization high-resolution ion mobility spectrometry - Mass spectrometry*. Analytical Chemistry, 1998. **70**(23): p. 4929-4938.
37. Gillig, K.J., et al., *Coupling high-pressure MALDI with ion mobility/orthogonal time-of flight mass spectrometry*. Analytical Chemistry, 2000. **72**(17): p. 3965-3971.

38. Ruotolo, B.T., et al., *Peak capacity of ion mobility mass spectrometry: Separation of peptides in helium buffer gas*. Journal of Chromatography B-Analytical Technologies in the Biomedical and Life Sciences, 2002. **782**(1-2): p. 385-392.
39. Clowers, B.H. and H.H. Hill, *Mass analysis of mobility-selected ion populations using dual gate, ion mobility, quadrupole ion trap mass spectrometry*. Analytical Chemistry, 2005. **77**(18): p. 5877-5885.
40. Clowers, B.H., et al., *Hadamard transform ion mobility spectrometry*. Anal Chem, 2006. **78**(1): p. 44-51.
41. Gillig, K.J., et al., *An electrostatic focusing ion guide for ion mobility-mass spectrometry*. International Journal of Mass Spectrometry, 2004. **239**(1): p. 43-49.
42. Kwasnik, M., et al., *Performance, resolving power, and radial ion distributions of a prototype nanoelectrospray ionization resistive glass atmospheric pressure ion mobility spectrometer*. Analytical Chemistry, 2007. **79**(20): p. 7782-7791.
43. Kwasnik, M., J. Caramore, and F.M. Fernandez, *Digitally-Multiplexed Nanoelectrospray Ionization Atmospheric Pressure Drift Tube Ion Mobility Spectrometry*. Analytical Chemistry, 2009. **81**(4): p. 1587-1594.
44. Kurulugama, R.T., et al., *Overtone Mobility Spectrometry: Part 1. Experimental Observations*. Journal of the American Society for Mass Spectrometry, 2009. **20**(5): p. 729-737.
45. Merenbloom, S.I., et al., *High-resolution ion cyclotron mobility spectrometry*. Anal Chem, 2009. **81**(4): p. 1482-7.
46. Valentine, S.J., et al., *Overtone Mobility Spectrometry: Part 2. Theoretical Considerations of Resolving Power*. Journal of the American Society for Mass Spectrometry, 2009. **20**(5): p. 738-750.
47. Revercomb, H.E. and E.A. Mason, *THEORY OF PLASMA CHROMATOGRAPHY GASEOUS ELECTROPHORESIS - REVIEW*. Analytical Chemistry, 1975. **47**(7): p. 970-983.
48. Siems, W.F., et al., *MEASURING THE RESOLVING POWER OF ION MOBILITY SPECTROMETERS*. Analytical Chemistry, 1994. **66**(23): p. 4195-4201.
49. Mason, E.A.M., E. W., *Transport Properties of Ions in Gases*. 1988, New York: Wiley.
50. Shvartsburg, A.A. and M.F. Jarrold, *An exact hard-spheres scattering model for the mobilities of polyatomic ions*. Chemical Physics Letters, 1996. **261**(1-2): p. 86-91.
51. Mesleh, M.F., et al., *Structural Information from Ion Mobility Measurements: Effects of the Long-Range Potential*. The Journal of Physical Chemistry, 1996. **100**(40): p. 16082-16086.
52. Wyttenbach, T., et al., *Effect of the long-range potential on ion mobility measurements*. Journal of the American Society for Mass Spectrometry, 1997. **8**(3): p. 275-282.
53. Harris, G.A. and F.M. Fernandez, *Simulations and Experimental Investigation of Atmospheric Transport in an Ambient Metastable-Induced Chemical Ionization Source*. Analytical Chemistry, 2009. **81**(1): p. 322-329.
54. Kwasnik, M. and F.M. Fernandez, *Theoretical and experimental study of the achievable separation power in resistive-glass atmospheric pressure ion mobility spectrometry*. Rapid Communications in Mass Spectrometry, 2010. **24**(13): p. 1911-1918.
55. Glaskin, R.S., S.J. Valentine, and D.E. Clemmer, *A Scanning Frequency Mode for Ion Cyclotron Mobility Spectrometry*. Analytical Chemistry, 2010. **82**(19): p. 8266-8271.
56. Valentine, S.J., R.T. Kurulugama, and D.E. Clemmer, *Overtone Mobility Spectrometry: Part 3. On the Origin of Peaks*. Journal of the American Society for Mass Spectrometry, 2011. **22**(5): p. 804-816.
57. Siems, W.F., L.A. Viehland, and H.H. Hill, Jr., *Improved momentum-transfer theory for ion mobility. 1. Derivation of the fundamental equation*. Anal Chem, 2012. **84**(22): p. 9782-91.

58. Stlouis, R.H. and H.H. Hill, *ION MOBILITY SPECTROMETRY IN ANALYTICAL-CHEMISTRY*. Critical Reviews in Analytical Chemistry, 1990. **21**(5): p. 321-355.
59. Clemmer, D.E. and M.F. Jarrold, *Ion mobility measurements and their applications to clusters and biomolecules*. Journal of Mass Spectrometry, 1997. **32**(6): p. 577-592.
60. Hoaglund-Hyzer, C.S., A.E. Counterman, and D.E. Clemmer, *Anhydrous protein ions*. Chemical Reviews, 1999. **99**(10): p. 3037-3079.
61. Collins, D.C. and M.L. Lee, *Developments in ion mobility spectrometry-mass spectrometry*. Analytical and Bioanalytical Chemistry, 2002. **372**(1): p. 66-73.
62. Bohrer, B.C., et al., *Biomolecule Analysis by Ion Mobility Spectrometry*, in *Annual Review of Analytical Chemistry*. 2008. p. 293-327.
63. Donohoe G. C.; Maleki, H.A., J. R.; Khakinejad, M.; Yi, J.; McBride, C.; Nurkiewicz, T. R.; Valentine, S. J., *A New Ion Mobility–Linear Ion Trap Instrument for Complex Mixture Analysis*. Anal. Chem., 2014. **86**(16): p. 8.
64. Tang, K., et al., *High-sensitivity ion mobility spectrometry/mass spectrometry using electrodynamic ion funnel interfaces*. Analytical Chemistry, 2005. **77**(10): p. 3330-3339.
65. Lee, S., et al., *Extracted fragment ion mobility distributions: A new method for complex mixture analysis*. International Journal of Mass Spectrometry, 2012. **309**: p. 154-160.
66. Shelimov, K.B. and M.F. Jarrold, *Conformations, unfolding, and refolding of apomyoglobin in vacuum: An activation barrier for gas-phase protein folding*. Journal of the American Chemical Society, 1997. **119**(13): p. 2987-2994.
67. Shelimov, K.B., et al., *Protein structure in vacuo: Gas-phase confirmations of BPTI and cytochrome c*. Journal of the American Chemical Society, 1997. **119**(9): p. 2240-2248.
68. Valentine, S.J., et al., *Disulfide-intact and -reduced lysozyme in the gas phase: Conformations and pathways of folding and unfolding*. Journal of Physical Chemistry B, 1997. **101**(19): p. 3891-3900.
69. Chan, S. and C.G. Enke, *Mechanistic study of hydrogen/deuterium exchange between [M – 1]– ions of chlorinated benzenes and D2O or ND3*. Journal of the American Society for Mass Spectrometry, 1994. **5**(4): p. 282-291.
70. Freitas, M.A., et al., *Gas-phase RNA and DNA ions. 1. H/D exchange of the M-H (-) anions of nucleoside 5'-monophosphates (GMP, dGMP, AMP, dAMP, CMP, dCMP, UMP, dTMP), ribose 5-monophosphate, and 2-deoxyribose 5-monophosphate with D2O and D2S*. Journal of the American Chemical Society, 1998. **120**(39): p. 10187-10193.
71. Evans, S.E., N. Lueck, and E.M. Marzluff, *Gas phase hydrogen/deuterium exchange of proteins in an ion trap mass spectrometer*. International Journal of Mass Spectrometry, 2003. **222**(1–3): p. 175-187.
72. Rand, K.D., et al., *Site-Specific Analysis of Gas-Phase Hydrogen/Deuterium Exchange of Peptides and Proteins by Electron Transfer Dissociation*. Analytical Chemistry, 2012. **84**(4): p. 1931-1940.
73. Rand, K.D., et al., *ETD in a Traveling Wave Ion Guide at Tuned Z-Spray Ion Source Conditions Allows for Site-Specific Hydrogen/Deuterium Exchange Measurements*. Journal of the American Society for Mass Spectrometry, 2011. **22**(10): p. 1784-1793.
74. Khakinejad, M.M., H.; Arndt, J. R.; Donohoe, G. C.; Valentine, S. J., *Combining Ion Mobility Spectrometry with Hydrogen-Deuterium Exchange and Top-Down MS for Peptide Ion Structure Analysis*. J. Am. Soc. Mass Spectrom. (submitted), 2014.
75. Swaney, D.L., et al., *Supplemental activation method for high-efficiency electron-transfer dissociation of doubly protonated peptide precursors*. Anal Chem, 2007. **79**(2): p. 477-85.
76. Yoo, H.J., et al., *Negative-ion electron capture dissociation: radical-driven fragmentation of charge-increased gaseous peptide anions*. J Am Chem Soc, 2011. **133**(42): p. 16790-3.

77. Cook, S.L., et al., *Comparison of CID, ETD and metastable atom-activated dissociation (MAD) of doubly and triply charged phosphorylated tau peptides*. *Journal of Mass Spectrometry*, 2012. **47**(6): p. 786-794.
78. Cook, S.L. and G.P. Jackson, *Metastable Atom-Activated Dissociation Mass Spectrometry of Phosphorylated and Sulfonated Peptides in Negative Ion Mode*. *Journal of the American Society for Mass Spectrometry*, 2011. **22**(6): p. 1088-1099.
79. Cook, S.L., O.L. Collin, and G.P. Jackson, *Metastable atom-activated dissociation mass spectrometry: leucine/isoleucine differentiation and ring cleavage of proline residues*. *Journal of Mass Spectrometry*, 2009. **44**(8): p. 1211-1223.

4. Online Deuterium Hydrogen Exchange and Protein Digestion Coupled with Ion Mobility Spectrometry and Tandem Mass Spectrometry¹

¹Reprinted in part with permission from *Analytical Chemistry: Online Deuterium Hydrogen Exchange and Protein Digestion Coupled with Ion Mobility Spectrometry and Tandem Mass Spectrometry*. Gregory C. Donohoe, James R. Arndt, Stephen J. Valentine.. *Anal. Chem.*, 2015, 87 (10), 5247-5254.

4.1. Introduction: Deuterium Hydrogen Exchange and IMS – MS

Hydrogen deuterium exchange-mass spectrometry (HDX-MS) is an isotopic labeling strategy used for the evaluation of protein structure,[1-3] folding dynamics[1, 2, 4-11] and as a method to characterize protein-protein and protein-drug interactions in the biopharmaceutical sector.[3, 9, 12] Many HDX-MS experiments use high performance liquid chromatography (LC) consisting of an immobilized pepsin column for online digestion followed by trapping and reversed phase separation of peptic fragments that are subsequently mass analyzed.[13, 14] Using this "bottom-up" approach, deuterium incorporation at backbone amide locations can be evaluated on a per-peptide basis. Despite much success,[1, 4, 15] bottom-up HDX-MS is limited by spatial resolution that is dependent upon the number of overlapping peptide fragments.

Although the techniques have been commonly accepted and highly successfully, the remaining difficulty regarding HDX-LC-MS and MS/MS experiments is mitigating backexchange before MS analysis. HDX-LC-MS methods require specialized cooling apparatuses (0 C), low pH (~2.5) mobile phases, high flow rates and fast gradients (~10 minutes or less) to minimize backexcahnge.[16] Because peptide separation is generally based on hydrophobicity, a particular problem arises in the higher rate of backexchange as certain peptides adopt altered solution conformations as they partition into the C₁₈ stationary phase.[17] Other studies have shown that the

solid support contained within immobilized pepsin columns can promote significantly high backexchange.[18] The relatively fast gradients can also create differences in retention times requiring data alignment algorithms for quantitative and qualitative comparisons between datasets.[19] Additionally, because the LC step must be performed quickly, co-eluting peptides can reduce ionization efficiency. This is particularly problematic with data dependant MS/MS which only samples the highest intensity precursor ions (top 5) for fragmentation per-elution-window. Peptide ion sensitivity is further reduced using non-activating ion transfer parameters to mitigate hydrogen/deuterium scrambling in the gas phase. For LC-MS/MS analysis, the compilation of these inherent difficulties may result in inadequate isotopic distributions of product ions from the analysis.

HDX studies have used commercial traveling wave ion mobility (TWIM) devices coupled with Time-of-flight mass analyzers for bottom-up peptide studies.[20, 21] In the work provided here, a low-pressure drift tube coupled to an LTQ Velos mass spectrometer (Thermo Scientific, CA) is used for per-residue deuterium analysis by ETD. It is further noted that TWIM instruments contain an ETD cell located before the mobility region,[22-24] meaning that the mobility separation is not utilized to distinguish precursor ion conformers. Thus, an advantage demonstrated in this work is the ability of drift tube IMS (DTIMS) to mobility separate ions before ETD without being subject to ion heating that would promote deuterium scrambling. That is, ions that traverse the low pressure drift tubes are thermolized, while TWIM instruments are shown to promote ion heating of mobility transferred ions exhibiting temperatures from ~400 K to ~7000 K.[25-27] Although these temperatures are dependent on the TWIM wave speed and wave

height as well as the trapping partial pressure compositions, other studies have shown that heating processes promote deuterium scrambling.[28, 29]

A goal of this proof-of-principle work is to demonstrate the replacement of the LC with a DTIMS instrumental platform for the evaluation of protein secondary structures. A continuous online deuterium hydrogen exchange (DHX) and pepsin digestion (PD) method performed prior to the IMS separation is demonstrated. DHX proceeds under exchange-out conditions,[30] where fully deuterated protein is exposed to H₂O. The protein exchanges deuteriums in unstructured regions faster than sites held in H-bonding networks.[30] The DHX-PD process takes ~60 seconds and only requires micro-cross assemblies and fused silica capillary, similarly fashioned to a design described for the characterization of the iron-saturated N-lobe of human serum transferrin.[31] The rapid DHX time (~32 seconds) in this study is used to backwash fast exchanging heteroatoms for a qualitative view of secondary structural elements.

The mobility measurement provides the capability to match, via extracted ion drift time distributions (XIDTDs)[32], labeled peptic peptide ions with the unlabeled peptide ions. Because the unlabeled ions were first identified using collision induced dissociation (CID), the technique transfers identification to deuterated peptides, allowing a straightforward deuterium retention evaluation. Due to the high reproducibility of the gas phase separation, XIDTD matching is performed without the need for dataset alignment. Another advantage of the online method is the ability to select a specific mobility range for MS and MS/MS analysis. Because the online system is continuous and is neither elution window nor intensity limited (as with data-dependent LC-MS/MS analysis), ETD can be performed on precursor ions over several minutes to produce

statistically adequate isotopic distributions of product ions. Lastly, this work presents the first solution-based deuterium exchange study using a low-pressure, linear-field IMS coupled with ion trapping MS-ETD.

4.2. Methods and Materials

4.2.1. Sample Preparation

Ubiquitin (bovine erythrocytes, 98%) and lyophilized pepsin (porcine, 3200-4500 units/mg protein) were purchased from Sigma-Aldrich (St. Louis, MO) and used without further purification. Deuterium oxide (99.9%), formic acid (99 %) and ammonium acetate were purchased from Sigma-Aldrich (St. Louis, MO). The peptide KKDDDDDIKIIK (90.6%) was purchased from Genscript (Piscataway, NJ, USA) and used without further purification. This peptide was used as a HDX or deuterium scrambling control (see below).

4.2.2. On – Line DHX – PD – IMS System

Ubiquitin Studies. Ubiquitin (0.5 mg) was added to 1.0 mL of D₂O (99.9 %) containing ammonium acetate (10 mM). The solution was incubated ~40 hours at room temperature. Note the 40 hour time period was utilized for the first of three replicate measurements. Subsequent replicate measurements were performed on successive days. Pepsin solutions were prepared by adding lyophilized powder (0.75 mg) to 1.0 mL 18 MΩ H₂O (6% formic acid v:v) pH ~2.0. A schematic of the online system is presented in Figure 1.1 in the Supplementary Information section (Figure S1). Briefly, the DHX reaction and subsequent quenching with simultaneous digestion was performed using three micro-cross assemblies (Upchurch Scientific Inc, Oak Harbor, Wa) connected with fused-silica capillary (360 μm o.d. × 50 μm i.d). Separate 500-μL syringes (Hamilton,

Reno, NV, USA) containing the deuterated ubiquitin solution and 18 MΩ H₂O were delivered to the first micro-cross assembly using high precision syringe pumps (KD scientific Holliston, MA,USA) at flow rates of 0.20 μL·min⁻¹ and 0.87 μL·min⁻¹

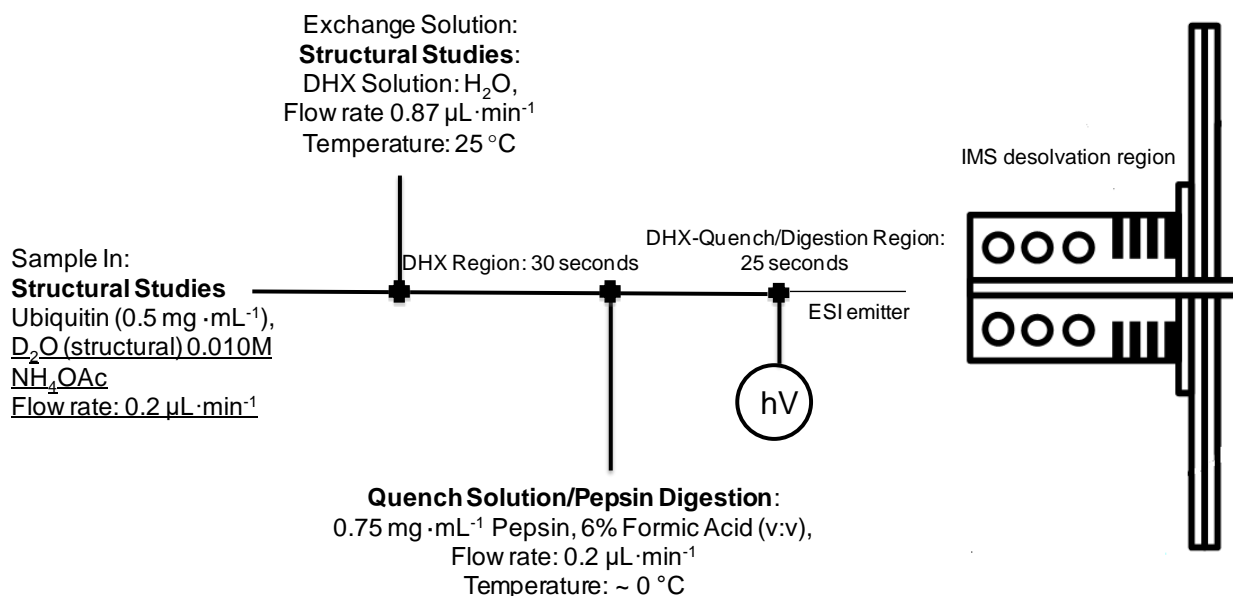


Figure 4.1. Schematic representation of the on-line system for DHX-PD-ESI-IMS-MS analysis. High precision syringe pumps were used to advance separate solutions simultaneously to mixing-tees (black crosses). At these locations, exchange reactions or digestion occurred along different lengths of capillary. The respective times for DHX and digestion are also indicated.

respectively. DHX of deuterated ubiquitin proceeded for ~29.6 seconds over a capillary length of 26.4 cm. This DHX-setup and exchange time was similar to that reported in previous exchange-out experiments for the determination of site specific interactions of Huntingtin protein exon 1 aggregates.[33] A third 500-μL syringe containing ice-cooled pepsin solution (pH ~2.0) was introduced by a syringe pump to a second micro-cross assembly at a flow rate of 0.20 μL·min⁻¹. DHX quenching and protein digestion was performed over a capillary length of 20.3 cm. Peptic peptides entered into a third micro-cross assembly connected to a 2.5 cm pulled tip nano-ESI emitter (360 μm o.d. × 50 μm i.d) giving a total digestion capillary length of 22.9 cm and a total digest time of ~22.4

seconds. Peptides were electrosprayed into the IMS instrument using a bias voltage of $\sim +1.9$ kV at a combined flow rate of $1.26 \mu\text{L}\cdot\text{min}^{-1}$. No direct heating of the source or desolvation region was applied. For unlabeled ubiquitin studies, the same protein concentrations, syringe flow rates and capillary lengths were used; however, ubiquitin was incubated in $18 \text{ M}\Omega \text{ H}_2\text{O}$ containing 10 mM ammonium acetate.

Here it is noted that no sample cleanup steps were performed. Although not necessary for the purified samples utilized in this study as demonstrated by the results presented below, because salt content may hinder ESI, sample cleanup for many protein samples may be required in order to take advantage of this direct infusion approach. That said, to some degree, the IMS separation can mitigate problems arising from noise produced by isobaric ions.[34]

4.2.3. Scrambling Control On – Line System

For the evaluation of scrambling, the peptide KKDDDDDIKIIK (0.5mg) was added to 1.0-mL of D_2O (99.9%) containing 10 mM ammonium acetate ($\text{pH} \sim 7.0$) and allowed to incubate for ~ 24 hours at 25°C . The peptide contains a fast exchanging KKDDDDD sequence and a slow exchanging IIKIIK C-terminal region. For these studies, the DHX solution served as the quench solution in that it was cooled with an ice pack and acidified to a final pH of ~ 2.5 . Flow rates for the peptide and DHX solutions were $0.20 \mu\text{L}\cdot\text{min}^{-1}$ and $1.00 \mu\text{L}\cdot\text{min}^{-1}$ respectively. Capillary lengths for DHX were the same as described for ubiquitin studies. It should be noted that the pepsin solution was not added to the online system, as the exchanged peptide must retain the intact sequence for scrambling determination. Instrumental parameters for ubiquitin

deuteration studies were selected based upon the peptide exhibiting a 0 % scrambling trend).[28, 29]

4.2.3.1. Optimized Parameters

Instrumental parameters used to mitigate HD-scrambling can be found in Appendix 1. These parameters were determined based on the scrambling control peptide resulting in 0 % HD-scrambling (see below).

4.2.3. IMS-MS: Instrumental Operation

IMS theory,[35-38] instrumentation,[39-45] and techniques[46-55] are described elsewhere in great detail. The IMS instrument contained a drift tube with dual ion funnels and two ion gates interfaced to a LTQ Velos (Thermo Electron, San Jose, Ca, USA) mass spectrometer that has been described previously.[56, 57] The LTQ Velos was outfitted with a commercial ETD source for the generation of fluoranthene radicals (Thermo Scientific, San Jose, Ca, USA). Figure 1.1 shows a schematic of the IMS-MS instrument with ETD capabilities and the locations of the ion funnels and gates within the drift tube. The source of the mass spectrometer was redesigned to incorporate a stacked-ring ion drift region by replacing the s-lens assembly (Figure 1.1). Briefly, ions were electrosprayed into the desolvation region and were focused through an “hourglass” electrodynamic ion funnel (F1 in Figure 1.1).[50, 58] The focused ions were periodically trapped at the first ion gate (G1 in Figure 1.1) and periodically pulsed into a 1-meter-long drift tube filled with He buffer gas (~2.72 torr at 300 K). Under the influence of a uniform electric field (~10 V·cm⁻¹), ions of different mobilities reached the second ion gate (G2 in Figure 1.1) at different times. Ions of select drift times (t_D) that passed through G2 were radially focused at the second ion funnel (F2)[50], and exited through a conductance-limiting aperture. The ion packet was subsequently transferred

by quadrupole and octopole rf guides before entering into the high pressure linear ion trap followed by mass analysis in the lower pressure trap.

4.2.3.1. Recording Two – Dimensional (2D) $t_D(m/z)$ Distributions.

Ion gates were constructed from lenses containing Ni grid (90% transmittance mesh; Precision Eforming, Cortland, NY, USA). G1 was composed of a single gridded lens located directly behind the outlet of the hour-glass funnel. During ion accumulation, G1 was biased ~45 V higher than the last lens of F1. For mobility measurements, an ion packet was pulsed into the drift tube by dropping the voltage at G1 for 150 μ s every 20 ms. A t_D was collected for mobility separated ions using a time-delayed voltage applied to the ion selection gate (G2). G2 consisted of two gridded lenses (Tyndall Geometry) spaced ~0.30 cm apart. An attractive field (2.5 V) pulsed at specific times between the lenses enabled ions of a selected mobility to pass for mass analysis. Ions of all other mobilities were eliminated with a repulsive field applied between the lenses (10.0 V). The gate timing of G2 was initiated relative to the introductory ion pulse at G1. By scanning the delay time across the entire t_D from 4.0 to 12.0 ms, at a step resolution of 200 μ s, 41 mobility-resolved mass spectra was collected. The introduction pulse at G1 and variable delay settings at G2 were controlled by 2 four-channel digital pulse generators (Stanford Research Systems, Sunnyvale, CA, USA).

4.2.4. Mass Spectrometry Measurements

Full mass spectra were collected for all ions by deactivating the two drift tube gates and setting the mass analyzer scan parameters over a m/z range of 75 to 2000 and enabling the automatic gain control (AGC). In this operation, the drift tube acted to transfer all ions into the LTQ. The AGC threshold is set to 3×10^6 ions and a mass

spectrum was collected. During t_D distribution generation, the AGC was disabled and a trap injection time of 400 ms (4 microscans) was selected. All mobility-resolved mass spectra were collected and averaged over 0.5 minutes.

4.2.4.1. CID – MS Experiments

Tandem mass spectrometry (MS/MS) using CID was conducted on unlabeled ubiquitin peptic peptide ions by isolating a mobility selected ion m/z . For these experiments, an isolation window of ± 3 Da relative to the centroid m/z resulted in the ejection of all other ions within the ion trap. Selected precursor ions were collisionally activated with He gas at a normalized collision energy of 30.0 % and an activation time of 10 ms. Product ion spectra were collected for 1.0 minute.

4.2.4.1.1. Identification of Precursor Ions.

For peptic peptide identification, the selected precursor m/z values were converted to mass based on charge state. The masses were then derived to determine $[M+H]^+$ ions. Using ExPaSY FindPept (<http://web.expasy.org/findpept/>) the unmodified 76 amino acid sequence of bovine ubiquitin was uploaded to perform *in-silico* digestion using pepsin at pH >2.0. The program generated $[M+H]^+$ ions at a mass tolerance of ± 2.0 Da having unique amino acid lengths. The corresponding sequences with experimentally matching m/z values were selected and entered into Protein Prospector (<http://prospector.ucsf.edu/prospector/cgi-bin/msform.cgi?form=msproduct>) for *in-silico* MS/MS fragmentation. Product ion spectra from the selected precursors collected from IMS-MS/MS experiments were compared to y - and b - fragment ions for identification.

4.2.4.2. Deuterated Samples and ETD Analysis.

The control peptide (KKDDDDDDIIKIIK) served to evaluate the optimal settings applied to the source, ion optics, lenses and transfer voltages to mitigate HD scrambling. These settings were changed until the control peptide follows a 0 % scrambling trend (see Supporting Information for parameters).[28, 29] Briefly, the F1 DC voltage (Figure 1.1) was set to 136.8 V, the RF voltage at F2 was set to 136.8 volts peak-to-peak, the voltages on the ion guides were set to 300 V peak-to-peak and no direct temperature was applied to the ESI source. For ETD studies, a specific precursor m/z was selected using a ± 8 Da window relative to the centroid m/z value. This wider selection window was used to confine the entire isotopic distribution. Furthermore, narrow selection windows have been shown to induce scrambling by resonance excitation.[28] ETD of selected $[M+3H]^{3+}$ precursor ions proceeded by introduction of fluoroanthene radicals into the LTQ for 100 ms. To ensure adequate isotopic distribution statistics of product ions, the resulting spectra were collected for 1.0 minute.

4.2.4.3. IMS-MS Data Sets.

Two-dimensional IMS-MS datasets were generated by converting each t_D resolved mass spectrum (.RAW file) to a separate text file (.TXT file). Using software developed in-house, the m/z values and intensities contained within this .TXT file at an associated t_D were converted into a three-column array file containing t_D , m/z , and intensity information. Intensity filters were applied to the dataset for spectral clarity and the output can be used to create a 2D IMS-MS heat plot based on a logarithmic intensity scale. Here, each pixel contained a t_D width of 200 μ s and a height of 0.0833 Da.

4.2.4.4. Comparative XIDTDs for Identification.

To generate XIDTDs[32], a separate in-house program was used to process the same three column array files (t_D , m/z , and intensity) by integrating intensity values across all t_D windows within a user-defined m/z range. The output comprised an integrated mobility distribution for specific m/z values. All data were normalized to the most intense spectral feature within each XIDTD. XIDTDs were matched based on a pixel t_D width of 200 μ s and a pixel height of 0.0833 Da. No dataset alignment was utilized for XIDTD matching between undeuterated and deuterated digest samples.

4.2.4.4. Per-Residue Deuterium Measurements.

Product ions generated from ETD (triplicate measurements) were signal averaged over 1.0 minute. The resulting spectrum was converted in much the same manner as described above. Briefly, the .RAW file was converted into a two column .TXT file containing m/z and associated intensity values. Using software developed in-house, deuterium uptake was calculated from average m/z determinations obtained by weighting the isotopic peaks according to their intensity values for each product ion. The output was a .TXT file containing the average m/z values that were then subtracted from the undeuterated product ion average m/z of the same charge state. The mass difference was reported as the amount of total deuterium retention for each fragment ion.

4.3 Results and Discussion

4.3.1 Comparing Peptides from 2D IMS-MS Datasets.

Figure 4.2A shows the two-dimensional 2D $t_D(m/z)$ distribution of undeuterated peptic peptides resulting from online PD-IMS-MS. Spectral features are first observed

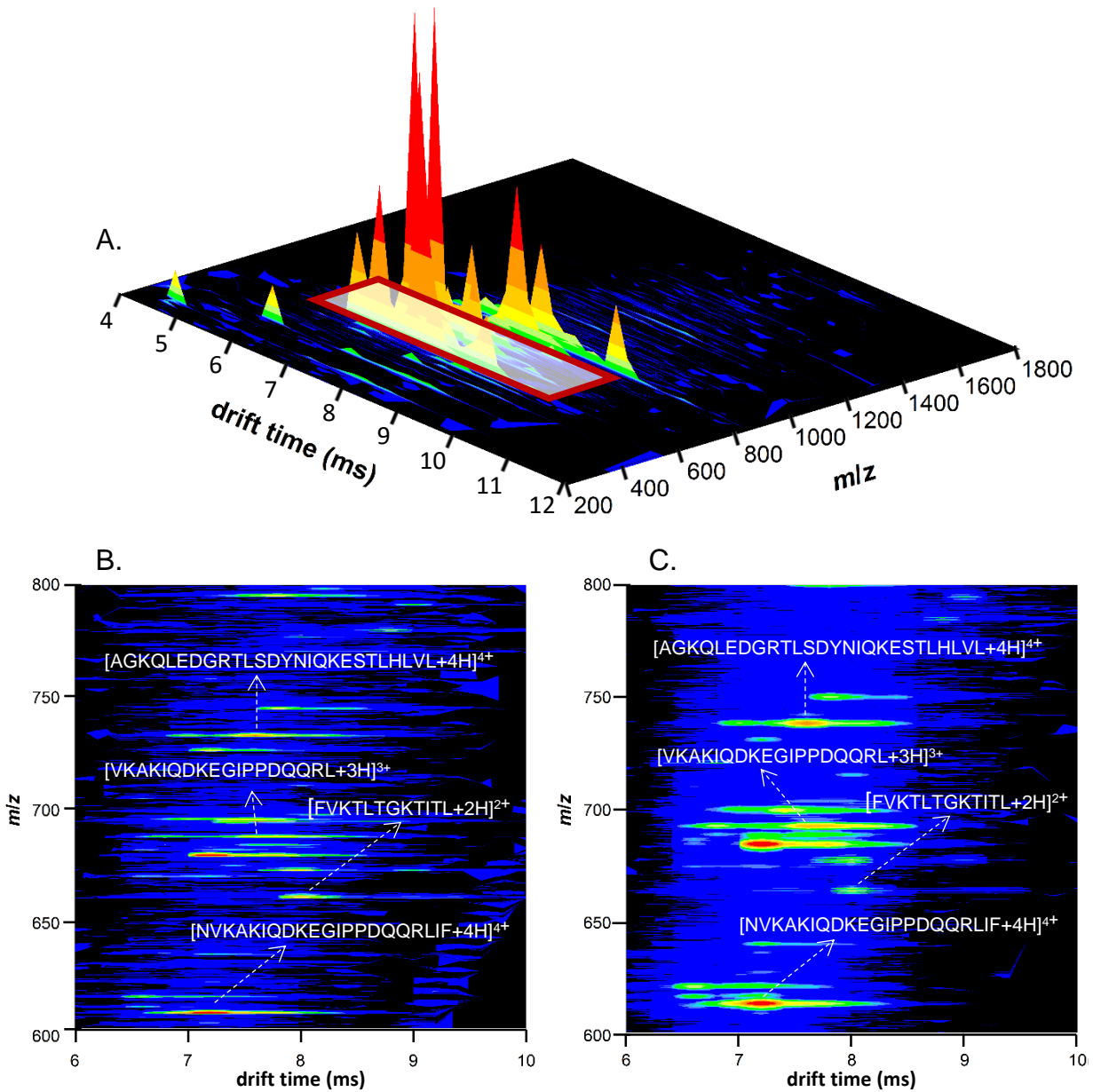


Figure 4.2 (A) Two-dimensional (2D) $t_D(m/z)$ raised-relief plot showing the resulting peptide ions generated from DHX-PD-IMS-MS of unlabeled ubiquitin. The dashed-line box represents the region from t_D ~6 to ~10 ms and a m/z range of 600 to 800. This region is used for comparative purposes in Figures B and C. (B) 2D $t_D(m/z)$ contour-plot of DHX-PD-IMS-MS analysis of unlabeled peptides extracted from the boxed region in Figure A. (C) 2D $t_D(m/z)$ contour-plot the DHX-PD-IMS-MS analysis of labeled peptides over the same $t_D(m/z)$ ranges as described above. The color maps for all plots are shown on a logarithmic scale (-2 to 3) in order to show the low-intensity ions.

at ~4.6 ms and extend to ~11.4 ms with the highest intensity peptide ions existing between a m/z range of ~550 to ~800. Spectral intensities for mobility separated ions ranged from only a few counts to $\sim 4.2 \times 10^3$. Figure 4.2B and 2C show the 2D $t_D(m/z)$ contour depicting expanded regions of the dataset (t_D 6.0 ms to 10.0 ms over a m/z range of 600 to 800) for undeuterated and deuterated peptides, respectively.

Collectively, Figures 4.2B and 4.2C show similar spectral features that display similar drift times, but differ in average m/z due to the incorporation of deuterium. It is also noted that deuterium retention broadens the isotopic distribution for given peptides (Figure 4.2C) and in some cases the isotopic envelopes are observed to overlap in the mass spectrum. For all sample sets, the fast proteolytic step generated larger peptides having sequence lengths between ~4 to ~25 residues and exhibit charge states from +1 to +4. With respect to LC-MS approaches, these larger peptide sequences are problematic, as deuterium evaluation at the residue level is based on the number of overlapping peptides. Comparatively, the longer sequences contain a larger number of basic residues resulting in higher charge states more amenable for ETD fragmentation.

4.3.2. Generating XIDTDs and Combining Collision Induced Dissociation (CID) for Unlabeled Peptides Identification.

A particular advantage of the IMS-MS measurement is the ability to generate an XIDTD for peptide ion analyzed. Additionally, XIDTDs allow a more exact comparison of features in IMS-MS plots (Figures 4.2B and 4.2C). For example, Figure 4.3A shows the

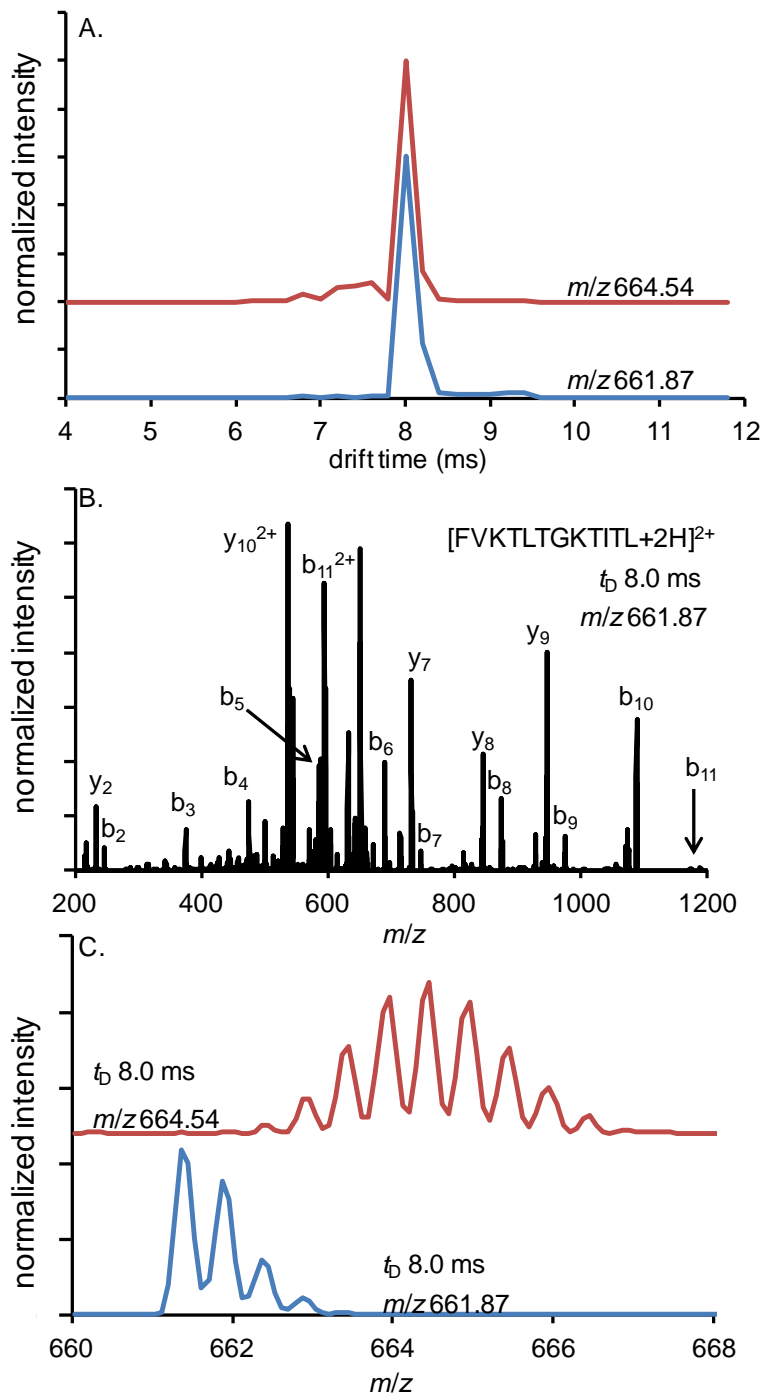


Figure 4.3. (A) XIDTD of the ion having an average m/z of 661.87 from undeuterated ubiquitin (blue trace) and the overlaid XIDTD (red trace) of the respective deuterated ion (average m/z of 664.54). All XIDTDs are normalized to the most intense spectral feature. (B) CID fragmentation spectrum obtained from the precursor ion having an averaged m/z of 661.87. Several b - and y - product ions are labeled that are consistent with the $[FVKTLTGKTITL+2H]^{2+}$ peptide ion assignment. (C) Overlays of Isotopic distributions for the peptide ion of average m/z 661.87 (blue trace) and the same peptide ion of average m/z 664.54 (red trace) extracted from the respective mass spectrum collected at $t_D \sim 8.0$ ms.

XIDTD of an undeuterated ion having an average m/z of 661.87. The XIDTD shows a dominant ion conformer type with a maximum intensity at ~ 8.0 ms for this given $[M+2H]^{2+}$ peptide ion. To some degree, the XIDTD becomes a spectral-fingerprint that is unique (t_D and intensity) for each peptide sequence. Isobaric ions are also present (e.g., at $t_D \sim 7.4$ ms); however, their low intensities do not allow an unambiguous assignment as separate peptide ions or different gas phase conformers.

Because the resulting proteolytic peptide ions are difficult to identify based solely on precursor m/z , an initial step in the IMS-MS approach is to separate and then identify undeuterated peptides ions using CID. The identification of peptide ions also serves to evaluate pepsin sequence coverage for ubiquitin. For example, ions of average m/z 661.87 are mobility separated and isolated by the LTQ for MS/MS analysis. Figure 4.3B shows the CID fragmentation spectrum obtained upon activation of these ions. Several b - and y - product ions are shown in the Figure 4.3B. Comparisons of these ions with *in-silico* fragments are consistent with an assignment of the precursor ions as $[FVKTLTGKTITL+2H]^{2+}$. This sequence matches the N-terminal end of ubiquitin, encompassing residues F⁴-L¹⁵. Crystal structure[59] comparisons show that residues F⁴-T⁷ form part of a beta-stranded region followed by a turn (residues L⁸-K¹¹) and a second beta stranded region from G¹⁰-L¹⁵. Upon sequence identification it is worthwhile to note that even though FVKTLTGKTITL spans two separate beta-stranded regions separated by a short turn, the XIDTD is indicative of a dominant single gas-phase conformation for the +2 charge state.

4.3.3. Matching XIDTDs Between Undeuterated and Deuterated Datasets.

Once the ions are identified, the high reproducibility of the gas phase separation is used to match mobility profiles generated during labeling studies. Because deuterium retention does not significantly affect the mobility profile (Figure 4.7, see below), XIDTDs of deuterated peptides can be mobility matched to the respective XIDTDs of the undeuterated ions. The top trace in Figure 4.3A (red line) shows the XIDTD for ions of average m/z 664.54 generated during DHX-PD-IMS-MS of labeled ubiquitin. Figure 4.3A shows that the labeled ions of average m/z 664.54 have similar XIDTD features as ions of m/z 661.87, with a single dominant conformation at $t_D \sim 8.0$ ms. It is noteworthy to mention that no dataset alignment was made for the overlays presented in Figure 4.3A. Instead, a bin-by-bin comparison (based on a $200 \mu\text{s}$ t_D -bin width) is used for spectral matching. Additionally, XIDTDs offer the ability to quickly assess deuterium retention by comparing undeuterated and deuterated precursor mass spectra recorded at $t_D \sim 8.0$ ms. Because deuterium incorporation increases the width of the isotopic envelope, reduced peak capacity and increased spectral congestion are problematic in DHX studies.[60] By changing the delay voltage at G2 (Figure 1.1), only select peptide ions having a $t_D \sim 8.0$ ms are examined for improved isotopic evaluation of deuterated peptide ions. Figure 4.3C shows the isotopic distributions for unlabeled and labeled $[\text{FVKTLTGKTITL}+2\text{H}]^{2+}$ ions selected at $t_D \sim 8.0$ ms. The top trace shows ions of m/z 664.54 having a broader isotopic distribution that is shifted in average mass due to deuterium retention relative to unlabeled ions. In this straightforward manner, it can be observed that $[\text{FVKTLTGKTITL}+2\text{H}]^{2+}$ ion retains $\sim 5.3 \pm 0.1$ deuteriums on average. Since the sequence spans structured portions of the protein, the peptide may be expected to show a degree of deuterium retention. Although this method requires an

initial identification analysis of unlabeled peptide ions prior to deuterium studies, we note that LC-DHX-MS/MS studies require the same process.[61] However, the relatively higher reproducibility of the IMS separation allows spectral feature matching (XIDTDs) between unlabeled and labeled samples without the need for dataset alignment.

4.3.4. Overall Per-peptide Deuterium Analysis.

Ubiquitin contains 144 labile hydrogens, where 72 are amide backbone, 69 are found on residue side chains and 3 sites are located on the N- and C-terminus. After DHX for ~30 seconds, the resulting deuterium retention was 50 ± 4 deuteriums determined from the m/z of undigested $[M+6H]^{6+}$ ubiquitin ions. Figure 4.4A shows secondary structural features for ubiquitin atop the primary sequence. These comprise of 5 beta-sheets (residues M^1-L^7 , $G^{10}-L^{15}$, $Q^{40}-F^{45}$, $G^{47}-L^{50}$ and $S^{65}-R^{72}$), an alpha-helix ($I^{23}-E^{34}$) and a 3/10 helix ($L^{56}-Y^{59}$). The corresponding deuterium retention for each identified peptide (MS/MS) is given in Figure 4.4C. In general, most identified peptide ions appear to originate from the terminal ends of ubiquitin. This may be due to increased pepsin accessibility to these regions despite the fast digestion time (~22 seconds). To a certain degree, retention levels appear to map the secondary structural elements of ubiquitin. In Figure 4B, residues M^1-L^{15} , spanning two beta-sheets separated by an unstructured turn retain 7.1 ± 0.3 deuterium after DHX. The next peptide F^4-L^{15} spans a similar portion of the N-terminus having a calculated deuterium level of 5.3 ± 0.1 . Here, F^4-L^{15} differs by 3 residues relative to M^1-L^{15} and suggests ~1.8 deuteriums are retained across M^1-F^4 . Other Top-down DHX-MS/MS studies have shown that residues M^1 and Q^2 display fast intrinsic exchange rates.[62] With this in mind, these results may suggest that deuterium retention is located on I^3 and F^4 .

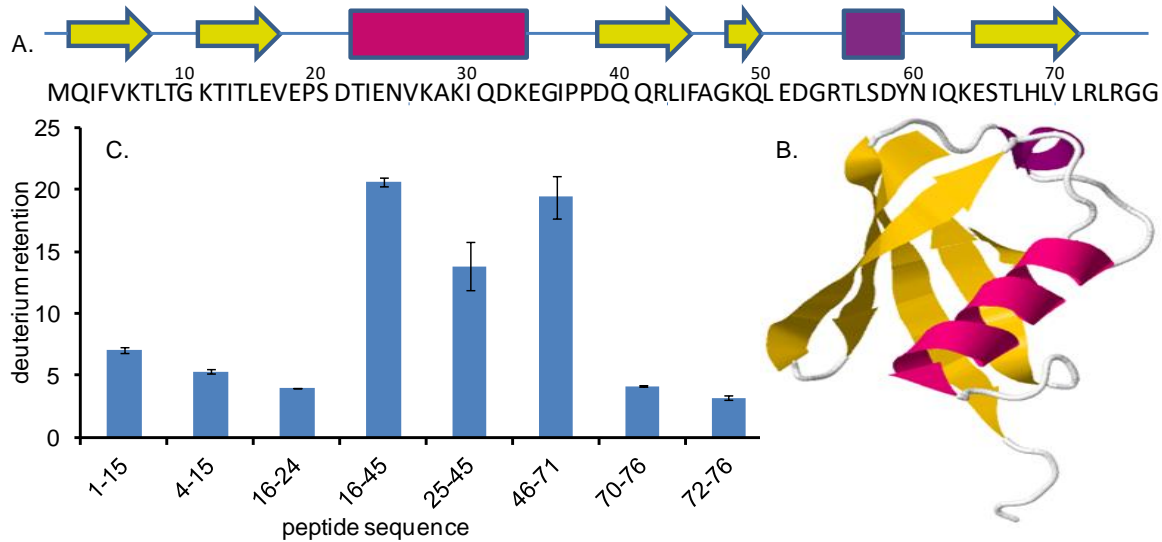


Figure 4.4. (A) Location of the secondary structural elements of ubiquitin atop the respective regions of primary sequence. Secondary structural elements are taken from (B) the ubiquitin crystal structure.[59] Areas in yellow and purple represent beta-strands and helical regions, respectively. Areas shown as blue lines are turns or unstructured regions (C) Total per-peptide deuterium content for MS/MS identified peptide ions (N=3).

Data for other peptide ions can be used to give a general evaluation of protection levels. For example, the peptide E¹⁶-E²⁴ spans a portion of the second beta-strand (E¹⁶-E¹⁸) followed by an unstructured turn (E¹⁸-T²²) and a portion of the peptide that extends into an alpha helix region (I²³-E²⁴). Utilizing the global deuterium level, the peptide has a calculated 0.49 ± 0.06 deuteriums per residue. Comparatively, residues N²⁵-F⁴⁵ extend across the alpha-helix and a third beta-sheet containing more (~ 65 %) residues compared to the E¹⁶-E²⁴ peptide. Here the calculated deuterium retention level per residue is 0.69 ± 0.09 . We note that the pre-residue retention for the former and latter peptides is highly correlated with the fraction of residues observed within regions of secondary structure. Because larger peptides often encompass several areas of secondary structural elements, deuterium location is difficult to interpret. In these cases, such peptides offer targets for MS/MS approaches using ETD.

4.3.5. Scrambling Control and Instrumental Studies.

The control peptide served to elucidate instrumental parameters to mitigate scrambling by optimizing IMS source voltages and tuning the MS transfer voltages (parameters given in Appendix 1). It should be noted that the theoretical backbone amide uptake for the DIIKIIK region should include 6 deuteriums. In this study, the $[M+H]^+$ ions showed a retention of 5.12 ± 0.01 deuteriums, where an additional backbone amide backexchanged (possibly at the backbone site I⁹-K¹⁰). With this assumption, the theoretical 100 % and 0 % scrambling line calculations were modified to include a total uptake of 5.12 and unchanged deuterium retention between c₈ and c₉ ions.

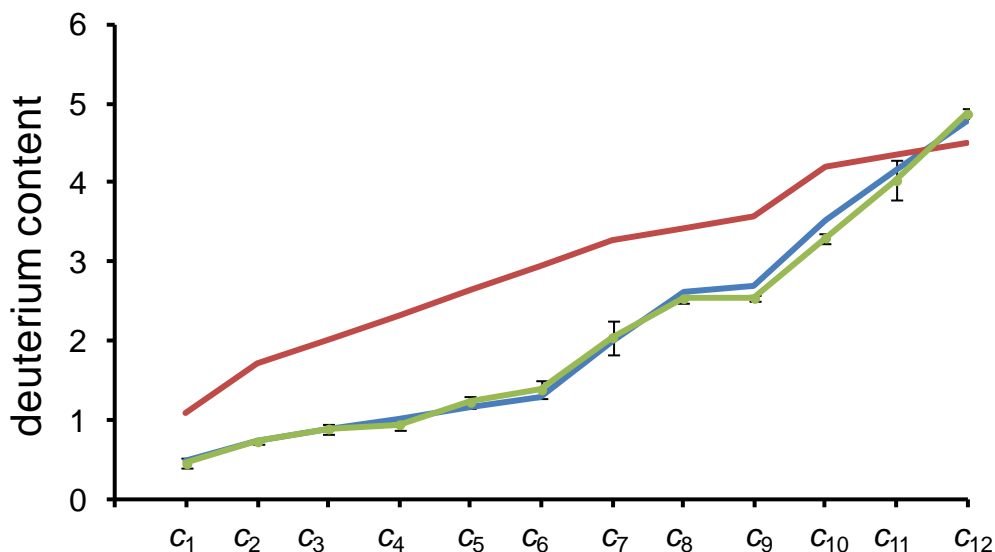


Figure 4.5. Theoretical scrambling traces showing red and blue traces for 100 % (red trace) and 0 % (blue trace) scrambling respectively. The green traces shows c-series ions generated from the DHX-IMS-ETD-MS analysis of KDDDDDIKIIK ($n = 3$) that matches closely to the 0 % scrambling model.

Upon DHX and in the absence of scrambling, the N-terminal region should exchange nearly all deuterium for hydrogen, while the C-terminal region should retain

deuterium at backbone amide locations. In the occurrence of scrambling, an even distribution of deuterium would be observable across all available sites. Figure 4.5 shows the theoretical retention plots generated as outlined by Zehl et al.[28] It can be seen in Figure 4.5 that the experimental data follow closely to the theoretical 0 % scrambling line.

4.3.6. IMS – ETD – MS of Deuterated Peptides for Per – Residue Analysis – Ubiquitin

Labeled [MQIFVKTLTGKTITL+3H]³⁺ ions generated from DHX-PD-IMS-MS measurements were selected for ETD analysis. Deuterium is calculated by subtracting the average mass of a given unlabeled c-ion from the average mass of the respective labeled c-ion. A lack of deuterium retention within a region of primary sequence is indicated by similar deuterium content values for adjacent c-ions (Figure 4.6A). Evaluation of Figure 4.6A shows deuterium retention beginning at I³ and increases to T⁷. However, deuterium content across residues F⁴ -K⁶ does not change by a full deuterium. Comparison to NMR[63] and top-down MS/MS[62] studies have shown strong protection across I³-V⁵. As such, it is instructive to consider the online, bottom up approach with respect to tertiary interactions. Notably, the first beta strand, M¹-T⁷, is situated between the second and fifth beta-strands collectively forming 12 H-bonding networks between M¹-T⁷ (Figure 4.4C).[64] In the case of pepsinolysis yielding the M¹-L¹⁵ ion, this H-bonding network is lost in the peptide and hence a degree of deuterium label may undesirably backexchange. This may be especially true at the interface of the DHX and quenching/digestion region where true quench conditions have not fully equilibrated. In that regard, top-down MS/MS studies appear to map the early N-terminus of ubiquitin with better accuracy.[62, 65]

In contrast to the N-terminal region, other residues appear to correctly map the location of secondary structures. For example, no change in deuterium content is observed for residues L⁸-K¹¹, indicating DHX across this region. Here, residues T⁷-G¹⁰ are consistent with an unstructured turn between the first and second beta-strand (Figure 4.4A). Deuterium content (Figure 4.6A) is seen to increase across residues K¹¹-L¹⁵, which appears to correctly correlate to the location of the second beta-strand beginning at G¹⁰. The relatively large error associated with K¹¹ and T¹² may be indicative of residue location. That is, residues that lay on the fringes of secondary structures are presumably less protected.[5] Generally, the deuterium content profile is consistent with the known crystal structure of ubiquitin (Figure 4.4A and C). Notably, these spectral consistencies further indicate that scrambling is largely mitigated, as under energizing conditions the deuterium label would be statistically randomized throughout the first few residues as well as those contained within the turn.

The online method was also used to evaluate other known structural regions of ubiquitin for comparative purposes. A prominent feature of ubiquitin is an alpha helical region across residues I²³-E³⁴. Using XIDTD spectral feature matching (see above), [NVKAKIQDKEGIPPDQQRLIF+4H]⁴⁺ ions spanning residues N²⁵-F⁴⁵ show a total deuterium retention of 13.8 ± 1.9 (Figure 4.4B) between labeled and unlabeled peptide ions. ETD analysis of deuterated [NVKAKIQDKEGIPPDQQRLIF+4H]⁴⁺ ions permit deuterium retention analysis across much of the alpha helical region and into the third beta-strand. Figure 4.6B shows a similar bar plot as described in Figure 4.6A for

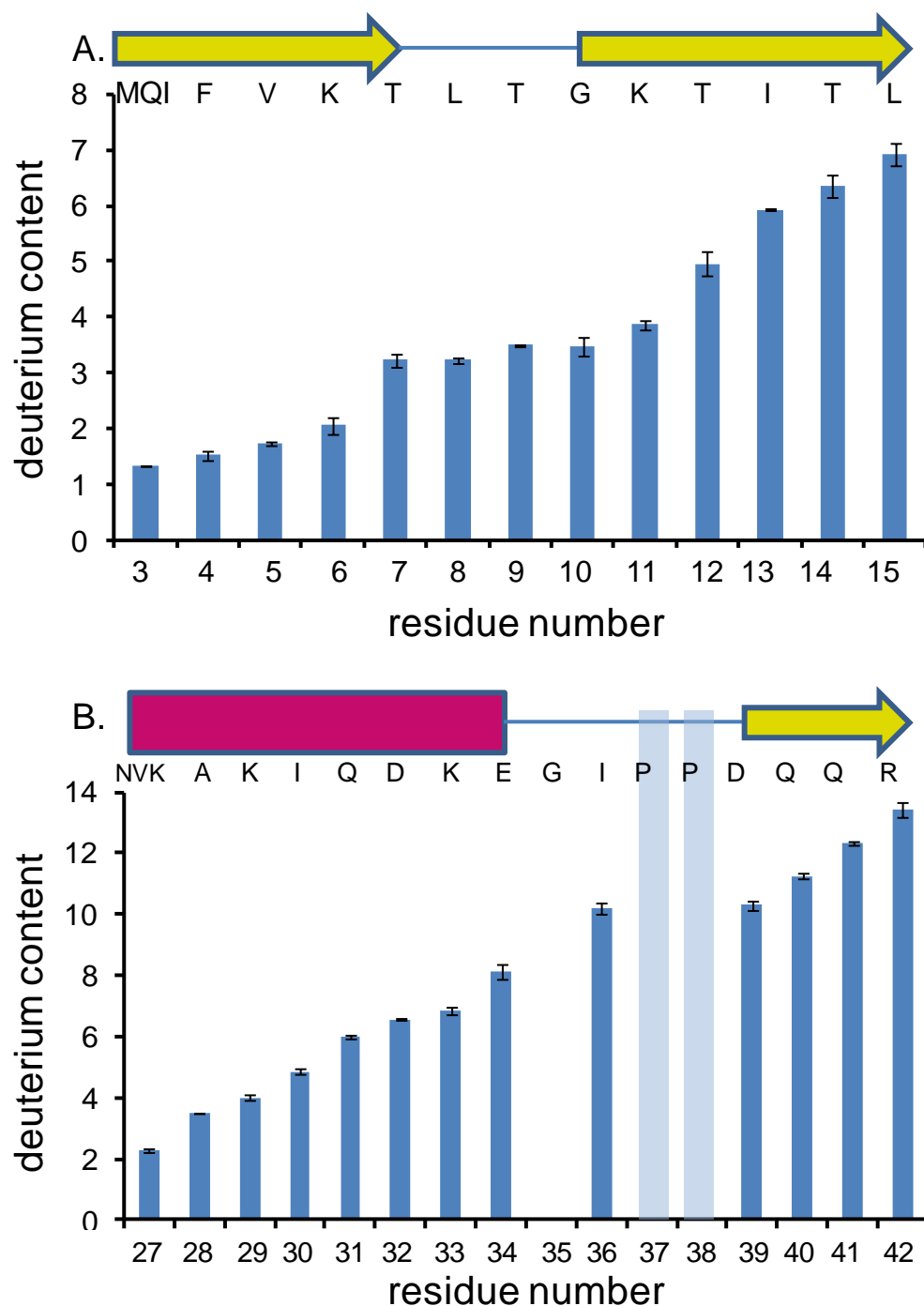


Figure 4.6. (A) Total deuterium content per residue, n , calculated from the c_{n-1} product ions generated by ETD from labeled $[MQIFVKTLTGKTITL+3H]^{3+}$ ions. The N-terminal region of ubiquitin spanning a beta strand (residues M¹-T⁷), turn (L⁸-G¹⁰) and second beta strand from (G¹⁰-L¹⁵) is also shown. (B) Total deuterium retention plot for residues N²⁵-R⁴² generated by ETD of labeled $[NVKAKIQDKEGIPPDQQLIF+4H]^{4+}$ ions. A section of the alpha-helical region and third beta strand across residues N²⁵-E³⁴ and D³⁹-R⁴², respectively, is also shown. The error was calculated from triplicate measurements of fragment ions.

residues N²⁵-R⁴². Overall, an increase in deuterium retention is observed across K²⁷-D³². Residue K³³ appears statistically similar to D³² in deuterium content. Other studies have shown that this residue has a relatively low protection level.[62] Deuterium content is seen to increase toward I³⁶. Interestingly, I³⁶ is located within a turn; however H-bonding throughout the region could permit a degree of deuterium retention.[63] The bar height of I³⁶ is similar in height to D³⁹ suggesting the latter residue exhibits DHX. Residue D³⁹ is located on the periphery of the third beta-strand and may be expected to have a reduced protection level. Residues Q⁴⁰-R⁴² span the third beta strand, where Figure 4.6B shows a successive increase in deuterium content. As before, a higher error appears to be associated with residues that occupy the fringes of secondary structural elements. With respect to the structured regions, these data show similar trends to those studies obtained from top-down DHX-ETD-MS analysis of ubiquitin.[62, 65]

Although the data correlate to results presented previously, they are presented here only as a qualitative comparison. The results should be treated with caution due to some limitations in the DHX experimental setup. For example, it is noted that incubation in D₂O for a minimum of 40 hours will not result in complete deuteration of backbone amide sites. Indeed, experiments for compact [M+6H]⁶⁺ ions demonstrate ~90% deuterium incorporation. Despite the incomplete exchange in, the results shown in Figure 4.6 demonstrate that sufficient incorporation has occurred in order to produce deuterium retention profiles portending exchange protection. Another limitation is that the deuterium content at the ESI needle tip is ~16%. Here we note that the flow rates of the protein sample and the exchange out solution were optimized based on ion signal

levels on our homebuilt instrument which led to these conditions. That said, deuterium uptake simulations (Figure 4.8) demonstrate that any deuterium retention by side-chains due to the ESI solvent composition does not affect the qualitative comparison presented in this proof-of-principle study. With this in mind, improvements in HDX methods will allow more substantial structural determinations to be made in the future.

4.3.7. Reproducibility of the On – Line DHX–PD–IMS–MS System

The online HDX and digestion set-up was reconstructed at the start of each trial (performed on separate days) with fresh back wash and digestion solutions which allowed the assessment of the reproducibility of deuterium retention profiles, pepsin digestion and the IMS-MS measurement. Table 4.1 shows eight identified peptides that were observed within each trial corresponding to 100 % protein sequence coverage. That full sequence coverage was observed in every run provides some context as to the reproducibility of the pepsin digestion for this proof-of-principle study. With regard to peptide deuterium retention between replicates (N = 3), coefficients of variation (CV) ranged from 0.3% to 14.0% for deuterated ions having average m/z values of 387.8 and 613.8, respectively. These respective ions correspond to peptides from the C-terminal tail region ([VLRLRGG+2H]²⁺ ions), and a portion of the alpha-helical region ([NVKAKIQDKEGIPPDQQLIF+4H]⁴⁺ ions).

As noted above, a particular advantage of the IMS measurement is the ability to match ions based on mobility profiles. Figure 4.7 shows the XIDTDs from eight ions observed across all replicates that were highly abundant. The most dominant spectral features observed in each XIDTD are reported as a single t_D value in Table 4.1. Notably, the most intense feature in each XIDTD exhibits the same t_D value in all

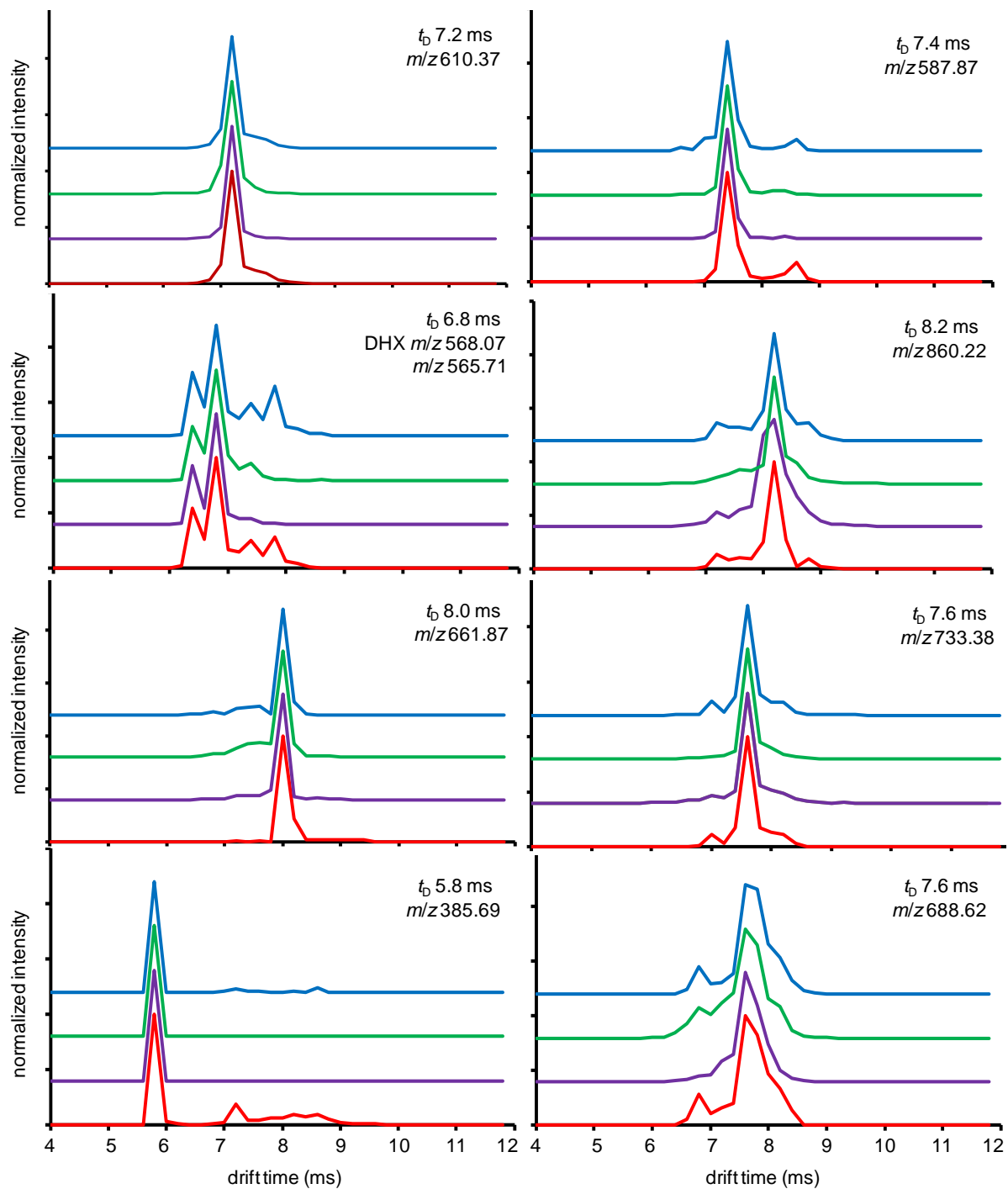


Figure 4.7. t_D distributions for the identified peptide ions presented in Table 4.1. For each panel, the bottom trace represents the t_D distribution obtained for the analysis of the unlabeled protein. The top three traces represent t_D distributions collected on successive days for the labeled protein experiments. The average m/z values of the unlabeled peptide ions and the t_D value of the dominant dataset feature are provided in each panel.

Table 4.1. Reproducibility of the online HDX-PD-IMS-MS system.

m/z^a	Average		Charge State	Ubiquitin Peptide Sequence ^c	DHX trial 1 (² H retention) ^d	DHX Trial 2 (² H retention) ^d	DHX Trial 3 (² H retention) ^d	Average ² H retention	CV ^e	t_D (ms) ^f	NRMSPD ^g
	Deuterated m/z^b										
565.71	568.07		3	1-15	6.96	6.93	7.38	7.09	3.55	6.8	17.2
661.87	664.54		2	4-15	5.24	5.20	5.59	5.35	4.01	8.0	4.7
587.87	590.44		2	5-15	5.48	5.00	5.00	5.16	5.37	7.4	4.1
860.22	865.38		4	16-45	22.00	18.96	21.00	20.65	7.50	8.2	7.8
610.37	613.83		4	25-45	13.20	12.28	16.00	13.83	14.01	7.2	4.3
688.62	692.03		3	26-43	10.74	9.72	10.26	10.24	4.98	7.6	7.4
733.38	738.24		4	46-71	21.32	17.96	19.00	19.43	8.85	7.6	3.3
385.69	387.77		2	70-76	4.16	4.16	4.14	4.15	0.28	5.8	1.2

^aAverage m/z of the assigned IMS-MS dataset feature. All peptides have been assigned using MS/MS analysis.

^bAverage m/z values of the respective assigned peptide ions after deuterium retention.

^cPrimary sequence range corresponding to each assigned peptide ion.

^dPeptide ion deuterium retention as determined by subtracting average m/z values in column a from those in column b and multiplied by z.

^eCoefficients of variation expressed as a percentage.

^fMeasured drift times of the dominant spectral features.

^gNormalized root-mean-square-deviation expressed as a percentage (<http://www.spiderfinancial.com/support/documentation/runxml/reference-manual/descriptive-stat>).

datasets including the unlabeled measurements. Although the high reproducibility of these values does not allow the determination of the error associated with the t_D measurement, a worst case error can be estimated based on the step size of the t_D bins. Therefore, using ± 0.2 ms as the t_D bin size, a single bin shift would result in an estimated maximum error of $\sim 2\%$ to $\sim 4\%$ across the t_D range for the observed ions. As evident from Figure 4.7, the true error is smaller and would only be determined with the use of much smaller t_D bin sizes (significantly greater experimental times). A related concern is the reproducibility of t_D distributions for the various ions. In order to determine the variation between the replicates with respect to XIDTDs, an average normalized root-mean-squared-deviation (NRMSD) and is described by the following equation:

$$\frac{\sqrt{\frac{\sum(y_1 - y_2)^2}{N_t}}}{y_{max} - y_{min}} \times 100\% \quad 4.1$$

In Equation 4.1, y represents the intensity at a given t_D value for the respective (first and second) t_D distributions and N_t is equal to the number of t_D values. It is noted that only y -values spanning the t_D range over which features are observed are used in this calculation. Values obtained from Equation 4.1 are reported as a percentage in Table 4.1. Average NRMSD values ranged from 1.2 % to 17.2 % for deuterated ions having average m/z values of 568.07 and 385.69, respectively. In general, the average NRMSD values are quite low ($< 8\%$) as shown in Table 4.1. This indicates high reproducibility in XIDTD profiles for separate replicate runs. It is again noted that no alignment is performed between datasets.

4.3.8. Assessment of the Effects of ESI Solvent Composition. A challenge of the HDX method employed in this demonstration is the relatively high deuterium content (~16%) within the ESI solvent. To model the effect of ESI solvent deuterium contribution, simulations for 100 ions were performed in which the side chain HDX sites within a peptide exhibit a 0.16 probability of containing a deuterium. The increase to average m/z for each c ion was then determined for the 100 ions. The deuterium contribution from the ESI solvent was then subtracted from the experimental results for the peptides shown in Figure 4.6. Figure 4.8 shows the simulated deuterium retention results for the two peptide regions described above. As evidenced by Figure 4.8, side chain deuterium incorporation from the ESI solvent would not significantly alter the overall deuterium retention profile (compared to Figure 4.6 above). That is, the relative protection as described in the manuscript is still observed. It is noted that the HDX method was largely determined by optimizing the overall peptide ion signal for this proof-of-principle study. In the future, greater effort will be utilized to optimize the HDX method in order to ensure more substantial structural determinations.

4.3.9. Instrumental Implications and Conclusion

This study demonstrates the utility of combining online DHX-PD and IMS-MS/MS for protein structural analysis without the need for condensed-phase separation. The high reproducibility of the linear-field, low-pressure IMS separation allows for XIDTD spectral matching of undeuterated and deuterated ions for rapid identification and deuterium retention calculations for individual peptides. For deuterium labeling studies, the IMS source, drift tube and interface regions are shown to transfer ions without excessive ion heating and deuterium scrambling. When combined with ion trapping and ETD capabilities of the LTQ, the method can reveal elements of protein secondary

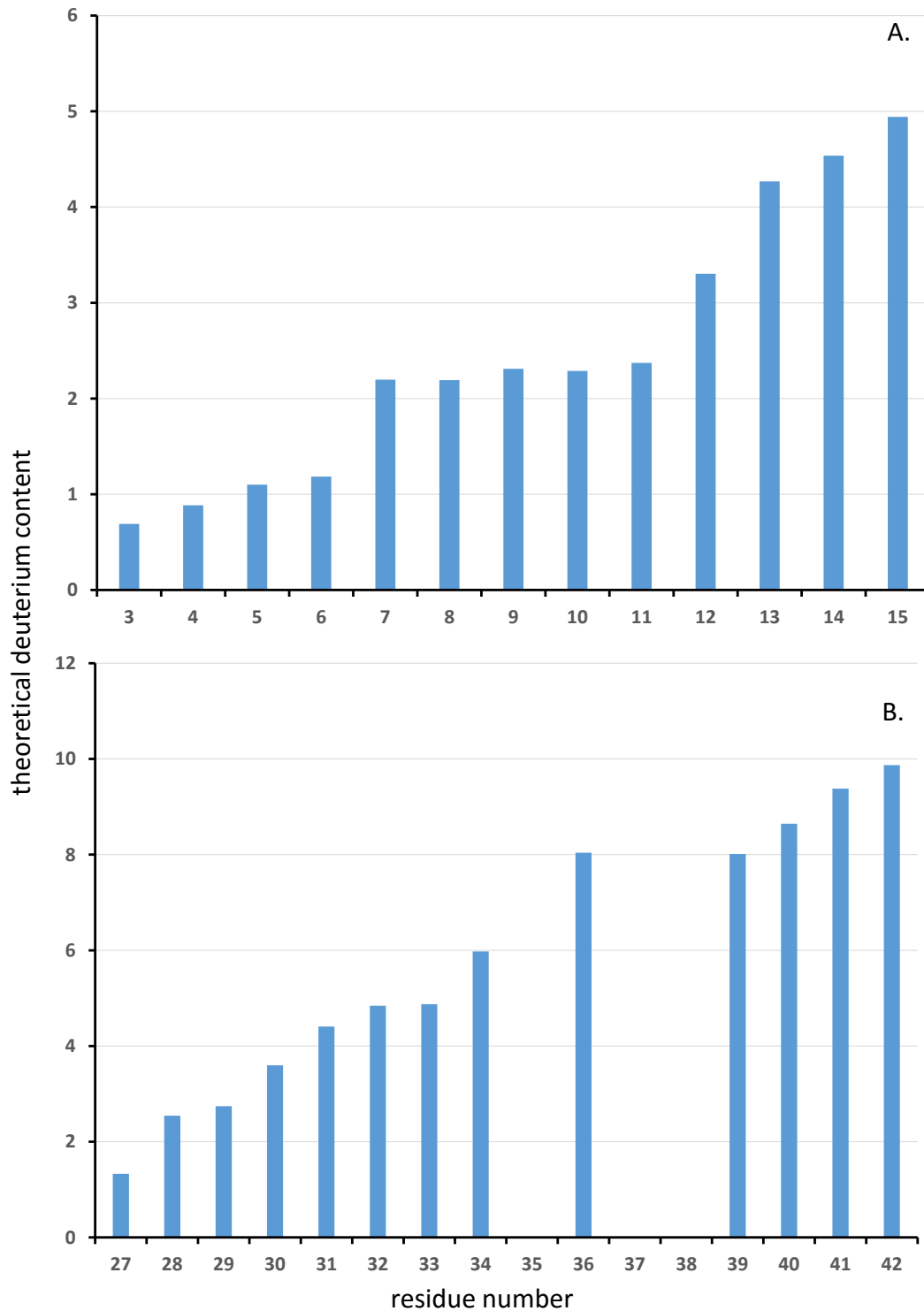


Figure 4.8. (A) Theoretical amide deuterium content per residue, n , calculated from the c_{n-1} product ions generated by ETD from labeled $[MQIFVKTLTGKTITL+3H]^{3+}$ ions. (B) Theoretical amide deuterium content plot obtained upon ETD of labeled $[NVKAKIQDKEGIPPDQQLIF+4H]^{4+}$ ions.

structure at a per-residue level. These data are consistent with the known secondary structural elements of ubiquitin.

Although the data provided here represent that obtained from a proof-of-principle study, it is noteworthy to mention that several improvements are envisioned to yield higher-efficiency structural determinations. Because applying non-activating transfer voltages to the IMS and MS devices in order to mitigate deuterium scrambling results in decreased sensitivity, changes in gas composition and front ion trapping funnel design[66] may improve the signal-to-noise ratio of low intensity ions without causing deuterium scrambling. Admittedly, other studies have used rapid mixing devices[67] to quickly equilibrate DHX and digestion regions prior to MS/MS analysis. This may further prevent the occurrence of undesirable backexchange events. Lastly, the single DHX time point is intended to serve as a rapid structural probe and does not capture protein dynamics as described by time-dependent DHX strategies. As such, the use of varying DHX times with online microfluidic devices[67-69] may yield informative kinetic studies that can be coupled to IMS-ETD-MS analysis.

4.4. References

1. Engen, J.R. and D.L. Smith, *Investigating protein structure and dynamics by hydrogen exchange MS*. *Anal Chem*, 2001. **73**(9): p. 256a-265a.
2. Engen, J.R., et al., *Partial cooperative unfolding in proteins as observed by hydrogen exchange mass spectrometry*. *Int Rev Phys Chem*, 2013. **32**(1): p. 96-127.
3. Wei, H., et al., *Hydrogen/deuterium exchange mass spectrometry for probing higher order structure of protein therapeutics: methodology and applications*. *Drug Discovery Today*, 2014. **19**(1): p. 95-102.
4. Engen, J.R., *Analysis of Protein Conformation and Dynamics by Hydrogen/Deuterium Exchange MS*. *Analytical Chemistry*, 2009. **81**(19): p. 7870-7875.
5. Kaltashov, I.A., C.E. Bobst, and R.R. Abzalimov, *H/D Exchange and Mass Spectrometry in the Studies of Protein Conformation and Dynamics: Is There a Need for a Top-Down Approach?* *Analytical Chemistry*, 2009. **81**(19): p. 7892-7899.
6. Kaltashov, I.A., C.E. Bobst, and R.R. Abzalimov, *Mass spectrometry-based methods to study protein architecture and dynamics*. *Protein Science*, 2013. **22**(5): p. 530-544.
7. Khanal, A., et al., *Pulsed hydrogen/deuterium exchange mass spectrometry for time-resolved membrane protein folding studies*. *J Mass Spectrom*, 2012. **47**(12): p. 1620-6.
8. Konermann, L., J. Pan, and Y.-H. Liu, *Hydrogen exchange mass spectrometry for studying protein structure and dynamics*. *Chemical Society Reviews*, 2011. **40**(3): p. 1224-1234.
9. Shi, X., et al., *Hydrogen Exchange-Mass Spectrometry Measures Stapled Peptide Conformational Dynamics and Predicts Pharmacokinetic Properties*. *Analytical Chemistry*, 2013. **85**(23): p. 11185-11188.
10. Skinner, J.J., et al., *Protein dynamics viewed by hydrogen exchange*. *Protein Sci*, 2012. **21**(7): p. 996-1005.
11. Keppel, T.R., B.A. Howard, and D.D. Weis, *Mapping Unstructured Regions and Synergistic Folding in Intrinsically Disordered Proteins with Amide H/D Exchange Mass Spectrometry*. *Biochemistry*, 2011. **50**(40): p. 8722-8732.
12. Berkowitz, S.A., et al., *Analytical tools for characterizing biopharmaceuticals and the implications for biosimilars*. *Nat Rev Drug Discov*, 2012. **11**(7): p. 527-40.
13. Mayne, L., et al., *Many Overlapping Peptides for Protein Hydrogen Exchange Experiments by the Fragment Separation-Mass Spectrometry Method*. *Journal of The American Society for Mass Spectrometry*, 2011. **22**(11): p. 1898-1905.
14. Zhang, H.M., et al., *Fast reversed-phase liquid chromatography to reduce back exchange and increase throughput in H/D exchange monitored by FT-ICR mass spectrometry*. *J Am Soc Mass Spectrom*, 2009. **20**(3): p. 520-4.
15. Jones, L.M., et al., *Online, High-Pressure Digestion System for Protein Characterization by Hydrogen/Deuterium Exchange and Mass Spectrometry*. *Analytical Chemistry*, 2010. **82**(4): p. 1171-1174.
16. Zhang, H.-M., et al., *Fast Reversed-Phase Liquid Chromatography to Reduce Back Exchange and Increase Throughput in H/D Exchange Monitored by FT-ICR Mass Spectrometry*. *Journal of the American Society for Mass Spectrometry*, 2009. **20**(3): p. 520-524.
17. Sheff, J., M. Rey, and D. Schriemer, *Peptide–Column Interactions and Their Influence on Back Exchange Rates in Hydrogen/Deuterium Exchange-MS*. *Journal of The American Society for Mass Spectrometry*, 2013. **24**(7): p. 1006-1015.
18. Wu, Y., S. Kaveti, and J.R. Engen, *Extensive deuterium back-exchange in certain immobilized pepsin columns used for H/D exchange mass spectrometry*. *Analytical Chemistry*, 2006. **78**(5): p. 1719-1723.

19. Venable, J.D., W. Scuba, and A. Brock, *Feature Based Retention Time Alignment for Improved HDX MS Analysis*. Journal of the American Society for Mass Spectrometry, 2013. **24**(4): p. 642-645.
20. Rand, K., et al., *ETD in a Traveling Wave Ion Guide at Tuned Z-Spray Ion Source Conditions Allows for Site-Specific Hydrogen/Deuterium Exchange Measurements*. Journal of The American Society for Mass Spectrometry, 2011. **22**(10): p. 1784-1793.
21. Iacob, R.E., J.P. Murphy, and J.R. Engen, *Ion mobility adds an additional dimension to mass spectrometric analysis of solution-phase hydrogen/deuterium exchange*. Rapid Communications in Mass Spectrometry, 2008. **22**(18): p. 2898-2904.
22. May, J.C. and J.A. McLean, *Ion Mobility-Mass Spectrometry: Time-Dispersive Instrumentation*. Analytical Chemistry, 2014.
23. Lermyte, F., et al., *ETD Allows for Native Surface Mapping of a 150 kDa Noncovalent Complex on a Commercial Q-TWIMS-TOF Instrument*. Journal of The American Society for Mass Spectrometry, 2014. **25**(3): p. 343-350.
24. Williams, J.P., et al., *Identifying drug metallation sites on peptides using electron transfer dissociation (ETD), collision induced dissociation (CID) and ion mobility-mass spectrometry (IM-MS)*. Chemical Communications, 2010. **46**(30): p. 5458-5460.
25. Merenbloom, S.I., T.G. Flick, and E.R. Williams, *How hot are your ions in TWAVE ion mobility spectrometry?* J Am Soc Mass Spectrom, 2012. **23**(3): p. 553-62.
26. Morsa, D., V.r. Gabelica, and E. De Pauw, *Effective Temperature of Ions in Traveling Wave Ion Mobility Spectrometry*. Analytical Chemistry, 2011. **83**(14): p. 5775-5782.
27. Shvartsburg, A.A. and R.D. Smith, *Fundamentals of traveling wave ion mobility spectrometry*. Anal Chem, 2008. **80**(24): p. 9689-99.
28. Zehl, M., et al., *Electron Transfer Dissociation Facilitates the Measurement of Deuterium Incorporation into Selectively Labeled Peptides with Single Residue Resolution*. Journal of the American Chemical Society, 2008. **130**(51): p. 17453-17459.
29. Rand, K.D., M. Zehl, and T.J. Jorgensen, *Measuring the hydrogen/deuterium exchange of proteins at high spatial resolution by mass spectrometry: overcoming gas-phase hydrogen/deuterium scrambling*. Acc Chem Res, 2014. **47**(10): p. 3018-27.
30. Pan, J., et al., *Structure and dynamics of small soluble A β (1-40) oligomers studied by top-down hydrogen exchange mass spectrometry*. Biochemistry, 2012. **51**(17): p. 3694-703.
31. Abzalimov, R.R., C.E. Bobst, and I.A. Kaltashov, *A New Approach to Measuring Protein Backbone Protection with High Spatial Resolution Using H/D Exchange and Electron Capture Dissociation*. Analytical Chemistry, 2013. **85**(19): p. 9173-9180.
32. Lee, S., et al., *Extracted fragment ion mobility distributions: A new method for complex mixture analysis*. International Journal of Mass Spectrometry, 2012. **309**: p. 154-160.
33. Arndt, J.R., et al., *Lysine residues in the N-terminal huntingtin amphipathic α -helix play a key role in peptide aggregation*. Journal of Mass Spectrometry, 2015. **50**(1): p. 117-126.
34. Counterman, A.E., et al., *Formation of peptide aggregates during ESI: Size, charge, composition, and contributions to noise*. Journal of the American Society for Mass Spectrometry, 2001. **12**(9): p. 1020-1035.
35. Mesleh, M.F., et al., *Structural Information from Ion Mobility Measurements: Effects of the Long-Range Potential*. The Journal of Physical Chemistry, 1996. **100**(40): p. 16082-16086.
36. Revercomb, H.E. and E.A. Mason, *THEORY OF PLASMA CHROMATOGRAPHY GASEOUS ELECTROPHORESIS - REVIEW*. Analytical Chemistry, 1975. **47**(7): p. 970-983.
37. Shvartsburg, A.A. and M.F. Jarrold, *An exact hard-spheres scattering model for the mobilities of polyatomic ions*. Chemical Physics Letters, 1996. **261**(1-2): p. 86-91.

38. Wyttenbach, T., et al., *Effect of the long-range potential on ion mobility measurements*. Journal of the American Society for Mass Spectrometry, 1997. **8**(3): p. 275-282.
39. Blase, R.C., et al., *Increased ion transmission in IMS: A high resolution, periodic-focusing DC ion guide ion mobility spectrometer*. International Journal of Mass Spectrometry, 2011. **301**(1-3): p. 166-173.
40. Clemmer, D.E., R.R. Hudgins, and M.F. Jarrold, *NAKED PROTEIN CONFORMATIONS - CYTOCHROME-C IN THE GAS-PHASE*. Journal of the American Chemical Society, 1995. **117**(40): p. 10141-10142.
41. Hoaglund, C.S., et al., *Three-dimensional ion mobility TOFMS analysis of electrosprayed biomolecules*. Analytical Chemistry, 1998. **70**(11): p. 2236-2242.
42. Kurulugama, R.T., et al., *Overtone Mobility Spectrometry: Part 1. Experimental Observations*. Journal of the American Society for Mass Spectrometry, 2009. **20**(5): p. 729-737.
43. Merenbloom, S.I., et al., *High-resolution ion cyclotron mobility spectrometry*. Anal Chem, 2009. **81**(4): p. 1482-7.
44. von Helden, G., T. Wyttenbach, and M.T. Bowers, *Conformation of macromolecules in the gas phase: use of matrix-assisted laser desorption methods in ion chromatography*. Science, 1995. **267**(5203): p. 1483-5.
45. Wittmer, D., et al., *ELECTROSPRAY-IONIZATION ION MOBILITY SPECTROMETRY*. Analytical Chemistry, 1994. **66**(14): p. 2348-2355.
46. Bohrer, B.C., et al., *Biomolecule Analysis by Ion Mobility Spectrometry*, in *Annual Review of Analytical Chemistry*. 2008. p. 293-327.
47. Clemmer, D.E. and M.F. Jarrold, *Ion mobility measurements and their applications to clusters and biomolecules*. Journal of Mass Spectrometry, 1997. **32**(6): p. 577-592.
48. Collins, D.C. and M.L. Lee, *Developments in ion mobility spectrometry-mass spectrometry*. Analytical and Bioanalytical Chemistry, 2002. **372**(1): p. 66-73.
49. Kurulugama, R.T., et al., *Development of a high-throughput IMS-IMS-MS approach for analyzing mixtures of biomolecules*. Journal of Proteomics, 2008. **71**(3): p. 318-331.
50. Shaffer, S.A., et al., *A novel ion funnel for focusing ions at elevated pressure using electrospray ionization mass spectrometry*. Rapid Communications in Mass Spectrometry, 1997. **11**(16): p. 1813-1817.
51. StLouis, R.H. and H.H. Hill, *ION MOBILITY SPECTROMETRY IN ANALYTICAL-CHEMISTRY*. Critical Reviews in Analytical Chemistry, 1990. **21**(5): p. 321-355.
52. Palumbo, A.M., et al., *Tandem mass spectrometry strategies for phosphoproteome analysis*. Mass Spectrom Rev, 2011. **30**(4): p. 600-25.
53. Palumbo, A.M., J.J. Tepe, and G.E. Reid, *Mechanistic insights into the multistage gas-phase fragmentation behavior of phosphoserine- and phosphothreonine-containing peptides*. J Proteome Res, 2008. **7**(2): p. 771-9.
54. Ruotolo, B.T., et al., *Analysis of phosphorylated peptides by ion mobility-mass spectrometry*. Anal Chem, 2004. **76**(22): p. 6727-33.
55. Ruotolo, B.T., et al., *Distinguishing between phosphorylated and nonphosphorylated peptides with ion mobility-mass spectrometry*. J Proteome Res, 2002. **1**(4): p. 303-6.
56. Donohoe, G.C., et al., *A New Ion Mobility-Linear Ion Trap Instrument for Complex Mixture Analysis*. Analytical Chemistry, 2014. **86**(16): p. 8121-8128.
57. Zucker, S.M., et al., *An ion mobility/ion trap/photodissociation instrument for characterization of ion structure*. J Am Soc Mass Spectrom, 2011. **22**(9): p. 1477-85.
58. Baker, E.S., et al., *Ion mobility spectrometry-mass spectrometry performance using electrodynamic ion funnels and elevated drift gas pressures*. J Am Soc Mass Spectrom, 2007. **18**(7): p. 1176-87.

59. Vijay-Kumar, S., C.E. Bugg, and W.J. Cook, *Structure of ubiquitin refined at 1.8 Å resolution*. J Mol Biol, 1987. **194**(3): p. 531-44.
60. Bou-Assaf, G.M., et al., *Advantages of Isotopic Depletion of Proteins for Hydrogen/Deuterium Exchange Experiments Monitored by Mass Spectrometry*. Analytical Chemistry, 2010. **82**(8): p. 3293-3299.
61. Konermann, L., S. Vahidi, and M.A. Sowole, *Mass Spectrometry Methods for Studying Structure and Dynamics of Biological Macromolecules*. Analytical Chemistry, 2013. **86**(1): p. 213-232.
62. Sterling, H.J. and E.R. Williams, *Real-Time Hydrogen/Deuterium Exchange Kinetics via Supercharged Electrospray Ionization Tandem Mass Spectrometry*. Analytical Chemistry, 2010. **82**(21): p. 9050-9057.
63. Johnson, E.C., et al., *Solution structure and dynamics of a designed hydrophobic core variant of ubiquitin*. Structure, 1999. **7**(8): p. 967-976.
64. Berman, H.M., et al., *The Protein Data Bank*. Nucleic Acids Research, 2000. **28**(1): p. 235-242.
65. Pan, J., et al., *Electron Capture Dissociation of Electrosprayed Protein Ions for Spatially Resolved Hydrogen Exchange Measurements*. Journal of the American Chemical Society, 2008. **130**(35): p. 11574-11575.
66. Ibrahim, Y.M., et al., *Improving Ion Mobility Measurement Sensitivity by Utilizing Helium in an Ion Funnel Trap*. Analytical Chemistry, 2014. **86**(11): p. 5295-5299.
67. Keppel, T.R. and D.D. Weis, *Analysis of Disordered Proteins Using a Simple Apparatus for Millisecond Quench-Flow H/D Exchange*. Analytical Chemistry, 2013. **85**(10): p. 5161-5168.
68. Rob, T. and D. Wilson, *A versatile microfluidic chip for millisecond time-scale kinetic studies by electrospray mass spectrometry*. Journal of the American Society for Mass Spectrometry, 2009. **20**(1): p. 124-130.
69. Wilson, D.J. and L. Konermann, *A capillary mixer with adjustable reaction chamber volume for millisecond time-resolved studies by electrospray mass spectrometry*. Anal Chem, 2003. **75**(23): p. 6408-14.

5. Helium Charge Transfer Dissociation Combined with Deuterium Hydrogen Exchange Mass Spectrometry

5.1 Introduction: Fragmentation Techniques and Hydrogen Deuterium Scrambling

Recent advances in tandem mass spectrometry (MS/MS) present techniques that are well suited to site-specific (per-residue) deuterium retention using both top-down[1-3] and bottom-up[4, 5] approaches. One important aspect of per-residue deuterium measurement is mitigating hydrogen/deuterium (HD)-scrambling. HD-scrambling occurs from the collisional-heating of peptide or protein ions that result in mobile protons.[6] Because protons can be mobilized before bond dissociation, the final location of the protons is different than starting location on the precursor ion. This becomes problematic during per-residue deuterium measurements attempting to assess protein structure. It is also important to note that HD-scrambling can occur as a result of 'harsh' declustering conditions applied to the ion optics of the mass spectrometer and ion isolation due to broadband excitation.[7] Therefore special attention must also be given to and instrumental parameters to insure ion are not activate prior to fragmentation.

Electron based fragmentation processes like ECD and ETD have been used for per-residue deuterium measurements without HD-scrambling.[5, 8-11] One limitation of ECD/ETD is the difficulty in fragmenting peptides exhibiting charge states $\geq +2$. With this in mind, it would be highly desirable to have access to a fragmentation technique that could proceed via odd electron or radical-induced pathways for low charge state precursors without proton mobilization.

Recently, a new MS/MS technique known as helium cation-charge transfer dissociation (He-CTD) of peptide and protein ions has been demonstrated using either helium cations[12] or cations from an air plasma.[13] Gaseous ions emitted during He-CTD achieve kinetic energies sufficient to overcome the Columbic barrier with biomolecular cations. He-CTD product ions are seen to result from both vibrationally- and radically-driven dissociation pathways that resemble those formed from both CID and ECD/ETD processes.[12, 13] Of particular interest is the ability of He-CTD to produce radical fragmentation regardless of precursor ion charge state.

In the present study, the combination of DHX with He-CTD-MS is explored. Because HD-scrambling is a significant concern, a model peptide specifically designed to determine HD-scrambling[7] is used for a theoretical and experimental scrambling evaluation. These experiments are directly compared to ETD experiments, which were obtained under non-scrambling conditions. Separate experiments used an online and continuous DHX system coupled with pepsin digestion (PD) and simultaneous DHX quenching for structural elucidation of deuterated ubiquitin. Using the non-scrambling conditions found with the model peptide, DHX-He-CTD-MS results are presented in a proof-of-concept, per-residue structural evaluation of the N-terminal region (residues 1-15) in ubiquitin. Since the N-terminal region contains both the fastest and slowest exchanging residues in the protein, an exchange-out time of ~50 seconds was sufficient to exchange unstructured areas while retaining deuterium on structured areas.

5.2 Methods and Materials

Ubiquitin (bovine erythrocytes, 98%) and lyophilized pepsin (porcine, 3200-4500 units/mg protein), Deuterium oxide (99.9%) and glacial acetic acid (99 %) were

purchased from Sigma-Aldrich (St. Louis, MO). The model peptide (MP) KKDDDDDIKIIK (90.6%) was purchased from Genscript (Piscataway, NJ, USA). Proteins and peptides were used without further purification and all other reagents were MS grade or the equivalent.

5.2.1. Sample Preparation

Ubiquitin (1.0 mg) was added to 1.0 mL of D₂O (99.9 %). The solution was incubated at 37 °C for 10 days and left for more than 3 weeks at room temperature. This method allowed for ~98 % deuterium incorporation of ubiquitin. Pepsin solutions were prepared by adding lyophilized powder (1.0 mg) to 1.0 mL acidified 18 MΩ H₂O (8% glacial acetic acid v:v) at pH ~ 2.0.

5.2.2. Modified Instrument

A schematic of the online system is presented in Figure 5.1 and has been previously described.[14] Briefly, the DHX reaction followed by quenching and simultaneous digestion was performed using two micro-Tee assemblies (Upchurch Scientific Inc, Oak Harbor, Wa) connected with PEEK capillary (1588 μm o.d. × 152 μm i.d). Using a 500-μL syringe (Hamilton, Reno, NV, USA), a high precision syringe pumps (KD scientific Holliston, MA, USA) delivered the deuterated ubiquitin solution to the first micro-Tee assembly at a flow rate of 0.60 μL·min⁻¹. The instrument-equipped syringe pump delivered the room temperature exchange-out solution at a flow rate of 10.0 μL·min⁻¹. DHX of deuterated ubiquitin proceeded for ~ 47.4 seconds over a capillary length of 50.8 cm. A third 500-μL syringe containing ice-cooled pepsin solution (pH ~2.0) was introduced by a KD scientific syringe pump to a second micro-Tee assembly at a flow rate of 0.80 μL·min⁻¹. DHX quenching and simultaneous protein digestion was

performed over a capillary length of 25.4 cm (~ 30 sec digestion time) and interfaced directly to the commercial ESI source. Resulting peptic peptides were electrosprayed into the MS instrument using a bias voltage of 4.0 kV at a combined flow rate of 11.40 $\mu\text{L} \cdot \text{min}^{-1}$.

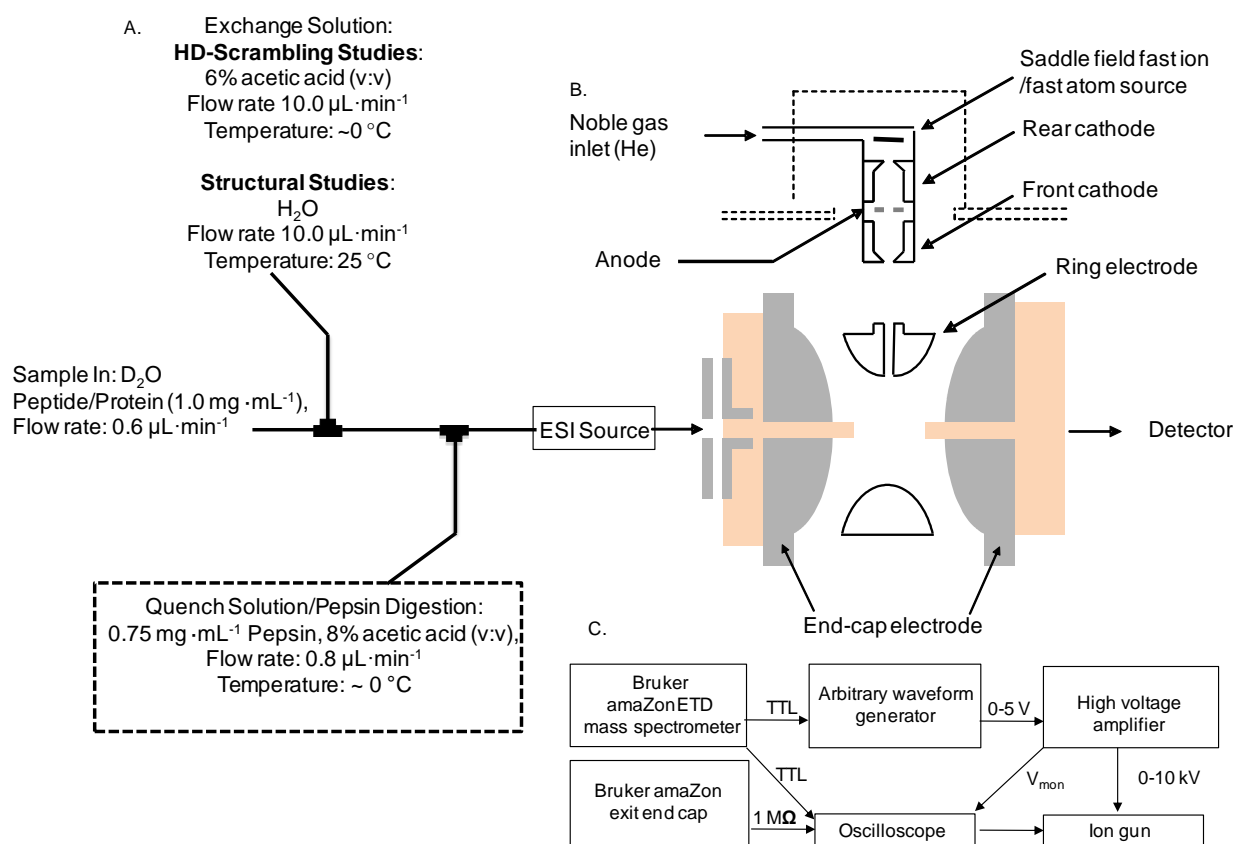


Figure 5.1. Schematic representation showing (A) the microfluidic online HDX system used in HD-scrambling and structural studies. This system was directly interfaced to the commercial Bruker electrospray ionization source. The dashed-boxed region encompassing the syringe containing the pepsin solution was removed for HD-scrambling studies (B) Modified quadrupole ion trap showing the location of the saddle field ion source for the generation of He⁺ cations. (C) The electronic components for pulsed operation during He-CTD-MS experiments.

5.2.3. HD – Scrambling Peptide

For the evaluation of H/D scrambling, the model peptide KKDDDDDIKIIK (1.0 mg) was added to 1.0 mL of D₂O (99.9 %) and allowed to incubate for ~24 hours at

25°C. An online time-resolved system for continuous DHX was used for scrambling studies. Briefly, a 500- μ L syringe (Hamilton, Reno, NV, USA) containing the deuterated peptide solution was delivered to a micro-Tee assembly using a high precision syringe pump (KD scientific Holliston, MA, USA) at a flow rate of 0.20 μ L \cdot min⁻¹. Using the instrument equipped syringe pump, acidified 18 M Ω H₂O (6 % acetic acid, pH ~ 2.5) was introduced to the second port of micro-Tee at 10.00 μ L \cdot min⁻¹. The DHX reaction of deuterated peptide occurred over a length of 10.1 cm resulting in an exchange-out time of ~ 11 seconds. The source region was heated to 100 °C and the capillary exit potential reduced to 50 V. A detailed list of instrumental parameters to mitigate HD-scrambling is given in the Supporting Information section. Instrumental parameters for ubiquitin deuteration studies were selected based upon the peptide exhibiting a 0 % scrambling trend (see Supporting Information) during ETD experiments (see below).

5.2.4. Mass Spectrometry Measurements and Parameters

Full mass spectra were collected for all ions by setting the mass analyzer scan parameters over a m/z range of 150 to 2000 and setting the ion charge control (ICC) to a target of 2×10^5 . Precursor mass spectra were collected over 1.0 minute with 10 μ scans/scan. A full list of instrumental parameters to mitigate HD-scrambling can be found in Appendix 2.

5.2.4.1. ETD Measurements

ETD analysis was conducted on isolated precursor ions using a selection window of ± 10 Da around the selected centroid m/z value. The ICC was disabled and a trap injection time of 1.0 ms was used. ETD of precursor ions was enabled by the introduction of fluoranthene radicals into the QIT for 40 ms. ETD Fragmentation spectra

were collected for 1.0 minute in order to adequately sample the resulting isotopic distribution of product ions.

5.2.4.2. He-CTD Measurements.

He-CTD measurements were similar to ETD measurements. Briefly, precursor ions were selected using ± 10 Da window around the centroid m/z value. The ICC was disabled and a quadrupole ion trap (QIT) injection time of 50 ms was used. A variable leak-valve was used to control the flow of He gas (1.40×10^{-5} mbar) through a saddle field source (Figure 5.1). He-CTD fragmentation was performed by introducing 6 keV helium cations into the QIT in square-wave pulse that was synchronized with the part of the scan cycle normally reserved for CID. The CID amplitude was set to zero to simply store the ions at the selected low mass cut-off value (e.g. m/z 150) during exposure to the helium cations. For the model peptide and HD-scrambling studies, product ion spectra were collected for 2 minutes with the He⁺ beam enabled followed by background collection for 2 minutes with the He⁺ beam disabled. For ubiquitin studies, these respective collections periods were 3 minutes and 2 minutes. Precursor and product ion spectra were signal averaged and background subtracted prior to processing.

5.2.5. Per-Residue Deuterium Measurements.

Mass spectra from both ETD and He-CTD were exported as ASCII files and converted into text files (.TXT). The text files were constructed as two-column arrays of m/z and intensity values. Using software developed in-house, deuterium retention was calculated from the deconvoluted product ion spectra by weighting c- or a-ion isotopologues according to their intensity values. The software creates a text output file

containing the average m/z values. Average m/z values for the unlabeled fragment ions are subtracted from those of the labeled fragment ions of the same charge state. This mass difference is reported as the amount of total deuterium retention for each detectable fragment ion.

5.3 Results and Discussion

5.3.1. Peptide Control Studies and HD – Scrambling Evaluation

To correctly evaluate the ability of He-CTD to retain a deuterium label, studies employing the model peptide (KKDDDDDIKIIK) first used ETD experiments to determine non-activating instrumental parameters (i.e., source conditions, transfer optics potentials, and rf amplitudes for ion trapping and isolation). Although the model peptide may not produce any high-order secondary structure, the peptide was designed to contain a fast exchanging *N*-terminal region and a slow exchanging *C*-terminal portion. That is, under DHX quench conditions, backbone amide residues including D⁷ through I¹² retain their deuterium label for several minutes.[10] Table 5.1 shows the theoretical limits (100% and 0%) for scrambling values calculated for the *c*-ion series of the model peptide as outlined by Zehl, et. al.[7] After online DHX-ETD-MS of [M+3H]³⁺ peptide ions, a comparison of experimental product ions resulting from ETD match closely to the theoretical 0% scrambling trend. This trend shows very little deuterium retention change across residues K¹ through D⁶, followed by a sharp increase in deuteration level with each successive *c*-ion. Comparatively, under activating conditions this trend is not observed and product ions would show higher levels of deuterium content.[7] Such a case would resemble that of the 100% scrambling trend (Table 5.1).

5.3.1.1. He-CTD HD-Scrambling Analysis

Figure 5.2A shows the He-CTD spectrum for the unlabeled $[M+3H]^{3+}$ peptide ions. This spectrum shows that observable *c ions* sequence much of the model peptide. Here, it is noted that sequence coverage spans c_5 through c_{12} , which covers a portion of the N-terminal region expected to not retain deuterium during DHX experiments. As discussed above, DHX-ETD-MS of the $[M+3H]^{3+}$ ions from the deuterated peptide has been used as a control to assess parameters that mitigate deuterium scrambling before proceeding with He-CTD and structural analyses. Pertinent parameters included a capillary exit of 50 V, Funnel 1 and 2 rf amplitudes (peak-to-peak) of 130 V and a trap drive of 40%. A complete list of instrumental parameters can be found in Appendix 2.

Table 5.1. HD-Scrambling analysis of $[KKDDDDDIKIK+3H]^{3+}$ *c*-ions generated from ETD-MS and He-CTD-MS

Residue ^a	Residue number	Theoretical 100 % Scrambling ^c	Theoretical 0 % scrambling ^c	ETD Experimental ^d	ETD CV ^e	Experimental (<i>c</i> -ion) ^d	CTD CV (<i>c</i> -ion) ^e
K	1	na	na	nd	na	na	na
K	2	1.32	0.61	nd	na	nd	na
D	3	2.07	0.96	0.92	5.6	nd	na
D	4	2.44	1.14	1.22	5.3	nd	na
D	5	2.82	1.31	1.33	3.2	nd	na
D	6	3.19	1.49	1.51	4.8	1.48	6.4
D	7	3.57	1.66	1.58	6.1	1.81	20.2
I	8	3.95	2.39	2.46	3.3	2.78	4.5
I	9	4.13	3.03	3.18	4.1	3.12	4.9
K	10	4.32	3.67	3.57	2.7	3.75	2.9
I	11	5.07	4.57	4.58	3.2	4.82	3.2
I	12	5.26	5.21	5.57	1.5	5.51	1.2
K	13	5.45	6.00	6.22	0.4	5.97	0.7

- Primary Sequence from model peptide (KKDDDDDIKIK).
- Assigned amide backbone number from the model peptide (KKDDDDDIKIK). Note the first amide heteroatom begins at residue 2.
- Theoretical deuterium content values for *c*-ions generated from ETD-MS of $[KKDDDDDIKIK+3H]^{3+}$ precursor ions.
- Average experimental deuterium content obtained by subtracting the average *m/z* of the labeled fragment ion from that of the unlabeled fragment ion.
- Coefficient of variation expressed as a percentage.
- Average experimental deuterium content obtained by subtracting the average *m/z* of the labeled fragment ion from that of the unlabeled fragment ion.

~

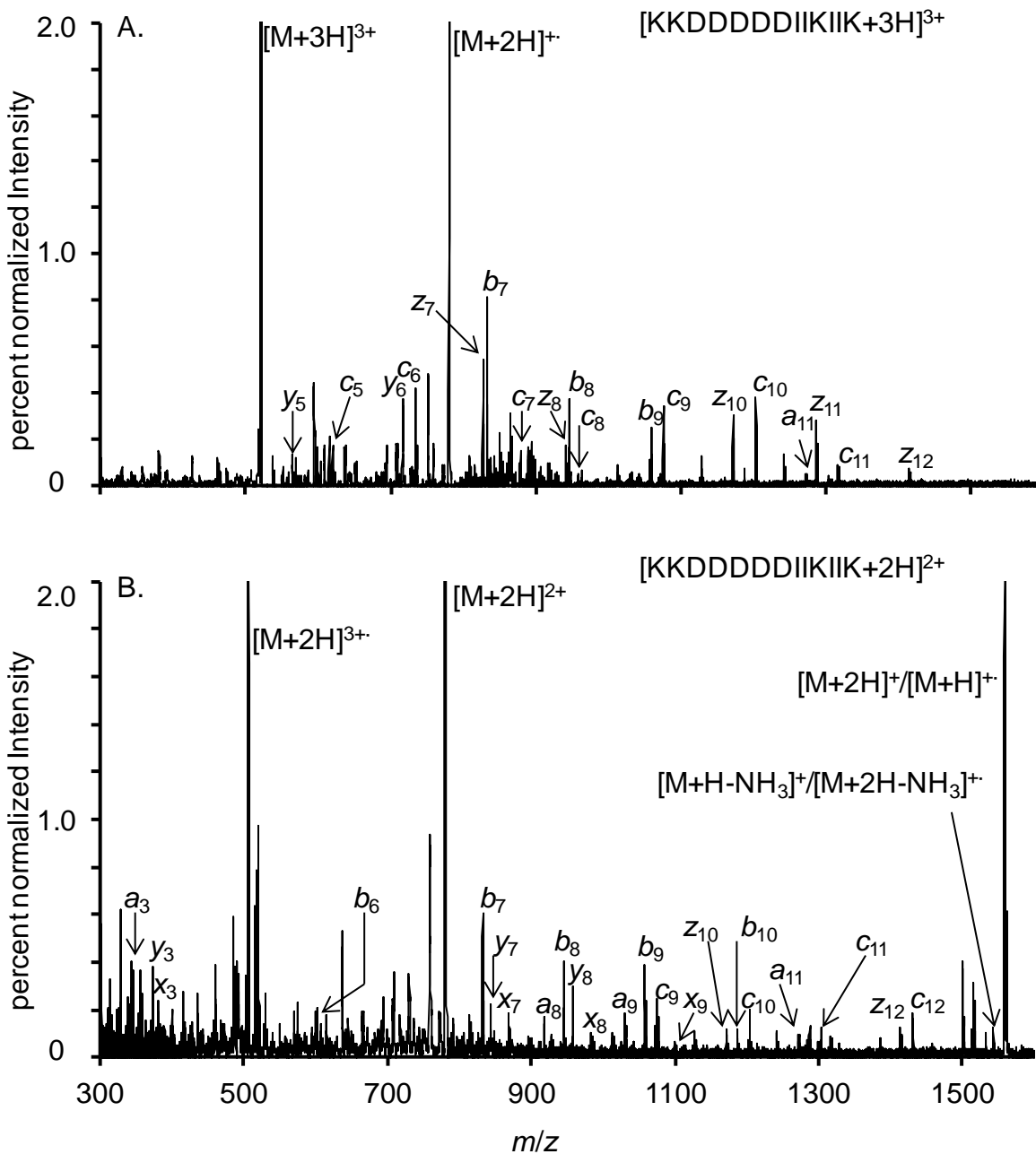


Figure 5.2. (A) He-CTD-MS spectrum of $[KKDDDDDDIIKIIK+3H]^{3+}$ precursor ions. Several product ions resulting from various fragmentation pathways are labeled. (B) MS-CTD spectrum of $[KKDDDDDDIIKIIK+2H]^{2+}$ precursor ions. Identified product ions resulting from CTD are labeled. Both Figure panels A and B have been normalized to respective precursor ion intensities and displayed as a percentage.

produced Table 5.1 gives per-residue deuterium retention for the deuterated model peptide observed upon DHX-He-CTD-MS of the $[M+3H]^{3+}$ peptide ions. Identified *c* and *a* ions resulting from He-CTD of the precursor ions were selected for direct comparisons to the theoretical HD-scrambling values (Table 5.1). Here (Table 5.1), product ions generated by He-CTD appear to match the 0% scrambling values established during the ETD control analysis. In general, coefficients of variation are less than 20% for replicate (N = 3) He-CTD trials. Similar to ETD studies, He-CTD product ions (Table 5.1) show that the deuteration content assessment begins at a relatively low level (c_5 and a_3 ions).

5.3.1. He – CTD Mechanistic Insights for *c* – ions

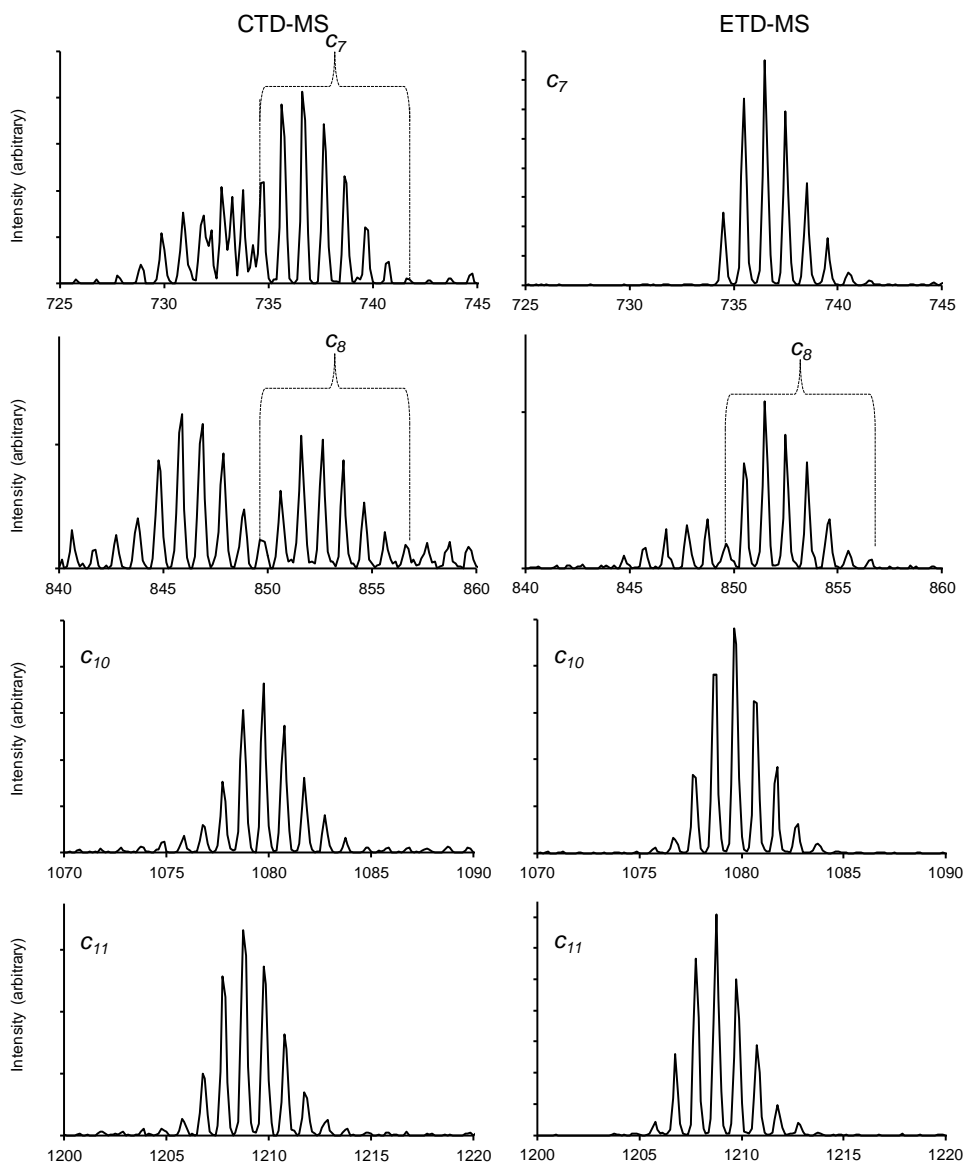
Because of the short interaction times, He-CTD is presumed to follow vertical activation (not adiabatic), and has been shown to fragment neutral molecules with appearance potentials on the order of 30 eV.[12] He-CTD therefore activates precursor ions through electronic and vibration modes. Fragment ions that result from both vibrational and radical (electronic) processes. Fragment ions can be seen in Figure 5.2A and 5.2B where several *y*, *b*, *c* and *z* ions were identified. However, it is instructive to consider the *c* ion series from our tandem MS measurements. He-CTD is performed with He^+ cations emitted with high kinetic energy (6 KeV) from the saddle field source. The main purpose of kiloelectronvolt energies is to overcome the Coulombic barrier of cation/cation reactions. Perhaps because of inelastic transfer of energy during result from proximal reagent He^+ ions abstracting an electron (EA ~24.6 eV) and creating a hole in the precursor ions. In turn, the electron deficient ion undergoes radical fragmentation, where the abstraction of an electron at the carbonyl leads to a McLafferty

rearrangement of an amide that is radical-driven. A γ -H[•] transfer from the side chain to the carbonyl produces a hydroxyl group and cleavage of the N-C α bond.

In contrast to *c* ions produced by ECD/ETD, this ion carries a positive charge at the hydroxyl group that is electron deficient. However, deconvolution of the isotopic distributions for He-CTD-generated *c* ion distributions that are very similar to those generated from ETD (Figure 5.3). That is, when considering singly-charged *c* ions from ETD, the charge site is presumably a protonated basic residue and would be 1 Da heavier than an oxidized, singly-charge *c* ion from He-CTD. It is possible that the *c ions* from He-CTD involve a double-hydrogen transfer during the rearrangement process. It is noteworthy to mention that several highly charged fragment ions may be observed in the He-CTD spectrum (Figure 5.2A and B) and are not clearly distinguishable for identification. The formation of *c*- and *z*-ions via electron transfer processes formed by irradiation of excited species[15, 16] has been previously reported. charge transfer, the activation energy obtained through He-CTD exceeds the electron affinity of the He⁺ cation and is on the order of 30 eV.[12] The formation of *c* ions can

Much like other electron based techniques, He-CTD fragmentation appears to occur rapidly and reflects a high energy, radical-driven mechanism. That is, dissociation occurs without significant proton mobilization or HD-scrambling. Furthermore, the modified QIT is operated at a relatively higher pressure (due to the saddle source and He gas flow) whereby any vibrationally excited ions are rapidly thermalized. With this in mind, the experimental results demonstrate that *c ions* resulting from He-CTD retain solution deuterium uptake levels.

In general, ETD and He-CTD product ions are similar. For example, Figure 5.3 shows a comparison between several c-ions as well as the charge reduced, singly-charged ions generated from both fragmentation methods. Both fragmentation techniques are very similar with regard to deuterium retention, isotopic distribution and relative intensity between isotopologues. This high degree of similarity further indicates, at least for these distinguishable ions, that He-CTD fragmentation of a 3+ precursor can proceed without HD-scrambling.



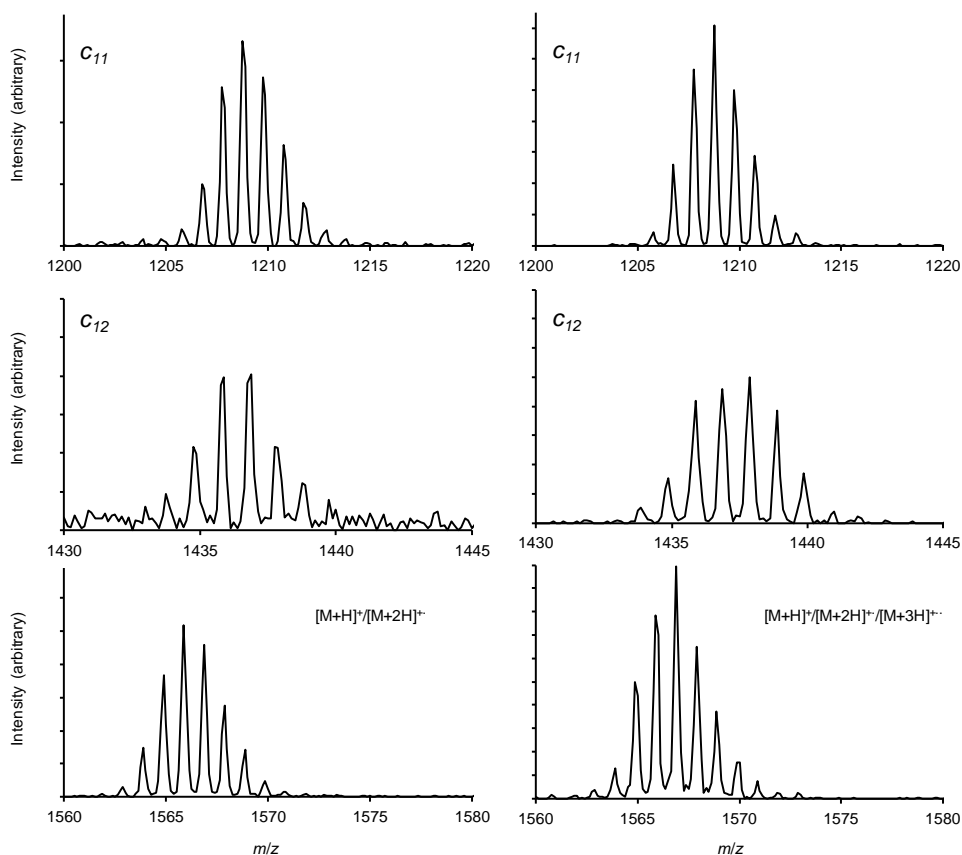


Figure 5.3. Left and right panels show identified deuterated *c*-ions resulting from He-CTD-MS and ETD-MS of KKDDDDDIKIIK after on-line DHX respectively. These panels allow comparisons to be made based on the deuterated isotopic distribution and relative abundances of the isotopologues. For the respective panels, these ions were used to generate values in Table 5.1. All spectra were collected under non-activating instrumental parameters. Each panel has resulted from a single replicate from the respective fragmentation techniques.

5.3.2. Ammonia Neutral Loss and N-terminal Scrambling

Due to the complexity of He-CTD fragmentation spectra, the wider isotopic distribution of deuterated product ions and the relatively low resolution of the QIT, some ions are not well resolved and accurate deuterium content determinations were not possible. The compilation of these limitations has resulted in reduced sequence coverage during DHX-He-CTD studies relative to ETD. This is especially true for the *N*-

terminal region of the model peptide, which is a region that is useful for assessing scrambling. Although the larger He-CTD *c ions* match the 0% scrambling values (Table 5.1), it should be noted that some studies have indicated a uniform deuterium content increases across these peptides.[11] In part, this is due to the higher population of heteroatom sites that become populated under energizing processes. With this in mind, other studies have shown that ammonia neutral loss of the N-terminal region following ETD can be used to assess scrambling in peptides.[10] Evaluation of the He-CTD spectrum for $[M+2H]^{2+}$ ions from the model peptide (Figure 5.2B) shows a notable abundance of intact precursor ions formed via electron transfer or H \cdot transfer resulting in charge reduced $[M+H]^+/[M+2H]^+$ molecular ions. Similar observations have been reported for $[M+2H]^{2+}$ angiotensin ions irradiated with a beam of high-energy plasma cations (air), in which electron transfer appeared to be the predominant mechanism for charge reduction.[13] ETD did not produce adequate fragmentation for discussion. Evaluation of the isotopic distribution (Figure 5.2B) of the charge-reduced molecular ion shows that it has a calculated mass that is ~ 1.4 Da greater than the average mass of the peptide. Also present in the He-CTD spectrum of $[M+2H]^{2+}$ ions (Figure 5.2B) is the presence of ammonia-loss product ions ($[M+H-NH_3]^+/[M+2H-NH_3]^+$). Figure 5.4A and B show the these ions and the charge reduced ions after He-CTD of unlabeled $[M+2H]^{2+}$ precursor ions, respectively. The difference between ions is calculated at 16.6 ± 0.1 Da and is consistent the loss of ammonia for $[M+H-NH_3]^+/[M+2H-NH_3]^+$ ions. The comparison of the charge-reduced ion and ammonia neutral loss ions can be used to monitor scrambling as performed previously for ETD.[10]

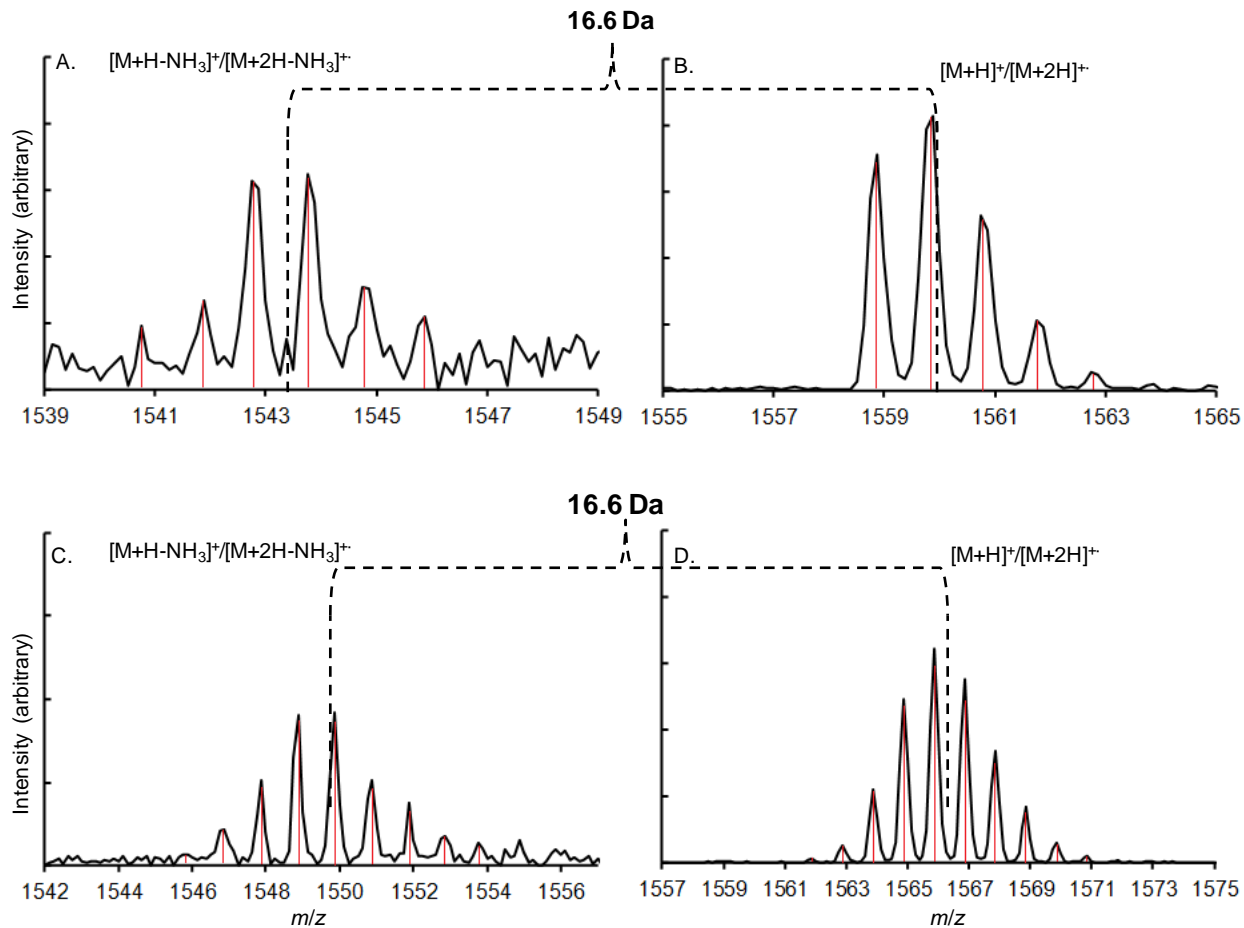


Figure 5.4. Isotopic distributions for (A) $[M+H-NH_3]^+/[M+2H-NH_3]^+$ ions and (B) $[M+H]^+/[M+2H]^+$ ions originating after MS-CTD of unlabeled $[M+2H]^{2+}$ model peptide precursor ions. Isotopic distributions for (C) $[M+H-NH_3]^+/[M+2H-NH_3]^+$ ions and (D) $[M+H]^+/[M+2H]^+$ ions generated from HDX-MS-CTD of $[M+2H]^{2+}$ model peptide precursor ions. The red lines show the centroid for each isotopologue used for m/z averaging calculations. Black dashed lines represent the average m/z determined from the isotopologues. The difference in the average m/z values between adjacent panels (i.e. A-B, C-D) were used for determining HD-scrambling (see text for details). In each adjacent panel the mass difference was calculated as the loss of ammonia.

He-CTD studies for the $[M+3H]^{3+}$ or $[M+2H]^{2+}$ precursor ions did not result in a full series of *c ions* required to fully evaluate HD-scrambling. Figures 5.4C and 5.4D shows the ammonia-loss and charge reduced ions upon DHX-He-CTD of $[M+2H]^{2+}$ precursor ions, respectively. The m/z difference (16.6 ± 0.1 Da) is very similar to that determined for the corresponding unlabeled ions. A statistical model[10] that considers

the overall deuterium content level and all exchangeable sites suggest that, in the case of 100% HD-scrambling, the deuterium content of the ammonia-loss ions would theoretically retain 5.7 deuteriums. Notably, the deuterium retention between the labeled and unlabeled ammonia-loss ions revealed a deuterium retention value of 6.3 ± 0.1 . The same total deuterium retention is also observed for the respective charge reduced ions (Figures 5.4B and 5.4D).

The agreement between the respective labeled and unlabeled product ions indicates that scrambling is not observed during the He-CTD fragmentation processes. That is, upon neutral ammonia loss from a precursor ion, the total deuterium level would be less than that of the intact ion. These results further indicate that HD-scrambling during the He-CTD process is largely not observed for the model peptide which has been specifically designed for HD-scrambling studies.[7]

5.3.3. DHX – He – CTD – MS Structural Determinations

With complementary scrambling models indicating that He-CTD generates *c ions* without proton mobilization, a proof-of-concept study was used to demonstrate structural determinations using ubiquitin as the model protein. Ubiquitin contains 144 labile hydrogens, where 72 are amide backbone, 69 are found on residue side chains and 3 sites are located on the *N*- and *C*-terminus. Using a continuous online microfluidic system, as described previously, DHX of labeled ubiquitin proceeded for ~48 seconds and resulted in the retention of $\sim 46 \pm 1$ deuteriums. This value was determined from the average *m/z* of undigested $[M+6H]^{6+}$, $[M+7H]^{6+}$ and $[M+8H]^{6+}$ ubiquitin ions. Presumably these deuteriums are located in structured regions of the protein rendering

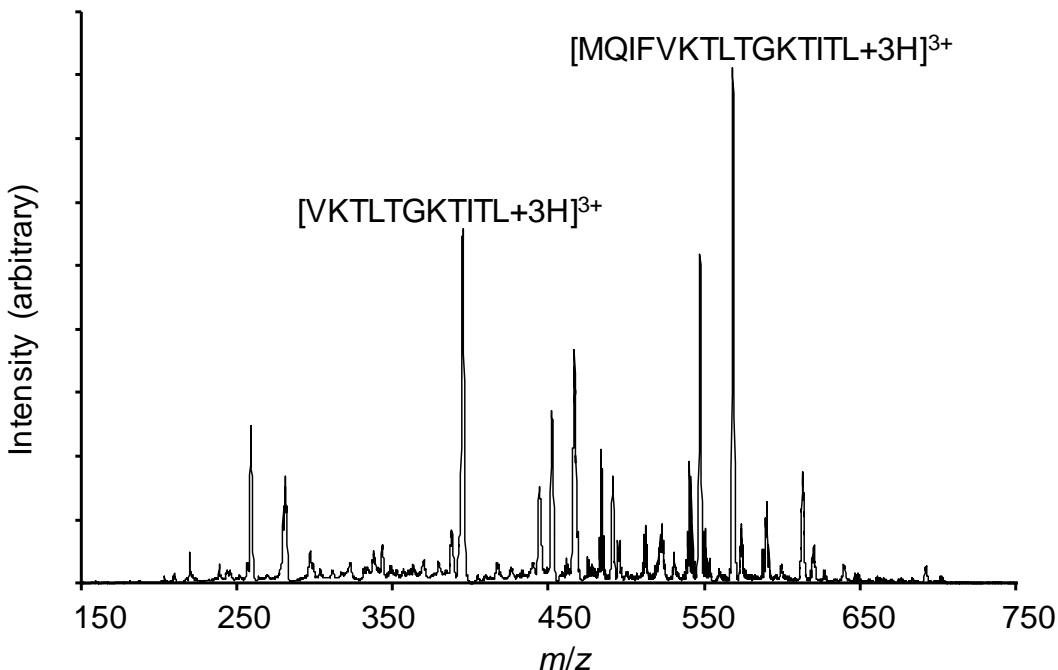


Figure 5.5. Full mass spectrum resulting from a single analysis of DHX-PD-MS of deuterated ubiquitin. The precursor ions used for He-CTD-MS and ETD-MS are labeled in the spectrum

them inaccessible to exchange during the time frame of the DHX process. For reference, Figure 4.4 (Chapter 4) shows the secondary structural features for ubiquitin as a function of the primary sequence. Known structural regions are composed of 5 beta-sheets (residues M¹-L⁷, G¹⁰-L¹⁵, Q⁴⁰-F⁴⁵, G⁴⁷-L⁵⁰ and S⁶⁵-R⁷²), an alpha-helix (I²³-E³⁴) and a 3/10 helix (L⁵⁶-Y⁵⁹).

Figure 5.5 shows the spectrum for a single replicate of labeled ubiquitin that has undergone the DHX and pepsin digestion (PD) prior to MS analysis. In general, most identified peptide ions appear to originate from the terminal ends of ubiquitin. These observations are similar to previous analyses using online DHX-PD-MS. This system was shown to be highly reproducible with respect to the observed peptide ions, the peptide deuterium content and the relative ion abundances.[14] Here, it is noted that the

goal of this work is to perform He-CTD on peptides originating from structured regions of labeled ubiquitin using an online DHX-PD-MS microfluidic system. The analysis is therefore limited to two peptide ions of the highest abundance that were present in all replicate studies.

5.3.3.1. Per – Residue ETD – MS Analysis: Control

[MQIFVKTLTGKTITL+3H]³⁺ ions generated from DHX-PD-MS measurements were selected for ETD analysis having a total deuterium retention level of 8.7 ± 0.6 . As before, deuterium content per-residue is calculated by subtracting the average mass of a given labeled c-ion from the average mass of the respective unlabeled c-ion. A lack of deuterium retention within a region of primary sequence is indicated by similar deuterium content levels for adjacent *c ions*. Evaluation of Figure 5.6A (red bars) shows deuterium retention beginning at I³ and increasing to T⁷. NMR[17, 18] and top-down MS/MS[3, 19] studies have shown strong protection across this region. In general, deuterium residue levels appear to correctly map the location of secondary structural elements. For example, no change in deuterium content is observed for residues L⁸-K¹¹ and values for residues T⁷-G¹⁰ are consistent with an unstructured turn between the first and second beta-strands. The deuterium content level (Figure 5.6A) is observed to increase across residues K¹¹-L¹⁵, which correctly correlates with the location of the second beta-strand (beginning at G¹⁰). Evaluating the deuterium content levels between residues G¹⁰ and K¹¹ shows a change by ~ 0.43 deuteriums. This small change suggests that residues on the fringe of secondary structural elements are less protected than residues that occupy locations within these elements.[20] For the ETD analysis of [MQIFVKTLTGKTITL+3H]³⁺ ions with respect to residue sequence coverage, ion

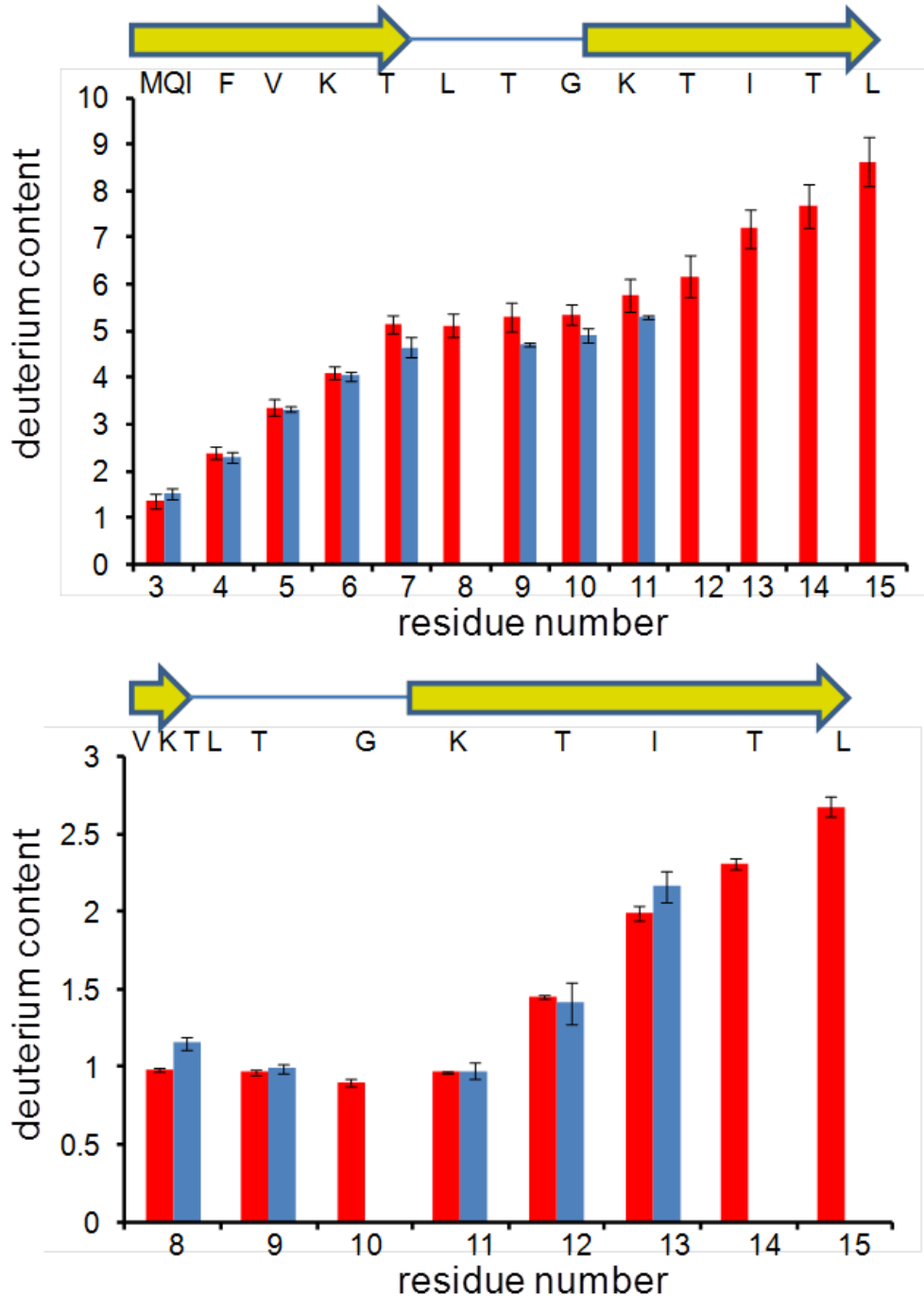


Figure 5.5 . (A) Bar plots show the total deuterium content per residue, n , calculated from the c_{n-1} product ions generated by ETD (red traces) and He-CTD (blue traces) from labeled $[MQIFVKTLTGKTITL+3H]^{3+}$ ions. The N-terminal region of ubiquitin spanning a beta strand (residues M¹-T⁷), turn (L⁸-G¹⁰) and second beta strand from (G¹⁰-L¹⁵) is also shown. (B) Total deuterium content plot for residues V⁵-L²⁵ generated by ETD (red traces) and He-CTD (blue traces) of labeled $[VKTLTGKTITL+3H]^{3+}$ ions. A section of the beta-stranded region and the second beta strand across residues V⁵-T⁷ and G¹⁰-L¹⁵, respectively, are also shown. The error was calculated from triplicate measurements of respective fragment ions.

deuterium content levels and qualitative structural trends are very similar to previous studies.[14]

Also originating from the N-terminal region, [VKTLTGKTITL+3H]³⁺ ions were investigated using DHX-PD-MS of labeled ubiquitin. Although the sequence overlaps significantly with [MQIFVKTLTGKTITL+3H]³⁺ ions, pepsin digestion at the carboxyl side of V⁵ significantly changes the deuterium content level. Figure 5.6B shows the deuterium content for *c ions* originating from [VKTLTGKTITL+3H]³⁺ precursor ions after HDX-ETD-MS of labeled ubiquitin. Evaluation of Figure 5.6B shows a deuterium content level of ~1 for residue T⁷ after HDX. A reduced deuterium level may be expected because much of the structured N-terminal region has been cleaved. Enzymatic digestion also reacts to form a primary amine from the backbone amide of V⁵, which can exchange (even under quench conditions) and further reduces the deuterium content level. Residues T⁷-G¹⁰ show no change in deuterium content, follow by an increase across residues K¹¹-L¹⁵. This trend is similar to that of [MQIFVKTLTGKTITL+3H]³⁺ ions (see above) and also appears to correctly map structured areas within ubiquitin.

5.3.3.2. Per – Residue He – CTD – MS Analysis

In order to provide direct comparisons between ETD and He-CTD fragment data for structural analysis, [MQIFVKTLTGKTITL+3H]³⁺ ions generated during HDX-MS were also selected for He-CTD experiments. Figure 5.6A shows the deuterium content level for *c ions* resulting from HDX-PD-He-CTD-MS. Evaluation of the deuterium content appears to begin at residue I³ and sequentially increases to T⁷. Interestingly, the deuterium content levels for these ions appear to be similar to the levels determined from ETD experiments. For example, the deuterium content for residues T⁷ - T⁹ appears

unchanged. This is consistent with the unstructured turn between beta-sheets as mentioned above. Although the deuterium content level is slightly lower than that determined by ETD, it is noteworthy that this region could have exchanged out to a higher degree before He-CTD studies. The highly structured region between I³-K⁶ shows similar deuterium content levels between ETD and He-CTD. A slight increase in deuterium content is observed for residue K¹¹ relative to T⁹. This trend is similar to that for the ETD analysis, where a small increase in deuterium content was observed for K¹¹. Together, these similarities suggest that He-CTD is capable of qualitatively determining areas of structure within labeled proteins and this further indicates that HD-scrambling is largely avoided.

Figure 5.6B shows the *c ions* resulting from HDX-He-CTD-MS of labeled [VKTLTGKTITL+3H]³⁺ ions. A very similar trend to that observed for ETD is noted for these ions. Residue T⁷ retains ~1 deuterium, which may be expected given the second peptic cleavage event between residues F⁴ and V⁵. As mentioned above, digestion converts the backbone amide to a primary amine that subsequently allows K⁶ to be accessible to exchange, further reducing the deuterium content. Reduced deuterium content has been reported in other peptides using pepsin digestion HDX-MS experiments.[21] The deuterium content level is unchanged across the unstructured region (T⁷ - T⁹) and appears to increase from G¹⁰-T¹². Residue G¹⁰ has a slightly lower deuterium content level reported for G¹⁰ from [MQIFVKTLTGKTITL+3H]³⁺ product ion determinations. Because this residue is located at the edge of the second beta-sheet, decreased protection may be expected.[20] However, other consistencies are noted. For example, the deuteration content increases at K¹¹ and is comparable with ETD data

(Figure 5.6B) as well as both experiments for [MQIFVKTLTGKTITL+3H]³⁺ ions (Figure 5.6A). Another consistency between ETD and He-CTD is the lower deuterium content level across the unstructured region, before the second beta-sheet, which was noted in Figure 5.6A.

Evaluation of both peptide ions reveals that He-CTD results in sequence coverage across residues M¹-I¹³ and allows for a qualitative view of secondary structure across the *N*-terminal region. For example, retention for the L⁸ residue was not observed in the He-CTD spectrum for [MQIFVKTLTGKTITL+3H]³⁺ ions; however, data for the L⁸ residue (Figure 5.6B) shows that deuterium content level is unchanged across residues L⁸-T⁹. As mentioned above, this observation is consistent with the unstructured turn between beta-sheets. Additionally, Figure 5.6B shows that deuterium content increases from T¹¹-I¹² which was also not observed upon He-CTD of [MQIFVKTLTGKTITL+3H]³⁺ ions. These residues are located within the second beta-strand and are expected to display a level of protection. Although He-CTD is currently not as efficient as ETD, the analysis from both precursor ions gives ~90 % sequence coverage across the *N*-terminal region of ubiquitin. Notably, these data are consistent with the known secondary structural elements within ubiquitin. Given the comparison between ETD and the resulting spectral consistencies, the compilation of these data suggest that HD-scrambling for is largely mitigated upon He-CTD.

5.4 Conclusion

Using ETD as the gold standard technique for per-residue HDX studies and a model peptide specifically designed to monitor HD-scrambling, separate experiments show that He-CTD generated *c ions* preserve the solution-phase deuterium label.

Generated *c ions* via ETD were used in a statistical analysis to determine instrumental parameters that resulted in 0 % HD-scrambling. Using these determined conditions, HDX-He-CTD-MS of $[M+3H]^{3+}$ labeled MP produced a series of *c-ions* that were compared to *c-ions* produced during ETD studies. Fragment *c-ions* produced by He-CTD were found to mirror a 0 % HD-scrambling trend based on theoretical ETD calculations. Because He-CTD efficiency is relatively low, a homologous series of either *ion* series was not generated. However, a complementary HDX-He-CTD-MS scrambling study using deammoniated product ions also revealed that HD-scrambling is mitigated. HD preservation was observed via the neutral loss of ammonia that was absent the incorporation of deuterium from labeled regions of the peptide. Using the determined non-scrambling conditions,

As a proof-of-concept study, a system for online HDX and pepsin digestion (PD) was combined with He-CTD for structural analysis of deuterium-labeled ubiquitin. Ions of highest abundance were selected and analyzed by ETD-MS and He-CTD-MS. Deuterium retention calculated from *c-ions* across residues M¹-L¹⁵ and V⁵-L¹⁵ are in good agreement with structural trends found in pre-residue studies using ubiquitin.[3, 14, 19] Lastly, ETD-MS and He-CTD-MS deuterium content level for the respective residues are highly similar. From these results it appears, at least for *c-ions*, that He-CTD may be used as a new technique for DHX structural studies of proteins.

5.5 References

1. Huang, R.Y.C., et al., *Hydrogen/Deuterium Exchange and Electron-Transfer Dissociation Mass Spectrometry Determine the Interface and Dynamics of Apolipoprotein E Oligomerization*. *Biochemistry*, 2011. **50**(43): p. 9273-9282.
2. Pan, J. and C.H. Borchers, *Top-down structural analysis of posttranslationally modified proteins by Fourier transform ion cyclotron resonance-MS with hydrogen/deuterium exchange and electron capture dissociation*. *Proteomics*, 2013. **13**(6): p. 974-81.
3. Pan, J., et al., *Electron Capture Dissociation of Electrosprayed Protein Ions for Spatially Resolved Hydrogen Exchange Measurements*. *Journal of the American Chemical Society*, 2008. **130**(35): p. 11574-11575.
4. Landgraf, R., M. Chalmers, and P. Griffin, *Automated Hydrogen/Deuterium Exchange Electron Transfer Dissociation High Resolution Mass Spectrometry Measured at Single-Amide Resolution*. *Journal of The American Society for Mass Spectrometry*, 2012. **23**(2): p. 301-309.
5. Rand, K.D., et al., *Protein Hydrogen Exchange Measured at Single-Residue Resolution by Electron Transfer Dissociation Mass Spectrometry*. *Analytical Chemistry*, 2009. **81**(14): p. 5577-5584.
6. Wysocki, V.H., et al., *Mobile and localized protons: a framework for understanding peptide dissociation*. *Journal of Mass Spectrometry*, 2000. **35**(12): p. 1399-1406.
7. Zehl, M., et al., *Electron Transfer Dissociation Facilitates the Measurement of Deuterium Incorporation into Selectively Labeled Peptides with Single Residue Resolution*. *Journal of the American Chemical Society*, 2008. **130**(51): p. 17453-17459.
8. Rand, K.D., et al., *Electron capture dissociation proceeds with a low degree of intramolecular migration of peptide amide hydrogens*. *J Am Chem Soc*, 2008. **130**(4): p. 1341-9.
9. Rand, K.D., et al., *Protein hydrogen exchange measured at single-residue resolution by electron transfer dissociation mass spectrometry*. *Anal Chem*, 2009. **81**(14): p. 5577-84.
10. Rand, K.D., et al., *Loss of Ammonia during Electron-Transfer Dissociation of Deuterated Peptides as an Inherent Gauge of Gas-Phase Hydrogen Scrambling*. *Analytical Chemistry*, 2010. **82**(23): p. 9755-9762.
11. Rand, K.D., M. Zehl, and T.J. Jorgensen, *Measuring the hydrogen/deuterium exchange of proteins at high spatial resolution by mass spectrometry: overcoming gas-phase hydrogen/deuterium scrambling*. *Acc Chem Res*, 2014. **47**(10): p. 3018-27.
12. Hoffmann, W. and G. Jackson, *Charge Transfer Dissociation (CTD) Mass Spectrometry of Peptide Cations Using Kiloelectronvolt Helium Cations*. *Journal of The American Society for Mass Spectrometry*, 2014. **25**(11): p. 1939-1943.
13. Chingin, K., et al., *Fragmentation of Positively-Charged Biological Ions Activated with a Beam of High-Energy Cations*. *Analytical Chemistry*, 2014. **86**(1): p. 372-379.
14. Donohoe, G.C., J.R. Arndt, and S.J. Valentine, *Online Deuterium Hydrogen Exchange and Protein Digestion Coupled with Ion Mobility Spectrometry and Tandem Mass Spectrometry*. *Analytical Chemistry*, 2015. **87**(10): p. 5247-5254.
15. Cook, S.L., O.L. Collin, and G.P. Jackson, *Metastable atom-activated dissociation mass spectrometry: leucine/isoleucine differentiation and ring cleavage of proline residues*. *Journal of Mass Spectrometry*, 2009. **44**(8): p. 1211-1223.
16. Misharin, A.S., et al., *Dissociation of peptide ions by fast atom bombardment in a quadrupole ion trap*. *Rapid Communications in Mass Spectrometry*, 2005. **19**(15): p. 2163-2171.
17. Johnson, E.C., et al., *Solution structure and dynamics of a designed hydrophobic core variant of ubiquitin*. *Structure*, 1999. **7**(8): p. 967-976.
18. Bougault, C., et al., *Quantitation of rapid proton-deuteron amide exchange using hadamard spectroscopy*. *Journal of Biomolecular NMR*, 2004. **28**(4): p. 385-390.

19. Sterling, H.J. and E.R. Williams, *Real-Time Hydrogen/Deuterium Exchange Kinetics via Supercharged Electrospray Ionization Tandem Mass Spectrometry*. *Analytical Chemistry*, 2010. **82**(21): p. 9050-9057.
20. Kaltashov, I.A., C.E. Bobst, and R.R. Abzalimov, *H/D Exchange and Mass Spectrometry in the Studies of Protein Conformation and Dynamics: Is There a Need for a Top-Down Approach?* *Analytical Chemistry*, 2009. **81**(19): p. 7892-7899.
21. Percy, A.J., et al., *Probing protein interactions with hydrogen/deuterium exchange and mass spectrometry—a review*. *Analytica chimica acta*, 2012. **721**: p. 7-21.

6. Future Directions: Applied 'Omics using IMS-MS Techniques

6.1. Post Translational Modifications: Phosphorylation

The IMS-CID-MS method was capable of determining the presence of phosphoserine and subsequently elucidating the site of modification. One advantage over traditional techniques was the ability to match product ions to respective precursors ions based on XIDTDs. Much of the matching capability is attributed high reproducibility of the mobility separation. Although, the experiment presented a proof-of-concept study, only a single phosphopeptide was considered. Future studies will conduct IMS-CID-ETD-MS experiments for a wider range of phosphopeptides. Here, it is noted that threonine and tyrosine are also capable of phosphorylation. Some studies have indicated that the fragmentation energetics and observed neutral losses are different for each phosphorylated residues.[1] This presents some challenges in determining a collision energy that is amendable across all phosphorylation possibilities. However, the ion activation region within the drift tube is highly tunable. Determining multiple ion activation voltages that can be stepped according to mobility is necessary for high throughput workflows.

6.1.1. Doubly – Phosphorylated Peptides from Complex Mixtures

With these critiques in mind, future experiments should not only address studies for a wider range of phosphorylated residues, but also residues that are doubly-modified. Some research has shown that hyper-phosphorylation is important for tauopathies.[2] Highly phosphorylated peptides may present the chance to observe unique fragment ions that are difficult to detect with traditional techniques. One difficulty

in detecting doubly phosphorylated peptides is that fragmentation may result in the neutral loss from both or a single residue. With traditional techniques using QqQ instrumentation, the last quad would have to be scanned quickly across several potential fragment ions to determine the presence of phosphorylation. Because many product ions are possible, selecting the correct fragment ion with high specificity would be difficult. As stated previously, one potential benefit may come from the ability to perform spectral matching based on XIDTDs where all product ions can be spectrally aligned back with the precursor ion.

6.1.2. Conducting IMS-CID-MS on Glycosylated Proteins

As a brief overview, glycosylation is a covalent post-translational modification occurring through enzymatic mechanisms often occurring within the golgi apparatus after protein synthesis at the ribosome.[3] Glycosylation is important for cellular recognition[4] and protein folding.[5] There are two classes of glycosidic bonds formed at the amide nitrogen of asparagines having a consensus sequence Asn-Xxx-Ser (where x cannot be proline) and at the hydroxyl oxygen of serine, tyrosine, and threonine. These respective classes are referred to as N- [6] and O-linked[7] glycosylation. Glycans themselves are complex structures consisting of branched, or unbranched, networks of oligosaccharides that are arranged through β 1-6 or β 1-4 glycosidic linkages.

Glycan structural elucidation is much more difficult than that described for peptides or proteins. Common MS/MS methods for glycan structural analysis use CID and UVPD to produce glycosidic cleavage ions.[8] It is noteworthy to mention that

GlcNAc and mannose are common moieties in glycan structures that produce fragment ion m/z values of 201, 202, 203 and 179 respectively. These fragment ions have been reported from $[M-H]^-$, $[M+H]^+$ and $[M+Na]^+$ precursor ions from ESI of non-reduced sugars.[8-10] Future experiments could use protein digests to rapidly scan for reporter fragment ions common for glycosylation (e.g. m/z 202 or 179). Using XIDTDs, the fragment ions can be related back to their respective precursor ion. Once matched, the precursor ions could then be mobility selected and isolated in the ion trap for ETD-MS. Since ETD retains PTMs, the modified residue could then be determined.

As described, the IMS-CID-ETD-MS method could potentially be used to scan for the presence of glycosylation events and identify modified residues. Because glycans are structurally diverse, another future experiment could attempt identifying the glycan from the modified protein. For these experiments, it is noted that linear ion traps suffer from low mass accuracy where high mass accuracy is often necessary for glycan identification. Considering this, the IMS-CID-ETD-MS method could offer potential targets for data dependent acquisition on mass spectrometers that achieve much higher mass accuracies (± 2 ppm). This may allow glycan identification based solely on high mass accuracy and library searching against known glycans.[3] Another possibility may be to use RNase for deglycosylation coupled with offline lectin affinity chromatography[11] or electrophoresis to isolate and purify glycans prior to MS analysis.[12] In this manner, glycans could be subjected to MS^n and their structures elucidated. Although this type of workflow would be lengthy, it combines the advantages of multiple platforms for increased structural detail.

6.2. Expanding the Usage of IMS-CID-MS in Metabolomic Workflows

The metabolite experiments presented in Chapter 2 were aimed at comparative metabolomic analysis. After PCA and MSⁿ the analyses found that lipids could be used to differentiate the sample cohorts. This allowed unique parallel CID analyses to be performed for rapid data independent workflows and identification. From these data it was observed that many ions were identified from lysophosphatidylcholines (LysoPC) precursors. In part this may be attributed to ESI bias towards LysoPCs. Across the two-dimensional t_D - m/z plot, it appears that this lipid class is oriented to occupy related conformation space. Such observations have also been shown by McLean and coworkers using a high-resolution drift tube. In these experiments the IMS-MS results suggested unique intrinsic molecular packing from four separate molecular classes (carbohydrates, lipids, quaternary ammonium salts and peptides).[13] Although such results represent the start of IMS-MS libraries for more accurate determinations, it is noted that these experiments can be extended by adding IMS-CID-MS.

McLean's conformational analysis of >300 lipid standards comprised of glucosylceramides, phosphatidylcholines, phosphatidylethanolamines, phosphatidylserine and sphingomyelin resulted in He_(g) CCS values, which ranged from 220 – 350 Å² over a m/z range of 800 – 1000.[13] These results suggest that lipids display similar intrinsic conformations in the gas phase. Theoretical metabolomic studies could benefit by matching mobility information with conformational libraries for qualitative analysis purposes. Given the similar CCS values across lipid classes, it still remains difficult to identify a specific lipid class. Even smaller lipids, such as LysoPCs (m/z ~500), shown in Chapter 2, demonstrated distinct drift times indicative of similar CCS values (although not reported).

Future experiments could be directed towards using similar lipid standards for IMS-CID-MS analysis. The goal would be to use the enhanced analytical space afforded by the mobility separation for fragment ions. This would allow the apparent CCS and m/z correlation between lipid classes to be broken. Similar experiments have been successfully applied to peptides. [14, 15] That is, fragment ions would have the same mobility as the precursor ion, but a better distinction between lipid classes would be made based on the m/z space. Here unique fragmentation patterns would emerge across a lipid class, even if two classes overlapped along the mobility separation. One important consideration is that the method would scan for the head region of the lipids. Not only does the region identify the lipid class, it represents a reporter ion and thus offers a spectral 'fingerprint' for lipid structure and class. Another important consideration is that the head region most often contains the charge site of the precursor ion. It is recalled that in Chapter 2, that the most dominant spectral features upon IMS-CID or MS/MS of LysoPC ions resulted from dissociation of the head region.

The application of IMS-CID-MS methodology for determining fine structural variation of lipid classes, expands on the concept of conformational ordering of biomolecules through fragment ions. The idea of using IMS-CID-MS to break CCS vs m/z correlations has been described for peptides.[16] It is felt, that this methodology would also expand mobility libraries for spectral matching and identification. It is noted that these libraries are in their infancy and the contributions of such results would be timely. These libraries are needed for data independent workflows, where high specificity and high throughput are at the heart of the technique.

6.3. Gas Phase HDX of Anionic Proteins

6.3.1. Comparing Cationic and Anionic HDX Deuterium Level: Structural Studies

Results of Chapter 3 report fundamental studies aimed at understanding protein-anionic structures in the gas phase. Through complementary studies involving IMS and gas phase HDX, insights into different conformers could be ascertained. One interesting observation was shown with compact and elongated conformations of ubiquitin that demonstrated different deuterium uptake values. This was attributed to the protein fold that allowed a greater exposure of exchangeable sites in elongated conformations that were otherwise inaccessible in relatively compact conformers. Other peptides contributing multimeric species showed reduced uptake and may be used in the future to indicate binding site interactions.

Some studies have indicated both similar and dissimilar conformations can be observed based on the polarity during native ESI-IMS-MS of smaller proteins.[17] Future directions may be able to compare protein cationic and anionic HDX values for different gas phase conformations. Here CCS values, exchange profiles and molecular dynamics may be able to show where protein conformations are different. This may also allow us to understand which residues are important for maintaining protein tertiary structures and how protein structure changes in the gas phase. By comparing the exchange profiles of both polarities a better picture of protein structure in the gas phase may emerge. For example consider a protein that has undergone ESI in negative polarity mode. In connection with CCS values and molecular dynamics, the HDX profiles may show how a particular portion of the protein becomes unfolded due to Coulomb repulsion of charge sites that is not experienced by the native solution structure. However, if we compare the complementary structure in positive mode, for

example, the HDX profiles and CCS values may not indicate any disruption of protein structure. Such results may direct better experimental conditions for determining more accurate CCS values and help future experiments determine the optimal polarity mode for CCS measurements.

6.3.2. Binding Faces of Acidic Proteins Involved in Protein Aggregates

An interesting area of research has been studying the binding interfaces of protein oligomers. Two candidate proteins that display a high number of acidic residues are α -synuclein and beta amyloid which form protein aggregates in Parkinson's and Alzheimer's diseases respectively. Acidic residues, such as aspartic acid and glutamic acid have pK_a s ~ 2.0 , giving these residues a negative charge in solution. Given the argument that different polarities can induce structural changes, a gas phase HDX experiment of anions may be used to ascertain interstitial binding faces of oligomeric proteins. Future experiments could incubate α synuclein over a defined period of time to induce oligomerization followed by native ESI in negative ion mode. The gas phase ions could then be labeled using negative gas phase HDX. A recent study by Arndt and coworkers showed reduced deuterium uptake for Nt17 heterodimer associated with the Huntington's protein in positive polarity mode (unpublished results). IMS coupled with molecular dynamics, the study revealed an anti-parallel arrangement of stacked α -helices that were involved into multimerization. A similar negative polarity method could benefit acidic protein studies that present oligomeric species.

6.3.3. Gas Phase HDX and Anionic Glycans: Structural Considerations and Separation Techniques

Lastly it is noted that glycans can be analyzed in negative polarity mode. Using IMS-MS, some studies have revealed that glycans display diverse structures in the gas phase. This is thought to be attributed to different gas-phase conformers as well as isomeric species. A method using negative mode gas phase HDX may be able to help differentiate glycans based on drift profiles and HDX uptake. Glycans appear to be strong candidates for HDX based on the high numbers of hetero-atomic groups (e.g. OH). Given that the HDX process is highly dependent on charge site location and proximal hetero-atomic sites, different HDX level could be expected based on glycan structure. Exchange distances have been optimized for cytochrome c conformers[18, 19] and peptide ion species.[20, 21] That is exchange occurs for species that are within threshold distances of charge sites and any accessible heteroatom may undergo exchange. For example, a branched moiety that is accessible for exchange based on a charge site proximity model, may be expected to undergo HDX. Comparatively, another glycan may have alternate branching resulting in decreased accessibility for exchange. It is also noted that the IMS is used as the isotopic labeling cell. That is, if glycan exchange profiles are different, they are no longer isobaric and can be separated based on the deuterated m/z values. Such results may be capable of differentiating glycans in the gas phase and further understanding glycan structure.

6.4. Solution – Based DHX Coupled with IMS-ETD-MS

6.4.1. Constructing a New Micro-fluidic Chip for On – Line Analysis

For DHX-IMS-ETD-MS experiments, the on-line system was constructed using high efficiency mixing-Tees and unfused silica capillary interfaced to a hand-pulled ESI

emitter tip. Future experiments could aim at constructing a micro-fluidic system. Here, a three-layer chip could be built. The center layer would be capable of introducing protein and exchange solution to a common point where mixing would occur. Over a defined length of an inner channel, exchange could proceed over a defined (controlled) period of time. Orthogonal to the exchange channel, an inlet for ice-cooled pepsin digestion solution would tee into the exchange channel and quench the reaction. This would also simultaneously cause digestion over a determined length. An outlet for digested sample could lead at the ESI source. The bottom layer would act to jacket the second layer from the quench solution to the outlet for ESI. This layer would use a continuous flow of cooled solution ($\sim 0^\circ\text{C}$) that would insure the quench/digestion region was maintained at $\sim 0^\circ\text{C}$. Lastly the top layer would act to encase the other two layers. A chip based system would be much more controllable and reproducible than the fused silica capillary reported in Chapter 3.

6.4.2. Increasing Sequence Coverage for Per-residue Studies

Another future direction would be to increase the per-residue sequence coverage afforded by ion fragmentation. In part, many of the peptides observed in Chapter 4 were doubly-charged, making efficient fragmentation via ETD difficult. Recently it has been shown that nitrobenzyl alcohol can increase the charge states of proteins without altering protein solution structure or HDX kinetics.[22] Here, an inlet for the infusion of nitrobenzyl alcohol could follow the pepsin digestion region to aid in increasing the charge state of peptides. Termed a supercharging agent,[23] such methodology may be beneficially for ETD per-residue studies employing a bottom-up approach.

6.4.3. Evaluating Larger Proteins

Chapter 4 studies used the small model protein ubiquitin to provide a proof-of-concept study aimed at combining drift tube IMS to DHX workflows. It is noted that in order to fully test the capabilities of the on-line IMS-ETD-MS system, a larger protein would be needed. For example, monoclonal antibodies are composed of two heavy (~50 kDa) and two amino acid light chains (~25 kDa) linked together via disulfide-bonds around the Fc region. Collectively these proteins are 150 kDa and would offer a much larger protein for study. It is also noted that pepsin cannot digest disulfide bonds. This may present other potential modifications to the microfluidic chip (see above) that could include an electrochemical reduction region after the DHX region, or other inlet ports for tris(2-carboxyethyl)phosphine (TCEP) or iodoacetamide for disulfide bond reduction prior to pepsin digestion.

6.4.4. Connecting Rapid Solution Structural Changes with Solution DHX and IMS-MS

Future experiments may be able to use a chip-based system combined with DHX-IMS-ETD-MS to rapidly monitor protein structural transformations. Here a deuterated protein could be infused and combined with a denaturant (H₂O:methanol) at the mixing port. It is important to note that that infusion of methanol would change DHX kinetics, thus no kinetic experiments would be conducted. Instead, the goal would be to monitor global deuterium levels resulting from different solution conformations at a single time-point. Capturing these changes would be dependent on the timescale of the structural transition as well as the allowed exchange period. Some studies have used a similar device to study structural changes after mixing ubiquitin with H₂O:methanol

(40:60) solution. The study indicated 2 dominant separate structures that were present for ~5 minutes.[24] After this time, the more native conformation merged into a single altered conformation. These structures were monitored using DHX after a 4 minute exchange out period. Notably, the separate conformers displayed different deuterium retention values. With this in mind, future experiments could perform a similar study aimed at connecting solution conformations using DHX with different gas phase structures determined by IMS. Such results may be able of linking solution structural changes to gas phase structures based on deuterium retention and CCS values.

6.5. Helium Charge Transfer Dissociation : Insights and Future Outlook

The low efficiency of the CTD process, coupled with the low resolution of the QIT and the complexity of CTD fragmentation reduced the number of distinguishable *c ions* in both HD-scrambling and structural studies. Future experiments will tailor the gas flow and emission energy of the cation beam to influence the efficiency and potentially the fragmentation characteristics in a more controlled fashion. Although not fully demonstrated in this study, CTD offers the ability to fragment lower charge state ions with high energy, radical-driven processes that would otherwise yield charge reduction during ETD. With this, future experiments would aim to fragment doubly- and singly-charged cations in order to determine deuterium content values. Such a method would significantly enhance *pe* –residue deuterium measurement and sequence coverage.

6.5.1. Using He – CTD for Anionic Peptides and Proteins

Future studies could also use He-CTD to fragment anionic peptides and proteins in the gas phase. Similar experiments have been reported for Xe cations irradiated with

negatively-charged peptides. The resulting fragmentation mechanism, termed negative electron transfer dissociation (nETD), is the reverse of the ETD process. Because He-CTD was shown to produce fragment ions without HD-scrambling for cationic species, perhaps the fragmentation technique could be used for anionic peptides and proteins. Indeed, part of the reason for exploring other fragmentation methodologies was to assess the possibility of combining such a technique with gas-phase HDX for per-residue studies.

6.5.2. Evaluating Other Ions for HD-Scrambling

Lastly, He-CTD produced a series of *a*-ions that may be beneficial for per-residue deuterium determinations. These fragments appear to result from radically driven processes similar to those described for ultraviolet photodissociation. That is, *a*-type ions result from homolytic cleavage of the C-C_α bond to form *a_n* and *a_n+1* ions. These *a+1* ions suggest that secondary dissociation of *b*-ions to form *a*-ions is not the dominant fragmentation pathway; however, such reactions cannot be ruled out. Future experiments may be able to determine if *a*-ions undergo HD-scrambling for use in structural studies.

6.5.3. Other Potential Usages; He – CTD – IMS – MS

Although, He-CTD results were proof-of-concept and are intended for qualitative comparisons, it is instructive to present a potential use of He-CTD for protein structural studies in which low charge states are more representative of native solution conditions.[25-27] Here, it is noted that much of IMS-MS measurements are directed at native-like conformations that may persist in the gas phase. Often, these native

conformations are low charge states and difficult to fragment with electron driven fragmentation. It has also been shown that for large protein complexes, CID produces charge asymmetric dissociation.[28] Considering this, it may be fruitful to develop new fragmentation techniques that address these problems. Certainly future experiments could leverage the advantages of cationic fragmentation and combine the technique with IMS-MS to analyze native protein complexes. Such experiments may open the door to new 'omics' analyses.

6.6. Ref

1. Palumbo, A.M., et al., *Tandem mass spectrometry strategies for phosphoproteome analysis*. Mass Spectrometry Reviews, 2011. **30**(4): p. 600-625.
2. Wang, J.Z., et al., *Abnormal hyperphosphorylation of tau: sites, regulation, and molecular mechanism of neurofibrillary degeneration*. J Alzheimers Dis, 2013. **33** **Suppl 1**: p. S123-39.
3. Zhu, Z.K. and H. Desaire, *Carbohydrates on Proteins: Site-Specific Glycosylation Analysis by Mass Spectrometry*, in *Annual Review of Analytical Chemistry, Vol 8*, R.G. Cooks and J.E. Pemberton, Editors. 2015. p. 463-483.
4. Wolfert, M.A. and G.J. Boons, *Adaptive immune activation: glycosylation does matter*. Nature Chemical Biology, 2013. **9**(12): p. 776-784.
5. Xu, C. and D.T.W. Ng, *Glycosylation-directed quality control of protein folding*. Nature Reviews Molecular Cell Biology, 2015. **16**(12): p. 742-752.
6. Apweiler, R., H. Hermjakob, and N. Sharon, *On the frequency of protein glycosylation, as deduced from analysis of the SWISS-PROT database*. Biochim Biophys Acta, 1999. **1473**(1): p. 4-8.
7. Zauner, G., et al., *Protein O-glycosylation analysis*. Biological Chemistry, 2012. **393**(8): p. 687-708.
8. Ko, B.J. and J.S. Brodbelt, *193 nm Ultraviolet Photodissociation of Deprotonated Sialylated Oligosaccharides*. Analytical Chemistry, 2011. **83**(21): p. 8192-8200.
9. Ritchie, G., et al., *Identification of N-linked carbohydrates from severe acute respiratory syndrome (SARS) spike glycoprotein*. Virology, 2010. **399**(2): p. 257-269.
10. Zhu, F., et al., *Mannose7 glycan isomer characterization by IMS-MS/MS analysis*. J Am Soc Mass Spectrom, 2012. **23**(12): p. 2158-66.
11. Alley, W.R., B.F. Mann, and M.V. Novotny, *High-sensitivity Analytical Approaches for the Structural Characterization of Glycoproteins*. Chemical Reviews, 2013. **113**(4): p. 2668-2732.
12. Alley, W.R. and M.V. Novotny, *Structural Glycomic Analyses at High Sensitivity: A Decade of Progress*, in *Annual Review of Analytical Chemistry, Vol 6*, R.G. Cooks and J.E. Pemberton, Editors. 2013. p. 237-265.
13. May, J.C., et al., *Conformational Ordering of Biomolecules in the Gas Phase: Nitrogen Collision Cross Sections Measured on a Prototype High Resolution Drift Tube Ion Mobility-Mass Spectrometer*. Analytical Chemistry, 2014. **86**(4): p. 2107-2116.
14. Koeniger, S.L., et al., *An IMS-IMS analogue of MS-MS*. Analytical Chemistry, 2006. **78**(12): p. 4161-4174.
15. Hoadlund-Hyzer, C.S., J.W. Li, and D.E. Clemmer, *Mobility labeling for parallel CID of ion mixtures*. Analytical Chemistry, 2000. **72**(13): p. 2737-2740.
16. Merenbloom, S.I., et al., *IMS-IMS and IMS-IMS-IMS/MS for separating peptide and protein fragment ions*. Anal Chem, 2006. **78**(8): p. 2802-9.
17. Allen, S.J., A.M. Schwartz, and M.F. Bush, *Effects of Polarity on the Structures and Charge States of Native-Like Proteins and Protein Complexes in the Gas Phase*. Analytical Chemistry, 2013. **85**(24): p. 12055-12061.

18. Valentine, S.J. and D.E. Clemmer, *H/D exchange levels of shape-resolved cytochrome c conformers in the gas phase*. Journal of the American Chemical Society, 1997. **119**(15): p. 3558-3566.
19. Valentine, S.J. and D.E. Clemmer, *Temperature-dependent H/D exchange of compact and elongated cytochrome c ions in the gas phase*. Journal of the American Society for Mass Spectrometry, 2002. **13**(5): p. 506-517.
20. Khakinejad, M., et al., *Combining ion mobility spectrometry with hydrogen-deuterium exchange and top-down MS for peptide ion structure analysis*. J Am Soc Mass Spectrom, 2014. **25**(12): p. 2103-15.
21. Khakinejad, M., et al., *Gas-Phase Hydrogen-Deuterium Exchange Labeling of Select Peptide Ion Conformer Types: a Per-Residue Kinetics Analysis*. J Am Soc Mass Spectrom, 2015.
22. Sterling, H.J. and E.R. Williams, *Real-time hydrogen/deuterium exchange kinetics via supercharged electrospray ionization tandem mass spectrometry*. Anal Chem, 2010. **82**(21): p. 9050-7.
23. Sterling, H.J. and E.R. Williams, *Origin of Supercharging in Electrospray Ionization of Noncovalent Complexes from Aqueous Solution*. Journal of the American Society for Mass Spectrometry, 2009. **20**(10): p. 1933-1943.
24. Hoerner, J.K., H. Xiao, and I.A. Kaltashov, *Structural and Dynamic Characteristics of a Partially Folded State of Ubiquitin Revealed by Hydrogen Exchange Mass Spectrometry†*. Biochemistry, 2005. **44**(33): p. 11286-11294.
25. Clemmer, D.E. and M.F. Jarrold, *Ion Mobility Measurements and their Applications to Clusters and Biomolecules*. Journal of Mass Spectrometry, 1997. **32**(6): p. 577-592.
26. Shelimov, K.B. and M.F. Jarrold, *Conformations, Unfolding, and Refolding of Apomyoglobin in Vacuum: An Activation Barrier for Gas-Phase Protein Folding*. Journal of the American Chemical Society, 1997. **119**(13): p. 2987-2994.
27. Shelimov, K.B., et al., *Protein Structure in Vacuo: Gas-Phase Conformations of BPTI and Cytochrome c*. Journal of the American Chemical Society, 1997. **119**(9): p. 2240-2248.
28. Wysocki, V.H., et al., *Surface-Induced Dissociation of Small Molecules, Peptides, and Non-covalent Protein Complexes*. Journal of the American Society for Mass Spectrometry, 2008. **19**(2): p. 190-208.

Appendix 1

Optimized Parameters Used for DHX-IMS-ETD-MS

Nano-ESI Parameters

Spray voltage (kV): 1.9

Desolvation Temperature (°C): no direct application

IMS Parameters

Source Funnel 1 DC voltage (V): 136.8

Funnel 2 RF voltage (V): 136.8

IMS length (meters): 1.00

Buffer Gas (g): He

Drift Pressure (torr): 2.72

Drift Field ($V\cdot cm^{-1}$): ~10

Gate 1 Trapping Containment Voltage (V): 25.0

Gate 2 (V): 7.5 V

Buffer Gas Temperature (K): ~300

Mass Spectrometer Parameters (LTQ Velos)

Ion Optics

Multipole 00 Offset (V): -2.00

Lens 0 Voltage (V): -3.00

Multipole 0 Offset (V): -8.00

Lens 1 Voltage (V): -10.00

Gate Lens Voltage

Multipole 1 Offset (V): -12.00

Multipole 1 Amplitude (V p-p): 300

Front Lens (V): -8.50

Appendix 2

Optimized Parameters Used for DHX-He-CTD-MS

ESI Parameters

Spray voltage (kV): 4.5

Desolvation Temperature (°C): 100

Instrumental Parameters: Bruker ETD AmaZon Quadrupole Ion Trap

Capillary Exit (V): 50

Funnel 1

RF (V): 130.0

In (V): 50.0

Out (V): 50.0

Lens (V): 15.0

Funnel 2

RF (V): 130.0

In (V): 12.0

Out (V): 10.0

Lens (V): 3.3

Octopole

RF(V): 75.0

1 DC (V): 2.3

Partition (V): 1.7

2 DC (V): 1.1

Focus 1

L1 (V): 0.5

L2 (V): -10.0

L3 (V): -6.0

L4(V): -6.0

Multipole:

RF(V): 36.7

DC(V): -4.0

Focus 4

L1(V): -4.0

L2(V): -5.0

L3(V): -75.0

Trap Drive: 40.0 %

**Expanding the Applications of Ion Mobility Spectrometry and Mass Spectrometry
in Integrative 'Omics Analyses**

Gregory C. Donohoe

**Dissertation submitted to the Eberly College of Arts and Sciences
at West Virginia University in partial fulfillment of the requirements
for the degree of**

Doctor of Philosophy in Chemistry

C. Eugene Bennett Department of Chemistry

APPROVAL OF THE EXAMINING COMMITTEE



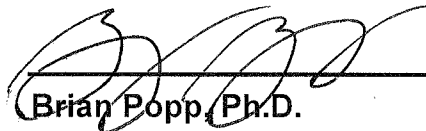
**Stephen Valentine, Ph.D.,
Chair**



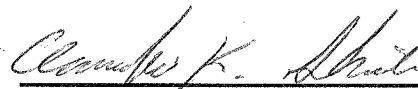
Lisa Holland, Ph.D.



Fred King, Ph.D.



Brian Popp, Ph.D.



Andrew Shiemke, Ph.D.

4-18-16

Date